Photothermal and Photoelectric Effects in Lithium-Ion Batteries: Mechanistic Insights and Performance Enhancement

Lifu Tan

Department of Engineering
University of Cambridge

This dissertation is submitted for the degree of
Doctor of Philosophy

Queens’ College July 2024

Declaration

This thesis is the result of my own work and includes nothing which is the outcome of work done in collaboration except as declared in the preface and specified in the text. It is not substantially the same as any work that has already been submitted, or, is being concurrently submitted, for any degree, diploma or other qualification at the University of Cambridge or any other University or similar institution except as declared in the preface and specified in the text. It does not exceed the prescribed word limit for the relevant Degree Committee

Lifu Tan
July 2024

Abstract

The growing demand for reliable, sustainable off-grid power solutions is especially significant for Internet of Things (IoT) devices. Solar energy, as a widely available renewable resource, has advanced energy-harvesting and storage technologies. Traditional solar-to-electricity setups rely on separate components, leading to larger device footprints and challenges with output voltage mismatches. This research explores an optimized, integrated system that combines light-harvesting and energy storage using a shared electrode, reducing device size and enhancing efficiency.

The key innovation lies in the material selection for the shared electrode, balancing electrochemical performance and photoactivity. To start with, graphitic carbon nitride and bismuth vanadate were selected as potential photo-active materials for photo-enhanced batteries. However, they were proven to be not suitable for the application from their electrochemical measurement due to the low capacity and degradation. Prussian blue analogues (PBAs) were then selected for their photothermal heating efficiency and compatibility as cathodes in photothermal-enhanced Li-ion batteries. Electrochemical testing under illuminated and dark conditions demonstrated that light-induced heating boosted battery performance, increasing capacity by up to 38% at high current densities. EIS measurements further confirmed reduced charge transfer resistance with illumination, underscoring the critical role of photothermal effects. A novel measurement technique, named impedance-based internal temperature estimation, clarified the impact of photothermal effects on battery performance. This study provides insights into how material properties and bias voltages can balance photothermal and photo-generated charge effects, advancing our understanding of photo-induced processes.

Furthermore, an in-depth examination of band alignment between the photoelectrode and counter electrode highlighted the mechanisms of charge transport, differentiating between photothermal and photoelectric effects through ultraviolet photoelectron spectroscopy (UPS) and UV-Vis spectroscopy in Li-ion batteries by using semiconducting metal oxide including anatase/rutile TiO_2 and Fe_2O_3. Results indicated that photothermal effects dominated at the applying voltage which is below the energy gap between the conduction band minimum and Li plating/stripping potential, while a higher bias voltage activated photoelectric effects by band-bending at the interface, revealing the influence of band alignment on charge transport. Overall, this work illustrates that the processes taking place in photo-batteries are intricate, and it offers new electrochemical protocols and techniques to gain insight into the mechanisms that govern the changes in behaviour when illuminating photo-batteries.

In conclusion, this work contributes valuable insights into integrating light-harvesting with energy storage systems, emphasizing the importance of material selection, photothermal effects, and precise measurement techniques. These findings support future advancements in photo-rechargeable batteries and sustainable energy technologies.

Acknowledgements

This PhD journey has been incredibly rewarding and challenging, and I owe its completion to the support and guidance of many individuals.

I would like to express my deepest gratitude to my supervisor, Prof. Michael De Volder. His patience, responsiveness, and kindness have been invaluable throughout my research. Despite my frequent weekend emails, meeting requests, and ordering notifications from EDRS, he has always been incredibly supportive and understanding. I am especially thankful to Dr. Buddha Deka Boruah for teaching me about photo-rechargeable batteries at the start of my PhD. His enthusiasm and dedication greatly helped me adapt to PhD research. I also express my gratitude to Dr. Sulki Park for assisting me with XRD. Additionally, I owe a debt of gratitude to Dr. Byungman Kim, Arvind Pujari, and Dr. Kohei Shimokawa. Our insightful scientific discussions as part of the photobatteries group provided tremendous help throughout my research. I acknowledge the funding and support from the ERC via Consolidator Grant (Mighty 866005) and the Cambridge Graphene Centre.

I also extend my gratitude to my friends in Cambridge, especially Mr. Hao Chen and Mr. Yang Wu, for their companionship and support during challenging times, particularly during the pandemic. Our shared experiences of conversations, dinners, playing sports, and laughing were always refreshing and recharging.

I could not have embarked on this journey without the unwavering support of my parents, Mr. Deqiang Tan and Mrs. Li Shen. I thank them deeply from the bottom of my heart for their love and encouragement. Lastly, I am profoundly thankful to my dearest partner, Jingchen Zhao, for her incredible support throughout my entire PhD journey. She has been with me every step of the way, witnessing my highs and lows. Meeting her three years ago was truly a blessing, and I am incredibly fortunate to have her by my side.

Table of contents

List of figures

List of tables

Chapter 1

Introduction

1.1 Photo-rechargeable energy storage devices

1.1.1 Background

In today's world, global energy consumption has surged dramatically, driven by population growth, climate change, and expanding human activities. [2, 3] Transportation, in particular, has become one of the most energy-intensive sectors. As a result, traditional non-renewable fossil fuels like coal, oil, and natural gas are becoming increasingly limited, raising concerns about future energy supply. Moreover, their extraction and combustion produce substantial greenhouse gas emissions, contributing to climate change and environmental degradation. [4] In this context, nuclear energy emerges as a powerful complementary solution. With its ability to generate large quantities of electricity without carbon emissions during operation, nuclear energy provides a stable, high-density power source that can effectively support the clean energy transition. However, its scalability and deployment limitations render it less feasible for widespread residential use. Consequently, renewable energy sources are being explored as sustainable alternatives to meet the rising global demand for energy. Among these, solar energy stands out as a promising solution due to its abundance, cleanliness, and scalability.

Solar energy holds immense potential, with the Earth's surface receiving approximately 100,000 terawatts of solar power every hour—far surpassing the annual global energy consumption. [5] Solar panels have become a key technology in reducing carbon emissions and dependence on non-renewable resources. From small residential rooftops to large-scale solar farms, solar power systems are widely adopted across the globe. [6–11] To date, all types of hybrid devices of solar cells have benefited the whole world greatly. By 2024, global installed solar capacity is expected to exceed 400 gigawatts. However, with the rapid expansion of solar energy adoption, the development of efficient energy storage systems is crucial to ensuring its long-term viability. [12–20]

One of the major challenges is efficiently storing solar energy for later use. [21–23] While significant progress has been made in solar-to-thermal, solar-to-biomass, and solar-to-electrochemical energy conversion, solar-to-electrochemical and solar-to-thermal energy storage systems stand out due to their high conversion efficiency, scalability, and flexibility. [24–32] In solar-to-electrochemical systems, the device typically consists of two main components: a solar cell to harvest energy and an electrochemical energy storage device (such as a rechargeable battery or supercapacitor) to store the energy. Traditional silicon-based photo-rechargeable devices are already used in various industries, powering portable electronics, wearable technology, outdoor gear, and off-grid equipment, as well as supporting smart city infrastructure and military applications. [33, 34]

Despite the widespread use of these energy devices, their current configuration, where the solar cell and energy storage system are separate, introduces complexities such as additional wiring and reduced energy efficiency. [35, 36] To overcome these challenges, integrating the solar cell and energy storage unit into a single device can drastically reduce the size and weight, enhancing portability and usability. Research has shown that combining these components with a shared electrode minimizes the device footprint while significantly improving gravimetric energy density by reducing ohmic losses.

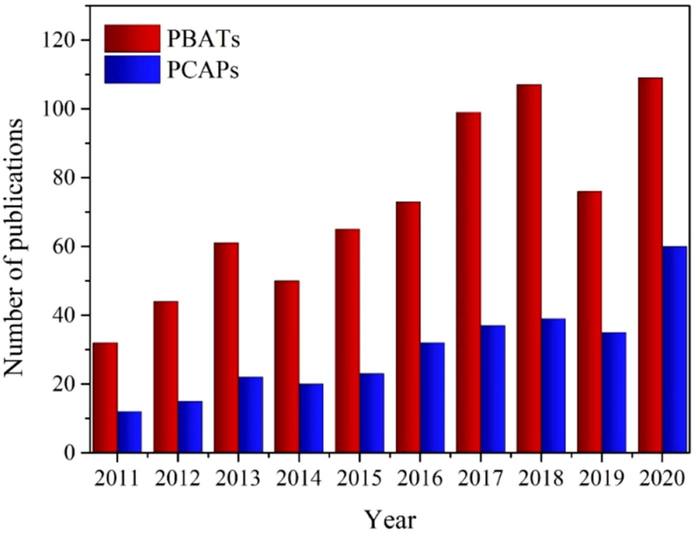

Fig. 1.1 Annual publication number on integrated photobatteries (red) and photocapacitors (blue) [37]

A novel approach is to integrate the solar harvesting and electrochemical energy storage units into one system using a shared electrode. This design eliminates the need for wire connections, resulting in more compact devices with higher flexibility, enhanced safety, and a better volume-to-weight ratio. While integrated photo-rechargeable devices such as photobatteries, photocapacitors, and photo redox flow batteries have shown promise, they remain largely confined to laboratory settings due to their low energy conversion efficiency. [38–49] As illustrated in Figure 1.1, the number of publications on integrated photo-induced devices has increased significantly since 2011, with photo-rechargeable batteries receiving the most attention due to their high energy density and capacity stability. [37]

For instance, photo-rechargeable lithium-ion batteries are heavily researched due to their high theoretical energy density of 3560 Wh/kg, while zinc-ion batteries are gaining traction for their low cost, safety, and high specific capacity of 820 mAh/g. [50–52] The key to enhancing these systems lies in the development of photoactive materials that are efficient in both energy storage and light-to-electricity conversion. Materials such as LiV_2O_5, V_2O_5, VO_2, and $g-C_3N_4$ have demonstrated the potential to fulfill this dual role, making them ideal candidates for future integrated photo-rechargeable energy devices. [53–58]

In summary, while significant strides have been made in solar energy and photo-rechargeable systems, continued innovation in material development and device integration is essential for addressing scalability and efficiency challenges, ultimately contributing to a more sustainable energy future.

1.1.2 Recent development of photo-rechargeable applications

Compared to conventional solar cell systems, integrated photo-rechargeable batteries use photoelectrodes to both convert and store energy from sunlight. Photobatteries can be classified into different categories based on factors such as the number of electrodes, electrochemical composition, or the active material in the photoelectrode.

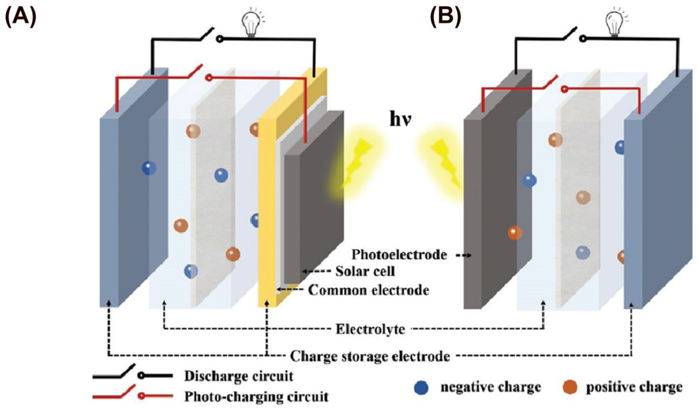

Fig. 1.2 Types of layout for photo-rechargeable batteries: (a) three-electrode, (b) two-electrode.[37]

One of the earliest reported photobatteries utilized a three-electrode system based on cadmium selenide/sulfur/silver sulfide (CdSe/S/Ag_2S). [59] As illustrated in Figure 1.2 (a), this configuration features a photoelectrode that captures solar energy, a working electrode that stores energy, and a counter electrode (also referred to as a common electrode) that facilitates the redox charge transfer process. Upon exposure to light, electron-hole pairs are generated within the photoelectrode. The electrons move to the energy storage electrode where they are stored electrochemically, while the holes migrate to the counter electrode, participating in the redox reaction until photocharging is complete. During discharge, the working electrode reconnects with the counter electrode, allowing the stored energy to be released. Extensive research has since explored this design using various photoelectrodes, such as silicon/silicon oxide and dye-sensitized titania (TiO_2) combined with materials like poly(3,4-ethylene dioxythiophene) (PEDOT). [60–63]

In contrast, a two-electrode integrated photobattery, as shown in Figure 1.2 (b), eliminates the need for a separate counter electrode by combining the photoelectrode and energy storage electrode into a single system. In this configuration, the photoelectrode performs both energy conversion and storage. Upon illumination, the generated electron-hole pairs are involved in redox reactions, either autonomously or with the assistance of an external voltage. If external voltage is required, these systems are referred to as "photo-assisted" rather than "photo-rechargeable," as light alone is insufficient to charge the battery. [64] Considerable research has been devoted to identifying suitable active materials for these configurations, including lithium iron phosphate ($LiFePO_4$) with dye N719, graphitic carbon nitride ($g-C_3N_4$), vanadium dioxide (VO_2), and vanadium pentoxide (V_2O_5)[65–69].

No matter what layouts are applied for these photo-rechargeable energy storage systems, one of the most critical factors is the energy conversion efficiency, solar energy to electrochemical energy can be described as the formula shown below,

$$\eta_{conversion} = \frac{E_{output}}{E_{input}} = \frac{E_{output}}{P_{in} t A_1} \tag{1.1}$$

in which, E_{output} and E_{input} correspond to the discharge energy output and solar energy input from the light source. P_{in}, t and A_1 represent the light intensity, illumination time and illuminated surface area, respectively.

In addition to energy conversion efficiency, energy density and power density are also key performance metrics for the commercialization and practical application of photo-rechargeable batteries. Energy Density refers to the amount of energy a battery can store relative to its mass or volume. This is commonly divided into mass energy density (specific energy), expressed in Wh/kg, and volume energy density (specific capacity), expressed in Wh/L. The mass energy density reflects how much energy the battery can provide per unit mass, making it a critical parameter for applications that prioritize lightweight energy storage solutions, such as mobile electronics and electric vehicles. The volume energy density, on the other hand, indicates how much energy the battery can store per unit volume, which is particularly important for space-constrained applications such as implantable medical devices and portable power sources. On the other hand, power Density is a measure of how quickly a battery can discharge its stored energy, expressed in W/kg or W/L. It reflects the battery's ability to provide high power outputs in a short period, which is essential for high-power electronic devices or systems that require rapid bursts of energy, such as during peak loads. Higher power density can enhance the performance of photo-rechargeable batteries in applications like electric vehicles, where quick energy delivery is crucial for acceleration, or in smart grids, where demand can fluctuate rapidly.

The first generation of photovoltaic technology, based on silicon solar cells, is well-developed and widely used in applications ranging from residential solar panels to satellites in outer space. Silicon-based solar cells can achieve efficiencies of over 30%. [70–72] However, limitations remain due to their size, cost, and environmental impact. As discussed earlier, integrated photo-rechargeable batteries with shared electrodes show significant potential as an alternative to conventional solar cells. To successfully convert and store energy in these devices, material selection is crucial. The active material must first be photo-active, meaning it can harvest solar energy by generating electron-hole pairs under illumination. Ideally, it should have a bandgap in the visible light range, between 1.6 eV and 3.2 eV. Additionally, the photoelectrode must have the capacity to store energy. In typical battery systems, energy storage occurs through either conversion or insertion reactions, requiring efficient charge storage during charge and discharge cycles with good cycling stability. The active material must also maintain photo and chemical stability without losing photoactivity over time. In this section, we introduce various new-generation, state-of-the-art photo-rechargeable devices, classified by configuration and working mechanism.

Dye-sensitized solar cells (DSSC)-battery system

The first novel design of the new-generation solar cell is Dye-sensitized solar cells (DSSCs). DSSCs were first introduced in 1988 by Gratzel Cells, and since then there has been intensive research on that.[73] In this system, the DSSC usually has a photoelectrode which contains a transparent conduction layer coated glass, wide bandgap semiconductor, dye, electrolyte and counter electrode[74]. The transparent conduction layer is generally made of fluorine-doped tin oxide (FTO, $SnO_2 : F$) or indium-doped tin oxide (ITO, $In_2O_3 : Sn$). To improve the overall efficiency of the solar cell, the conductive layer needs to possess a high transmittance (over $\sim$75%) and low resistance (below 18 Ω/cm^2). The wide bandgap semiconductor layer is generally coated on the conductive glass by using TiO_2, ZnO, or SnO_2 to increase the charge transfer efficiency by blocking the electrolyte and the current collector. These materials usually have a bandgap range from 3.0 eV to 3.2 eV. The dye is generally covalently bonded on the porous semiconducting layer. In this case, the role of the dye is to absorb light and generate electron-hole pairs. In order to achieve that, the dye needs to absorb a wide range of light in the visible region. It is also required to be both thermally and chemically stable under various conditions. The energy level alignment is crucial as well for photo-electrons transfer and regeneration[75–77]. The electrolyte usually contains cations, solvents, ionic liquids, additives and a redox couple system. The most common electrolyte systems have I^-/I_3^-, Br^-/Br_2^- and SCN^-/SCN_2 as the redox couples[78–80]. The role of the electrolyte is to carry the redox couples which take part in the regeneration of the ground stage of the dye. Similar to the dye, the electrolyte is desired to be chemical, thermal, and electrochemical stable and does not react with the dye or any other components of the DSSC. Apart from those properties, the electrolyte is required to transfer ions efficiently and does not absorb too much light. The counter electrodes (CE) are commonly made from platinum or carbon, the role of the CE is to transfer photogenerated electrons and participate the reduction of the redox couples.

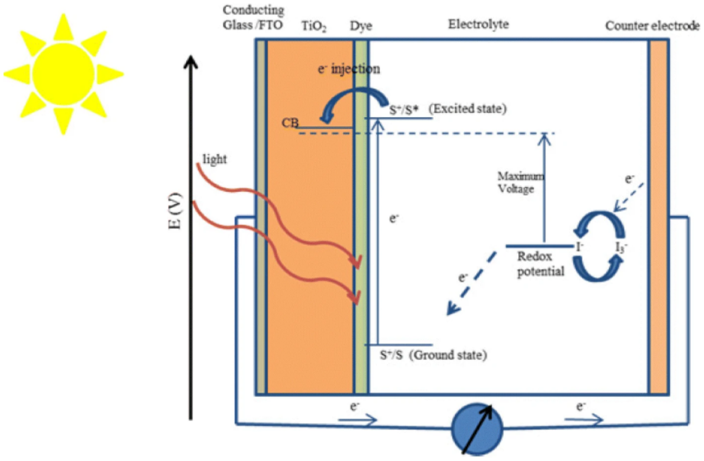

Fig. 1.3 Construction and working principle of the dye-sensitized nanocrystalline solar cells. [81]

The general working mechanism can be shown in Figure 1.3, when light illuminated the dye, the photo-generated electrons first change to an excited state and move to the conduction band of TiO_2. The photo-electrons shift to the conduction band of the TiO_2 because the energy level lies just below the excited state of the dye. At the same time, the dye becomes oxidised due to the remaining holes, which are blocked by the valence band of TiO_2 because the energy level is lower than the ground state of the dye, and the photo-generated holes do not recombine with the photo-generated electrons. On the other hand, the photo-generated electrons were then transferred to the counter electrode through the conductive FTO glass and external circuit, where the I_3^- was reduced to I^- by the electrons and completed the regeneration process. At last, another cycle begins with the reduced dye giving out electrons again under illumination and oxidising back to I_3^-.

The very first integrated DSSC-based solar battery was introduced in 2004 by Nagai and Segawa using a typical Grätzel cell and a conducting polymer charge–storage electrode[82]. The arrangement of the energy-storable dye-sensitized solar cell(ES-DSSC) contains a three-electrode system as shown in the figure below,

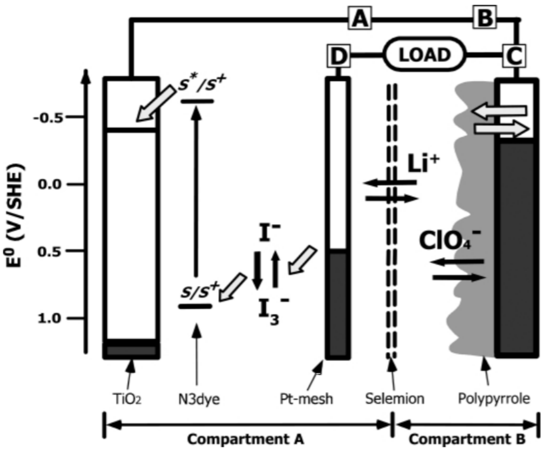

Fig. 1.4 The configuration of the ES-DSSC. White arrows represent the electron transfer at the interfaces. Each set of black arrows represents the diffusion of ionic species. [83]

This paper gives a fundamental setup of the energy storage DSSC system. Compartment A is the DSSC part, a Ru-complex dye was used, where charges are generated and separated. Compartment B is used to store the charges by using polypyrrole on ITO. The working mechanism can be explained as follows, when the device is charged under illumination, D and C are disconnected and photo-electrons are generated from the N3dye and then transported to the polypyrrole through TiO_2. At the same time, the I^- from the electrolyte was oxidised to $\mathrm{I_3}^-$ due to the loss of electrons. This loss of electrons is caused by the charge balance within the dye. Photocharge is complete when the polypyrrole is fully doped. In the discharging process, C and D are connected with a load. The previously stored electrons in polypyrrole move to the Pt-mesh and reduce the oxidised $\mathrm{I_3}^-$ electrolyte, which completes a full photo charge-discharge cycle.

In 2020, Kim et al. introduced a groundbreaking photo-rechargeable battery that leverages the synergy of a Dye-Sensitized Solar Cell (DSSC) and $LiMn_2O_4$, achieving remarkable overall efficiency even under indoor light conditions[84]. The innovative configuration, illustrated in Figure 1.5, comprises a photo-electrode, a storage electrode, and an auxiliary discharge electrode. The photo-electrode construction involves coating FTO with a TiO_2 layer, featuring two distinct thicknesses of TiO_2 to effectively utilize scattered light from the initial layer.

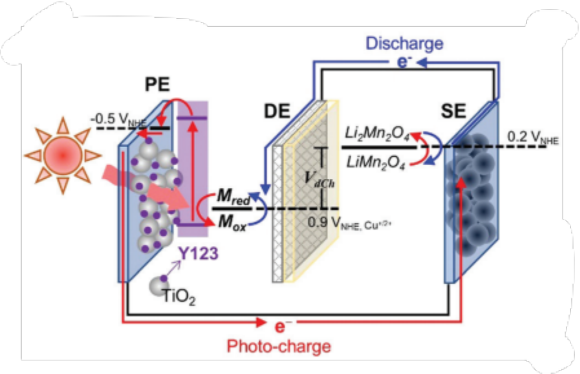

Fig. 1.5 Working principle. Different electrolytes were used for the PE and the SE, respectively: a mediator in acetonitrile for the PE and 0.8 M $LiClO_4$ in acetonitrile for the SE.[84]

During the photo-charging stage, the photoelectrode and the storage electrode are interconnected. When light strikes the dye, charge separation occurs, with photo-electrons transitioning from the highest occupied molecular orbital (HOMO) to the lowest unoccupied molecular orbital (LUMO) in the dye. These electrons are then captured by the conduction band of TiO_2 and subsequently directed towards the $LiMn_2O4$ storage electrode through the external circuit. The photo-generated electrons actively participate in the reduction reaction of graphene-wrapped lithium manganese oxide (LMO), as illustrated by the equation below:

$$LiMn(III)Mn(IV)O_4 + Li^+ + e^- \rightarrow dye^* + Li_2Mn(III)Mn(III)O_4 \tag{1.2}$$

Simultaneously, the photo-oxidized dye molecules undergo regeneration by receiving electrons from the mediator within the photo-electrode compartment. The mediator undergoes oxidation during this regenerative process, as depicted in the equations below:

$$M_{red} \rightarrow M_{ox} + ne^- \tag{1.3}$$

$$D_{ox} + e^- \rightarrow D_{red} \tag{1.4}$$

During the discharging process, the connection is established between the storage electrode and the discharge electrode. At the anode, oxidation occurs in the $Li_2Mn(III)Mn(III)O_4$ electrode, facilitating the movement of Li ions through the electrolyte and the generation of electrons that flow towards the Pt electrode, producing electricity. Simultaneously, when electrons reach the Pt electrode, a reduction reaction transpires at the mediator, restoring the dye-sensitized photo-rechargeable battery to its initial state.

In conclusion, DSSCs offer an alternative to traditional silicon-based solar cells due to their simplicity, cost-effectiveness, and flexibility. There are several advantages compared to traditional silicon solar cells. First, the cost is generally lower and cheaper to manufacture due to the use of low-cost materials and fabrication techniques. Secondly, the thin and flexible nature of DSSCs makes them suitable for applications where traditional rigid solar cells may not be practical. Lastly, DSSCs can efficiently convert diffused sunlight and perform well under low-light conditions, making them suitable for indoor applications. However, the light-electric conversion efficiency is generally lower than conventional solar cells. Moreover, the long-term stability under different environmental conditions still needs improvement and scaling up also remains a challenge. Last but not least, DSSCs are still essential solar cells, which means they generate electricity but do not store it. In most of the DSSC systems, a three-electrode system is still required to generate and store energy. Table 1.1 shows a comprehensive summary of the DSSC-based photobatteries regarding their battery types, characteristics and performance.

Perovskite solar cells(PSCs)-battery system

Perovskite was first discovered in 1893 by H.L. Wells.[85] In general, perovskite has an ABX_3 stoichiometry and a cubic crystal structure, where A is a monovalent cation such as caesium, methylammonium, or formamidinium; B is divalent lead, tin or germanium; and X is a halide anion. However, it only began to draw attention in the scientific field in the 1990s in the light-emitting and transistors field in the interest of its unique electronic and optical properties. In 2009 Kojima et al. used Organometal Halide Perovskites as Visible-Light Sensitizers for photovoltaic cells, which opened the gateway for perovskite-based photovoltaic devices.[86] Since then, perovskite-based nanomaterials have earned enormous attention in photovoltaics due to their extraordinary properties like broad-wavelength spectrum absorption, adjustable bandgap, high conductivity, low recombination rate, high defect resilience and high charge diffusion length.[87–89] Since 2009, Perovskite-based photovoltaics have achieved power conversion efficiency (PCE) from 3% to 25.5%.[90]

Figure 1.6 demonstrates a light absorption and generation of free carriers process in typical PSCs. When light is illuminated on the active layer in PSC, photo-generated electrons and holes are separated. The photo-generated electrons are transferred to the electron transporting layer, usually TiO_2, and collected by the transparent FTO-coated glass electrode. The photo-generated holes are collected by the hole transporting layer and transferred to

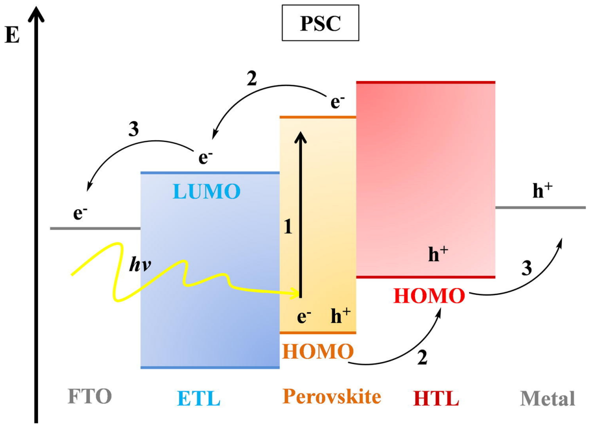

Fig. 1.6 Band diagram and main processes and PSC: 1. Absorption of photon and free charges generation; 2. Charge transport; 3. Charge extraction. [91]

the thermally evaporated gold back electrode layer.[91] Like DSSCs, perovskite-based nanomaterial usually acts only as the energy harvester in photo-rechargeable devices and the perovskite solar cells connect physically with the battery system.[92]

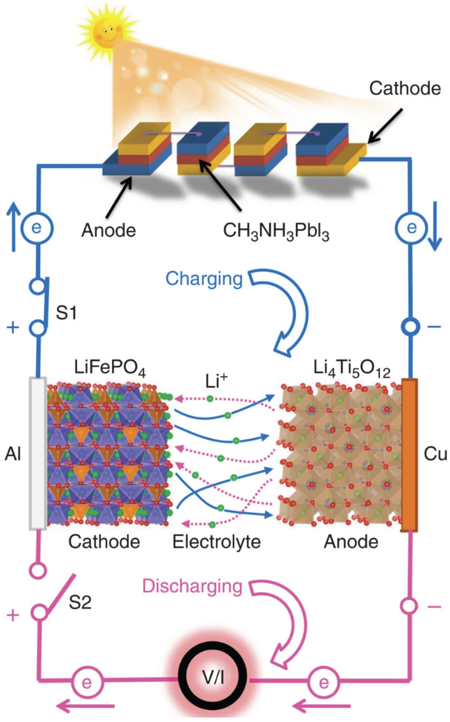

Fig. 1.7 Schematic diagram of the fabricated system of PSC–LIB. [93]

In 2015, Xu et al. reported a novel integrated PSC-LIB system as shown in Figure 1.7, the PSCs are connected in series in order to charge the LIB. Under illumination, photogenerated holes and electrons within the PSCs flow into the cathode and anode of the LIB. This current flow from the PSC to the LIB (top, Figure 1.5) charges the battery through the extraction of lithium ions from the $LiFePO_4$ into the $Li_4Ti_5O_{12}$. During the discharge process, energy stored in the LIB can be released to an external load (bottom, Figure 1.5) by turning off switch S1 and turning on switch S2. This discharge process is accompanied by the insertion of lithium ions from the anode to the cathode.

In a more recent study from 2018, Ahmad et al. introduced a groundbreaking integrated device that seamlessly combines energy storage and simultaneous photocharging. The researchers utilized polycrystalline metal-halide-based 2D perovskite materials, characterized by the general formula $(RNH_3)_2MX_4$ (where R represents an organic moiety, M denotes a metal, and X signifies a halide). Specifically, the chemical composition of the 2D lead bromide employed in the study can be expressed as $(C_6H_9C_2H_4NH_3)_2PbI_4$ (CHPI). Remarkably, the nonphoto-chargeable 2D lead bromide perovskite cells exhibited a specific capacity of 410 mAh/g. Notably, this result surpassed the capacity of graphite, a widely used material in commercial lithium-ion batteries.[94]

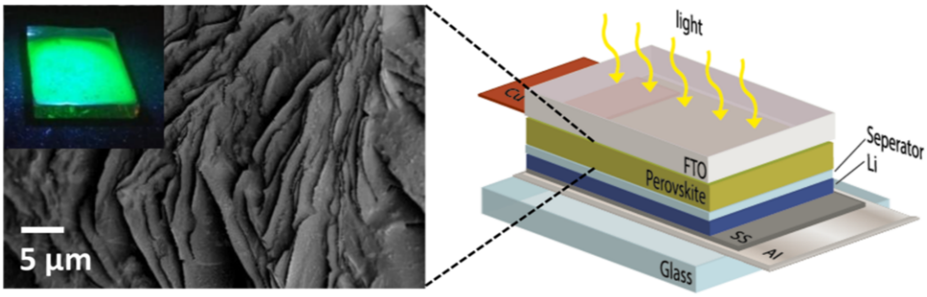

Fig. 1.8 Schematic diagram of perovskite photobatteries. [94]

The device architecture, depicted in Figure 1.8, reveals a meticulously designed structure that includes a thin film consisting of 2D perovskite-rGO-PVDF, positioned between a fluorine-doped tin oxide (FTO) substrate and a separator. In addition, a copper foil is incorporated to enhance charge conduction for the FTO. The exceptional performance of the fully light-charged device is showcased by its capability to illuminate a commercial 3 V white light LED continuously for over an hour, as illustrated in Figure 1.9.

This research posits that energy storage within the system involves a synergistic interplay of intercalation and conversion mechanisms, substantiated by the expansion in the d-spacing and distinctive peak alterations observed in the X-ray diffraction (XRD) results.[95] During the discharge process, particularly towards 1.85V or lower, an intercalation reaction takes place, resulting in an observable increase in d-spacing compared to the pristine electrodes. As the voltage descends below 1.4V, the XRD data reveals the disappearance of perovskite peaks, and novel peaks emerge when the voltage reaches 0.3V, indicative of a conversion

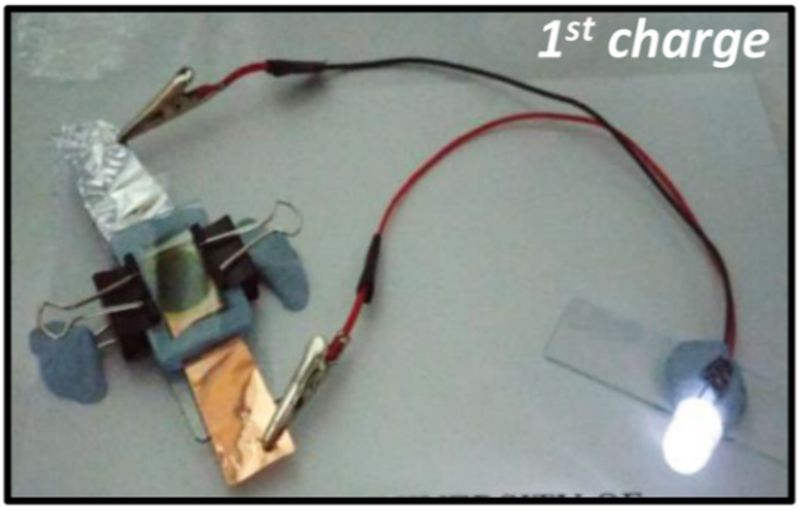

Fig. 1.9 A 3 V LED powered by a CHPI photobattery after the first cycle of photocharging. [94]

reaction. The corresponding chemical formula elucidating this conversion reaction can be derived as follows:

$$2Li + (C_6H_9C_2H_4NH_3)_2PbI_4 \rightarrow 2(C_6H_9C_2H_4NH_3I) + 2LiI + Pb(m) \tag{1.5}$$

Figure 1.10 elucidates the energy level diagram of the designed structure, providing valuable insights into the charge separation and transfer processes. The operational mechanism of the Photo-Rechargeable Organo-Halide Perovskite Batteries, detailed in Figure 1.11, unfolds as follows: when the energy of incident photons surpasses the band energy during photocharging, electrons undergo excitation and are subsequently collected by the fluorine-doped tin oxide (FTO) electrode through reduced graphene oxide (rGO) and phenyl-C61-butyric acid methyl ester (PCBM). Subsequently, the negative charge carriers traverse the external circuit and amass at the lithium (Li) metal counter electrode.[96, 97] Simultaneously, the residual holes within the perovskite drive the Li-ion out and undergo recombination with the accumulated electrons. Despite the integrated device demonstrating a conversion efficiency of 0.034%, the relatively low efficiency primarily stems from the short carrier lifetimes (approximately 200 ps) and short diffusion lengths (less than 100 nm) of electrons and holes in 2D perovskites, where a significant portion either recombines or becomes trapped.[98] Furthermore, the battery experiences capacity loss during the initial cycles, attributed to factors such as material morphology deterioration during charging and discharging, the formation of insulating solid-electrolyte-interfaces (SEI), and the alloying of lead (Pb) metal from equation 1.5 with Li metal. The formation of Li_xPb $(0 < x < 4.4)$ induces substantial volume expansion, resulting in electrode cracking and delamination of electrical contacts.[99]

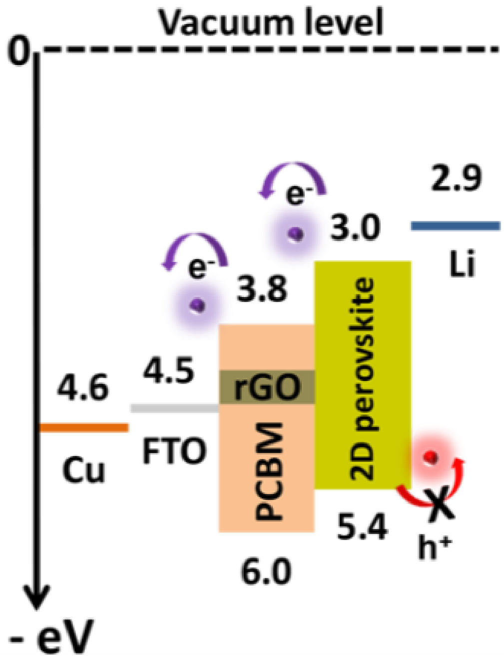

Fig. 1.10 Schematics of the photocharge generation, transfer, and storage mechanisms in perovskite photobatteries. [94]

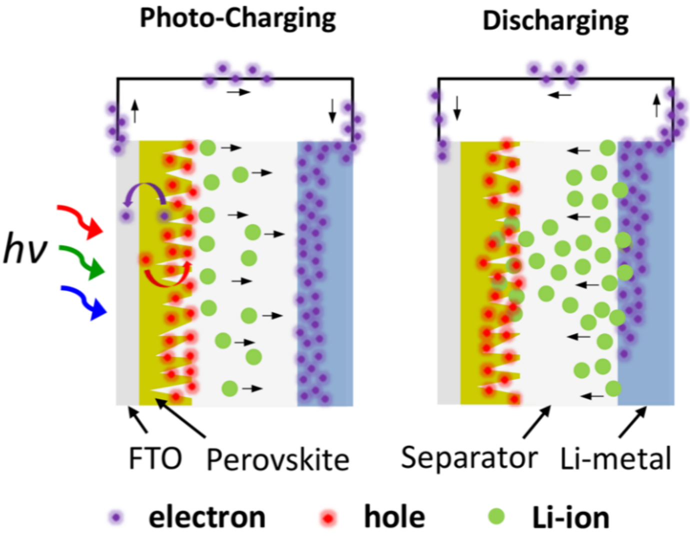

Fig. 1.11 Photo-charging and discharging of perovskite photobatteries. [94]

To summarize, this investigation effectively showcased the light-harvesting potential of metal halide perovskite in a Lithium-ion battery. Nevertheless, the conversion efficiency was limited to 0.034% due to irreversible side reactions. Furthermore, the photoelectrode incorporates toxic elements like Pb, underscoring the imperative for additional research into lead-free perovskites.

Overall, PSCs are a promising technology with the potential to replace Si solar cells. Compared to DSSCs, PSCs have reached an energy conversion efficiency of over 25% by 2024, reaching over Si solar cells.[100] Furthermore, the bandgap of perovskite materials can be easily tuned for better absorption of the solar spectrum and potentially higher efficiencies. However, PSCs can degrade when exposed to moisture, oxygen, and UV light, so maintaining the performance in complex environments can be challenging. Recently, several studies have focused on three-electrode and fully integrated two-electrode halide-perovskites photo-rechargeable batteries, which showed much higher energy conversion efficiency than other integrated photobatteries.[101–104] However, full integration of PSC-photo batteries is still challenging because the stability and photo-activity of perovskite-based nanomaterials suffered tremendously from photo-corrosion and structural change due to ion intercalation. Last but not least, many high-efficiency perovskite materials contain lead, which can be concerning due to its environmental and health effects. Therefore, continued research and development are still expected to solve these issues.

Other semi-conducting material-battery system

Various types of layered metal oxides with different elemental compositions have been extensively studied, and many are now commercialized and used in applications ranging from mobile devices to the automotive sector. [105] For example, transition metal oxides (TMOs) such as tin oxide (SnO_2), tungsten oxide (WO_3), and nickel oxide (NiO) are commonly used in gas sensors, electrochromic devices, and photocatalysis. Specifically, SnO_2 serves as a gas sensor for carbon monoxide, while WO_3 and NiO are employed in smart windows and displays due to their electrochromic properties. In addition, metal oxide-based materials have gained significant attention for their roles in the degradation of organic compounds and energy applications. When exposed to light with photon energy exceeding the bandgap, these materials generate photogenerated electron-hole pairs that can participate in chemical reactions. [106] For optimal functionality under the solar spectrum—comprised of approximately 47% visible light and only 5% UV light—the bandgap of the semiconductor should ideally range from 1.6 eV to 3.2 eV. However, only a limited number of TMOs, such as Cu_2O, MnO_2, and Co_3O_24, have narrow bandgaps that make them suitable for visible light applications. Therefore, material selection remains crucial as we seek TMOs with visible light bandgaps that have also been extensively studied in battery research. The following section lists some of the most studied TMO materials reported for use in photobatteries.

Ferric oxide (Fe_2O_3) is a promising material for batteries with a high theoretical specific capacity of 1007 $mAhg^{-1}$ due to its porous structure and large surface area, it is also one of the most abundant metal oxides on earth, therefore, Fe_2O_3 is rather cheap and environmentally friendly.[107, 108] Apart from that, Fe_2O_3 is also an n-type semiconductor with a bandgap around 2.5 eV, which is suitable for visible light absorption. Up to now, Fe_2O_3 has been intensively involved in batteries, photocatalysis, water-splitting, gas sensing and so on.[109–111] Hence, Fe_2O_3 is a potential photo-active material for photobatteries with these combined properties. Up till now, there has been growing research on the photo-charging and photo-enhanced ability of Fe_2O_3 Li-ion batteries and iron-ion batteries.[112, 113]

In a recent development in 2023, Chamola et al. unveiled a groundbreaking photo-rechargeable Li-ion battery that harnessed the capabilities of nanoporous Fe_2O_3. The photocathode, a pivotal component in this innovation, was ingeniously crafted, featuring a sophisticated arrangement of multi-walled carbon nanotubes (CNT), Fe_2O_3 nanorods network, carbon additive (PCBM), NMP, and PVDF meticulously integrated on a carbon felt substrate, as illustrated in Figure 1.12. The strategic inclusion of additional CNT and PCBM elements served a dual purpose, enhancing both the electrode's conductivity and providing an optimized pathway for efficient charge transfer.

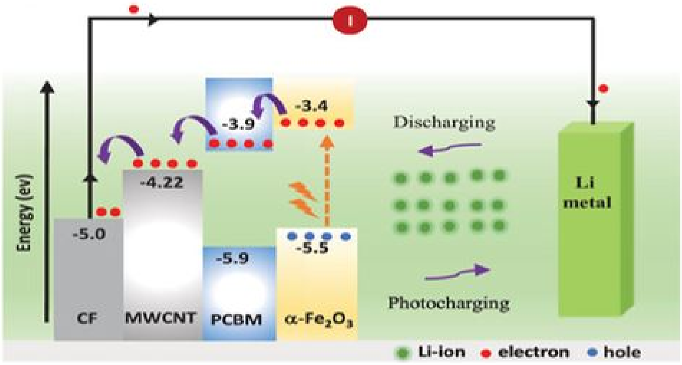

Fig. 1.12 Energy band diagram of $\alpha - Fe_2O_3$ based Li-PRB.[114]

Illustrated in Figure 1.12, the operational dynamics of the photo-rechargeable Li-ion battery (Li-PRB) based on $\alpha - Fe_2O_3$ unfolds through the lens of its energy band diagram. When subjected to radiant light, $\alpha - Fe_2O_3$ absorbs photons with energies surpassing its bandgap. This absorption triggers the generation of electron-hole pairs, with the liberated electrons and holes efficiently channeled through the energy-conducive pathways formed by the conduction bands of PCBM and MWCNT towards the carbon felt current collector. Subsequently, the photo-excited electrons traverse the external circuit, amassing at the anode.

Concurrently, the photogenerated holes initiate the oxidation of Fe^0 to Fe^{3+} and subsequently participate in the delithiation process within the photocathode. As lithium ions (Li^+) migrate toward the anode through the electrolyte, they combine with the photo-excited electrons, culminating in the completion of the photo-charging process. The electrochemical reactions governing this process are encapsulated in the following equations:

$$2Fe^0 + 6h^+ \rightarrow 2Fe^{3+} \tag{1.6}$$

$$2Fe^{3+} + 3Li_2O \rightarrow Fe_2O_3 + 6Li^+ \tag{1.7}$$

However, it is worth noticing that ferric oxide is a conversion-type metal oxide during the charge and discharge process, which can be converted to Fe during the lithiation process. Fe is metal and does not have a bandgap, this is problematic in photo-rechargeable devices. But as a photo-thermal battery, it is still able to generate heat and boost the electrochemical performance of the devices.

Cobalt oxide (Co_3O_4) is a common transitional metal oxide with exceptional charge storage performance for batteries, it shows high theoretical specific capacity, stability and rate performance. Furthermore, Co_3O_4 is also a p-type semiconductor with a direct bandgap of around 1.4 eV to 1.8 eV and an indirect bandgap of around 2.2 eV, which covers most of the visible light region. Due to its narrow bandgap, cobalt oxide has been widely investigated in photocatalysis. Upon light illumination, Co_3O_4 can generate photo carriers which promote the photocatalysis reaction by reducing the energy barrier.[115] Hence, Co_3O_4 has drawn great attention as the photocatalyst in Zn-air and Li-air batteries.[116, 117] Moreover, Co_3O_4 has also been involved in light-assisted and photocatalysis-assisted supercapacitors.[118, 119]

In 2019, Tomon et al. introduced a pioneering photoactive Zn-air battery that employed spinel-type cobalt oxide as the photo air cathode. The experimental setup involved a quartz container equipped with a window, allowing controlled exposure to an external light source. Synthesized via a hydrothermal method and subsequently subjected to calcination, the resulting Co_3O_4 particles boasted a particle size of approximately 25 nm.

In an effort to substantiate the photoactive characteristics of Co_3O_4 within the Zn-air battery (ZAB) framework, a dedicated photocathode was meticulously engineered using ITO glass. Upon exposure to light, a discernible reduction of 0.19 V in the charge/discharge potential gap relative to Zn was observed, indicative of the photocharging effect in action. This phenomenon was primarily attributed to the influence of photo-generated charges, which played a pivotal role in diminishing the overpotentials associated with the oxygen evolution reaction (OER) and oxygen reduction reaction (ORR).

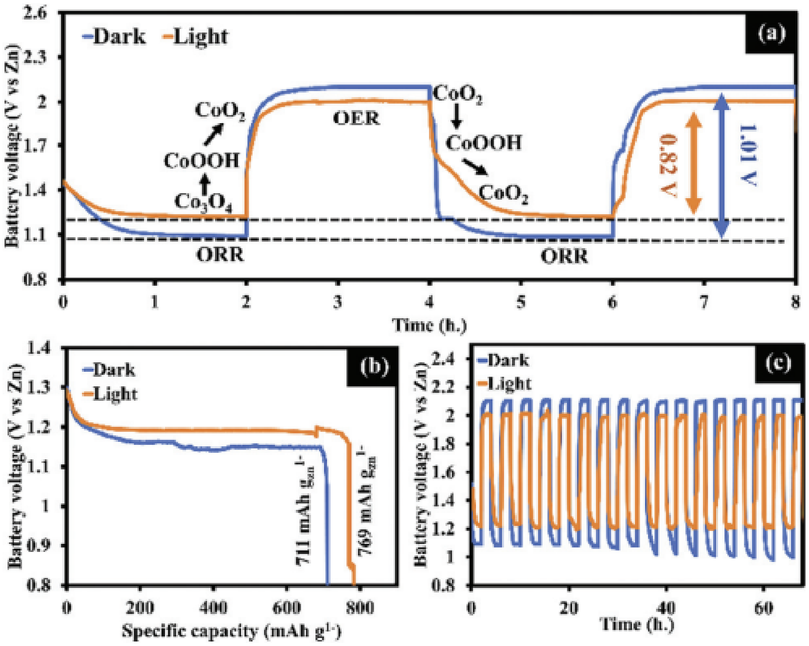

Fig. 1.13 (a) Initial charge/discharge profile of the Zn–air battery, (b) the specific capacity at 20 $mAcm^{-2}$, and (c) long-term stability of the Zn–air battery under light illumination and dark conditions.][115]

Furthermore, the specific capacity exhibited notable enhancement, surpassing a remarkable 10% improvement under the influence of light illumination. These findings underscored the pivotal role of Co_3O_4 as a photoactive component, contributing to the optimization of charge/discharge characteristics and overall performance in the ZAB system.

Critical to understanding the material's photoactive properties, the bandgap energy (E_g) and valence band position (VB) were meticulously characterized. Employing UV-visible spectroscopy and ultraviolet photoelectron spectroscopy (UPS), Tomon et al. determined that Co_3O_4 exhibited a direct bandgap of 2.24 eV and an indirect bandgap of 1.36 eV. Additionally, the valence band edge was identified at -5.68 eV[115]. This comprehensive analysis laid the foundation for exploring the photocharging capabilities of the Zn-air battery, shedding light on its potential applications in energy storage systems.

MoO_x is an n-type semiconductor with oxygen content between 2 to 3. By altering oxygen vacancies in the crystal structure, the electroconductivity can be tuneable. And more importantly, bandgap can vary between 2.8 to 3.6 eV.[120, 121] Due to the visible light bandgap and high reversible capacity of 1258 $mAhg^{-1}$, Molybdenum oxide has attracted great attention in energy storage, photocatalyst and photovoltaics.[122–124] Its photocatalytic ability makes it highly researched mainly in photoassisted Li-O_2 batteries.[125–128] More importantly, its tuneable bandgap also makes it useful in photo-rechargeable Li and Na ions batteries.[129, 130]

In 2017, Lou et al. presented a Solar-Rechargeable Sodium-Ion Intercalation Battery featuring a photoelectrode (MoO_3) and a dark electrode (MnO_2 or Pt)[131]. The underlying photo intercalation reaction at the electrode surface is expressed by the general equation:

$$TX_2 + e^-(hv) + h^+(hv) + M^+_{solv} \leftrightarrow TM_{int}X_2 + h^+ \tag{1.8}$$

Here, TX_2 and $TM_{int}X_2$ represent non-intercalated and intercalated transition metal dichalcogenides, respectively. The terms e^- (hv) and h^+ (hv) denote photogenerated electrons and holes, while M^+_{solv} signifies the ionic species in the electrolyte intended for intercalation. This equation captures the essence of the photo intercalation process occurring at the electrode surface.

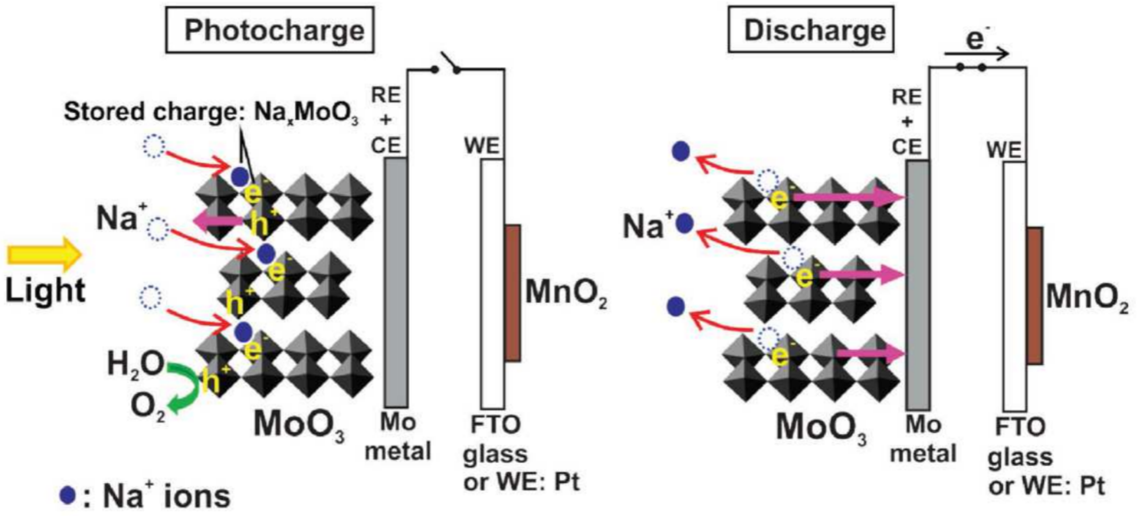

Fig. 1.14 Photocharging and discharging mechanisms in a Solar-Rechargeable Sodium-Ion Intercalation Battery. [32]

In this specific configuration illustrated in Figure 1.14, MoO_3 serves as the counter and reference electrode, while MnO_2 or Pt functions as the working electrode. The operational mechanism is elucidated by the following processes:

When light illuminates MoO_3, photo-induced electrons and holes undergo separation, depicted by the following reactions:

$$MoO_3 + hv \rightarrow MoO_3^* + e^-(hv) + h^+(hv) \tag{1.9}$$

The electrons then combine with the Na^+ ions and are stored in the lattice structure of MoO_3 as Na_xMoO_3 through the equation below:

$$MoO_3^* + xe^-(hv) + xNa^+ \rightarrow Na_xMoO_3 \tag{1.10}$$

Simultaneously, the holes separated during the previous photo-excitation react with water as they move to the surface of the electrode, as shown in the equation below:

$$4h^+(hv) + H_2O \rightarrow 4H^+ + O_2 \tag{1.11}$$

During the battery discharge, Na^+ ions de-intercalate from Na_xMoO_3, and the stored electrons flow through the circuit and travel to the MnO_2 or Pt working electrode. This process results in a constant current, as indicated by the equation below:

$$Na_xMoO_3 \rightarrow MoO_3 + xe^-(hv) + xNa^+ \tag{1.12}$$

Compared to Li-ion batteries based on MoO_3, where x is generally reported to be between 0.1 to 1.5[132, 133], the phase composition (i.e., x-value) of Na_xMoO_3 in the charged and discharged electrodes under 0.2 Wcm^{-2} illumination is determined to be 1.1 and 0.7, according to X-ray photoelectron spectroscopy (XPS) results, indicating a high-capacity photo intercalation process. However, upon the immediate removal of the discharge current, the potential suddenly increases from the dark open-circuit voltage (OCV) of 0.26V to 0.4V. This is caused by the partial deintercalation process of Na^+ ions from Na_xMoO_3 as the MoO_3 undergoes a reverse two-phase reaction mechanism from Na_xMoO_3 to $\alpha - MoO_3$, which has a higher potential than the previous phase. The paper also found that during the photo intercalation process of MoO_3, it was first transformed to $\approx Na_{0.33}MoO_3$ following zeroth-order kinetics; then this phase changes to Na_xMoO_3 by a solid solution reaction, where 0.33 < x < 1.1. By using UV–vis spectroscopy, the MoO_3 electrodes also exhibited good stability and semiconducting properties, as the results showed reversible shifts in the conduction and valence band edge positions and a concurrent narrowing/widening of the host optical bandgap, in agreement with the theoretical model.

In conclusion, this work indicates the potential of using MoO_3 as a photo-intercalation material for aqueous Na-ion photo-batteries, employing bifunctional electrodes. However, there is a lack of evidence demonstrating the stability of MoO_3 under illumination and fast charging conditions, which warrants further research.

Vanadium oxides are presented in different oxidation states and crystalline structures, including V_2O_5, VO_2 and V_6O_{13}, each of the oxides shows individual chemical, optical and electrical properties which attract considerable attention in catalyst, energy storage and solar energy applications. In addition to that, vanadium is also one of the most abundant elements on our planet, leading to cheap cost and non-toxicity.[134] So far, V_2O_5 and VO_2 have both been earnestly investigated in Lithium-ion batteries due to their high specific capacity and energy density as well as catalyst due to their photocatalytic properties. Combining these two aspects, vanadium oxides become suitable materials for photoelectrodes for batteries.[135]

In the year 2020, Boruah et al. presented a photo-rechargeable battery featuring nanofibers of vanadium pentoxide (V_2O_5) in conjunction with zinc metal.

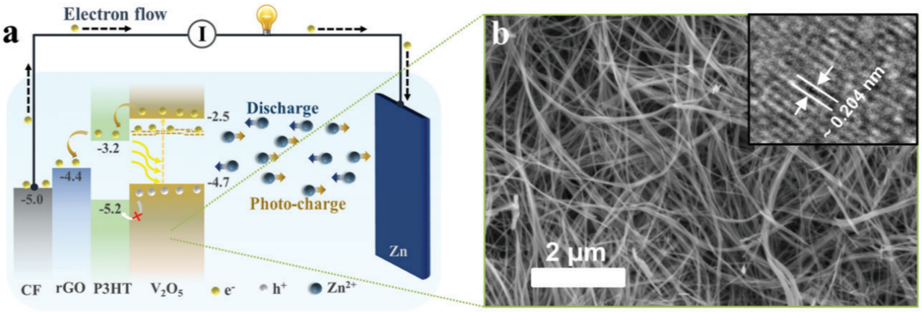

Fig. 1.15 (a) Schematic illustration of the photo-charging mechanism of photo-ZIBs. (b) SEM image of V_2O_5 nanofibers (scale bar 2 μm) and inset showing a high-resolution TEM image. [136]

This article underscores the significance of incorporating a hole-blocking layer of P3HT, as illustrated in Figure 1.15(a). P3HT serves the crucial function of impeding the migration of photo-excited holes, facilitating the de-intercalation of Zn^{2+} ions from the cathode. Furthermore, P3HT boasts a bandgap of 2.0 eV, which is smaller than the 2.2 eV bandgap of V_2O_5. This difference enables the absorption of photons with lower energy in P3HT, facilitating charge separation. Electrons can traverse through rGO, while holes move through V_2O_5. The inclusion of rGO in the photocathode is also pivotal, as it enhances the observed charge carrier lifetime by promoting the efficient transport of photo-excited charge carriers from V_2O_5 to rGO. So far, Vanadium oxides have been widely involved in Zn-ion, Li-ion photo-rechargeable, accelerated batteries and Zn-ion capacitors.[137–142]

Titanium oxide (TiO_2) is a very common n-type semiconductor which has been used in various fields. It has been widely investigated due to its unique chemical and physical properties, low cost, non-toxic and stability. So far, TiO_2 shows great potential in energy storage and photocatalysis.[143] It was first reported in 1972 by Akira Fujishima and Kenichi Honda about the ability of electrochemical photolysis of water.[144] However, TiO_2 has a wide bandgap of 3.2 eV, which means only a small proportion of solar light in the visible region can be utilised. Nevertheless, it has been reported that photogenerated electrons and holes can suffer from charge recombination. Therefore, controlling the absorption region and reducing the recombination effect are keys to further improving the physical and chemical properties. As for energy storage, titanium oxide-based materials have been widely in Lithium-ion batteries due to their low cost, low toxicity, safety, cycling life, etc. Titanium oxide exists in different polymorphs, including rutile, anatase, brookite and bronze B. Among all of them, rutile has the most thermodynamically stable structure and scatters more white light. However, this form suffers from low electronic conductivity and limited ion diffusion, which is unsuitable for energy storage applications.[145] Anatase on the other hand is able to store more Li ions within its lattice. More importantly, it appears to have better surface chemistry and higher conduction band value, which makes it more suitable for both energy storage and photocatalytic applications. Overall, combining the photocatalytic and charge storage properties, Titanium oxide can be a potential photoelectrode material for photo-rechargeable batteries. As we mentioned previously, TiO_2 has been widely used in DSSCs as the charge transfer layer due to its wide bandgap. In integrated photo devices, TiO_2 has been intensively involved in photo-assisted Li-ion, Li-CO_2, $Li-O_2$ and Zinc-air batteries.[146–151]

In 2021 Hu et al. demonstrated a light-motivated Lithium-ion battery by using a SnO_2/TiO_2 heterojunction[152]. As illustrated in Figure 1.16 (a), the heterojunction features SnO_2 grown along TiO_2 (110) nanoarrays, with the TiO_2 nanoarrays synthesized on carbon cloth through a two-step hydrothermal method. The TEM-HAADF image in Figure 1.16 (b) reveals that the TiO_2 nanorods exhibit a diameter of approximately 200 nm, and the SnO_2 nanosheet shell has a thickness of around 30 nm.

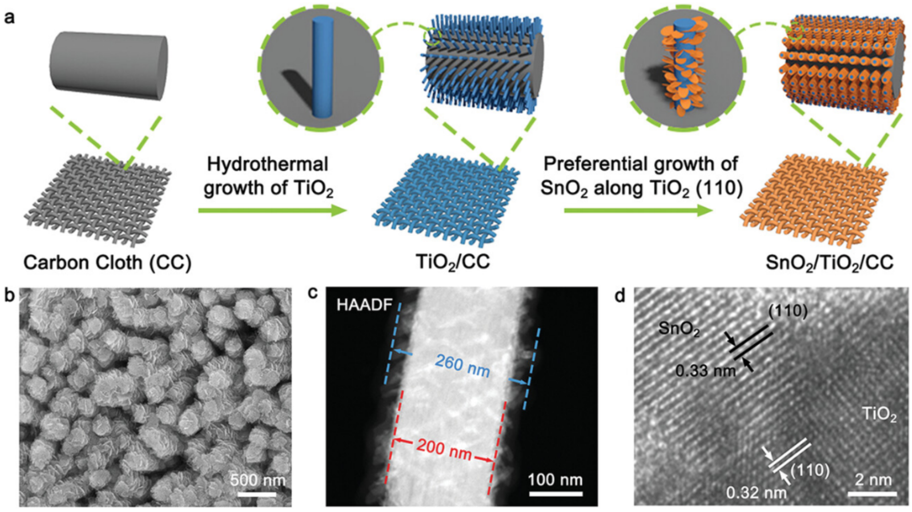

Fig. 1.16 a) Schematic illustration for synthesizing the SnO_2/TiO_2/CC electrode; b) SEM, c) TEM-HAADF, and d) high-resolution TEM images of the SnO_2/TiO_2 heterostructure.[152]

Additional electrochemical performance assessments were conducted using a coin cell system, as illustrated in Figure 1.17. A Xenon lamp with a filter was employed as the light source to eliminate any temperature-related effects on cell performance. Remarkably, under illumination, there was a noticeable enhancement in areal specific capacity, increasing from 1.91 to 3.47 $mAhcm^{-2}$. Importantly, this heightened capacity was sustained over 100 cycles, highlighting outstanding stability with no discernible signs of degradation.

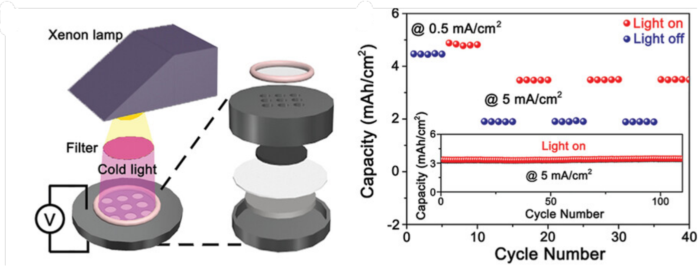

Fig. 1.17 Light-transmitting coin cell test system. (Left) Capacity variation of the SnO_2/TiO_2/CC at 5.0 $mAcm^{-2}$ under light-on and light-off states (the inset shows the cycling stability under light irradiation) (Right).[152]

Metal Chalcogenides usually contain transition elements from groups IV to VII B and VI A group elements.[153] They generally have the formula of MX_2 with a 2D layered structure, where M is a transition element in groups IV B (Ti, Zr, Hf), V B (V, Nb, Ta), VI B (Mo, W), or VII B (Tc, Re) and X is the chalcogen element in the VI A group (S, Se, Te). Due to the flexibility in element compositions and layered structures, the physical and chemical properties are tunable.[154] So far, 2D transition metal chalcogenides have been widely involved in catalytic activity, thermoelectric, superconductor, energy storage and photovoltaics fields. Following these properties, transition metal chalcogenides can be a potential active material in photobatteries. However, there are still challenges to overcome, such as ensuring energy conversion efficiency, stability and scalability. Despite these hurdles, the flexibility of chalcogenide-based nanomaterials offers opportunities for innovation, allowing batteries to be tailored for specific needs and conditions. In essence, chalcogenide-based nanomaterials hold great potential for advancing energy storage technology, especially in photo-rechargeable batteries. To date, there have been numerous amounts of research on the wide range of metal chalcogenides-based photo-induced devices including Germanium selenide (GeSe), Cadmium sulfide (CdS), Molybdenum Disulfide (MoS_2), TiS_2 and so on.[155–158]

In 2021, Boruah et al. showcased a photo-rechargeable Zinc-ion battery utilizing Molybdenum Disulfide (MoS_2)[159]. The photocathode, designed in a layer-by-layer configuration, comprised carbon felt, ZnO, and MoS_2. ZnO played a crucial role as the hole-blocking layer, mitigating recombination effects between electrons and holes while providing a conduit for electron transfer to the current collector. Additionally, UV-vis spectroscopy revealed that MoS_2 possesses a bandgap of 1.9 eV, surpassing the bandgaps of their earlier materials, V_2O_5

(2.2 eV) and VO_2 (2.3 eV), contributing to heightened solar-conversion efficiency compared to previous Zn-ion battery reports.

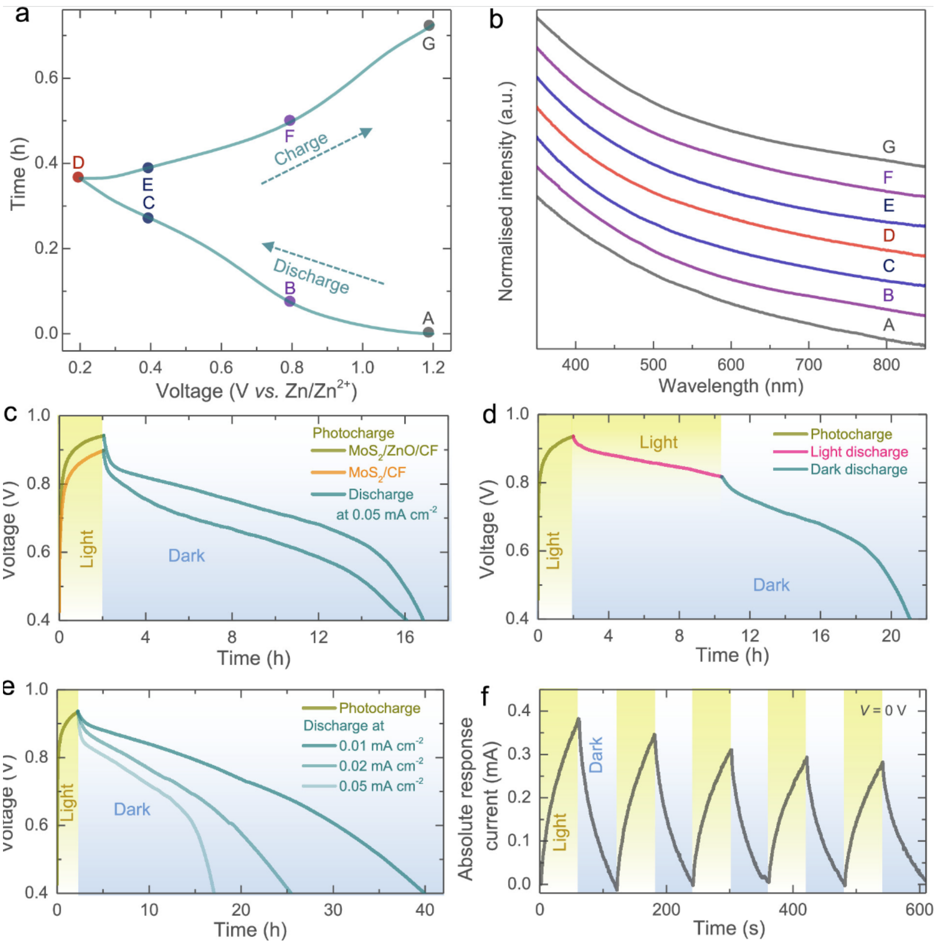

Fig. 1.18 ((a) Galvanostatic 2nd discharge-charge cycle of a hv-ZIB. (b) Absorbance spectra of the photocathode material at different SOC indicated in part a. (c) Photocharging experiments using an LED source (455 nm, 12 $mWcm^{-2}$) of electrodes with and without the ZnO coating, followed by discharge curves at a specific current of 0.05 $mWcm^{-2}$ in dark conditions. (d) Photocharge (455 nm) followed by discharge at 0.05 $mWcm^{-2}$ in illuminated and dark conditions. (e) Photocharge (455 nm) and discharges at different specific currents. (f) Chronoamperometry test of the h-ZIB under alternating dark and illuminated 455 nm) states at V = 0V.[159]

Molybdenum Disulfide (MoS_2) showcased impressive photo-stability throughout both discharge and charge cycles, as evidenced by the findings presented in Figure 1.20 (b). Notably, the bandgap of MoS_2 remained consistent irrespective of the stage of charge, emphasizing its robust stability. This consistency assumes heightened importance for the photo-charging functionality of the battery, especially considering the potential phase transition of MoS_2 from the semiconducting 2H phase to the metallic 1T phase. Furthermore, the photo battery, as illustrated in Figure 1.20 (c to f), demonstrated a unique capability – it could charge solely through exposure to light without the need for any external current application. This remarkable feature resulted in a substantial voltage increase of 0.99 V over a 2-hour illumination period. Such a capability holds promise for enhancing the efficiency and versatility of the battery, opening up new possibilities for harnessing light as a source of energy in the absence of conventional charging methods.

Organic materials have emerged as viable alternatives for rechargeable batteries, as evidenced by recent research efforts.[160–162] In contrast to many inorganic materials, organic-based substances offer the advantage of easy customization of their physical and chemical properties through modification of synthesis methods. Moreover, these organic materials are frequently derived from dyes or leaves, typically possessing bandgaps within the visible light spectrum. This characteristic renders them promising candidates for exploration as photo-sensitive materials. Up to now, there have been various organic materials developed in photo-rechargeable applications including Li-O_2 batteries, DSSCs and Lithium-ion batteries.[163–165]

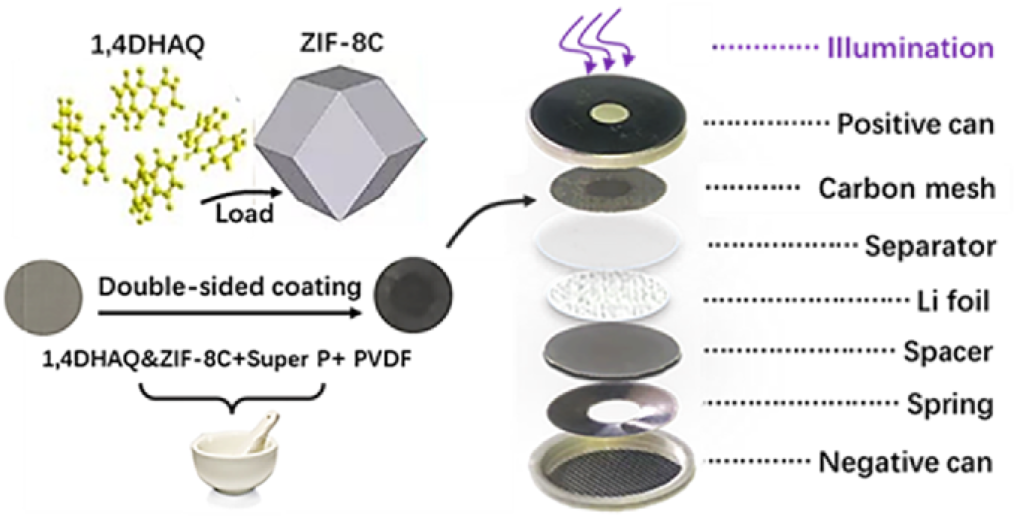

Fig. 1.19 Schematic diagram of light-assisted coin-cell assembly based on 1,4DHAQ&ZIF-8C.[166]

In 2023, Yang et al. introduced a photo-rechargeable Lithium-ion battery utilizing an organic cathode composed of 1,4-Dihydroxyanthraquinone (1,4DHAQ)[166]. The device exhibited improvements in specific capacity and lithium-ion mobility, with a notable 39% reduction in charge transfer resistance observed through Electrochemical Impedance Spectroscopy (EIS) measurements. The configuration of the photo-assisted battery is depicted in

Figure 1.19, featuring a perforation at the cell's top for light exposure. The photocathode comprises 1,4DHAQ&ZIF-8C as the photoactive material, along with conductive carbon and PVDF. The mixture of 1,4DHAQ and porous carbon ZIF-8C is optimized for enhanced conductivity of 1,4DHAQ, leading to improved electrochemical properties.

The electrochemical measurement of the 1,4DHAQ&ZIF-8C photo-assisted lithium-ion battery was then characterised by using potentiostatic charge/discharge method.

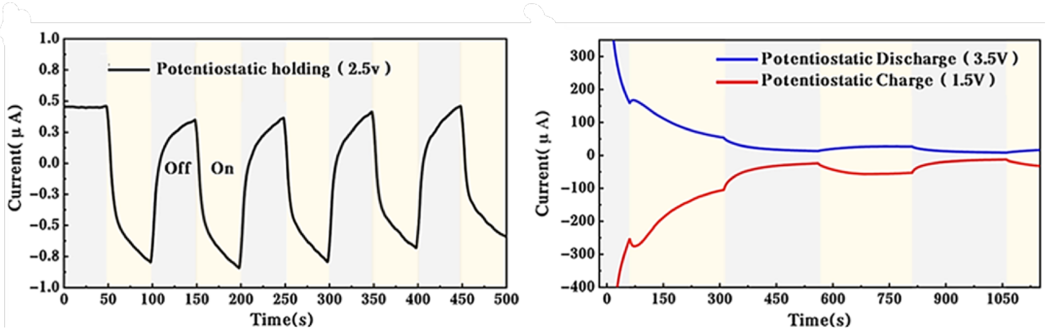

Fig. 1.20 Potentiostatic charge/discharge response at 0V bias voltage (the open- circuit voltage of tested battery was 2.5V and the test voltage of electrochemical workstation was also set to 2.5V; thus, the bias voltage was 0V). (Left) Potentiostatic charge/discharge curves at a bias voltage of ±1V. (E) Rating performance under illumination/dark conditions. (Right)[166]

As depicted in Figure 1.20 (left), when the battery was maintained at 2.5 V, creating a zero-bias voltage between the device and the work station, a negative discharge current was observed under illumination. Furthermore, the battery exhibited an even higher current output under various bias voltages, as illustrated in Figure 1.20 (right).

In conclusion, integrated photo-rechargeable battery systems can simultaneously absorb light and convert it into storable energy. Therefore, selecting and optimizing bifunctional electrode materials with high light absorption and energy storage capacity is crucial. While semiconductor materials like metal oxides, chalcogenides, and organic photovoltaics are currently of great interest, exploring a broader range of materials is essential for further improving light-to-electricity conversion efficiency and energy capacity. Additionally, the stability and compatibility of these bifunctional electrode materials during the cycling process are also critical factors to consider. Last but not least, heat generation must be taken into account while evaluating the photo-charging ability. When analysing the boosted performance of the devices, cautions are needed to distinguish the photocharging effect and the photo-thermal effect.

Table for the photo-rechargeable batteries systems

Photoelectrode	Battery type	Characteristics	Performance	Ref.
DSSC	LIB	double-sided TiO_2 nanotubes	$\eta_{efficiency}$=0.82%	[167]
	Redox battery	Acid/polysulfide pre-treated Ni foam	$\eta_{efficiency}$=1.7%	[168]
	LIB	LFP/CNTs/N719 dye photo-cathode	η=0.06%-0.08%	[42]
	Assisted LIB	TiO_2/CdS QDs/Cu_2S (Cu_xS) electrode	3389% capacity boost	[169]
	Assisted Li-S battery	FTO/TiO_2/S/N719 dye electrode	3 times capacity boost	[170]
	LIB	Graphene-wrapped LMO	η_{500lux}=13.2%	[171]
	Assisted Li-O_2 battery	Ti metal gauze with rutile TiO_2 nanorods	Reduced overpotential	[172]
	Li–I_2 redox flow battery	Dye-sensitized TiO2 photoelectrode	20% energy saving	[173]
	Na-I_2 battery	Dyed TiO_2 and $Fe_2(MoO_4)_3$	0.6V photocharging potential	[174]
	KIC	FeSe2/N–C photoelectrode	35.7% energy barrier reduction	[175]
	Li–I_2 RFB	I_2@AC/N719-dye/TiO_2 photoelectrode	3.38% electricity saving	[176]
	LIB	Li_xTiO_2 nanoparticles	$\eta_{efficiency}$=0.5%	[177]

Table 1.1 Performance of representative DSSC-based photobatteries

Battery types	Photoelectrodes	$\eta_{conversion}(\%)$	Capacity ($mAhg^{-1}$)	Ref.
Zn-air battery	$\alpha - Fe_2O_3$	-	-	[178]
Li–O_2 battery	$\alpha - Fe_2O_3\&BiVO_4$	-	-	[168]
LIB	$\alpha - Fe_2O_3$ nanorods	1.988%	522.4 mAh/g (500mA/g)	[114]
Zn-air battery	Spinel-type Co_3O_4	-	769 mAh/g (20 mA/cm^2)	[115]
SIB	MoO_3	-	-	[131]
ZIB	V_2O_5	1.2%	370 mAh/g (50mA/g)	[136]
ZIB	VO_2	0.18%	315 mAh/g (200mA/g)	[179]
LIB	V_2O_5	0.22% (1SUN)	161 mAh/g (200mA/g)	[180]
LIB	LiV_2O_5	9%	215 mAh/g (0.5A/g)	[181]
Magnesium ion capacitor	VO_2	-	63.80 F/g (0.65 A/g)	[181]
ZIB	$VO_2/C@SiCuOC$	0.016%	0.39 mAh/cm^2 (1.0 mA/cm^2)	[182]
LIB	TiO_2	-	440 mAh/g (C/7)	[183]
C-TiO_2 supercapacitor	TiO_2 nanoparticles	-	27.3 mF/cm^2 (0.05 mA/cm^2)	[183]
ZIB	$Co_2P - CoP - NiCoO_2$	6%	210 mAh/g (2A/g)	[159]
Perovskite-based supercapacitor	$CH_3NH_3PbBr_3$ single crystals	0.02%	85 F/g (1.0 mA/cm^2)	[184]
Zinc–Tellurium Battery	Perovskite/Te	0.31%	785 mAh/g (100mA/g)	[185]
Solar seawater battery	anatase-TiO_2 nanotube	-	-	[186]

Table 1.2 Performance of representative integrated photobatteries

Battery types	Photoelectrodes	$\eta_{conversion}(\%)$	Capacity $(mAhg^{-1})$	Ref.
LIB	Defective TiO_2	4.4% (1 A/g)	322.3 mAh/g (50mA/g)	[187]
Li–O_2 Battery	WO_3 Nanowire	-	-	[188]
Li–O_2 Battery	$g-C_3N_4$-decorated WO_3 nanowire	-	-	[188]
LIB	$LiMn_2O_4$	-	65 mAh/g (3.2-4.07V)	[189]
LIB	CuO foam	0.34%	580.7 mAh/g (150mA/g)	[190]
LIB	$LiMn_2O_4/TiO_2$	-	174 mAh/g (30mA/g)	[190]
Vanadium photoelectrochemical cell	GC/MWCNT/CdS	-	-	[191]
LIB	GeSe nanoparticle	-	850 mAh/g (0.1A/g)	[190]
ZIB	ZnO/MoS_2	1.8% (455nm)	340 mAh/g (100mA/g)	[159]
Li-CO_2 battery	In_2S_3@CNT/SS (ICS)	-	-	[192]
LIB	MoS_2/MoO_x NRs	0.05%	162 mAh/g	[193]
LIB	TiS_2-TiO_2	0.23%	586 mAh/g	[193]
LIB	Organo-Halide Perovskite	0.034%	410 mAh/g	[193]
LIB	Hexagonal $Cs_3Bi_2I_9$ Nanosheets	0.43%	975 mAh/g	[193]
LIB	Organo-Halide Perovskite	0.034%	410 mAh/g	[193]
LIB	Hexagonal $Cs_3Bi_2I_9$ Nanosheets	0.43%	975 mAh/g	[193]
Perovskite-based supercapacitor	$CH_3NH_3PbBr_3$ single crystals	0.02%	85 F/g (1.0 mA/cm^2)	[184]

Table 1.3 Performance of representative integrated photobatteries (continued)

Battery types	Photoelectrodes	$\eta_{conversion}(\%)$	Capacity ($mAhg^{-1}$)	Ref.
LIB	SnO_2/TiO_2 nanoarrays	26.9% (5 mA/cm^2)	3.47 mAh/cm^2 (5 mA/cm^2)	[152]
ZIB	$Co_2P-CoP-NiCoO_2$	6%	210 mAh/g (2A/g)	[159]
Li–O_2 Battery	Co-TABQ	-	-	[194]
LIB	Tetrakislawsone	-	333 mAh/g (50mA/g)	[195]
LIB	1,4DHAQ&ZIF-8C	0.047%	285 mAh/g (100mA/g)	[190]
LIB	$LiMn_2O_4/TiO_2$	-	174 mAh/g (30mA/g)	[190]
Zn-air battery	PDTB and TiO_2	-	-	[196]
Zinc–Tellurium Battery	Perovskite/Te	0.31%	785 mAh/g (100mA/g)	[185]

Table 1.4 Performance of representative integrated photobatteries (continued)

1.2 Photothermal-enhanced energy storage devices

1.2.1 Background

Different from the previously mentioned photo-electric conversion effect, light can also be converted into heat, which is generally called the photo-thermal effect. [197] This photo-thermal effect can be commonly observed in our daily lives, most of the heat is absorbed by our surroundings, creating a suitable climate and environment for us to live in. When we are under sunlight, we can feel the heat on our skin, but if we touch a black car, we notice the car is hotter than our skin. Therefore, this photo-thermal effect can vary regarding emissivity, porosity, colours, transparency, and many other physical and chemical properties. [198–200] There are multiple ways to quantify the ability which a photo-thermal material to absorb light and convert light to thermal energy, the first method is measuring how absorbed solar energy is converted into thermal energy which involves measuring the temperature increase and calculating the heat generation induced by incident light. The photothermal conversion efficiency (η) can be expressed as[201]:

$$\eta = \frac{Q}{E} = \frac{cm\Delta T}{pst} \tag{1.13}$$

In this equation, Q represents the thermal energy generated by the absorber, E stands for the total energy of the incoming light, c and m denote the specific heat and mass of the photothermal material, ΔT is the temperature increase of the material under light irradiation, p is the power density of the light source, and s and t represent the radiation area and time. This method takes into account all incident light, including reflected, scattered, absorbed, and transmitted photons originating from the incident light, as input energy. The advantage of this strategy lies in considering only absorbed photons contributing to the generation of thermal energy in the photothermal material. However, as heat generation depends on the amount of used photothermal material, direct comparisons of efficiency values among different materials are challenging.

Another way to estimate the photo-thermal conversion efficiency is by considering the heat loss to surroundings from a heating and cooling process, the equation below shows the expression of the photo-thermal conversion efficiency η[202]:

$$\eta = \frac{hs(T_{max} - T_{sur}) - Q_{dis}}{I(1 - 10^{-\alpha_\lambda})} \tag{1.14}$$

In the given equation, h denotes the heat transfer coefficient, s represents the surface area of heat transfer, T_{max} is the equilibrium temperature, T_{sur} represents the temperature of the surrounding environment, Q_{dis} stands for the heat dissipated by the surrounding environment, I is the radiation intensity of the incident light, and α_λ represents the absorbance of the photo-thermal material at the wavelength λ. This equation selectively considers only the absorbed photons as input energy, effectively eliminating the influence of heat transfer and the concentration of the photo-thermal material on the light-to-heat conversion efficiency. Such quantitative elimination enables a direct comparison of the photo-thermal conversion abilities among various materials. However, it's crucial to acknowledge that numerous parameters within this equation require experimental measurement. Some of these parameters are non-trivial and possess the potential to significantly impact the ultimate value of the photo-thermal conversion efficiency.

To date, there has been a wide range of nanomaterials including nanostructured metal, semiconductors, carbon-based nanomaterials, and organic polymers showcasing outstanding photo-thermal conversion ability.[203–206] However, there is very limited research on how photothermal heating affects the electrochemical performance of an energy storage device. I believe that by introducing a controlled photothermal effect, the batteries' performance and lifetime can be maximized.

As we mentioned previously, the photo-thermal effect involves the interaction between light and heat, therefore, the optical properties are crucial to explain the working mechanism of the photo-thermal material.

Localized surface plasmon resonance (LSPR)

Localized Surface Plasmon Resonance (LSPR) is a phenomenon observed in metallic nanoparticles when their electrons collectively oscillate in response to incident light, leading to a resonance in the absorption or scattering spectrum. In the context of photothermal materials, LSPR plays a crucial role in enhancing light absorption and, consequently, in promoting the efficient conversion of light into heat.

When exposed to light, metallic nanoparticles experience a resonance condition where the frequency of incident light matches the natural frequency of the nanoparticle's free and polarizable surface electrons. This resonance results in a significant enhancement of the absorption cross-section of the nanoparticles,

especially in the visible and near-infrared regions of the electromagnetic spectrum. The photo-excited electrons escape their original state and oscillate with the external electromagnetic fields around their surfaces. In order to return to their stable phase, photo-excited electrons are rapidly converted to a nonradiative generation of electron-hole pairs through Landau damping. The electron-hole pairs generate hot charge carriers and interact with the lattice structure of the metallic nanoparticles. In the end, the heat is dissipated to the surroundings by phonon-phonon collisions.

The LSPR phenomenon is tunable based on the size, shape, and composition of the metallic nanoparticles. By adjusting these parameters, researchers can tailor the LSPR characteristics to match specific wavelengths of interest, optimizing the photothermal response.

In summary, LSPR in photothermal materials offers a versatile and controllable means of enhancing light absorption and converting it into heat, opening up possibilities for a range of applications in fields such as medicine and renewable energy. Researchers continue to explore new materials and designs to optimize LSPR for specific applications.

Thermal Vibrations of Molecules

The working mechanism of the photo-thermal effect for organic polymers and other carbon-based nanomaterials can be classified as thermal vibrations of molecules. Under illumination, electrons from the π and π^* orbitals can be readily promoted from the highest-occupied molecular orbital (HOMO) stage to the lowest-unoccupied molecular orbital (LUMO) stage. When the excited electrons return to the ground state, heat is released through vibration-electron coupling

In summary, the photothermal effect in carbon-based materials involves the absorption of light, electronic excitation, vibration-electron coupling, and the subsequent conversion of absorbed energy into heat. This mechanism has practical applications in fields such as medicine, energy conversion, and materials science.

Nonradiative Relaxation

Regarding semiconductors, different from metallic structures, there are no sufficient free electrons for plasmonic interaction. However, when the semiconductor is illuminated with photon energy higher than the bandgap, electron-hole pairs are created. the energy of these excited electrons can be released either by emitting photons or by transferring to the material lattice through nonradiative relaxation processes due to the recombination of charge carriers. The excess energy of the excited carriers is transferred to the lattice vibrations (phonons) of the semiconductor. This localized heating causes a temperature increase in the lattice structure.

The efficiency of the photothermal effect is influenced by the recombination of charge carriers within the semiconductor. Surface and bulk recombination processes play a crucial role in determining the overall heat generation. Two common nonradiative relaxation processes in semiconductors are Shockley-Read-Hall recombination and Auger recombination. These processes contribute to heat generation by redistributing energy among carriers. In Shockley-Read-Hall Recombination, midgap energy states, known as trap levels, are created within the bandgap due to the presence of defects or impurities. This type of recombination involves carriers relaxing to these trap levels before recombining. In Auger recombination, this process involves three carriers, and the excess energy from the recombination of carriers is transferred to another carrier, increasing the likelihood of further nonradiative processes.

The efficiency of the photothermal effect in semiconductors can be optimized by controlling factors like the semiconductor's bandgap, defect density, and the specific material used. Tailoring these parameters is essential for maximizing the heat generation for different applications. Understanding and manipulating the photothermal effect in semiconductors allows for the development of advanced technologies in fields like medicine, energy, and sensing. Researchers continue to explore novel materials and methodologies to enhance the performance of semiconductor-based photothermal systems.

1.2.2 Recent development of photothermal-enhanced applications

To date, there has been a great number of materials that possess high photo-thermal conversion efficiency. In order to achieve optimal performance, the selection of photothermal materials plays a critical role, just as in photo-rechargeable battery development. The chosen materials must possess high solar absorption capabilities while also being stable under operational conditions. Furthermore, their structural properties, such as surface area and thermal conductivity, influence their overall efficiency in transferring heat to water or other mediums. Furthermore, the photo-thermal effect has been widely investigated and involved a range of applications including water heating and vapor generation, seawater desalination, wastewater purification, energy storage, photothermal actuators and robots, and photothermal therapy (PTT). In terms of energy storage, recent research generally focuses on storing solar energy in vapour and heated water. These systems typically focus on capturing solar energy in the form of heated water or vapor, which can later be utilized for power generation or other purposes. In this section, we will explore the recent developments in photothermal-enhanced applications, focusing on the materials and mechanisms that enable high-efficiency solar-to-heat conversion and their potential for various technological solutions.

Water heating and vapor generation

In water heating and vapor generation applications, photothermal materials are often employed to accelerate solar evaporation processes. This happens through two primary mechanisms: volumetric heating, where the photothermal materials are dispersed within the water, and interfacial heating, where the materials float on the water surface, confining heat and minimizing energy loss to the bulk water. For instance, carbon-based materials such as graphene and carbon nanotubes are popular due to their high photothermal conversion efficiency and ability to absorb a broad range of light wavelengths, ensuring optimal heat transfer to the water. Additionally, advances in nanofabrication have allowed for the development of structured materials that minimize heat loss while maximizing evaporation rates. The following table presents a summary of the recent studies and performance metrics of photothermal materials used in water heating and vapor generation, highlighting key material types, evaporation rates, and efficiencies.

Material types	Water evaporation rate	$\eta_{evaporation}(\%)$	Ref.
Au NP Plasmonic nanofluid	6.27 kg/m^2h (10SUN)	0.65%	[207]
Graphitized carbon black	10.9 kg/m^2h (10SUN)	0.69%	[208]
Carbon fibre/PEHG/PS	1.3 kg/m^2h (1SUN)	0.8%	[209]
CNT membrane/silica	1.32 kg/m^2h (1SUN)	0.82%	[210]
Au NP Plasmonic nanofluid	6.27 kg/m^2h (10SUN)	0.65%	[207]
Graphitized carbon black	10.9 kg/m^2h (10SUN)	0.69%	[208]
Carbon fibre/PEHG/PS	1.3 kg/m^2h (1SUN)	0.8%	[209]
CNT membrane/silica	1.32 kg/m^2h (1SUN)	0.82%	[210]
Exfoliated graphite/carbon foam	11 kg/m^2h (10 kW/m^2)	0.85%	[211]
Spongy carbon nanosheet	1.4 kg/m^2h (1SUN)	0.92%	[211]
Nanoporous graphene sheet	1.5 kg/m^2h (1SUN)	0.8%	[212]
Hierarchical graphene foam	1.4 kg/m^2h (5 kW/m^2)	0.9%	[213]
GO film	1.45 kg/m^2h (1SUN)	0.94%	[214]
RGO–silk-fabric	1.48 kg/m^2h (1SUN)	1.02%	[215]
Wood–Graphene Oxide	14.02 kg/m^2h (12SUN)	0.83%	[216]
CNT modified filter paper	1.15 kg/m^2h (1SUN)	0.75%	[216]
rGO–Fe_3O_4	1.3 kg/m^2h (1SUN)	0.8%	[217]
MoS_2/BNC	6.15 kg/m^2h (5.35 kW/m^2)	0.81%	[218]
Black gold membranes	15.5 kg/m^2h (20SUN)	0.57%	[219]
PDA-coated PVDF	0.49 kg/m^2h (0.75 kW/m^2)	0.45%	[220]

Table 1.5 Performance of representative Solar Thermal water evaporation

Material types	Water evaporation rate	$\eta_{evaporation}(\%)$	Ref.
Al-based plasmonic structure	5.7 kg/m^2h (4SUN)	0.9%	[221]
HCuPO–PDMS composite	1.85 kg/m^2h (1SUN)	0.636%	[222]
Janus copper foil/foam skeleton	2.21 kg/m^2h (1SUN)	0.88%	[223]
3D cup-shaped $CuFeMnO_4$	2.04 kg/m^2h (1SUN)	1%	[224]
MoO_{3-x} QDs	4.95 kg/m^2h (5SUN)	0.62%	[225]
TiNOX-coated Al plate	1.063 kg/m^2h (1SUN)	0.7%	[226]
Close-packed Ag NPs	5 kg/m^2h (4SUN)	0.8%	[227]
3D AuF composite gel	1.3565 kg/m^2h (1SUN)	0.85%	[228]
Au-deposited nanoporous template	5.5 kg/m^2h (4SUN)	0.9%	[229]
Multilayer PPy nanosheets	5.5 kg/m^2h (4SUN)	0.9%	[230]

Table 1.6 Performance of representative Solar Thermal water evaporation (continued)

Material types	Photothermal conversion efficiency	Laser source	Ref.
MnO_x/PDA nanobombs	34.8%	1064 nm	[231]
Sb_2O_3	44%	1210 nm	[232]
Fe_3O_4/GO nanosheets	55.89%	808 nm	[233]
FeS-PEG-CAI NPs	56.51%	1064 nm	[234]
CuS@PDA/Pd	57.9%	1060 nm	[235]
γ-Fe_2O_3 nanocrystal	59.85%	1064 nm	[236]
$Fe_3O_4/Cu_{1.77}Se$	67.6%	1064 nm	[237]
DTTVBI nanoparticles	45.8%	808 nm	[238]
PTTe nanoparticles	47.5%	1064 nm	[239]
V-shaped DUT850	60%	808 nm	[240]
Aza-BODIPY dimers	60.3%	915 nm	[241]
N^+TT-mCB NPs	78%	808 nm	[242]

Table 1.7 Performance of representative Solar Thermal water evaporation (continued)

In summary, the recent development of photothermal materials has led to more efficient and scalable applications for solar water heating and vapor generation, addressing critical needs for clean water production and sustainable energy solutions. These innovations not only provide practical uses in daily life but also hold promise for addressing larger environmental challenges.

Photothermal Therapy

Photothermal therapy (PTT) is an emerging application that harnesses the ability of photothermal nanomaterials to convert light into heat, making it highly promising for biomedical uses, particularly cancer treatment. By selectively targeting tumors with photothermal agents, light can be used to generate localized heat, effectively killing cancer cells without harming surrounding healthy tissues. The photothermal nanomaterials used in PTT include metallic nanostructures (e.g., gold and silver nanoparticles), carbon-based materials, polymers, and semiconductor nanoparticles. These materials are chosen for their strong light absorption, efficient light-to-heat conversion, and biocompatibility. Gold nanoparticles, in particular, are widely researched due to their tunable localized surface plasmon resonance (LSPR), allowing precise control over the photothermal response by adjusting the size, shape, and material composition.The tables below show the recently developed photo-thermal material for PTT.

Material types	Photothermal conversion efficiency	Laser source	Ref.
Polymer nanoengager	88%	1064 nm	[243]
Manganese(IV) complex	71%	730 nm	[244]
Sn-based nanosheets	37.9%	808 nm	[245]
Fe-based 2D nanosheets	43.3%	1064 nm	[246]
SCNTs/MCNTs	59.3%/57.8%	808 nm	[247]
Mn nanoparticles	22.1%	1064 nm	[248]
Au-Pd heterostructures	41.9%	808 nm	[249]
Au-Por nanosheets	53.6%	808 nm	[250]
Au nanostars	63.6%	785 nm	[251]
Fe nanoparticles	67%	808 nm	[252]

Table 1.8 Performance of representative photothermal therapy research

Material types	Photothermal conversion efficiency	Laser source	Ref.
$AgCu_2O$ nanoparticles	71.68%	785 nm	[253]
Ag/Au nanostrcuture	87.28%	808 nm	[254]
Flower-like MnO_2	21.3%	808 nm	[255]
$IrWO_x$-PEG nanoparticles	27%	808 nm	[256]
CuSe heterostructures	31.9%	808 nm	[257]

Table 1.9 Performance of representative photothermal therapy research (continued)

In summary, the field of PTT has seen significant progress through the development of various photothermal nanomaterials, with a focus on enhancing efficiency and biocompatibility. These materials hold great potential for non-invasive, targeted cancer therapies, making PTT an attractive alternative to conventional treatments.

Phoththermal-enhanced energy storage

Recently, there has been an increased interest in studying the effect of shining light on battery electrodes with the view to either increase performance metrics such as the rate capability or capacity or to directly harvest light energy and store it. However, shining light on these photo-batteries changes their temperature, and recent work has shown that the effect of heating on electrochemical enhancement has been underestimated.[258] If one's goal is to increase battery rate performance or capacity using light, then maximizing the light-induced heat generation is a suitable strategy.

In semiconducting materials, different from metallic structures, there are no sufficient free electrons for plasmonic interaction. However, when the semiconductor is illuminated with photon energy higher than the bandgap, electron-hole pairs are created. the energy of these excited electrons can be released either by emitting photons or by transferring to the material lattice through nonradiative relaxation processes due to the recombination of charge carriers. The excess energy of the excited carriers is transferred to the lattice vibrations (phonons) of the semiconductor. This localized heating causes a temperature increase in the lattice structure.

The efficiency of the photothermal effect is influenced by the recombination of charge carriers within the semiconductor. Surface and bulk recombination processes play a crucial role in determining the overall heat generation. Two common nonradiative relaxation processes in semiconductors are Shockley-Read-Hall recombination and Auger recombination. These processes contribute to heat generation by redistributing energy among carriers. In

Shockley-Read-Hall Recombination, midgap energy states, known as trap levels, are created within the bandgap due to the presence of defects or impurities. This type of recombination involves carriers relaxing to these trap levels before recombining. In Auger recombination, this process involves three carriers, and the excess energy from the recombination of carriers is transferred to another carrier, increasing the likelihood of further nonradiative processes.

The efficiency of the photothermal effect in semiconductors can be optimized by controlling factors like the semiconductor's bandgap, defect density, and absorbance spectrum. Tailoring these parameters is essential for maximizing the heat generation for different applications. Understanding and manipulating the photothermal effect in semiconductors allows for the development of advanced technologies in fields like medicine, energy, and sensing. Researchers continue to explore novel materials and methodologies to enhance the performance of semiconductor-based photothermal systems.

To date, there has been a great number of materials that possess high photo-thermal conversion efficiency. With the recent development of nanomaterials, this light-to-heat conversion is further improved by tailoring the nanostructures including the compositions, particle sizes, shapes, and so on. Furthermore, the photo-thermal effect has been widely investigated and involved a range of applications including water heating and vapour generation, seawater desalination, wastewater purification, energy storage, photothermal actuators and robots, and photothermal therapy (PTT). In terms of energy storage, recent research generally focuses on converting solar energy to heat energy. For instance, Zheng et al. reported a Zn–air battery based on the photothermal effect.

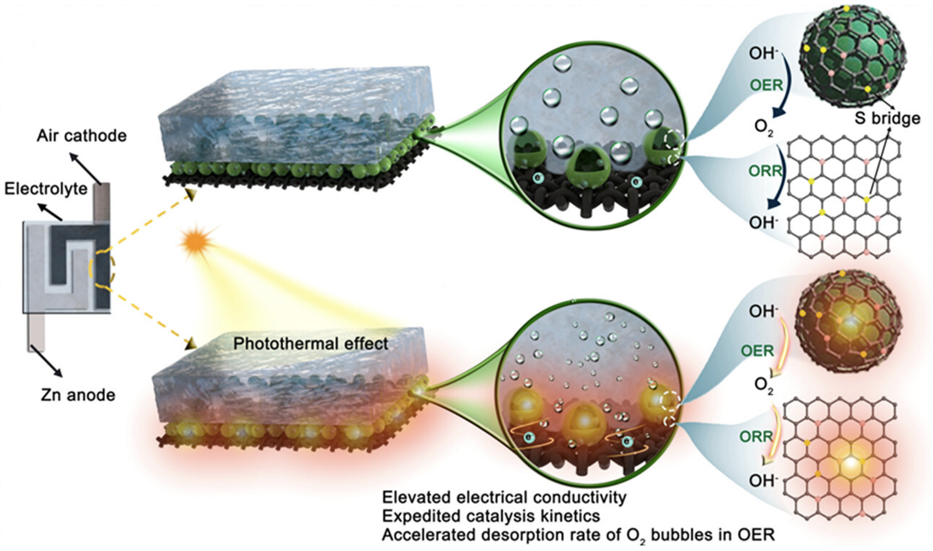

Fig. 1.21 Schematic depiction of working mechanism for photoresponsive Zn–air batteries based on FeNi-S, N-HCS. [259]

Upon the rise of temperature in the working electrode under illumination, the electrochemical kinetics, electrical conductivity, and desorption rate of O_2 bubbles of the air electrode are improved. Therefore, electrochemical performance during charge and discharge is optimised.

In a different system, Wang et al. presented an innovative approach to improving the performance of poly(ethylene oxide) (PEO)-based all-solid-state lithium-sulfur batteries (ASSLSBs) through the use of photothermal materials. [260] The primary challenge with PEO-based electrolytes is their low ionic conductivity at room temperature, requiring high-temperature environments to function efficiently. The authors propose a photothermal-enhanced design to address this issue, allowing for efficient operation at room temperature.

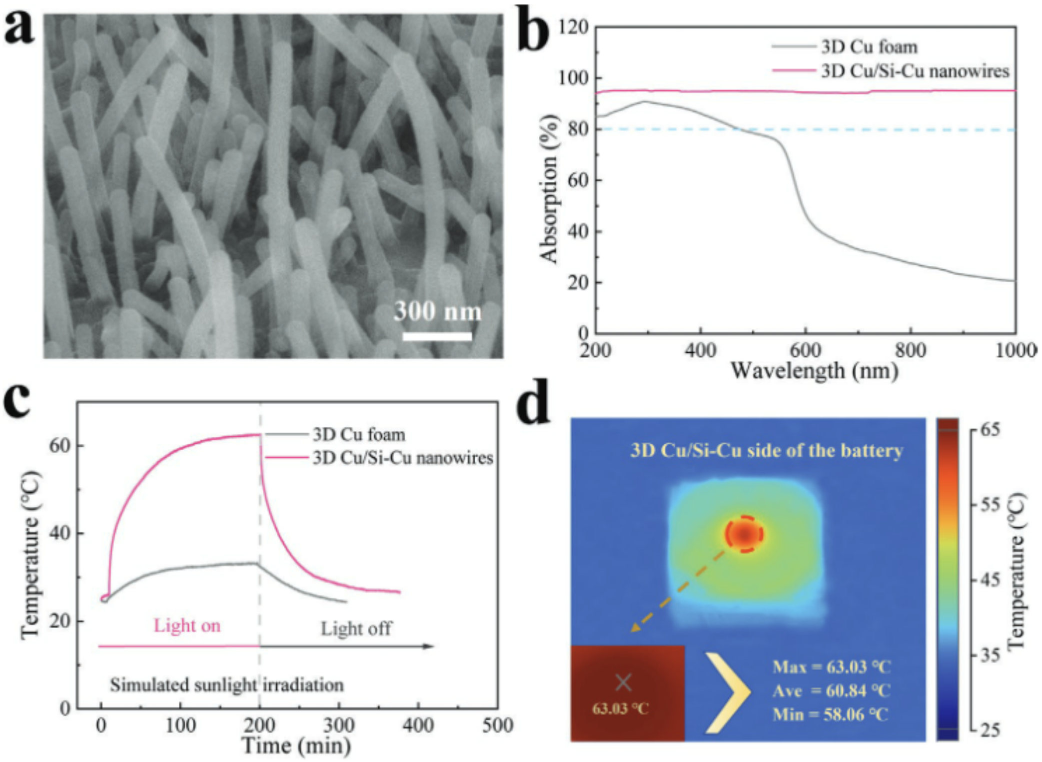

Fig. 1.22 a) SEM image of the 3D Cu/Si-Cu nanowires. b) Light absorption ability of the 3D Cu foam or the 3D Cu/Si-Cu nanowires. c) Temperature change of the sulfur cathode side in the 3D Cu foam or the 3DCu/Si-Cu nanowires-based polymer ASSLSB at room temperature under sunlight irradiation (Xe-lamp). d) IR image on the 3D Cu/Si-Cu nanowires side in the polymer ASSLSB at room temperature under sunlight irradiation (Xe-lamp). [260]

In this study, a 3D Cu/Si-Cu nanowire structure was developed for enhanced light trapping and photothermal conversion. The process involved depositing silicon film onto nanowires, followed by the reduction of CuO with hydrogen to achieve the final structure, with nanowire diameters between 50–60 nm. The X-ray diffraction (XRD) analysis confirmed successful silicon deposition. The structure demonstrated remarkable light absorption capabilities, with a peak absorption of 94.9% across a broad wavelength range (200–1000 nm), significantly outperforming traditional 3D Cu foam. To assess its photothermal conversion efficiency, the system was tested under simulated sunlight using a Xe-lamp. The cathode side of the battery incorporating the 3D Cu/Si-Cu nanowires achieved a temperature of 61.8°C under light irradiation (250 mW/cm²), compared to just 33.6°C for the 3D Cu foam, demonstrating superior photothermal performance. The temperature response varied proportionally with light intensity, reaching up to 70.2°C at 300 mW/cm². These results confirm the rapid and efficient photothermal conversion of the 3D Cu/Si-Cu nanostructures, attributed to their unique light-trapping and heat-conducting properties.

In conclusion, photothermal materials can enhance the performance of energy storage by improving thermal regulation. The increased temperature from photothermal materials accelerates ion mobility and reduces the resistance of electrodes and electrolytes, leading to improved charge/discharge rates and enhanced cycling stability. By integrating photothermal materials into energy storage systems, researchers aim to optimize both energy harvesting from solar sources and the conversion of this energy into storable forms. This dual functionality positions photothermal nanomaterials as promising candidates for next-generation energy storage devices, where efficient heat conversion and storage can enhance overall performance and sustainability.

1.3 Thesis Motivation and Outline

The growing need for efficient, sustainable, and scalable energy storage systems has driven significant research in the field of energy storage devices, particularly those that can integrate renewable energy sources like solar power. Among these systems, photothermal-enhanced batteries hold great promise due to their ability to harness and convert light into heat, thereby improving overall battery performance. However, despite the increasing interest in photo-enhanced systems, a clear distinction between photothermal batteries and photo-rechargeable batteries is often lacking in the literature. This has led to misinterpretation of the electrochemical results and confusion regarding the mechanisms governing these systems.

The motivation of my PhD thesis primarily lies in two main aspects: (i) investigating novel nanomaterials with bifunctional properties for developing two-electrode integrated photo-rechargeable batteries and (ii) uncovering the true mechanism of photo-induced effects, specifically the role of the photothermal effect in enhancing energy storage performance.

In the first phase of my research, I focused on material selection and synthesis, aiming to find active materials that exhibit both excellent electrochemical performance and photoactive properties. This led to the exploration of graphitic carbon nitride (g-C_3N_4) and bismuth vanadate ($BiVO_4$), but significant challenges arose in material synthesis and device optimization as described in chapter 3.

As the research progressed, the importance of charge movement and band alignment became evident. The second phase of my research thus focused on the fundamental mechanisms behind photo-induced charge transfer and the often-overlooked role of heat generated from illumination. Thermal effects present a significant challenge in isolating true photo-charging mechanisms within photo-rechargeable systems. Photoelectric and photothermal processes often interact, making it difficult to distinguish whether performance enhancements stem from actual photo-induced charge generation or from temperature-related influences on the device's electrochemical properties. Elevated temperatures can increase the mobility of charge carriers and decrease interfacial resistance, which may improve the apparent charging performance but are not a result of true photoelectric effects. This overlap introduces complexity in identifying the contributions of thermal and photoelectric processes, particularly in systems where light-induced heating affects material properties. Studies on semiconductor-based photodevices provide valuable insights into the ways thermal effects influence device behaviour. For instance, in photovoltaic cells, heat generated from prolonged illumination can alter the bandgap, reduce the open-circuit voltage, or increase recombination rates, all of which affect device efficiency. Similar challenges arise in photo-rechargeable batteries, where heat can decrease internal resistance or increase reaction kinetics, mimicking the effects typically attributed to photo-charging. Past research on photothermal and photoelectric materials demonstrates that careful experimental controls are necessary to isolate the thermal contributions from true photo-induced processes. To accurately distinguish between thermal and photoelectric effects, it is essential to employ characterization techniques that can differentiate these contributions. For instance, by conducting electrochemical impedance spectroscopy (EIS) under both illuminated and dark conditions and at various controlled temperatures, it is possible to measure changes in charge transfer resistance and identify temperature-dependent effects that might otherwise be attributed to photoelectric activity. Based on this motivation, chapter 4 delves into my investigation of Prussian Blue Analogues (PBAs), where I confirmed that the photothermal effect plays a significant role in enhancing battery performance. This chapter provides insights into the synthesis and characterization of PBAs and highlights the importance of controlling reaction parameters to optimize their performance.

The final phase of my PhD aimed to further explore photothermal effects using well-known photoactive metal oxides such as TiO_2 and Fe_2O_3. Additionally, using ultraviolet photoelectron spectroscopy (UPS) and UV-visible spectroscopy can provide insight into electronic band structures and energy level shifts, helping to isolate photothermal effects from true photoelectric responses. Chapter 5 investigates these materials in-depth, using electrochemical impedance spectroscopy (EIS) and other techniques to distinguish between photothermal and photoexcitation effects under illumination. This chapter also discusses how these findings contribute to a better understanding of the transition between photothermal and photo-rechargeable systems and the implications for future device design.

Chapter 6 summarizes the key findings of this thesis, particularly the identification of the photothermal effect as a critical factor in improving photo-enhanced battery systems. The complexity of these interactions highlights the importance of understanding how thermal effects influence device performance. By developing and applying robust methods to differentiate thermal and photoelectric contributions, researchers can gain clearer insights into the true photo-charging mechanisms in photo-rechargeable systems. This distinction is critical for advancing the design of devices that are efficient and stable, even under varying thermal conditions. Apart from that, this chapter also outlines potential future work, such as the exploration of more advanced materials and optimization strategies for photothermal and photo-rechargeable devices.

In conclusion, this PhD research advances the understanding of photothermal effects in energy storage devices, offering a clearer framework for distinguishing between photo-induced mechanisms. This work will aid researchers in developing more accurate methodologies and better-performing devices in the rapidly evolving field of photo-enhanced energy storage.

Chapter 2

Synthesis and characterisation method

2.1 Material preparation

2.1.1 Graphitic carbon nitride (g-C_3N_4)

The production of $g-C_3N_4$ involves the use of commercially purchased urea (Sigma Aldrich) as a precursor for this graphite-like semiconducting material. Large-scale synthesis of $g-C_3N_4$ is achieved through a thermal treatment method.[261] To initiate synthesis, 2 grams of urea undergoes a drying process in a vacuum oven at 80°C for 3 hours. The dried urea is then carefully transferred to a white crucible, covered with a lid, and wrapped in aluminum foil to ensure temperature consistency during the subsequent thermal treatment. The crucible containing the urea is then placed in a muffle furnace (KSL1100) under ambient air conditions, with the furnace operating in a fume hood to prevent the release of NH_3 into the surroundings. The furnace temperature is gradually increased to 530°C at a heating rate of 20°C/min and held at this level for another 3 hours. During this process, the urea thermally decomposes, releasing gases and resulting in the formation of $g-C_3N_4$ As the furnace cools to room temperature, a distinctive yellow powder of graphitic carbon nitride material is observed and subsequently collected. To refine the synthesized powder, it undergoes thorough washing with deionized water and ethanol. A vacuum filtration method is employed to remove any residual substances, and the final powder is then subjected to a drying phase in a vacuum oven at 120°C for 24 hours.

2.1.2 Bismuth vanadate ($BiVO_4$)

$BiVO_4$is synthesized using a novel controlled hydrothermal method with an autoclave at high temperature. First, a diluted nitric acid solution is prepared by adding 5 ml of concentrated nitric acid (95%, Thermal Fisher) to 65 ml of deionized water. This reaction solvent is then divided into two separate parts and transferred into two beakers. 2.25 mmol of $Bi(NO_3)_3 \cdot 5H_2O$ (Sigma Aldrich) is measured and placed into one of the beakers containing the diluted nitric acid. A magnetic stir bar is placed in the beaker, and the solution is stirred at 500 rpm for around 10 minutes. Meanwhile, 2.25 mmol of NH_4VO_3(Sigma Aldrich) is measured and added to the other beaker, where it is also stirred for 10 minutes. Next, the $Bi(NO_3)_3 \cdot 5H_2O$ solution is slowly added drop by drop into the NH_4VO_3 solution using a 3 ml plastic pipette while stirring at 300 rpm at room temperature. The mixture is stirred for an additional 5 minutes before the ammonia solution (Fisher Scientific UK Ltd) is added dropwise. A digital pH meter (Hanna Instruments Ltd) monitors the pH throughout this process. Initially, the solution shows a pH of around 0 due to the nitric acid. As the ammonia solution is added, a yellow precipitate begins to form, and the pH gradually rises until it reaches approximately 7. The mixture, now containing the yellow precipitate, is stirred for an additional 10 minutes at room temperature. After stirring, the reaction mixture with the precipitate is transferred to a Teflon reactor, which is then placed inside a stainless steel autoclave. The autoclave is heated in an oven at 180°C for 24 hours, followed by cooling to room temperature before opening. The resulting product is washed thoroughly with deionized water and ethanol via centrifugation at 9000 rpm for 20 minutes, with three additional rinses using deionized water and ethanol to remove residual substances. Finally, the washed product is dried in a vacuum oven at 60°C for 3 hours before further characterization and application.

2.1.3 Sodium-rich rhombohedral Prussian blue (Na-PB)

The synthesis of Na-PB involves a modified precipitation method conducted at room temperature, this material is selected due to its exceptional cycling stability of the sodium-rich rhombohedral Prussian blue at elevated temperatures. The process begins by preparing Solution A, a mixture comprising 7.5g of sodium citrate (J.T. Baker) and 1.67g of $FeSO_4 \cdot 7H_2O$ (Acros Organics), with deionized water added to reach a volume of 100 ml. To prevent the oxidation of Fe^{2+} ions, Solution A is bubbled with nitrogen gas while being stirred at 500rpm for 1 hour. Simultaneously, Solution B is created by dissolving 7.5g of sodium citrate and 1.96g of $Na_4Fe(CN)_6 \cdot 10H_2O$ (Sigma Aldrich) in deionized water, also reaching a volume of 100 ml. Nitrogen gas is employed to prevent oxidation, and Solution B is stirred until complete dissolution of $Na_4Fe(CN)_6 \cdot 10H_2O$ is achieved. Subsequently, Solutions A and B are transferred into a constant pressure drop funnel and a three-neck flask (under N_2), respectively. Solution A is added dropwise into solution B, and the resulting mixture is stirred at 500rpm for 6 hours, followed by ageing for several hours before centrifugation. The precipitate is subjected to washing with deionized water and ethanol three times, sequentially.

Finally, the wet powder is dried in a vacuum oven at 120 °C for 12 hours. Parallel synthesis of Prussian blue analogues is conducted using a similar method, but no nitrogen gas is bubbled during the precipitation process. Both samples are synthesized to allow for a comparative analysis and subsequent characterization for further investigation.

2.2 Electrode fabrication

2.2.1 Drop-casting electrode

One commonly employed method for preparing electrodes in photo-enhanced batteries is drop casting onto carbon felt. Carbon felt, with its high surface area, excellent conductivity, and flexible structure, serves as an ideal substrate for supporting photoactive materials. The drop casting technique allows for uniform deposition of photoactive materials onto the carbon felt, creating a functional electrode that can effectively interact with both light and electrochemical processes. This straightforward yet efficient method plays a crucial role in the fabrication and optimization of photo-enhanced batteries.

Graphitic carbon nitride (g-C_3N_4)

For the preparation of the photocathode, a slurry with a composition ratio of 93:2:5 for $g-C_3N_4$, reduced graphene oxide (rGO), and polyvinylidene fluoride (Solef 6020) is formulated. The rGO is synthesized from graphene oxide (GO) using a method similar to that described by Buddha et al. [262]. To produce rGO, a 0.4 wt% GO solution in water is obtained from Graphenea. The GO is then dried in a vacuum oven at 80°C for 24 hours to yield solid GO. This solid GO is reduced at 350°C in an environment of helium and hydrogen gas at a flow rate of 100 sccm for 3 hours using a tubular chemical vapour deposition (CVD) furnace. To prepare the slurry, 2 mg of reduced graphene oxide (rGO) is dissolved in 1 mL of N-Methyl-2-pyrrolidone (Sigma Aldrich) and subjected to ultrasonication for 6 hours. After this, 93 mg of graphitic carbon nitride ($g-C_3N_4$) is added to the rGO solution. This mixture is then placed on a centrifugal mixer and stirred at 500 rpm for 12 hours. In parallel, a polyvinylidene fluoride (PVDF) solution is prepared by dissolving 5 mg of PVDF powder in 2 mL of NMP using a magnetic stirrer at 1000 rpm until the solution is clear. Subsequently, the solution which contains 5 mg of PVDF binder is added to the mixture of $g-C_3N_4$ and rGO. This combined solution is then stirred for an additional 6 hours at 500 rpm to ensure thorough mixing. To prepare the photocathode, a drop-casting process is used to deposit 40 μL of the slurry, containing $g-C_3N_4$, reduced graphene oxide, and PVDF, onto pieces of carbon felt (Sigracet GDL 39 AA carbon graphite paper, SGL Carbon) serving as current collectors. The carbon felt electrodes, each with a diameter of 14 mm, underwent UV-Ozone treatment to clean and activate the surface. The weight of the carbon felt electrodes is measured before applying the slurry. After drop-casting, the photocathodes are dried at 60°C for 12 hours. Following the drying process, the weight of the samples is remeasured to calculate the mass of the active material on the carbon felt electrodes.

Bismuth vanadate ($BiVO_4$)

The battery slurry is first made with synthesized $BiVO_4$, rGO and PVDF. The composition of the slurry is synthesized $BiVO_4$: rGO: PVDF=80:10:10. A solution with a concentration of 5mg/ml PVDF in NMP is prepared. In order to make the $BiVO_4$ slurry for photo-LIB, 80mg of $BiVO_4$ powder is weighted and needs to be ground into a finer morphology by using a bowl grinder. Then, 10mg of rGO is carefully weighed in the powder hood before adding it to the bowl grinder. The mixed powder is then ground again before being transferred to a 7ml glass vial. After that, 2ml of NMP is added to the glass vial inside the fume hood in order to disperse the powder particles. The electrode solution is then subjected to an ultrasonication process at 100% power at 37kHz for 6 hours. The electrode solution is then placed on a mixer at 1300rpm for 3 hours before adding 2 ml of the PVDF in NMP solution with a concentration of 5mg/ml. In the end, the electrode slurry is mixed again with the speedmixer for another 20 minutes at 1500 rpm before further fabrication. The current collector used is Sigracet GDL 39 AA carbon graphite paper, SGL Carbon. This carbon-based current collector is chosen for its high electrical conductivity, large surface area, and mechanical stability. Additionally, its porous structure allows light to pass through the electrode, enhancing the efficiency of light-charging performance. The electrode is cut into a small circular shape with 14mm in diameter. The carbon felt is then subject to UV-Ozone treatment for 20 minutes in order to clean the surface and modify the surface activation. The weight of the carbon felt is measured as the difference in mass between carbon felt only and dropcasted carbon felt electrode is equalled to the mass of the active material. Then, 20μL of the electrode slurry is dropcasted on the carbon felt. First, 10μL of active material is dropcasted on the carbon felt, and the slurry is shaken well before another 10μL of the active material is dropcasted on the carbon felt. The reason why it is done this way is that the $BiVO_4$ tends to aggregate at the bottom. These separated steps also help the slurry to spread on carbon felt more evenly. The mass loading of the active material is again controlled at 1 mg/cm^2. The dropcasted carbon felt electrodes are then placed on plastic rings. The plastic rings are then placed on a glass substrate before transferring on a hot plate at 60 °C for 12 hours. After drying, the weight of the carbon felt electrodes is measured to calculate the mass of the active material on the carbon felt electrodes. Commercial $BiVO_4$ photo-electrodes are also prepared by using the same approach for comparison.

Sodium-rich rhombohedral Prussian blue (Na-PB)

The slurry for the Prussian blue analogue Na-PB electrode is prepared by blending Na-PB, carbon black Super-P (Thermal Fisher), and PVDF. The slurry composition ratio is Na-PB: carbon black Super-P: PVDF=70:20:10, where carbon black Super-P served as the conductive additive to enhance electrode conductivity. The mixing procedure and the drop-casting method remained consistent with the one employed for $BiVO_4$.

Anatase/rutile TiO_2 and Fe_2O_3

The slurry for the anatase TiO_2 electrode is prepared by mixing anatase TiO_2 nanoparticles, carbon black Super-P, and PVDF. The slurry composition adhered to the ratio anatase TiO_2: carbon black Super-P: PVDF=90:5:5. First, 180 mg of commercial anatase TiO_2 nanoparticles with particle size <25 nm which is purchased from MERCK LIFE SCIENCE UK LTD is weighted with 10 mg Super-P carbon. The mixed powder is then ground with mortar and pestle in order to achieve a more homogeneous form. After that, 0.5 ml of 20 mg/ml PVDF in NMP solution is added to the anatase TiO_2 and Super-P mixer. Then the combined product is sonicated for 30 minutes before placing into a speed mixer. The parameter for the speed mixer is 2000 rpm and 20 minutes. The same approach is applied to the commercial rutile TiO_2 (Sigma Aldrich <100 nm particle size) and Fe_2O_3 (Sigma Aldrich <100 nm particle size) with the same composition and mixing procedures. The slurry which contains anatase/rutile TiO_2 or Fe_2O_3 nanoparticles, carbon black Super-P, and PVDF is drop-casted on carbon felt. The carbon felt is first cut with a diameter of 10 mm and pre-treated in a UV-Ozone machine. 20 μL battery slurry is dropcasted at the centre of the carbon felt. The coated electrodes are dried on a hot plate overnight. The weight of the electrodes is measured before and after drop-casting in order to calculate the mass loading of the active material.

2.2.2 In-situ grown electrodes

In photobatteries, the choice between in-situ grown electrodes and drop-casting/blade-coating electrodes significantly impacts performance. In-situ grown electrodes are directly synthesized on the current collector through methods like hydrothermal growth or electrodeposition, leading to strong adhesion, better light absorption, and enhanced electron transport. These electrodes offer improved electrochemical stability and higher photoconversion efficiency due to the direct interface between the active material and the current collector. However, they require more complex and optimised fabrication processes.

Prussian blue by electroplating method (EP Fe-PB/CF)

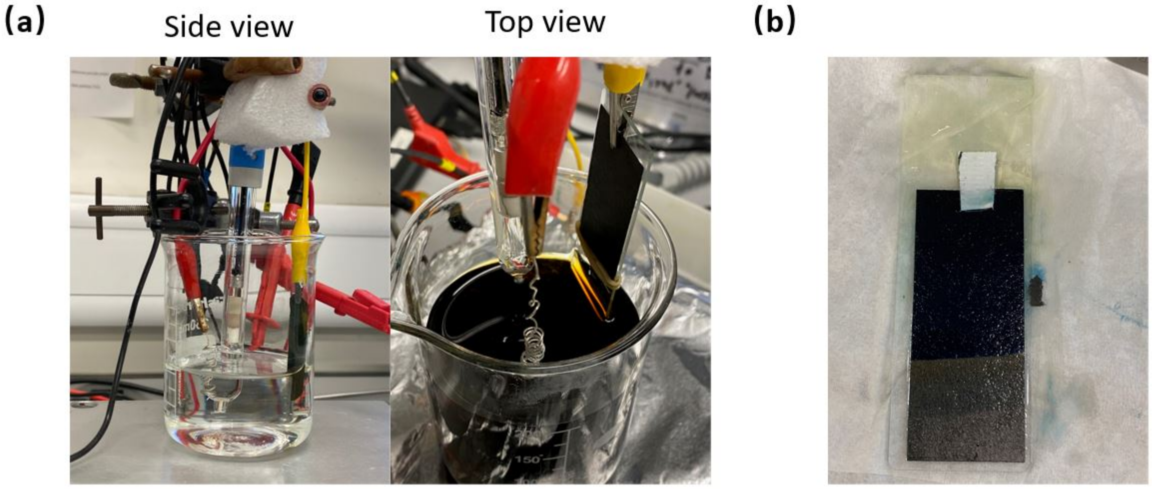

Fig. 2.1 Image of (a) the electroplating setup. (b) EP Fe-PB/CF electrode.

The electrode is prepared by electroplating Prussian blue on carbon felt with a constant current density at selected times. First, a solution is prepared with 5 mL 0.05 M HCl (VWR INTERNATIONAL LTD), 10 mL 0.05 M $K_3[Fe(CN)_6]$ (FISHER SCIENTIFIC UK LTD), and 10 mL 0.05 M $FeCl_3.6H_2O$ (Sigma Aldrich). The solution is then mixed by a magnetic stirrer at room temperature for 30 mins. The electroplating is done by using a three-electrode system with carbon felt as the working electrode, Ag/AgCl/0.1 M KCl as the reference electrode and a platinum wire as the counter electrode as shown in Figure 2.1 (a). The setup is connected to an Autolab PGSTAT302N potentiostat/galvanostat. The EP Fe-PB/CF electrode is prepared by galvanostatically depositing PB at 20 $\mu A/cm^2$ for 30 s, 60 s and 90 s. During the electro-deposition, a magnetic stirrer is placed in the solution to ensure homogeneous deposition. The electrodes are then resined with DI water and dried in an oven at 60 °C overnight.

Prussian blue by a facile hydrolytic precipitation method

To synthesize the first photoelectrode, HP Na-PB/CF, 20 mmol of sodium hexacyanoferrate(II) decahydrate ($Na_4Fe(CN)_6 \cdot 10H_2O$) is dissolved in 100 ml of deionized water (DI H_2O) and stirred thoroughly. A piece of carbon felt, pre-treated with UV-Ozone to enhance its wettability, is immersed in the solution. Then, 1 ml of 37% hydrochloric acid is added, and the solution is heated to 80°C while being vigorously stirred. After 24 hours, the carbon felt is removed and placed into a vacuum oven to dry overnight at 60°C. The prepared carbon felt, now coated with Prussian Blue, is cut into 9 mm diameter discs for use as photocathodes in photo-LIBs, labelled HP Na-PB/CF.

For the second photoelectrode, HP Fe-PB/CF, 20 mmol (6.5844 g) of potassium ferricyanide ($K_3Fe(CN)_6 \cdot 10H_2O$) is dissolved in 100 ml of DI H_2O and stirred thoroughly. The UV-Ozone pre-treated carbon felt is then immersed in the solution. After the addition of 1 ml of 37% hydrochloric acid, the solution is heated to 60°C under vigorous stirring for 24 hours. The carbon felt is subsequently removed, dried in a vacuum oven overnight at 60°C, and precision-cut into 10 mm diameter discs for use as photocathodes, labelled HP Fe-PB/CF.

2.3 Device fabrication

2.3.1 Conventional coin cells

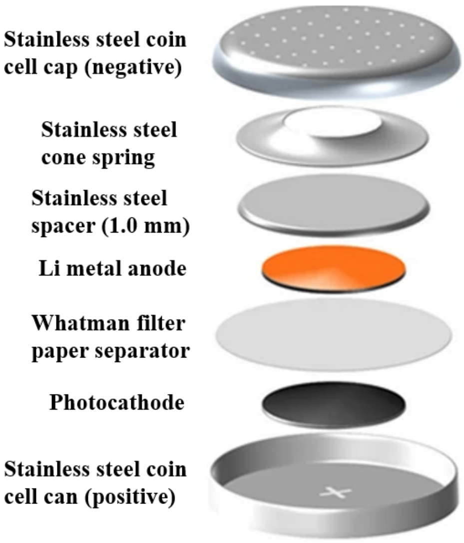

Fig. 2.2 Schematic illustration of the conventional coin cell architecture

A conventional coin cell (CR2032-Cambridge Energy Solutions) type lithium-ion battery is assembled by using the photoelectrode in order to study the electrochemical properties of the active material. The entire assembly process took place in a glove box filled with Ar to prevent the degradation of the hygroscopic electrolyte and lithium metal (H_2O and $O_2 < 0.5$ ppm). Initially, the photocathode is positioned at the bottom of a coin cell can, and a layer of Whatman glass microfiber filter paper separator is placed on top. Subsequently, 70μL of $LiPF_6$ electrolyte in EC/DEC=50/50 (v/v) is evenly distributed onto the separator. Finally, a lithium metal counter electrode is carefully positioned on the separator, followed by the placement of the spacer, spring, and coin cell cap before closely sealing with a Coin Cell crimper machine. The assembled cells underwent overnight drying before electrochemical measurement. A schematic representation of the final structure is shown in Figure 2.2 where the individual components are separated for clarity.

2.3.2 Optical coin cells

In order to analyse the electrochemical performance under illumination, coin cells with an optical window are fabricated as shown in Figure 2.3. Before assembling in the glovebox, the coin cell can (positive) is modified by drilling a hole of 10 mm in diameter and sealed with the optical window (cathode side) using EPOXY (EVO-STIK). Aluminium foil (Targray) is first cut into a round shape with 16 mm in diameter using a coin cell disc cutter machine and then punched a hole in the centre with 10 mm in diameter. This custom-made aluminium spacer is used to contact the photoelectrode to the coin cell casing. The spacer and spring are also different from the previous conventional coin cells with lower thickness to prevent the cracking of the optical window within the coin cell under high crimping pressure (∼1000 psi).

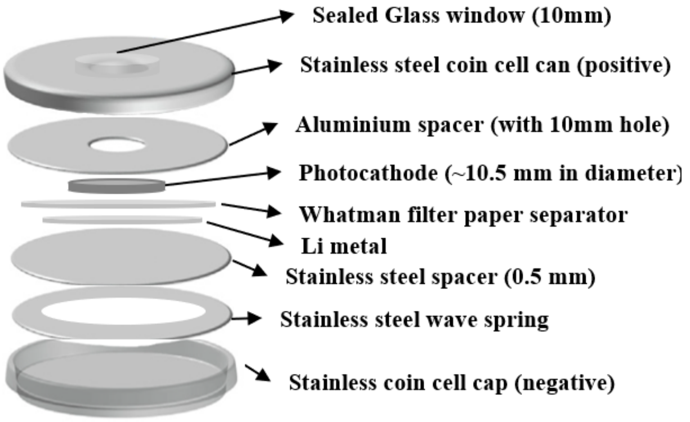

Fig. 2.3 Schematic illustration of the optical coin cell architecture

2.3.3 Layered photodetectors (PDs)

The purpose of making a photodetector (PD) for the active material used in photobatteries is to evaluate and optimize the photoelectric properties of the material, ensuring that it effectively absorbs light and converts it into electrical energy.

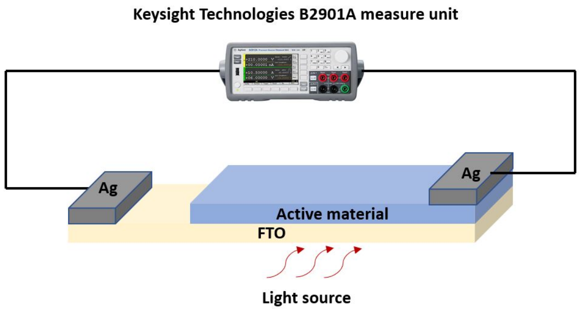

Fig. 2.4 Schematic illustration of the layered photodetector.

In order to prove the ability of charge separation and transportation in g-C$_3$N$_4$/rGO and $BiVO_4$/rGO, a photo-detector is designed and the light response is measured. Figure 2.4 shows the schematic illustration of the layered photodetector design. Initially, reduced graphene oxide (rGO) is drop-casted onto an FTO-coated glass substrate and dried on a hot plate at 80°C for 30 minutes. Subsequently, $g-C_3N_4$ powder is sonicated with deionized water (DI H_2O) for 30 minutes, and the resulting dispersion is drop-casted onto the FTO-coated glass. This is followed by additional drying on a hot plate at 80°C for 3 hours. After drying, the silver paste is applied to the $g-C_3N_4$/rGO/FTO surface. Current-time (I-t) measurements are conducted using a Keysight B2901 source measure unit, with photocurrent recorded by alternating between dark and light conditions every 60 seconds at external bias voltages of from -0.4 V to 0.4V. Figure 2.5 (a) shows a schematic demonstration of the photodetector, the stacked FTO/rGO/$g-C_3N_4$/Ag is believed to generate and separate photo-generated electrons, which can also proved by the corresponding energy band diagram. The electrons generated by the $g-C_3N_4$ under illuminated conditions transport to rGO and FTO, and holes on the other hand move to the Ag contact and transfer through the external circuit. The same procedure is applied to the stacked FTO/rGO/$BiVO_4$/Ag PD as shown in Figure 2.5 (b).

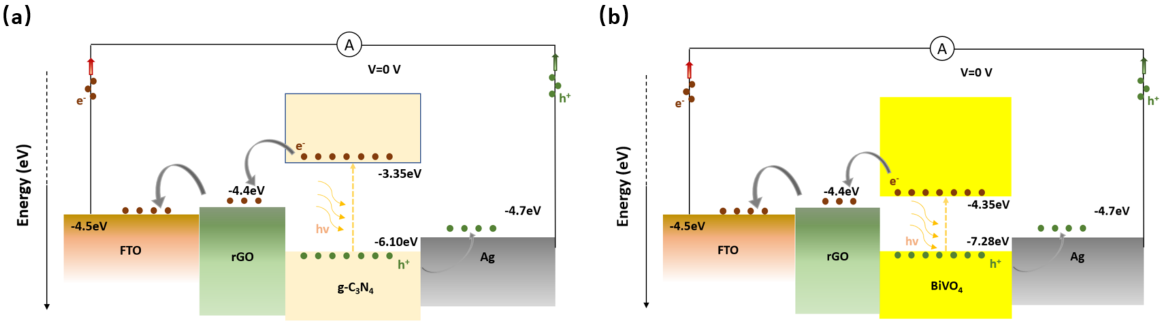

Fig. 2.5 The energy band diagram of the (a) stacked FTO/rGO/$g-C_3N_4$/Ag photodetector. (b) stacked FTO/rGO/$BiVO_4$/Ag

2.3.4 Interdigitated electrodes (IDEs)

An interdigitated electrode (IDE) design refers to a structure where two sets of electrodes are arranged in a comb-like, interlocking pattern without physical overlap. The fingers of each electrode alternate, creating a high surface area for interaction with the active material. IDEs are particularly useful for detecting changes in conductivity in thin films, biological materials, or gaseous environments, as even small changes in the material between the electrode fingers can result in measurable changes in the overall conductivity, which can be used to understand the photothermal effect on active material. Figure 2.6 shows the schematic illustration of the interdigitated electrode design.

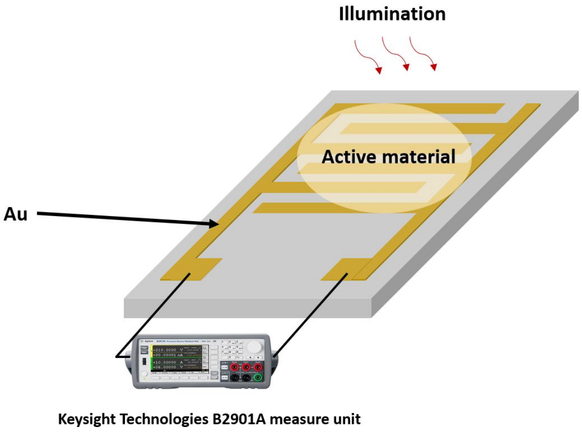

Fig. 2.6 Schematic illustration of the interdigitated electrode.

Prussian blue analogues (PBAs)

The carbon felt containing the synthesized PBAs first undergoes sonication with additional DI H_2O for 30 minutes. Subsequently, the resulting dispersion is drop-cast onto the Au-PB-Au interdigitated electrode and dried on a hot plate at 80 °C for 3 hours. Current-time (I-t) measurements are conducted using a Keysight B2901 source measure unit, with current recorded under alternating dark and light conditions every 25 seconds at an external bias voltage (V= -1.0 to 1.0 V).

Anatase, rutile TiO_2 and Fe_2O_3 nanoparticles (NPs)

The photo response of anatase, rutile TiO_2 and Fe_2O_3 nanoparticles is evaluated by using a planar Au-Au interdigital electrode (IDE) configuration. A solution for drop-casting is first prepared by mixing 140 mg ground active material with 500 μl 40 wt% CMC/DI water solution and 25 μl 10 mg/l SBR/DI water solution. Here, the CMC and SBR are used for modifying the viscosity of the drop-casting slurry and improving the adhesion between the IDE metal contact and the active material. Compared to slurry without binder materials, it can reduce the risk of cracking or delamination caused by the expansion and contraction of the active materials during measurement.

2.4 Characterisation techniques

2.4.1 Scanning electron microscope (SEM)

In my work, the SEM is used intensively to observe the surface structure of electrode materials such as the anodes including lithium metal and carbon felt and cathodes including g-C_3N_4, $BiVO_4$, PBAs, anatase, rutile TiO_2 and Fe_2O_3 nanoparticles. Understanding the surface morphology is important because it affects the battery's electrochemical performance, including charge/discharge rates and capacity. Moreover, The size and shape of active material particles can significantly influence the performance of a battery. SEM helps in measuring the particle size distribution, which can affect the surface area available for reactions and the rate of ion diffusion. Furthermore, the SEM is also used to understand the degradation mechanisms of electrodes, where the morphology of the surface can be compared after multiple charge/discharge cycles in order to observe any cracking, particle detachment, and loss of contact between active materials and the current collector.

The powder samples are prepared by placing a small amount of the aforementioned electrode material onto the double-sided carbon tape on the SEM stub. After that, the surface is gently blown by using compressed air to ensure an even distribution of the powder across the tape. Finally, the powder is lightly pressed by using a clean plastic spatula to prevent the powder from shifting during imaging. The morphologies of the electrode material and anodes at various magnifications are checked by Phenom ParticleX Desktop SEM at an accelerating voltage between 5 and 15 kV.

2.4.2 X-ray diffraction (XRD) spectroscopy

In general, XRD is used to study the crystalline structure, phase composition, and lattice parameters of the materials. In my study, XRD is often applied to verify that battery materials are phase-pure because impurities or secondary phases can negatively affect the electrochemical performance of batteries. Moreover, XRD can be used in situ to monitor the structural changes in battery materials during charge/discharge cycles. This is important for understanding how the crystal structure evolves as lithium ions are inserted or extracted from the material. Comparing XRD patterns before and after cycling helps determine if the material maintains its original phase during the battery operation and a reversible phase change indicates a stable electrode material that can maintain its performance over many cycles.

The as-synthesised powders are finely ground in an agate mortar and pestle for 15 min, then the powders are loaded on PMMA ring sample holders. The XRD measurement is then carried out using a Bruker D8 Advance powder X-ray diffractometer with Cu Kα radiation and a scan rate of 6° min^{-1}.

2.4.3 UV-vis absorption spectroscopy

UV-Vis spectroscopy measures how a material absorbs light across the ultraviolet (UV) and visible (vis) spectrum. The absorption spectra of a photoactive material reveal the range of wavelengths the material can absorb, which directly influences its ability to convert light energy into electrical or thermal energy. Moreover, the absorption edge in the UV-Vis spectrum can be used to calculate the bandgap of the material using a Tauc plot. The bandgap energy is crucial for understanding the photoelectric properties, as it determines the energy required to excite electrons from the valence band to the conduction band, thereby generating charge carriers.

The tested samples which contain the electrode material are sonicated in ethanol for 15 minutes before adding to UV cuvettes (BRAND). Another reference sample is prepared by adding ethanol only. Then, the optical properties and the bandgap of the material are determined using a PerkinElmer UV/Vis/NIR Spectrometer (Lambda 750). The ex-situ UV-Vis absorption spectra of the photocathodes are measured at certain discharge and charge states, the same assembly procedure is applied as the PB/CF photo-LIBs. The cycled photo-LIBs at the selected stage of charge are disassembled and the photo-electrodes are washed with DI water followed by drying at 120 °C for 12 hours in the vacuum oven. The electrodes are then sonicated for 1 hour.

2.4.4 Electrochemical measurement

Electrochemical measurements are fundamental for understanding the performance, efficiency, and mechanisms of batteries. These measurements help assess various properties such as capacity, resistance, charge/discharge behaviour, cycling stability, and overall efficiency of a battery system. For both the conventional coin cell and photobatteries, the electrochemical properties of the electrode is characterised in a half-cell configuration against Li metal, which is conducted using a Biologic VMP-3 galvanostat.

Cyclic Voltammetry (CV)

CV is used to analyze the redox behaviour of the battery's electrode materials and understand the electrochemical reactions taking place. In the Li-ion battery systems during a CV scan, a linearly varying potential is applied to cells and the resulting current is measured. The potential is typically swept between two set limits, and then reversed, forming a cycle. The current vs. potential curve reveals oxidation and reduction peaks that correspond to lithium intercalation or deintercalation processes. Furthermore, CV can also indicate the reversibility of the redox processes. Sharp and reproducible peaks suggest stable, reversible reactions, while broad or shifting peaks indicate irreversible reactions or degradation.

Galvanostatic Charge-Discharge (GCD)

GCD measurements are a fundamental electrochemical technique for evaluating the performance and characteristics of batteries and supercapacitors. It involves charging and discharging the device at a constant current and measuring the voltage response over time. In batteries, the GCD curves often show voltage plateaus during charging and discharging, which correspond to phase transitions or intercalation/deintercalation processes in the electrode materials. Moreover, GCD is commonly used for cycle life testing, where the battery is repeatedly charged and discharged over hundreds or thousands of cycles to evaluate its long-term stability. Moreover, GCD can be used to test the rate capability, which the battery is charged and discharged at different current rates (C-rates). More importantly, GCD is used to calculate the specific capacity (Q), which is a measure of the amount of charge a battery can store. It is usually expressed in mAh/g or mAh/cm^2.

Electrochemical Impedance Spectroscopy (EIS)

EIS is used to study the charge transfer resistance, ionic conductivity, and electrode-electrolyte interface properties in batteries. A typical Nyquist plot obtained from EIS shows semicircles and linear regions that correspond to charge transfer resistance (Rct) and diffusion impedance (Warburg impedance), respectively. In our photothermal effect study, EIS can also help in monitoring the photothermal effects in photobatteries by analyzing changes in impedance with varying light intensity, which correlates with the internal temperature rise due to the photothermal effect.

Chronoamperometry (CA)

The CA tests measure the current responses as a function of time when a constant potential is applied. In my work, CA is performed to study the light-induced effect. The results are used to calculate the charging rate during the illumination process and track the changes in current over time as a response to temperature variations. Furthermore, CA tests are also used to distinguish photothermal from photoelectric contributions by analyzing the current transients during light-on and light-off periods.

Chapter 3

Exploration of materials for photo-enhanced batteries

3.1 Motivation

3.1.1 G-C_3N_4

Graphitic carbon nitride (g-C_3N_4) has emerged as a promising material for photosystems due to its intrinsic electronic structure, which supports visible-light absorption, enabling it to harness a broader spectrum of solar energy compared to materials limited to UV light. Its moderate band gap (2.7 eV) aligns well with the solar spectrum, allowing efficient photon capture under natural sunlight. Additionally, g-C_3N_4's structure, consisting of layered polymeric sheets, facilitates modifications such as doping and surface functionalization. This adaptability provides flexibility in fine-tuning its electronic and optical properties, allowing the optimization of charge carrier separation and transfer efficiency, which are critical for high-performance photocatalytic and photovoltaic applications. g-C_3N_4 is also relatively stable under irradiation and resistant to photo-corrosion, contributing to its durability and reliability in prolonged usage within photosystems. This stability ensures consistent performance over time, addressing a common limitation in other semiconductor-based photocatalyst. Furthermore, g-C_3N_4's ability to form various nanostructures (e.g., nanosheets and nanotubes) increases its effective surface area, enhancing its interaction with reactants in photocatalytic systems. This structural versatility maximizes the active sites available for light-induced reactions, boosting the overall efficiency of processes such as water splitting or pollutant degradation. In summary, g-C_3N_4's visible-light activity, tunable structure, stability, and potential for structural diversity make it a compelling candidate for developing advanced photosystems that are both efficient and adaptable to various solar energy applications.

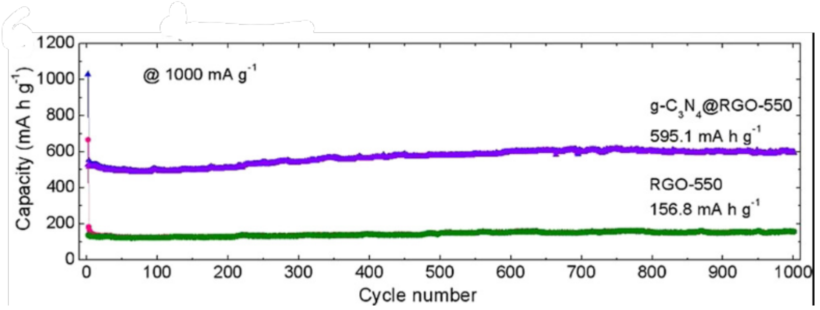

Fig. 3.1 Long cycling capability of RGO-550 and $g-C_3N_4$@RGO-550 electrodes at 1000 mAg^{-1}. [263]

$g-C_3N_4$ has been widely investigated in rechargeable lithium-ion batteries due to high surface area, porous structure and acceptable capacity, in 2018 Wang et al. reported a $g-C_3N_4$/reduced graphene oxide composites as anode, the addition of $g-C_3N_4$ can hinder accumulation of graphene and generates numbers of N-active sites for Li^+ storage. The device was able to achieve an outstanding rate performance with 595.1 mAh/g after 1000 cycles under 1000 mA/g as shown in Figure 3.1. [263]

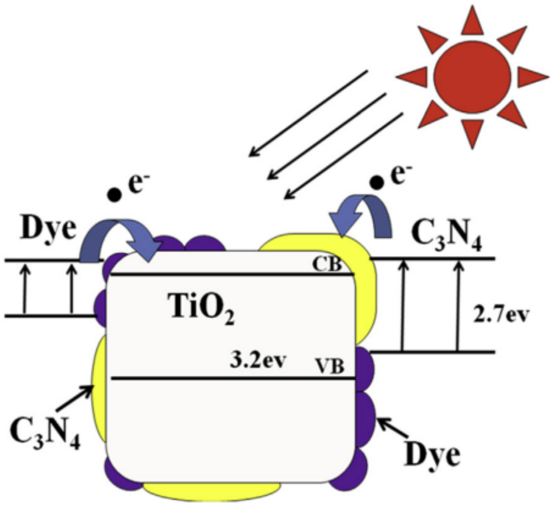

Fig. 3.2 Diagram of $g-C_3N_4$ as blocking layer to increase power conversion efficiency of DSSCs. [264]

There has also been a large amount of research on the application of $g-C_3N_4$ in solar cells. For instance, in 2014 Xu et al. presented a $g-C_3N_4$ modified TiO_2 nanosheets, and the conversion efficiency of the DSSC was improved by almost 28% by simply coating a layer of $g-C_3N_4$ on TiO_2 nanosheets. Here, the $g-C_3N_4$ is used as the blocking layer for electron backward recombination with electrolyte and the performance of the DSSC is enhanced as shown in Figure 3.2.[264]

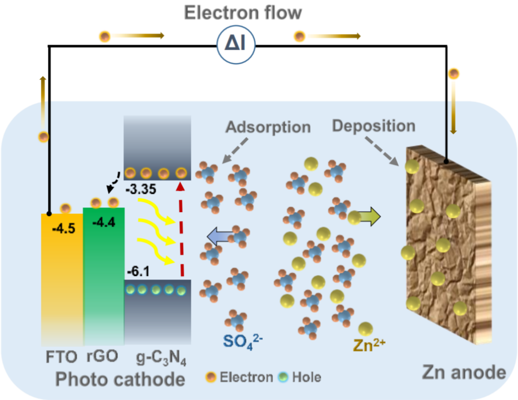

Fig. 3.3 Energy level diagram of the Photo-ZIC demonstrating the participation of photogenerated electrons and holes for photo-charging under illumination. [265]

Regarding $g-C_3N_4$ in single electrode application, in 2020 Boruah et al. reported a photo-rechargeable zinc ion capacitor(ZIC) using 2D graphitic carbon nitride as the photocathode which harvests solar energy and stores charges at the same time.[265] Figure 3.3 shows the Schematic illustration of the photocathode configuration, reduced graphene oxide is added to $g-C_3N_4$ aiming to facilitate the transport of photoexcited electrons. It not only acts as a conductive additive but also plays a part as a selective electron transport layer. When incident photons cause charge separation in $g-C_3N_4$, photo-generated electrons flow through rGO and FTO and agglomerate at the Zn anode by the external circuit, positive Zn^{2+} ions from the electrolyte can be assisted to combine with electrons. In addition to this, the photo-generated holes stay at the photocathode and attract the negative SO_4^{2-} ions from the 2 M $ZnSO_4$ electrolyte. In summary, this process allows Photo-ZICs to photo charge under illumination.

In conclusion, g-C_3N_4 has proven to be a promising material for photo-rechargeable batteries, showing great potential to advance energy storage technology. Its ability to absorb visible light makes it ideal for photocharging applications, as it can efficiently initiate electrochemical processes within the battery, leading to better charging performance. G-C_3N_4's photocatalytic activity is another key feature that allows it to generate electron-hole pairs when exposed to light. This is essential for charge separation and the subsequent electrochemical reactions that drive the photo-recharging process. Plus, being made from carbon and nitrogen, g-C_3N_4 is an eco-friendly and sustainable choice. Its abundance and ease of production make it appealing to those seeking green energy solutions. Despite some challenges, like the tendency for photogenerated charges to recombine and its limited electrical conductivity, ongoing research is finding ways to overcome these issues. Techniques such as doping with other elements and combining g-C_3N_4 with other materials are being explored to boost its overall performance and efficiency. These efforts are crucial for making g-C_3N_4-based photo-rechargeable batteries a viable option for the future of sustainable and efficient energy storage. Table 3.1 also highlights other applications of g-C_3N_4 in solar cells and photo-enhanced energy storage.

Configuration	Photoelectrode	$\eta_{conversion}(\%)$	Ref.
DSSC	g-C_3N_4/conductive carbon black	5.09%	[264]
DSSC	g-C_3N_4/TiO_2	4.73%	[266]
DSSC	g-C_3N_4/ZnO	4.5%	[267]
DSSC	g-C_3N_4/CdS/TiO_2	2.31%	[268]
Perovskite solar cell	g-C_3N_4/carbon	14.34%	[269]
Perovskite solar cell	Exfoliated g-C_3N_4	15.8%	[270]
Perovskite solar cell	g-C_3N_4/MoO_3/Ag	19.49%	[271]
Perovskite solar cell	g-C_3N_4/SnO_2 QDs	22.13%	[272]
Li-O_2 battery	g-C_3N_4/carbon paper	-	[273]
Li-O_2 battery	g-C_3N_4 coated carbon paper	-	[274]
Li-O_2 battery	Defective g-C_3N_4	-	[274]
Li-O_2 battery	g-C_3N_4/rGO	-	[275]
Li-O_2 battery	g-C_3N_4/graphene	-	[276]
Zn-air battery	g-C_3N_4/CuZIF-67	-	[276]
Zn-ion capacitor	g-C_3N_4/$ZnFe_2O_4$	-	[277]
Zn-ion capacitor	g-C_3N_4/rGO	-	[265]

Table 3.1 Performance of representative g-C_3N_4 in solar cells and photo-enhanced energy storages.

3.1.2 BiVO$_4$

In the past few years, vanadium-based oxides including LiV_3O_8, Li_3VO_4,V_2O_5, and LiV_2O_5 have been investigated intensively due to their brilliant physical and chemical properties such as low toxicity, earth-abundant and high stability.[278–280] More recently, Bismuth vanadate($BiVO_4$) has been indicated as one of the novel anode materials for energy storage applications.[281, 282] This can be explained by the double chains of VO_6 octahedra with metal cations between the interlayer space within the material that promotes the intercalation/deintercalation of Li ions, giving rise to exceptional electrochemical performance. More importantly, $BiVO_4$ is noticeably appealing as a photocatalyst for water splitting, as it has both a narrow bandgap of around 2.4 eV resulting in visible light absorption and a suitable valence band edge which provides a strong driving force for water oxidation by photogenerated holes.[283–287]

In 2017, Dubal et al. fabricated a lithium-ion Battery with a hydrothermally synthesized fern architecture $BiVO_4$. For rechargeable lithium-ion batteries, monoclinic $BiVO_4$ can utilise its layered structure to intercalate and de-intercalate lithium ions in a larger content compared to other layered materials. This paper explored the fundamental cell reactions within the lithium-ion battery and its physicochemical and electrochemical properties are investigated by using a full lithium-ion battery with $LiFePO_4$ as a cathode and the fern structured $BiVO_4$ as an anode[288]. In order to characterise the electrochemical performance of $BiVO_4$, the cell was tested in a half-cell configuration against Lithium metal as the counter electrode.

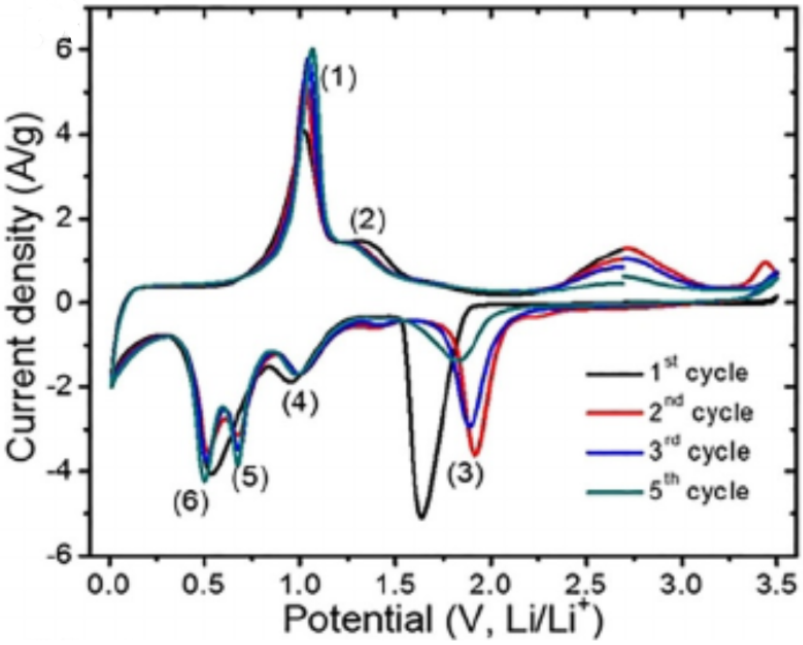

Fig. 3.4 Cyclic voltammetry (CV) curves measured at 1mV/s scan rate for the first five cycles. [288]

Figure 3.4 shows the CV measurement of the $BiVO_4$/Li half cell at 1mV/s scan rate for 5 cycles. This image presents a detailed explanation of different intercalation/de-intercalation processes of Li ions in $BiVO_4$/Li half cell. In the first cycle, four reduction peaks can be observed at around 1.94V, 1.64V, 0.88V, and 0.52 V.[289] After the first cycle, the peaks at 0.52 break into two peaks, which correspond to the reduction of V^{4+} to V^{3+} and formation of Li_3Bi. The peak at 0.88V shows the reduction of V^{5+} to V^{4+} and the peak at 1.64V is attributed to the formation of metallic Bi. The first peak at 1.94V originates from the decomposition of the electrolyte and the formation of the solid–electrote interface(SEI). For the first anodic cycle, three peaks can be obtained at 0.96V, 1.42V, and 2.74V, which each peak corresponds to the de-alloying of Bi, oxidation of V^{3+} to V^{5+} and the oxidation of metallic Bi, respectively. It is worth noticing that the peaks at 2.74V and 1.64V disappeared after the first cycle, which means those reactions are irreversible. It is intriguing that the peak at 2.74V also shifted to a higher voltage, leading to the decomposition of $BiVO_4$. Apart from those peaks, both the alloying and de-alloying of Bi peaks at cathodic 0.71V and anodic 0.96V and The peaks of redox transitions of V at 0.88V and 0.49 V for cathodic and 1.37–1.64 V for anodic are reversible. The CV measurement concludes that $BiVO_4$ can provide two charge storage mechanisms including alloying/de-alloying and faradaic redox transitions leading to high capacity. By understanding the different peaks which match with different reactions, it is possible to alter the voltage window for the photo-LIB, so that the cell can work in the range where only alloying/de-alloying reaction takes place and $BiVO_4$ remains as the photoactive material on the electrode. The overall reaction of $BiVO_4$ with Li should involve 6 Li-ions according to the equation,[290]

$$BiVO_4 + 6Li^+ \rightarrow Li_3Bi + Li_3VO_4 \tag{3.1}$$

Regarding the bifunctional performance of $BiVO_4$ in photo-induced energy storage applications. Momeni et al. reported a light chargeable two-electrode photo-supercapacitor based on MnS nanoflowers deposited on V_2O_5-$BiVO_4$ photoelectrodes in 2023. [291]

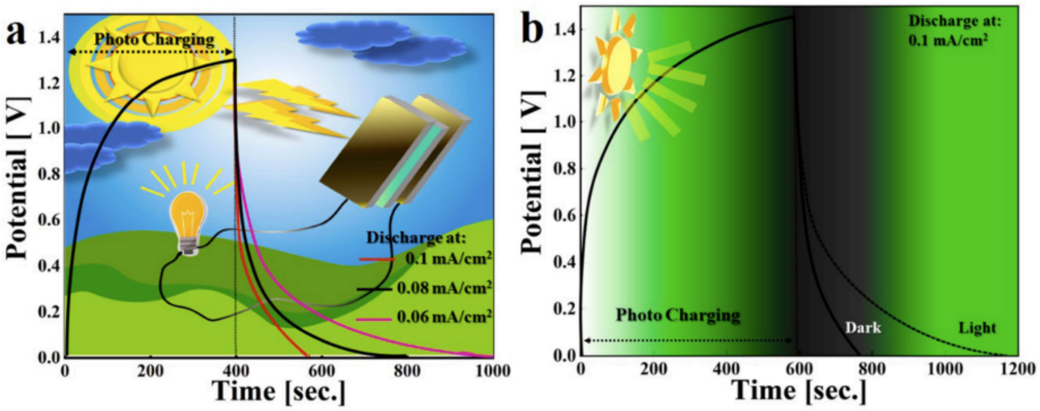

Fig. 3.5 (a). Photo-charge of this SSC device for 600 s and its electrochemical discharge in dark and light (b) or galvanostatic discharge in light and then dark conditions. [291]

The photocharging effect was confirmed by galvanostatic charge and discharge test, the MnS@V_2O_5-$BiVO_4$//MnS@V_2O_5-$BiVO_4$ device can be solely charged by light without applying any external current as shown in Figure 3.5 (a). Furthermore, the potential of the photo-capacitor rose to 1.3 V only after 400 s of illumination before discharging under various current densities. The photo-charging effect was then proved in the light charge-light discharge condition and light charge-dark discharge condition as shown in Figure 3.5 (b), it can be observed that the device was discharged much slower than in the dark condition. This is due to the photogenerated carriers charging the device simultaneously.

In conclusion, $BiVO_4$ holds significant potential as a photoanode material in photobattery applications due to its suitable bandgap, good light absorption properties, and stability under photoelectrochemical conditions. In my work, the material properties of $BiVO_4$ will be investigated using a series of characterisation techniques. In order to understand whether $BiVO_4$ is suitable for acting as the photoelectrode for lithium-ion batteries, $BiVO_4$ photo half-cells against lithium metal were assembled to test the electrochemical performance under both dark and light conditions. Table 3.2 showcases the various applications of $BiVO_4$ in energy harvesting and storage devices.

Battery types	Photoelectrode	$\eta_{conversion}(\%)$	Ref.
Zn-air battery	$BiVO_4/V_2O_5$	-	[292]
Graphite supercapacitor	Mns/V_2O_5-$BiVO_4$	-	[291]
Semiconductor SSC	$BiVO_4$ QDs	0.36%	[293]
Liquid photovoltaic cell	Mo-doped $BiVO_4$ films	0.2%	[294]
Liquid photovoltaic cell	$BiVO_4$	0.7%	[295]
Photo electrocatalytic cell	$WO_3/BiVO_4$	-	[296]
PbS capacitor	BiVO4–PbO_x	-	[297]
Li-O_2 battery	$BiVO_4$ nanoplates	-	[298]
V-F battery	$BiVO_4$ thin film	0.085%	[299]
Zn-iodine RFB	$BiVO_4/TiO_2$-SnO_2	-	[300]
Photoelectrochemical cell	Au NPs/$BiVO_4$	-	[301]
Seawater Na-ion Battery	$BiVO_4$	3.92%	[276]

Table 3.2 Performance of representative $BiVO_4$ in solar cells and photo-enhanced energy storages

3.2 Results and Discussion

3.2.1 G-C_3N_4

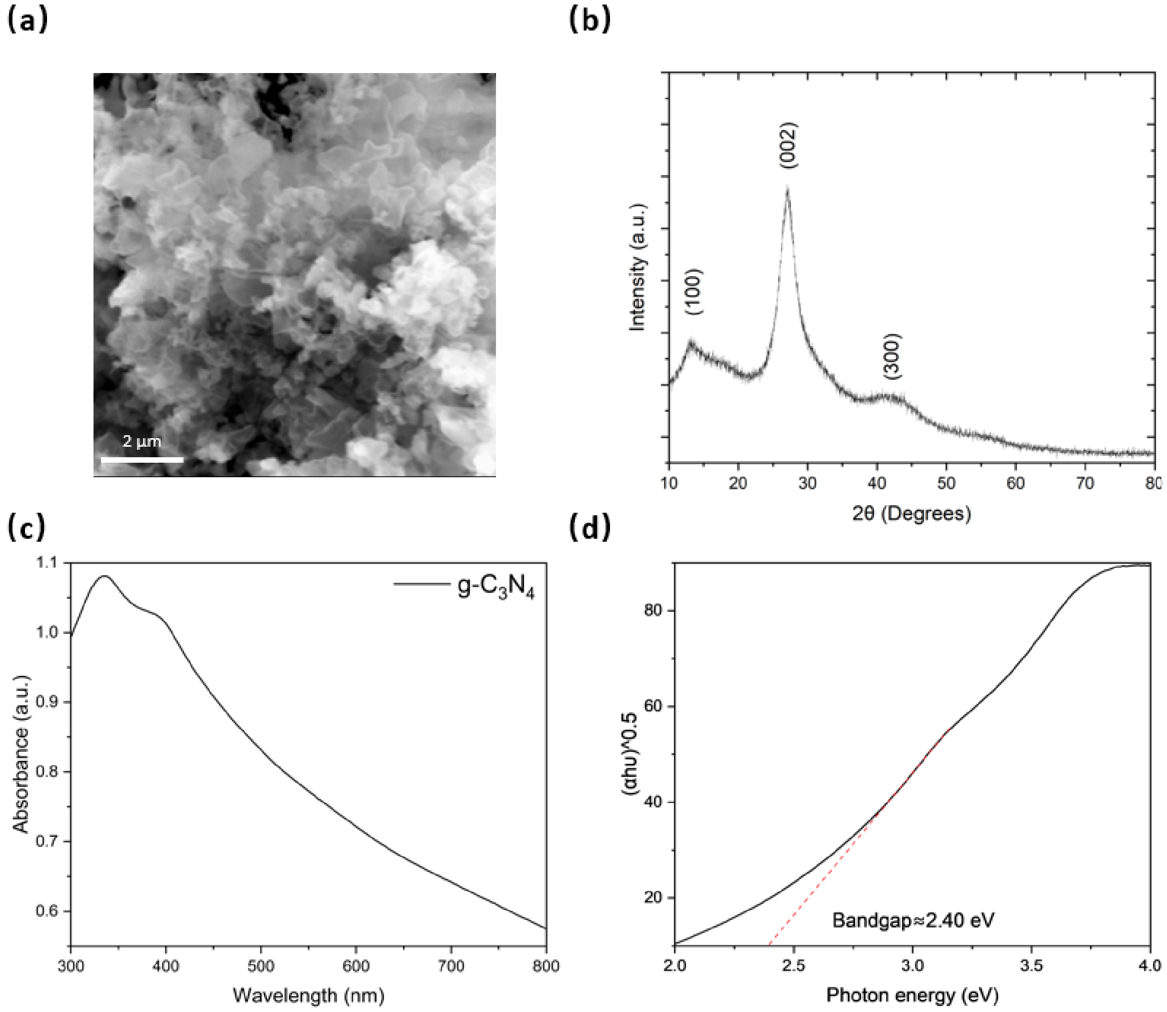

Fig. 3.6 (a) SEM image of synthesized g-C_3N_4. (b) XRD pattern of synthesized g-C_3N_4. (c) Optical absorption spectrum of synthesized g-C_3N_4. (d) Tauc plot of synthesized g-C_3N_4.

Figure 3.6 (a) presents the SEM image of g-C_3N_4, revealing a structure of stacked flat sheets with visible wrinkles and irregular shapes. Pores within the g-C_3N_4 sheets are clearly observed, which is beneficial for applications that require a high surface area, such as catalysis and energy storage. Figure 3.6 (b) displays the XRD pattern of g-C_3N_4, where three distinct peaks are evident. The (100) peak around 13° corresponds to the in-plane structural packing motif of tris-s-triazine units, while the (002) peak around 27° reflects the interlayer stacking of the conjugated aromatic system in g-C_3N_4, indicating the interlayer distance in its graphitic structure. Additionally, a weak peak around 44° suggests the regularity and periodicity of the layer stacking in g-C_3N_4. The sharpness and intensity of these peaks also indicate the high crystallinity of the synthesized g-C_3N_4. In Figure 3.6 (c), the absorbance of g-C_3N_4 was measured as a function of wavelength, which shows a peak absorbance at around 350 nm. By using this result, the band energy of $g-C_3N_4$ can be determined by using the Tauc plot method, which can be based on the equation below:

$$(\alpha hv)^{1/n} = A(hv - E_g) \tag{3.2}$$

Where α is the absorption coefficient of the material, h is the Plank's constant, υ is the frequency of light, n is a constant (0.5 for direct bandgap semiconducting material and 2 for indirect semiconducting material.), and E_g is the bandgap energy.

In order to use the Tauc plot, the x-axis representing wavelength must first be converted to photon energy using the Planck-Einstein relation, $E = hc/\lambda = 1240/\lambda$. Simultaneously, the y-axis needs to be transformed into $(\alpha h\upsilon)^{1/n}$, which can be calculated from 2.302*absorbance*photon energy. The conversion of α from absorbance can be explained using Beer-Lambert law as shown below:

$$I = I_0 e^{-\alpha x} \tag{3.3}$$

$$I/I_0 = e^{-\alpha x} = e^{-\alpha l} \tag{3.4}$$

$$log(I/I_0) = log(e^{-\alpha l}) = -log(e)\alpha l = -0.4343\alpha l \tag{3.5}$$

$$log(I_0/I) = -log(I/I_0) \equiv A = 0.4343\alpha l \tag{3.6}$$

$$\alpha = 2.302(A/l) \tag{3.7}$$

Here, I is the intensity of the transmitted light, I_0 is the intensity of the incident light, A is the absorbance, and l is the thickness of the measuring cuvette, 1 cm in our case. Given that $g-C_3N_4$ is an indirect bandgap material, the Tauc plot of $g-C_3N_4$ can be found, as depicted in Figure 3.6 (d). By extrapolating this linear region to the abscissa, the optical bandgap of the material can be determined. The Tauc plot shows an indirect bandgap of 2.40 eV, this result is similar to other experimental results from the literature. [302, 303]

To confirm the charge separation and transportation ability of $g-C_3N_4$/rGO under the illuminated condition, a photodetector was designed, details of photodetector design and fabrication are demonstrated in the experimental section. As shown in Figure 3.7 (a), no response current was measured at 0 V bias in the dark, and under illumination, a positive current is observed, which indicates that the rGO/$g-C_3N_4$ configuration can effectively generate and transport photo charges upon light. Under illumination, the current (I)-time (t) curve shows a large increment of photo-induced current (I $\approx$ 2 μA) under no bias voltage with a blue LED under the light intensity of approximately 144 mW/cm^2. The I-V curve in Figure 3.7 (b) also shows the photocurrent of the stacked photodetector at the range bias voltage from -0.4 V to 0.4 V under both dark and light conditions. The shift of the results clearly shows the generation of photocurrent.

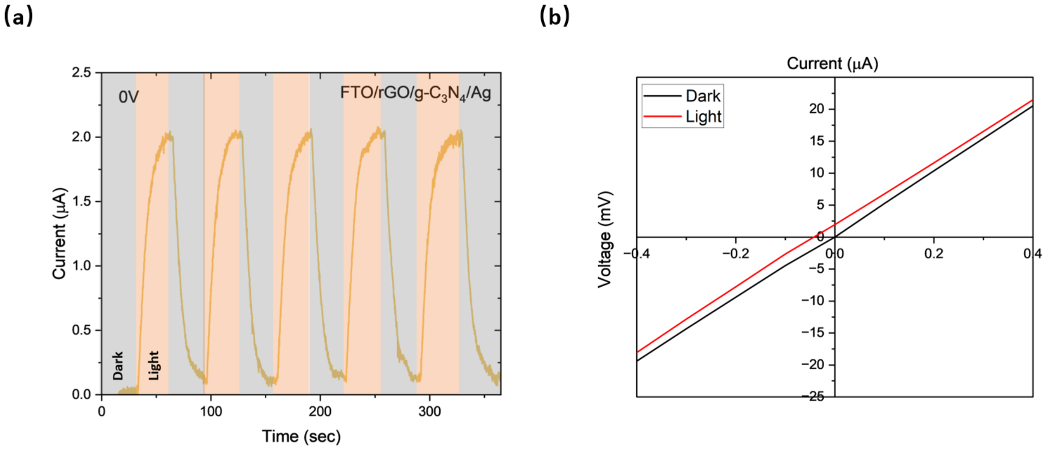

Fig. 3.7 (a) Response current of the FTO/rGO/$g-C_3N_4$/Ag PD under alternating dark and illuminated conditions at 0V applied bias. (b) Current-voltage curves of the planar FTO/rGO/$g-C_3N_4$/Ag PD in dark and illuminated conditions.

The $g-C_3N_4$/Li half-cell was cycled at a cycling density of 100mA/g at a voltage window of 3V to 4V, and the specific capacity was calculated and plotted against the cycle number.

The specific capacity was calculated by,

$$C_{spe} = C/m_{act} \tag{3.8}$$

$$m_{act} = \Delta m * P \tag{3.9}$$

Where C_{spe} is the specific capacity, C is the discharge or charge capacity, m_{act} is the mass of active material, Δm is the difference in mass before and after the drop-casting process, P is the percentage of the active material in the slurry, 0.93 in $g-C_3N_4$ slurry. Figure 3.8 (a) shows the Galvanostatic discharge–charge curves at 100 mA/g at the 1st, 100th and 200th cycle in dark conditions. Unfortunately, the specific capacity is very low at around 10 mAh/g. Figure 3.8 (b) depicts the long-term performance of the $g-C_3N_4$/Li half-cell. It is noteworthy that the coin cell still shows a limited capacity with 10 mAh/g over 200 cycles. When compared to values reported in the literature, this capacity is notably lower. [99] However, the amount of conduction additive in those systems is relatively high with around 20% to 30% of the slurry composition, which can potentially reduce the light absorbed on the photoelectrode. [304] We also performed CVs for the $g-C_3N_4$ Li-ion batteries under dark conditions as shown in Figure 3.8 (c) and (d). The figures showed no interaction reactions but capacitance at various scan rates from 0.2 to 1.0 mV/s. This could possibly explain why the low specific capacity from the GCD results. Again, this is mainly caused by the low conductivity of the $g-C_3N_4$.

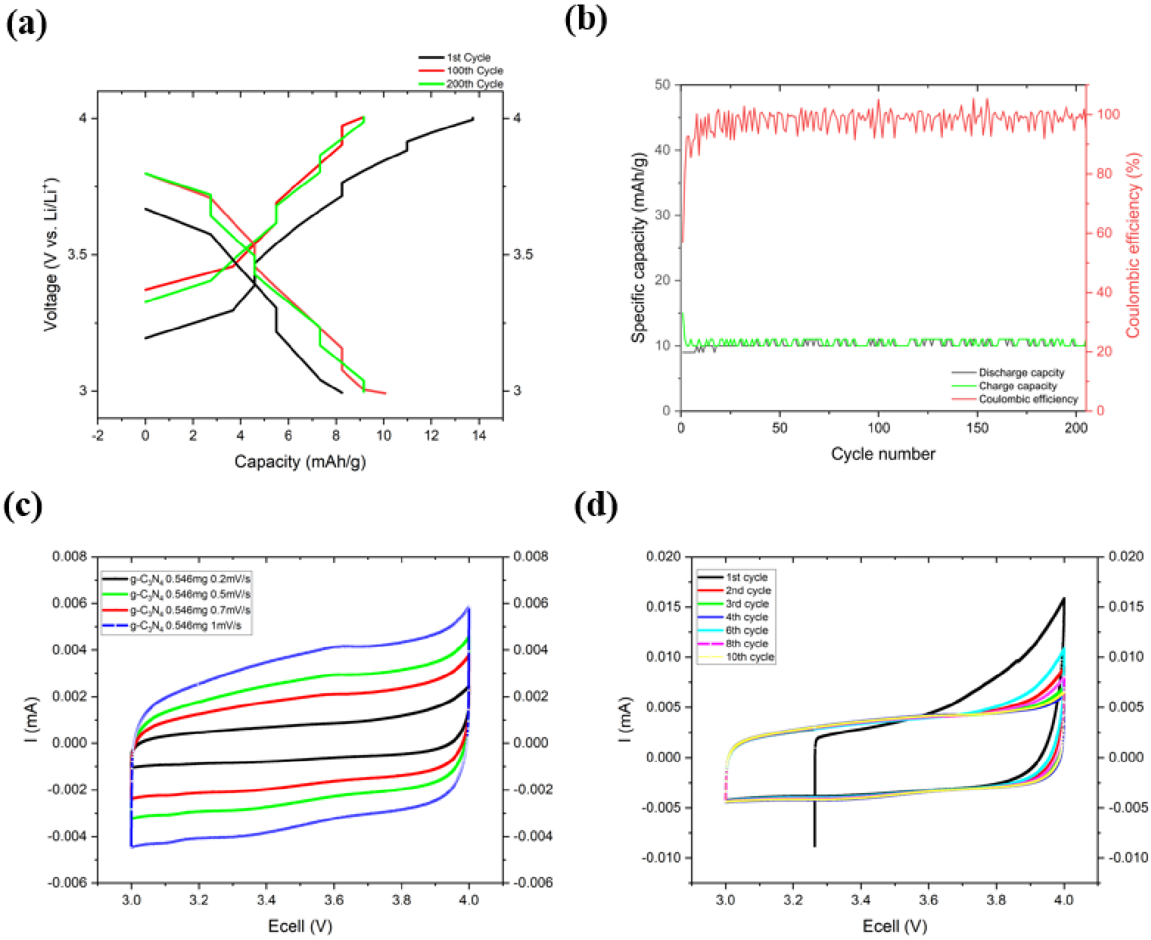

Fig. 3.8 (a) Galvanostatic discharge–charge curves at 100 mA/g at 1st, 100th and 200th cycle in dark conditions. (b) Long-term cycling performance of $g-C_3N_4$ half-cell against Li metal. (c) Cyclic Voltammetry (CV) for $g-C_3N_4$ at various scan rates. (d) CV curves for $g-C_3N_4$ at 1.0 mVs^{-1} for 10 cycles.

Despite the low capacity from our GCD results, we still performed the GCD and CV tests under illuminated conditions under blue LED under the light intensity of 128 mW/cm^2.

First, the GCD curves were collected for the 25th cycle in the dark and the 25th cycle in the illuminated condition as shown in Figure 3.9 (a), there has been a 60% increase in the specific capacity from 9.64 mAh/g to 15.42 mAh/g under illumination.

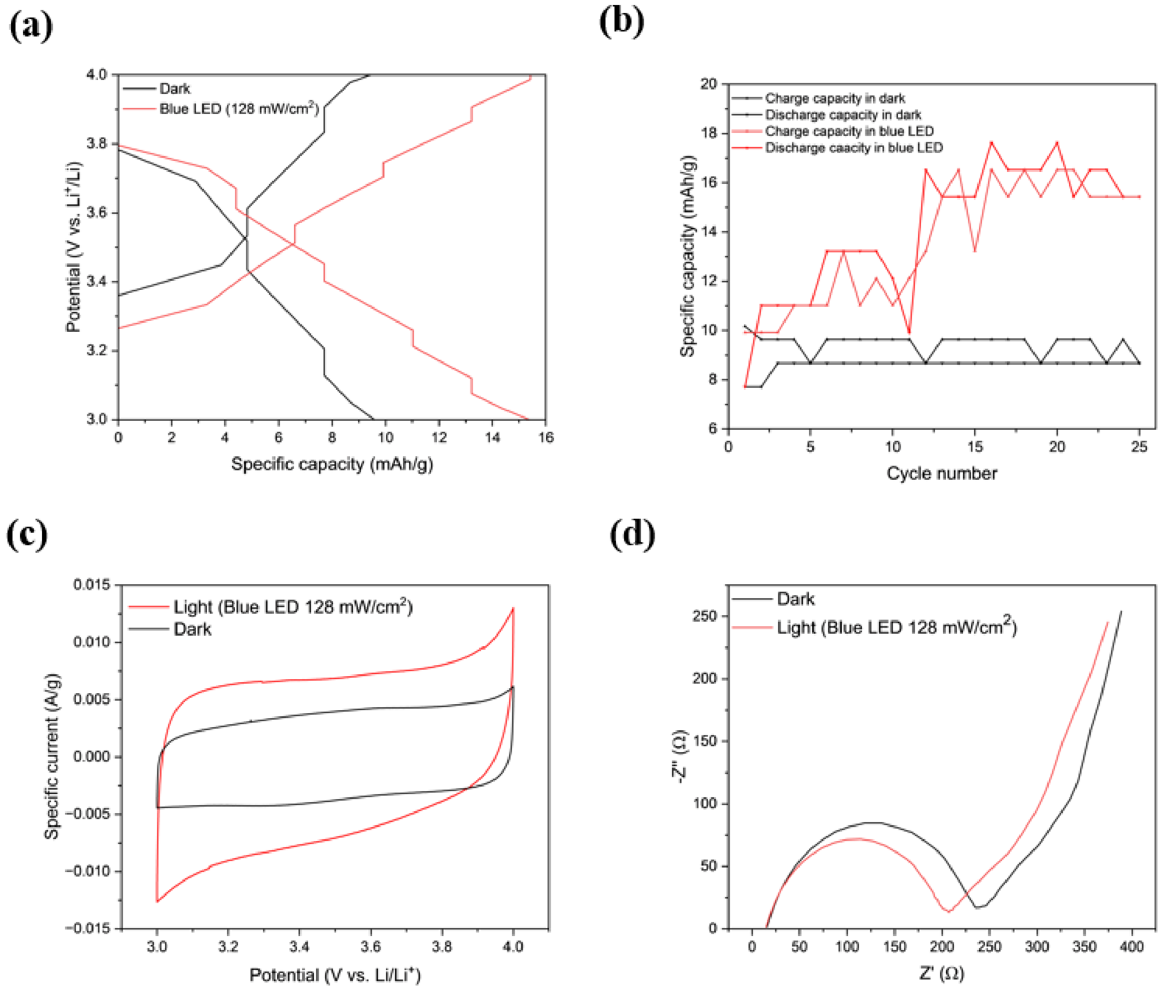

Fig. 3.9 (a) Galvanostatic discharge–charge curves at 100 mA/g under both dark and light conditions. (b) Long-term cycling performance of $g-C_3N_4$ half-cell against Li metal under both dark and light conditions. (c) Cyclic Voltammetry (CV) for $g-C_3N_4$ at 1.0 mVs^{-1} under both dark and light conditions. (d)) EIS measurement of photo-LIB obtained after the 2nd galvanostatic discharge cycle to 50% SoC in the frequency range of 10 mHz-100 kHz at 10 mV amplitude with dark and illuminated conditions.

Moreover, the average specific capacity over 25 cycles under illumination is 43.4% higher than in dark conditions calculated in Figure 3.9 (b). Furthermore, a total enhancement of 123.4% in the total area of the CV curves can be observed under blue LED as shown in Figure 3.9 (c). Figure 3.9 (d) shows the AC impedance spectra of the $g-C_3N_4$ photobatteries before and after illumination, where a decrease of 13.4% in combined series resistance and charge transfer resistance is shown from 240.9Ω to 208.6Ω.

The low conductivity restricts efficient charge transport, which impacts both photocurrent generation in photodetectors and capacity in Li-ion cells. Incorporating conductive materials or doping could address this issue. Although photo-assistance increases the electrochemical performance, the overall capacity is still lower than conventional anode materials. Modifying the morphology or using composites with higher conductivity could improve storage capacity.

3.2.2 BiVO$_4$

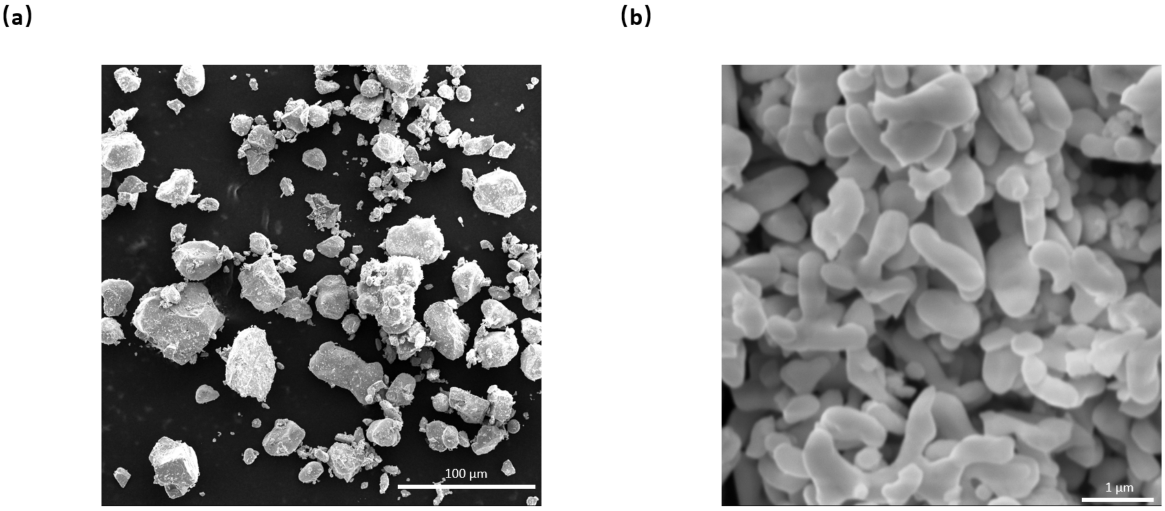

Fig. 3.10 SEM image of (a) commercial BiVO$_4$. (b) synthesized BiVO$_4$.

As depicted in Figure 3.10 (a), the SEM image portrays a commercial $BiVO_4$ sample with secondary particle sizes ranging from approximately 10 μm to 80 μm based on scale. The wide size distribution is mainly due to the aggregation of the primary BiVO$_4$ particles. In contrast, the dimensions of the synthesized BiVO$_4$ as shown in Figure 3.10 (b) range from approximately 1 μm to 2 μm, indicating a considerably smaller size compared to the commercial sample. Due to the difference in particle size, the scale of the SEM images is different in order to have an overview of the particle microstructure. Furthermore, there is an observable transformation in shape, the synthesized BiVO$_4$ has a worm-like porous structure with a smooth surface. The reduced particle size can effectively increase the surface area-to-volume ratio, creating more active sites for electrochemical reactions and contributing to a higher specific capacity. Moreover, the increased surface area also allows for more efficient light absorption, increasing the light conversation efficiency.

Figure 3.11 (a) depicts the X-ray diffraction (XRD) pattern of the synthesized $BiVO_4$ powder obtained through the hydrothermal method. The outcome reveals a pristine monoclinic scheelite single-phase structure, with no discernible peaks associated with other phases or impurities. The narrow line widths and robust intensity collectively suggest a high degree of crystallinity in the synthesized material. In Figure 3.11 (b), the crystal structure of monoclinic scheelite $BiVO_4$ is illustrated. The unit cell of this structure comprises a BiO_8 dodecahedron and a VO_4 tetrahedron. Specifically, the vanadium (V) atom is intricately linked to four oxygen (O) atoms within a tetrahedral site, while the bismuth (Bi) atom is surrounded by eight oxygen atoms originating from eight distinct VO_4 tetrahedral units. This arrangement delineates the intricate geometric configuration within the crystal lattice.

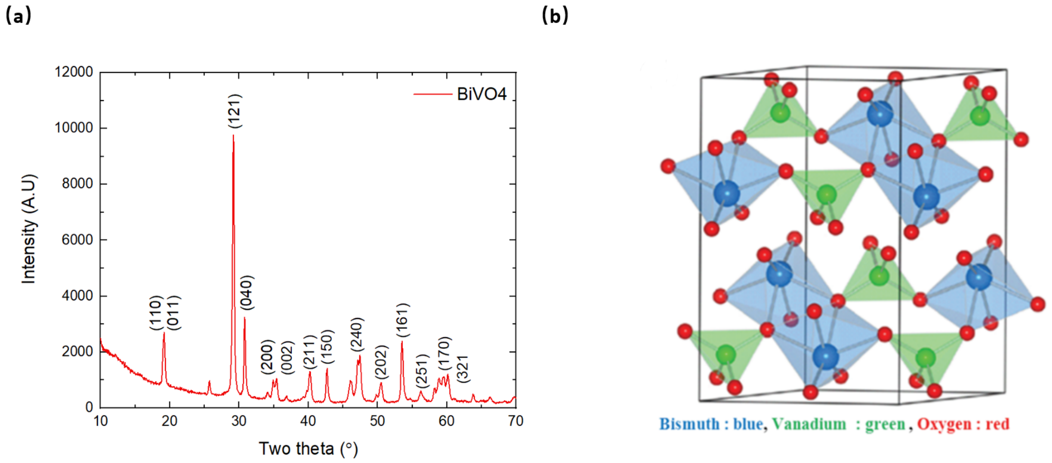

Fig. 3.11 (a) XRD pattern of the synthesized $BiVO_4$ powder. (b) Crystal structure of monoclinic scheelite $BiVO_4$.

In Figure 3.12 (a), the absorbance spectrum of $BiVO_4$ shows a peak at around 450 nm in the visible region. By using the Tauc plot as shown in Figure 3.12 (b), the bandgap of the synthesized $BiVO_4$ is approximately 2.31 eV, similar to what I found in the literature.[305] Figure 3.13 demonstrates the response current for the rGO/BiVO$_4$ PD under the blue LED, it can be clearly observed that there has been an increase in current ($\approx 3\mu$A) under 0V bias voltage. This result shows the ability to generate charge carriers for BiVO$_4$ under illumination. However, the current shows fluctuation throughout the test. This possibly results from the poor charge transport and high recombination losses due to the low conductivity of BiVO$_4$. The I-V curve in Figure 3.13 (b) also shows the photocurrent of the stacked photodetector at the range bias voltage from -4.0 V to 4.0 V under both dark and light conditions. The shift of the results demonstrates the generation of photocurrent.

To evaluate the electrochemical performance of both commercially available and synthesized $BiVO_4$, I conducted tests within a voltage range from 0.01 V to 3.5 V at a current

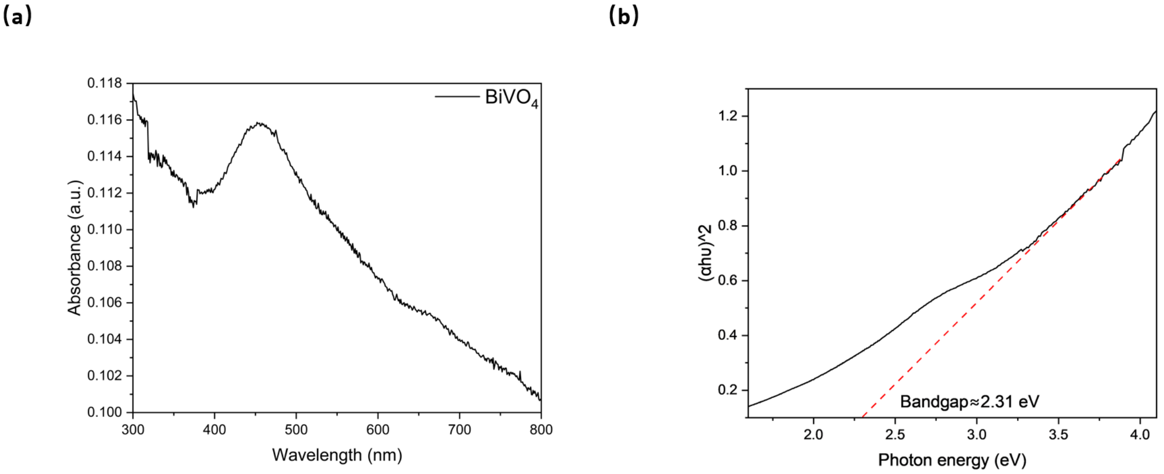

Fig. 3.12 (a). UV-VIS spectroscopy of synthesized $BiVO_4$. (b). Tauc plot of synthesized $BiVO_4$.

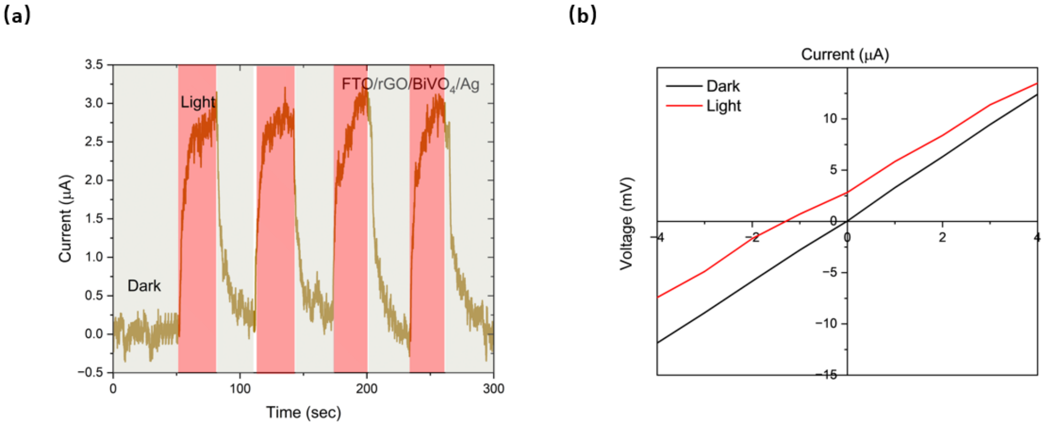

Fig. 3.13 (a) Response current of the FTO/rGO/BiVO$_4$/Ag PD under alternating dark and illuminated conditions at 0V applied bias. (b) Current-voltage curves of the planar FTO/rGO/BiVO$_4$/Ag PD in dark and illuminated conditions.

density of 50 mA/g, as shown in Figure 3.14, for comparison with existing literature results. In the initial discharge cycle, a plateau was observed at approximately 1.8 V vs. Li/Li$^+$, corresponding to the insertion of Li ions for both commercial and synthesized $BiVO_4$.[306] Additionally, more prominent plateaus below 1.0 V vs. Li/Li$^+$ were noted, associated with the alloying/dealloying of Bi and redox transitions of V, which align with previous literature findings.[288] Interestingly, both cells exhibited exceptionally high capacity, exceeding the specific capacities reported in the literature.

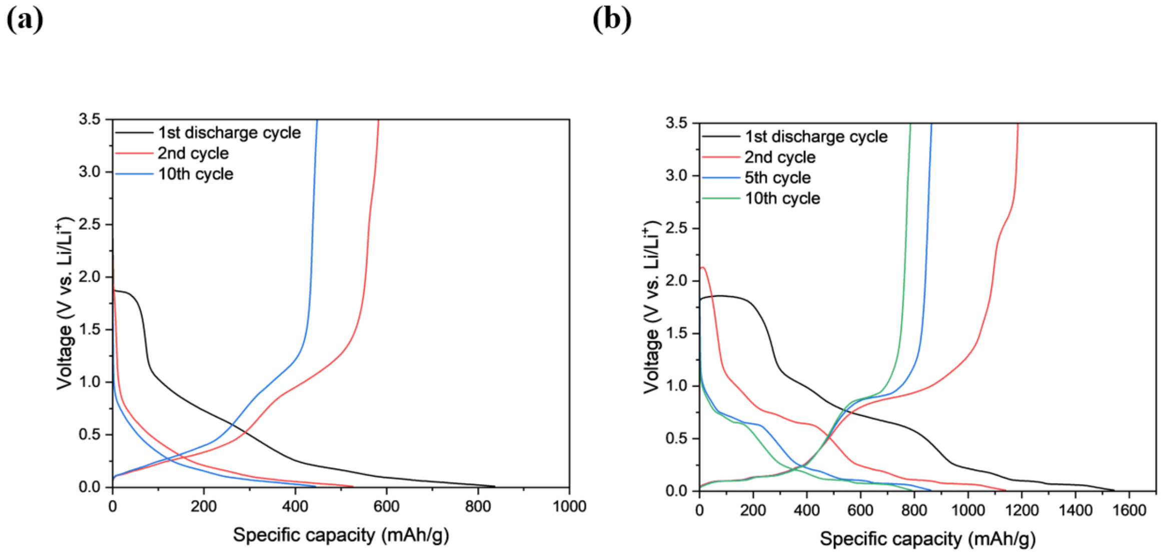

Fig. 3.14 (a) GCD curves of commercial $BiVO_4$ at selected cycle number with a current density of 50 mA/g.(b) GCD curves of synthesized $BiVO_4$ at selected cycle number with a current density of 50 mA/g.

In order to investigate the exceptionally high capacity, we compared our coin cell structures with the report and found that the current collector they used is Copper foil. In our batteries, carbon felt is used due to its ability to allow light to go through. However, the capacity may be impacted by the carbon felt current collector, because it has been reported that, at relatively low potentials versus Li, lithium ions can intercalate into the carbon felt.[307]

A GCD test was conducted using only the carbon felt (CF) as the electrode against Li metal, without any active material, at the same current applied to the synthesized $BiVO_4$, as shown in Figure 3.15. Notably, the specific capacity increases rapidly below approximately 1.0 V vs. Li/Li$^+$, indicating that Li ions can be inserted into the carbon, resulting in an unusually high specific capacity.

To assess the photocharging performance, it is essential to consider that alloying and dealloying processes typically occur below 1.0 V vs. Li/Li$^+$, resulting in the formation of Li_3Bi. Although this transformation appears highly reversible according to the GCD

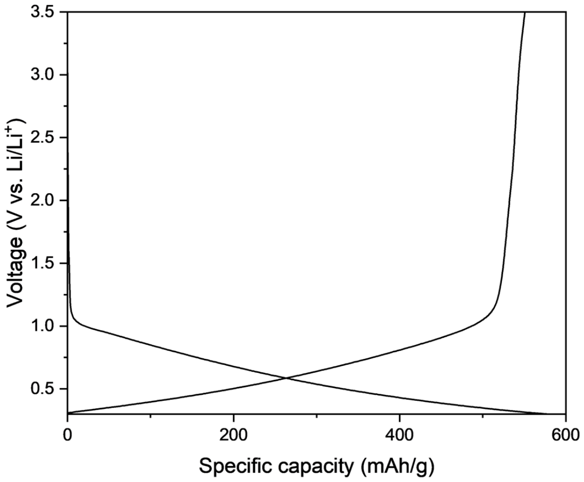

Fig. 3.15 GCD curves of bare carbon felt vs. Li metal at the 2nd cycle number.

results, the bandgap and photoactive properties of the resulting product remain uncertain. To further investigate, an additional GCD measurement was performed within a voltage range of 1.7 V to 3.5 V to determine whether the intercalation reaction at 1.8 V vs. Li/Li$^+$ could be reversible without fully converting $BiVO_4$ to Li_3Bi. As depicted in Figure 3.16 (a), the commercial $BiVO_4$/Li cell initially achieved a specific capacity of approximately 80 mAh/g, but this capacity declined rapidly after the first cycle. Similarly, the synthesized $BiVO_4$ exhibited a quick capacity reduction over successive cycles, as shown in Figure 3.16 (b).

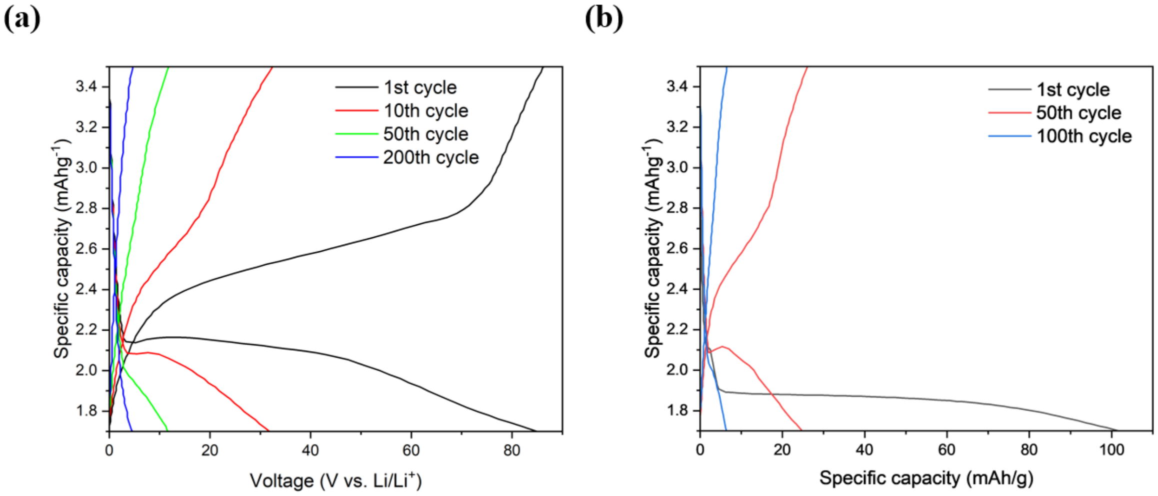

Fig. 3.16 (a) GCD curves of commercial $BiVO_4$ at selected cycle number with a current density of 50 mA/g.(b) GCD curves of synthesized $BiVO_4$ at selected cycle number with a current density of 50 mA/g.

It appears that the lower bound of the voltage window is too low to contribute to the capacity and the plateau at around 1.8 V is still not reversible. In order to obtain a reasonable specific capacity, the voltage window from 1.0 V to 2.5 V was applied. The reason why the higher boundary of the voltage is also altered is because no capacity can be obtained between 2.5 V to 3.5 V. As shown in Figure 3.17, I was able to achieve a suitable specific capacity at 1.0 V to 2.5 V potential range. The specific capacity is maintained at around 130 mAh/g over 20 cycles. However, I am still not able to maintain the insertion reaction at 1.8 V and the trend of the GCD results after the first cycle looks like a typical conversion-type reaction. Despite the sharp capacity loss during the first few cycles due to the activation of the electrode material, as well as to decomposition of the electrolyte and formation of an SEI on the electrode, the capacity remains stable after the 10th cycle without dramatic degradation.

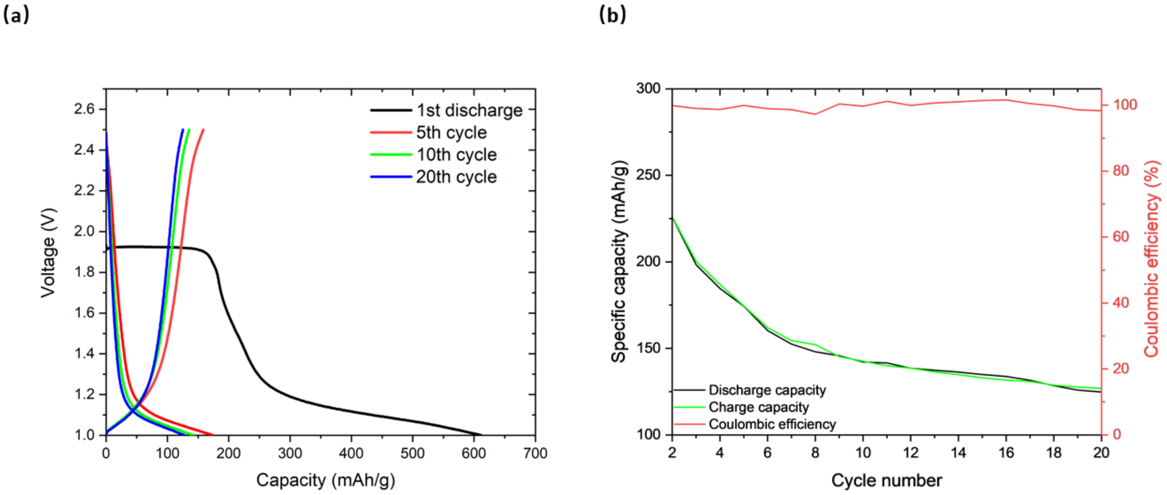

Fig. 3.17 (a) GCD curves of synthesized $BiVO_4$ at selected cycle number with a current density of 50 mA/g. (b) Long-term cycling performance of synthesized $BiVO_4$.

Despite the challenge of maintaining the plateau at around 1.8 V which keeps $BiVO_4$ material integrity and photoactivity, I still assembled some photobatteries and tested the cell after 10 cycles under blue LED illumination at the light intensity of 128 mW/cm^2 to investigate any change in the specific capacity as shown in Figure 3.18 (a).

Comparing the GCD curves at the first cycle for each condition, the specific capacity shows a slight increase of 7.3% from 178.6 mAh/g to 191.7 mAh/g. However, I believe this capacity enhancement is strongly affected by the capacity fade of the active material. Figure 3.18 (b) also shows the charge and discharge capacity under dark and light conditions over 10 continuous cycles. Even with the large capacity loss possibly due to the instability of $BiVO_4$ material or the electrolyte under light or thermal conditions. I am still able to observe

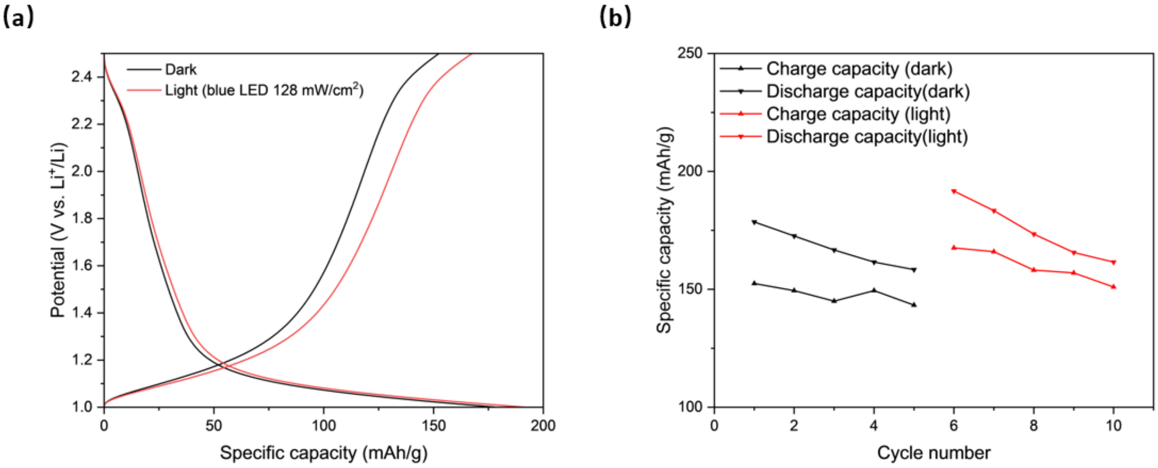

Fig. 3.18 (a) GCD curves of synthesized $BiVO_4$ at selected cycle number with a current density of 50 mA/g under blue LED illumination. (b) Cycling performance of synthesized $BiVO_4$ over 10 cycles under both dark and light conditions.

a capacity enhancement under illuminated conditions. Therefore, capacity retention under both illuminated and heated conditions will be a key factor in future material selection.

3.2.3 Conclusion and overlook

The synthesis of g-C_3N_4 was successfully achieved, and the material was characterized using SEM, XRD, and UV-vis spectroscopy. A photodetector (PD) composed of rGO/g-C_3N_4 was fabricated, demonstrating photo-current generation under illumination. However, the g-C_3N_4/Li half-cell exhibited limited specific capacity due to the material's inherently low conductivity. Additionally, $BiVO_4$ with a porous structure was synthesized using a hydrothermal method and characterized through SEM, XRD, and UV-vis spectroscopy. By carefully optimizing the voltage window to 1.0–2.5 V, a capacity of approximately 140 mAh/g was achieved after 20 cycles. Photo batteries were subsequently fabricated to evaluate electrochemical performance under both dark and illuminated conditions. While photo-enhancement was observed under blue LED illumination in the galvanostatic charge-discharge (GCD) results, the conversion-type reaction curves raised questions regarding whether the observed behavior was due to photo-generated electron-hole pairs or other underlying mechanisms.

Previous investigations into the photocharging effects in g-C_3N_4 and $BiVO_4$ revealed a tendency to focus primarily on the properties of individual photoactive materials rather than the complete battery system. Earlier studies, including the work by Pujari et al., emphasized the importance of the overall system, particularly the charge transport between electrodes,

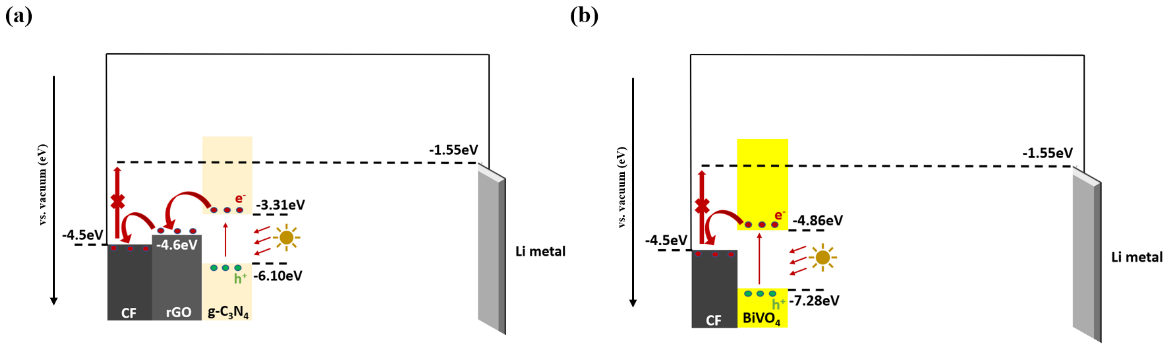

Fig. 3.19 The band alignment vs. Li metal in (a) g-C_3N_4 photobattery. (b) $BiVO_4$ photobatter.

rather than just the photoactivity of the photoelectrode. [308] Figure 3.19 presents the band alignment for the g-C_3N_4 and $BiVO_4$ photobatteries previously fabricated. It has been shown that achieving effective photocharging requires the conduction band of the photoelectrode to be positioned higher than the lithiation potential. However, even when photo-generated charge carriers are separated and transported to the current collector, the lack of sufficient driving force to reach the counter electrode, due to a mismatch in band alignment between the photoelectrode and Li metal, which prevents effective photobattery charging under light alone.

Additionally, previous work has noted that heat generated from illumination can enhance electrochemical performance by improving specific capacity, rate capability, Li diffusion rate, and reducing charge transfer resistance. However, elevated temperatures can adversely affect the battery's lifespan and cycling stability. This has shifted the focus of the current study toward understanding the effects of photo-induced heat on battery performance. Building on prior research, the selection of thermally stable materials that retain performance under both illumination and elevated temperatures will be critical for future experiments.

Chapter 4

Photothermal enhancement of Prussian blue cathodes for Li-ion batteries

4.1 Motivation

Prussian blue, first discovered in Johann Conrad Dippel's laboratory in 1724, was later synthesized by John Woodward.[309] Initially used as a pigment during the 18th and 19th centuries, Prussian blue became well-known for its vibrant colour. In 1936, Keggin and Miles utilized X-ray diffraction to study its chemical and crystal structure. Their research revealed a cubic crystal structure with Fe^{2+} and Fe^{3+} ions alternating on a face-centred cubic (FCC) lattice. [310] Over the years, Prussian blue and its analogues (PBAs) have become the focus of extensive research due to their versatile applications in fields such as cancer therapy, hydrogen storage, sewage treatment, biosensing, and seawater desalination. These transition-metal hexacyanoferrates are prized for their open framework structure, abundant redox-active sites, and robust structural stability. Prussian blue and its analogues exhibit a remarkable ability to store large alkali cations, facilitating the rapid transportation of ions, including sodium and potassium, through their large ionic channels and interstices. This capability has driven intensive research in recent years. Another noteworthy feature is the minimal change in volume or geometry during ion insertion, which contributes to their long cycling life. Additionally, the cost-effectiveness of the compounds used to synthesize Prussian blue and its analogues further enhances their appeal for various applications. These unique strengths and limitations stem from the interaction between alkali ions and the crystal structure. The general electrochemical equation for the insertion of an alkali metal into a PBA is demonstrated below:

$$A_X P^J [R^K (CN)_6]_{1-Y} \cdot wH_2O + A^+ + e^- \rightarrow A_{X+1} P^J [R^{K-1} (CN)_6]_{1-Y} \cdot wH_2O \tag{4.1}$$

In the electrochemical equation, where A represents an alkali metal ion, and P and R denote transition-metal ions octahedrally coordinated to six cyanide ligands via the nitrogen and carbon atoms, respectively. The variable y represents the fraction of vacancies within the hexacyanoferrate complex ion, signifying the presence of primary lattice defects.

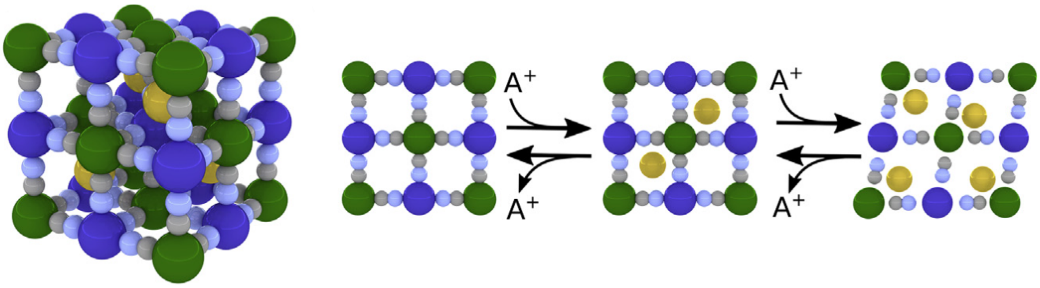

Fig. 4.1 The schematic crystal structures of PBA frameworks. [88]

Figure 4.1 shows the crystal structure of PBAs, the Prussian blue analogues have a face-centred cubic geometry and open-framework lattice. Here, the green and dark-blue atoms are transition-metal ions at the R site and P site, respectively. The yellow atoms are inserting ions. Grey atoms are carbon and light-blue atoms are nitrogen. The green atoms at the centre of the hexacyanometallate complex which connect with carbon atoms give the PBAs their open framework and cubic geometry.[311] When ions are inserted into the subcubes of the crystal, they can be stored inside as the transition-metal ions change oxidation state, it also states that at the high concentration of Alkali-metal ions, the crystal can distort to a less symmetric rhombohedral shape. The bond between the R site and the carbon atom can have a drastic effect on the lattice parameter, channel size and ionic conductivity. It is worth noticing that even with an insertion of an ion into the subcube, it has been reported that during insertion of the lithium ions, the volume of the unit cell in manganese hexacyanoferrate decreases 3.5%,[312] this is caused by the increase in electron density, leading to the shrinkage in hexacyanometallate complex. The R site can also influence the reaction potential, for example, hexacyanomanganate(III/II) has a reaction potential of 0V versus the standard hydrogen electrode. In comparison, hexacyanochromate(III/II) has a reaction potential of -0.8V versus the standard hydrogen electrode(SHE).[313] Recently, there has been more attention to hexacyanoferrates as cathode material because of their exceptional reaction potential of 1 V versus SHE. Apart from that, hexacyanoferrates are also very stable at high temperatures and in acidic conditions. This stability makes PBAs rather appealing as low-risk electrode materials despite the presence of cyanide ligands.

In contrast, the P site exerts a milder influence on the crystal geometry, with the channel size typically exhibiting a linear dependence on the ionic radius of the P-site cation. However, the P-site ions can significantly impact the reaction potential of the R-site. Higher ionic potentials (the quotient of charge and radius) result in a higher insertion potential. This phenomenon is attributed to the increased polarization of the σ bond in the cyanide ligand, enhanced π back bonding, and a lower energy level of the t_{2g} orbitals on the R-site ion. Among the commonly chosen elements for the P site in Prussian blue analogues—iron, manganese, and cobalt—all exhibit electrochemical activity within the stability window of organic electrolytes, enabling two-electron redox reactions. This electrochemical activity allows for the full utilization of the crystal structure's potential in ion storage.

Prussian blue-based materials are highly versatile and can be tailored for specific applications by modifying their composition and structure. Current research aims to further optimize these materials to enhance efficiency, stability, and scalability in various photo devices, thereby advancing renewable energy and optoelectronics. The Prussian blue analogue I am investigating has a general formula of $A_xM[Fe(CN)_6]_y \cdot zH_2O$, where A indicates an alkali metal ion such as Li+, Na+, K+ and so on, M denotes transition metal ions such as Fe, Co, Ni, Mn, Cu, Mn and so on, where 0 < x < 2 and 0 < y < 1. Within the cubic lattice structure, the M^{2+} ions are sixfold coordinated to the nitrogen atoms of the C-N ligands, and Fe^{2+} ions are octahedrally neighbored with the carbon atoms of the C-N ligands, forming a three dimensions compact framework containing wide ionic channels and vast interstitial sites. In general, Prussian blue analogue compounds contain two different redox-active centres: $M^{2+/3+}$ and $Fe^{2+/3+}$ couples, both of which can undergo a complete electrochemical redox reaction if M are Fe, Co, Mn and so on.

A very recent report in 2020 from Wang et. al indicated a sodium-rich rhombohedral Prussian blue for sodium-ion batteries, which also demonstrated reversible structural transformations between rhombohedral, cubic, and tetragonal structures upon sodium-ion intercalation and deintercalation. In the end, large-scale production of the $Na_{2-x}FeFe(CN)_6$ was presented and a full pouch cell was assembled as shown in Figure 4.2. The full pouch cell showed excellent capacity retention of 78% over 1000 cycles.

The electrochemistry for the Sodium-ion battery can be expressed as the equation below,

$$Na_2M^{II}[Fe^{II}(CN)_6] \leftrightarrow NaM^{III}[Fe^{II}(CN)_6] + Na^+ + e^- \tag{4.2}$$

$$NaM^{III}[Fe^{II}(CN)_6] \leftrightarrow M^{III}[Fe^{III}(CN)_6] + Na^+ + e^- \tag{4.3}$$

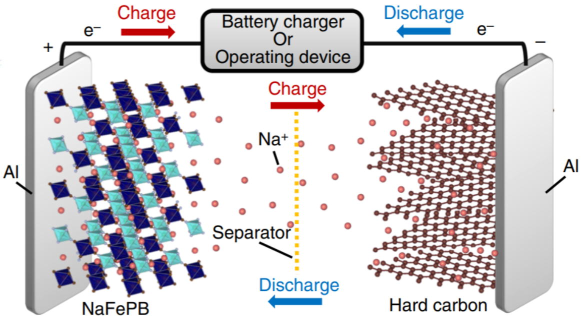

Fig. 4.2 Working mechanism of pouch full cell. [314]

As we can tell from the equation, the complete electrochemical redox reaction contributes to a two-electron transfer capacity through a reversible 2 Na^+ insertion reaction/extraction process. For instance, the $Na_2FeFe(CN)_6$ has a theoretical capacity of 170mAh/g according to its formula weight and the two-Na+ insertion in each PBA unit. This capacity is much larger than many transitional metal oxides and phosphate, which have sodium ions insertion capacity of 100mAh/g to 150mAh/g and 120mAh/g respectively.[315] Thus. the Na-PB is the second focused material I investigated during my PhD project.

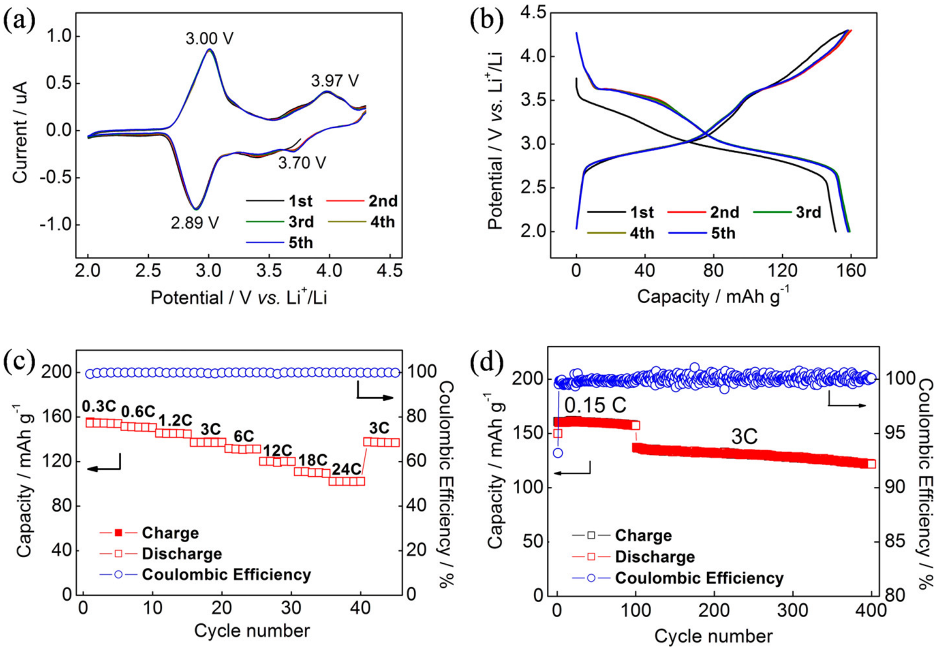

Fig. 4.3 Electrochemical characterizations of $FeFe(CN)_6$ electrode: (a) CV curves measured at a scan rate of 0.1 mVs^{-1}; (b) galvanostatic charge/discharge experiments at a 0.15 C rate (1 C = 160 mAg^{-1}); (c) rate performance from 0.3 to 24 C; (d) long-term cycle performance at various currents of 0.15 and 3 C rates. All the cells were tested in the potential range of 2.0-4.3 V vs Li^+/Li. [316]

In 2016 Wu et al. reported a low defect $FeFe(CN)_6$ framework for Li-ion battery[316], as shown in Figure 4.3 (a), the CV curves show a two-step Li insertion reaction, which can be explained by the equations below:

$$Fe^{3+}[Fe^{3+}(CN)_6] + Li^+ + e^- \leftrightarrow LiFe^{3+}[Fe^{2+}(CN)_6] \tag{4.4}$$

$$LiFe^{3+}[Fe^{2+}(CN)_6]] + Li^+ + e^- \leftrightarrow Li_2Fe^{3+}[Fe^{2+}(CN)_6] \tag{4.5}$$

Moreover, the rate performance and long-term stability for $FeFe(CN)_6$ were excellent up to 400 cycles as shown in Figure 4.3 (c) and (d). Therefore, Fe-PB is one of the focused materials I investigated and adapted to photo-batteries.

There have also been noteworthy findings indicating that certain Prussian blue analogues exhibit photocatalytic properties. In 2014, Li et al. synthesized Prussian blue/TiO_2 nanocomposites, employing them as a heterogeneous photo-Fenton catalyst for the degradation of organic pollutants in water.[317] Additionally, in 2018, Gao et al. reported that Prussian blue analogue $BiFe(CN)_6 \cdot 4H_2O$ possesses exceptional visible light catalysis capabilities. This active material, as determined through UV-Vis spectroscopy, is calculated to have a narrow optical bandgap of 1.63eV. Notably, this bandgap holds particular significance in the context of photo-active material for photo-enhanced battereis.

In addition, several studies have shown that PBA analogues are efficient at photo-thermal heating, arising from their ability to absorb light in the visible or near-infrared (NIR) spectrum efficiently and convert that absorbed energy into non-radiative heat as a result of electronic transitions within the PBA. Because of this, PBA nanoparticles have found applications in biomedical applications, such as photo-thermal therapy for cancer treatment. [318–320]

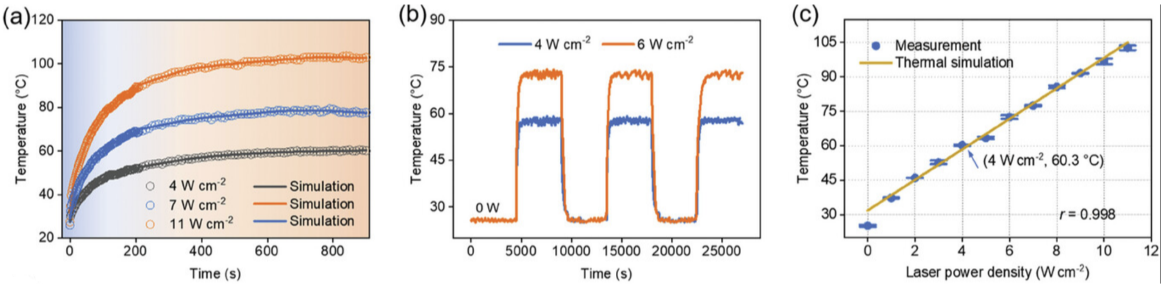

Fig. 4.4 a) Heating curves of the coin cell irradiated under various laser power densities. b) Recycling heating profiles of the cell under intermittent heating. Hold each step for 75 min. c) Temperature of the cell generated by an 808 nm laser as a function of laser power density. [321]

In a very recent paper in 2023, Wang et al. reported a solid-state Lithium metal battery by using a photothermal-based solid polymer-based electrolyte (PT-SPE). [321] The PT-SPEs consist of Prussian blue nanoparticles, PEO and lithium bis(trifluoromethanesulfonyl)imide (LiTFSI). The reason why Prussian blue is used in the SPE is due to the high photo-thermal conversion efficiency as shown in Figure 4.4. Under various laser intensities, the temperature of the coin cell increases dramatically. Additionally, the temperature also increases linearly with increasing laser power.

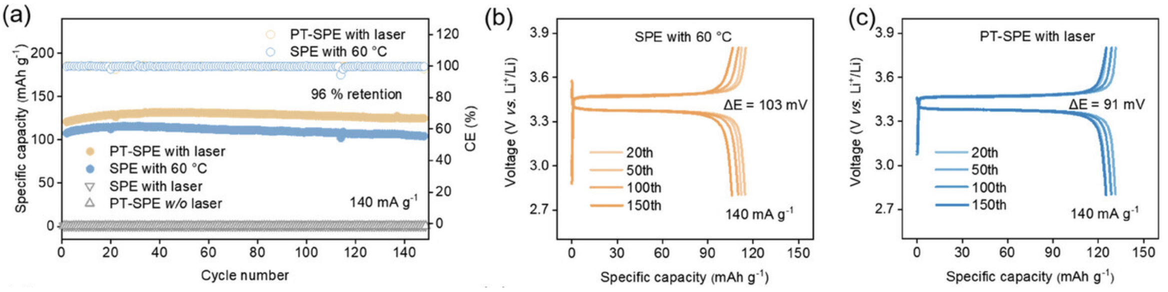

Fig. 4.5 a) Cycling performance of LFP/Li cells as a function of cycle number. Charge-discharge curves of b) LFP/SPE/Li cell under 60°C and c) LFP/PT-SPE/Li cell cycled under the laser. [321]

The electrochemical performance of the cell is also boosted due to the photo-thermal effect as shown in Figure 4.5. In Figure 4.5 (a), the specific capacity for PT-SPE with laser is higher than the SPE without Prussian blue at 60°C and the comparison without laser. Without photo-thermal effect, the capacity of the cell is negligible. Moreover, the cycling stability of the cell for both PT-SPE with laser and SPE without Prussian blue at 60°C is maintained at around 96% retention and no side reaction is observed for the Prussian blue electrolyte with laser illumination. Overall, by introducing a photo-thermal effect within the system, the Li ions diffusion barrier is largely reduced. Furthermore, the incorporation of a photothermal effect into polymer electrolytes has the potential to enhance ion transport and stabilize solid–solid interfaces even at room temperature. This paper also gives me the motivation to fabricate PBA photothermal batteries.

Prussian blue analogues (PBAs) have garnered significant attention as materials for rechargeable batteries due to their unique properties. For instance, $Na_2FeFe(CN)_6$ (Prussian white) demonstrates a specific capacity of 170 mAh/g in sodium-ion batteries, while $Li_2FeFe(CN)_6$ exhibits a capacity of 190 mAh/g in Li-ion batteries [322, 323]. Beyond their electrochemical potential, PBAs are notable for their light absorption capabilities, particularly in the visible and near-infrared regions of the electromagnetic spectrum. This property facilitates a photothermal effect, likely driven by nonradiative relaxation processes common in semiconducting materials [324, 325].

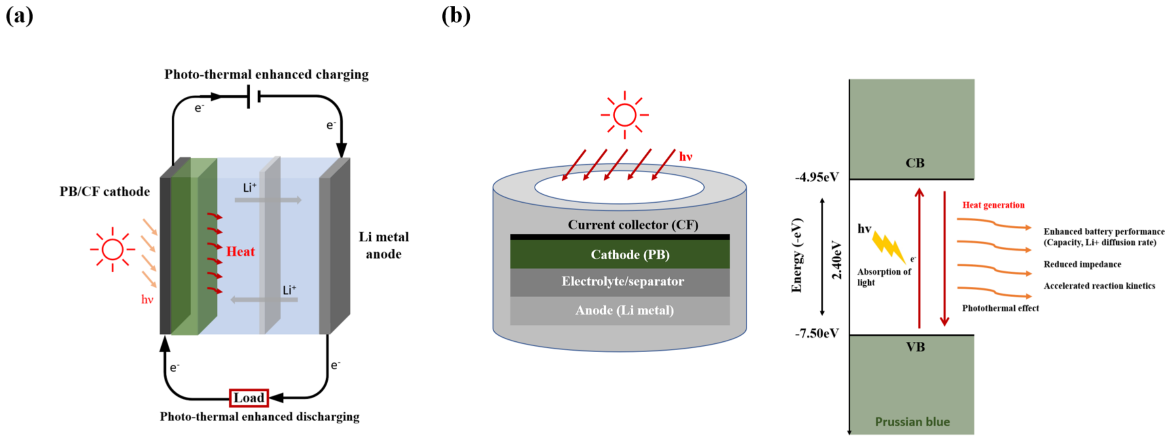

Fig. 4.6 (a) (b) Schematic of photo-thermal enhanced PBA/Li half-cell.

When PBAs are exposed to photons with sufficient energy, electron-hole pairs are generated. The excited electrons can release energy either by emitting photons or by transferring it to the lattice through nonradiative relaxation. This process often results in localized temperature increases. Nonradiative relaxation can occur via mechanisms such as Shockley-Read-Hall and Auger recombination [326, 327]. In Auger recombination, the energy from electron-hole recombination is transferred to another carrier within the conduction or valence band, which subsequently thermalizes through lattice vibrations. Shockley-Read-Hall recombination, on the other hand, is influenced by material defects or impurities that create midgap energy states, enabling a two-step trap-assisted recombination process [328]. Both mechanisms are associated with thermal energy exchange, contributing to heat generation.

Several studies have demonstrated that PBAs are efficient in converting absorbed light in the visible and NIR spectrum into nonradiative heat through electronic transitions. This photothermal property has found applications in fields such as photo-thermal therapy for cancer treatment [318–320]. In the context of battery systems, these properties are being leveraged to enhance the performance of lithium-ion batteries (LIBs). Specifically, PBAs serve as LIB cathodes while simultaneously benefiting from efficient photothermal heating.

To explore this, PBA photocathodes were synthesized using a precipitation reaction, with Prussian blue nanocrystals grown directly onto a carbon felt current collector, creating a binder-free system to address conductivity issues. Under illumination, the increased temperature reduced cell impedance, enhancing the battery's charging rate. This effect was characterized using a combination of Electrochemical Impedance Spectroscopy (EIS), Li-ion diffusion measurements, and rate performance tests. The results revealed that cycling the battery under illumination led to capacity increases of 14.0% and 37.9% at specific currents of 100 mA/g and 1600 mA/g, respectively. These findings underscore the potential of photothermal heating to significantly improve the electrochemical performance of PBA cathodes in LIBs.

This study explores the development of a photothermal-enhanced lithium-ion battery (Photo-LIB) featuring a photocathode composed of Prussian blue analogues (PBAs) as the active material and carbon felt as the current collector, designed to improve both thermal and electrical conductivity, as illustrated in Figure 4.6(a). The combination of PBAs and the photo-thermal effect offers a promising approach for advancing light-enhanced battery technologies, providing a sustainable and efficient means of utilizing solar energy for energy storage applications.

The photo-thermal effect, commonly observed in materials with semiconducting properties, occurs when absorbed light energy initiates non-radiative relaxation processes, leading to localized temperature increases. The ability to understand and control this effect is critical for optimizing the performance of light-enhanced batteries and other technologies that rely on light-induced heating to improve functionality. This synergistic integration of photothermal properties with battery design represents an innovative pathway for the development of advanced energy storage systems.

The photo-thermal lithium-ion batteries (LIBs) developed in this study incorporate a glass window that allows light to penetrate and reach the Prussian blue analogue (PBA) coated on a carbon felt substrate. In this system, Prussian blue acts as the active material, while the carbon felt serves as the current collector, providing electrical conductivity in the illuminated area near the glass window, as depicted in Figure 4.6(b).

Upon illumination, the photo-thermal effect is induced on both the electrode and the electrolyte. PBAs are well-known for their ability to absorb light efficiently, particularly in the visible and near-infrared (NIR) regions. When exposed to photons with sufficient energy, electron-hole pairs are generated within the PBA material. This absorbed light energy initiates the photo-thermal effect, wherein the excited electrons undergo nonradiative relaxation processes. Instead of emitting photons, the energy is released as heat through mechanisms such as Shockley-Read-Hall and Auger recombination, leading to a localized temperature increase within the PBA material.

The increase in temperature resulting from this photo-thermal effect has a significant impact on the electrochemical performance of the lithium-ion battery. It enhances key performance metrics, including specific capacity, lithium-ion diffusion rate, and reaction kinetics, while also reducing impedance. These improvements collectively demonstrate the potential of leveraging photo-thermal effects to optimize battery performance and advance the design of next-generation energy storage systems. [329–332]

4.2 Results and discussion

4.2.1 Na-PB by a modified precipitation method

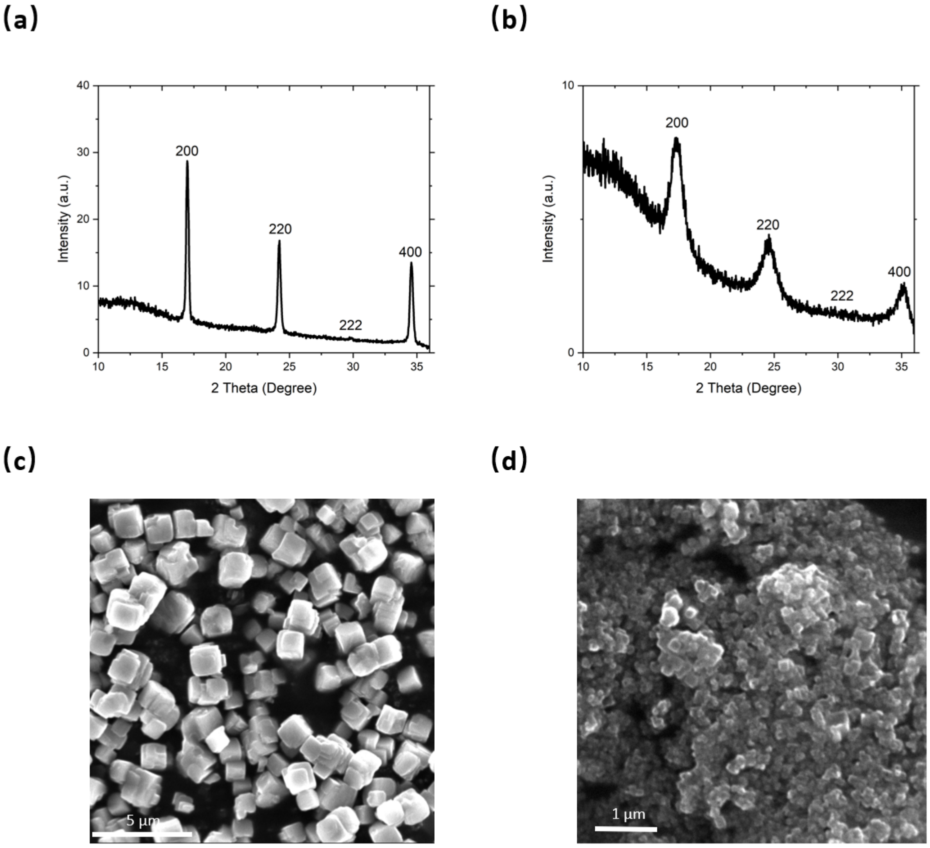

Fig. 4.7 XRD pattern of (a) highly crystalline Na-PB. (b) poorly crystalline Na-PB. SEM image of (c) highly crystalline Na-PB. (d) poorly crystalline Na-PB.

Figure 4.7(a) presents the XRD pattern of highly crystalline Na-PB, showcasing a prominent peak at approximately 17°, corresponding to the (200) plane. Additional peaks are observed at 24° (220 plane), 30° (222 plane), and around 35° (400 plane), confirming a face-centered cubic lattice structure with the space group Fm3m. Similarly, the XRD pattern for Na-PB synthesized without nitrogen gas bubbling, shown in Figure 4.7(b), displays the same characteristic peaks for the (200), (220), (222), and (400) planes. However, the peak intensities are lower, indicating reduced crystallinity of the product. Figure 4.7(c) provides an SEM image of the highly crystalline Na-PB, revealing particle sizes of approximately 2 μm. The introduction of nitrogen gas enhances nucleation time, resulting in larger and more uniform particles. Nevertheless, some non-uniform nanocube growth is visible, which may contribute to stability issues during battery cycling. In contrast, Figure 4.7(d) depicts the SEM image of poorly crystalline Na-PB synthesized without nitrogen gas. These nanoparticles are significantly smaller and exhibit a tendency to aggregate, further reflecting differences in crystallization conditions.

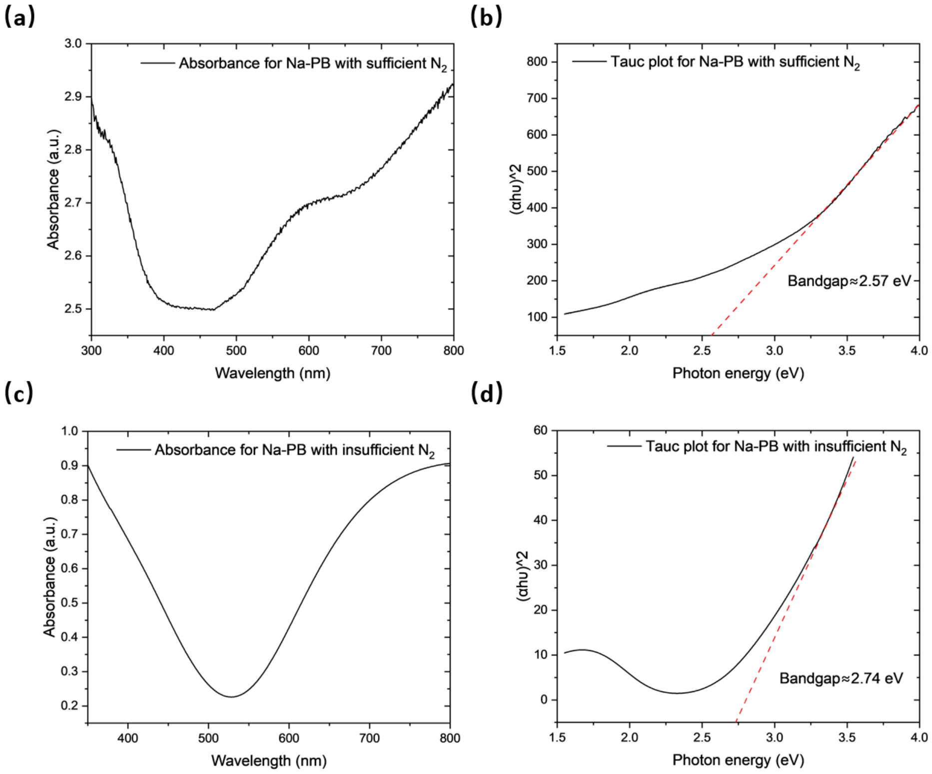

Fig. 4.8 (a) UV-vis spectrum of highly crystalline Na-PB. (b) Tauc plot of highly crystalline Na-PB. (c) UV-vis spectrum of poorly crystalline Na-PB. (d) Tauc plot of poorly crystalline Na-PB.

The absorbance spectrum of highly crystalline Na-PB shows a low absorbance at around 450 nm as shown in Figure 4.8 (a). PBAs are known to be direct bandgap material.[333] By using the Tauc plot in Figure 4.8 (b), the bandgap of the highly crystalline Na-PB is estimated at around 2.57 eV. In Figure 4.8 (c), the poor crystalline Na-PB shows a similar absorbance spectrum with a bandgap of around 2.74 eV as shown in Figure 4.8 (d).

Galvanostatic charge/discharge (GCD) test and Cyclic Voltammetry (CV) were first done to investigate the electrochemical performance of the Na-PB/Li half cell. As shown in Figure 4.9 (a), the half cell was first discharged and charged at 100 mAg^{-1}. Both cells showed two plateaus at the potential range from 2.0 V to 4.2 V vs Li/Li^{+}. However, the second plateau after around 3.2 V is significantly reduced for the Na-PB with insufficient N_2, and the corresponding charge/discharge capacities are also lowered.

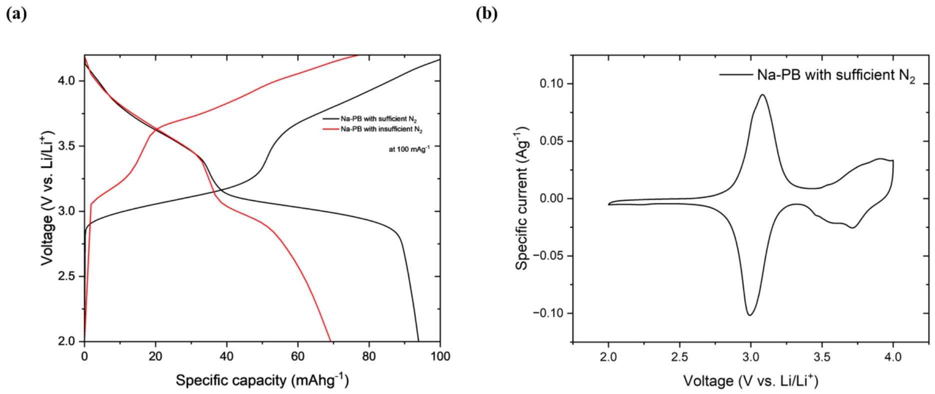

Fig. 4.9 (a) Galvanostatic charge/discharge (GCD) test at 100 mAg^{-1} synthesized Na-PBs and commercial PB. (b) Cyclic Voltammetry (CV) for synthesized Na-PB at 0.1 mVs^{-1}.

The CV was then employed for the Na-PB with sufficient N_2 sample as shown in Figure 4.9 (b), two sets of anodic and cathodic peaks can be observed at 3.0 V and 3.8 V. The first set of peaks at 3.0 V is related to the redox reactions of high spin Fe^{2+} connected with N atoms, and the peak at higher potential corresponds to the low spin Fe^{2+} connected with C atoms[334]. Combining the CV and GCD results, the peaks match the plateau at various potential range.

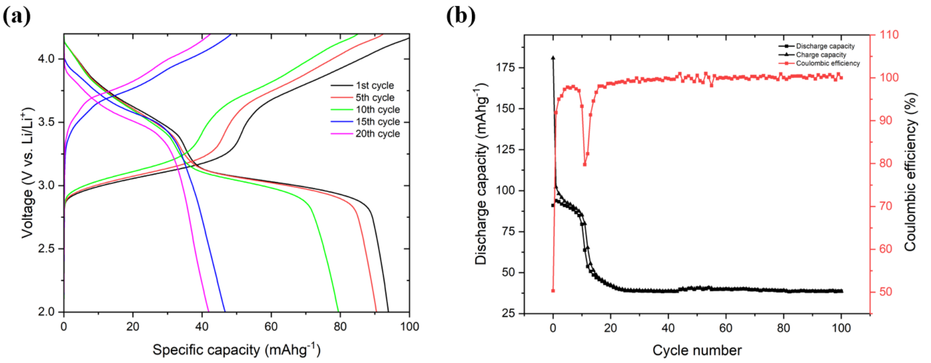

Fig. 4.10 (a) Galvanostatic charge/discharge (GCD) curve at various cycle numbers at 100 mAg^{-1}. (b) Cycling stability and Coulombic efficiency over 100 cycles at 100 mAg^{-1}.

The cycling stability of the Na-PB with sufficient N_2 Li half cell is shown in Figure 4.10. It has been shown that the cell started to degrade after 10 cycles. This reduction in capacity mainly results from the second plateau between 2.8 V to 3.1 V disappearing as shown in Figure 4.10 (a). From Figure 4.10 (b), the long-term cycling performance shows a sharp drop in Coulombic efficiency at the 10th cycle. This can be caused by loss of active material, electrolyte degradation or other side reactions.

Overall, Na-PB appears to lack stability in Li-ion batteries, likely due to the challenges in controlling nitrogen gas during synthesis. The SEM images reveal irregularly shaped Na-PB particles, even with sufficient N_2 applied during the process. Given the difficulties associated with its fabrication, I decided to focus on other Prussian Blue Analogues (PBAs) that offer simpler synthesis methods and more stable electrochemical performance.

4.2.2 Fe-PB electrode by an electroplating method

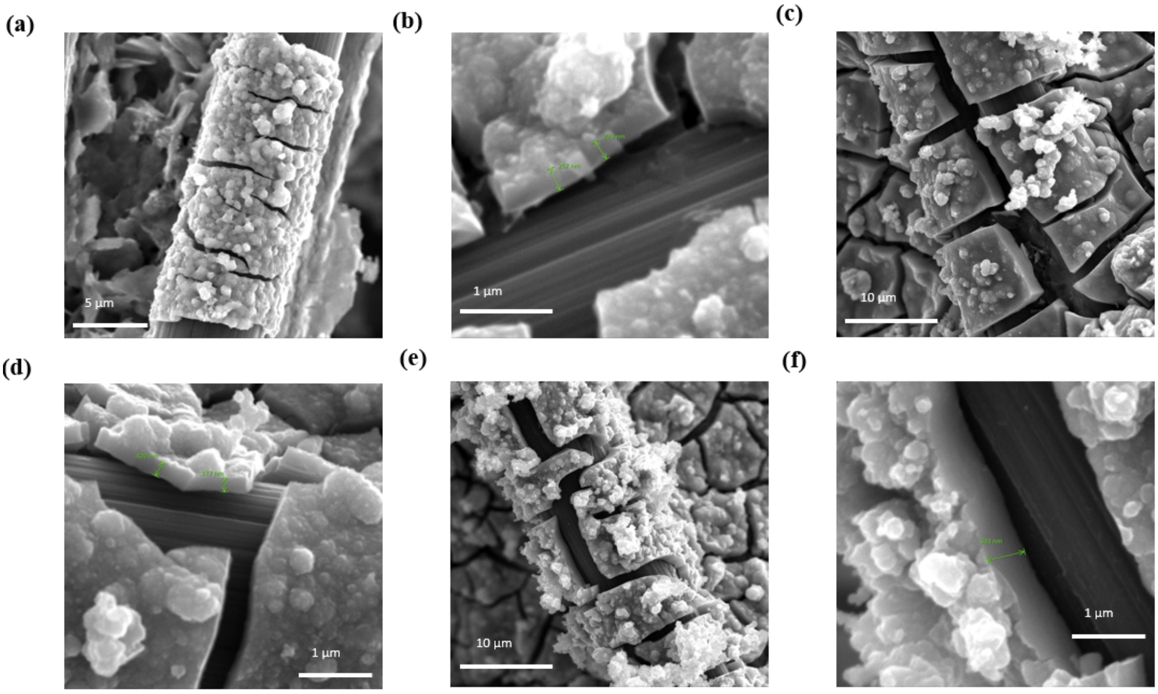

Fig. 4.11 SEM for FE-PB/CF electrode with (a)(b) 30s electroplating time. (c)(d) 60s electroplating time. (e)(f) 90s electroplating time.

As shown in Figure 4.11, the electro-plating PB/CF electrodes have been successfully synthesized and Fe-PB is coated on the fibres of carbon felt (details in the method section). It has been found that with longer electro-deposition time, the thickness of the PB layer becomes bigger. The layer has a thickness from 200 nm to 600 nm depending on the deposition time. However, it can be observed that many cracks are produced and some residues are grown on the layer of Fe-PB.

The X-ray diffraction (XRD) plot of electro-deposited Prussian blue is presented in Figure 4.12, the large peak at 27 degrees and 54 degrees corresponds to the carbon felt. Apart from this, the XRD pattern shows characteristic peaks from the PB crystal structure with high crystallinity and no impurities.

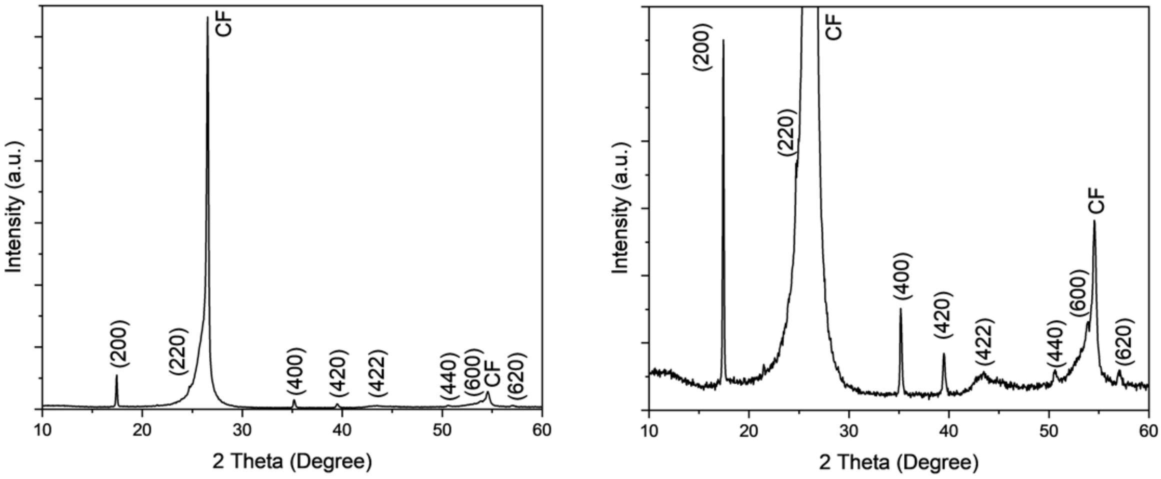

Fig. 4.12 XRD pattern of electro-deposition Fe-PB/CF electrode, zoomed version on the left.

As shown in Figure 4.13 (a), the UV-VIS spectra of electroplating PB show a low absorbance at around 500 nm. The Tauc plot from the UV-VIS spectra presents a bandgap estimation of around 2.01 eV, which lies within the visible light region.

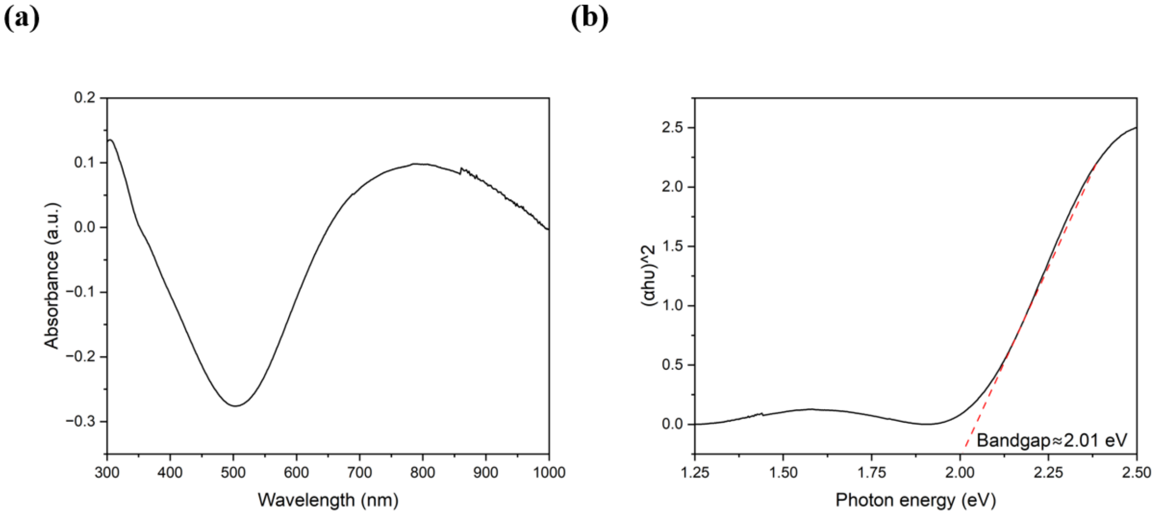

Fig. 4.13 (a) UV-VIS spectra of electro-deposition Fe-PB. (b) Tauc plot of electro-deposition Fe-PB.

To explore the electrochemical performance of the electro-deposition Fe-PB, GCD tests were first done for the three samples mentioned above with different deposition times. As shown in Figure 4.14, the GCD tests were performed under the potential window between 2.0 V to 4.0 V with a current density of 10 mA/g.

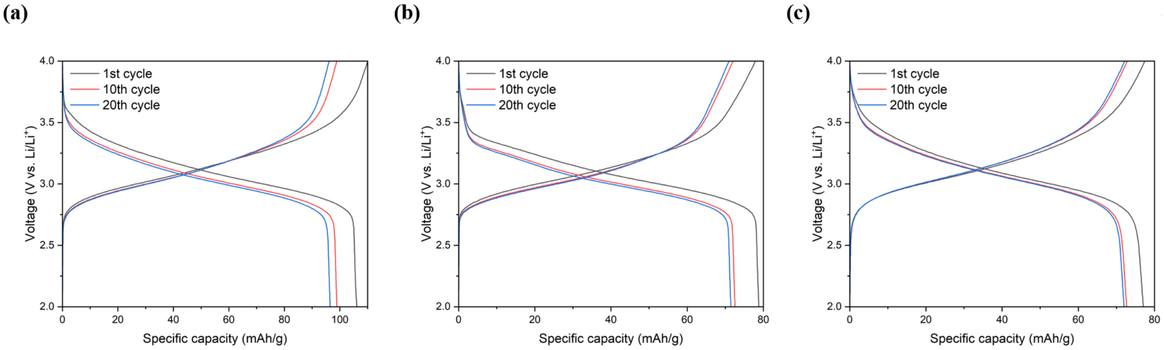

Fig. 4.14 (a) GCD test of 90-second electro-deposition Fe-PB, (b) 60-second electro-deposition Fe-PB, (c) 30-second electro-deposition Fe-PB under the current density of 10 mA/g.

It is worth noticing that the capacity is larger with a longer deposition time of the PB. However, the capacity retention of the longer-deposited electrode is lower than the shorter samples. Over 20 cycles, the 90-second PB electrode shows a capacity fade of 9.1%, the 60-second PB electrode presents a capacity fade of 9.3% and the 30-second PB electrode demonstrates a capacity fade of 6.6%. The large capacity fade for the 90-second and 60-second PB electrodes is possibly due to the larger cracking I saw in the SEM images of the CF/PB electrodes. The electro-plated PB/CF electrodes show good capacity stability over 20 cycles. However, the specific capacity is much lower than other reported PB Li-ion batteries. This is possibly due to the cracking and bad contact between the active material and the carbon felt.

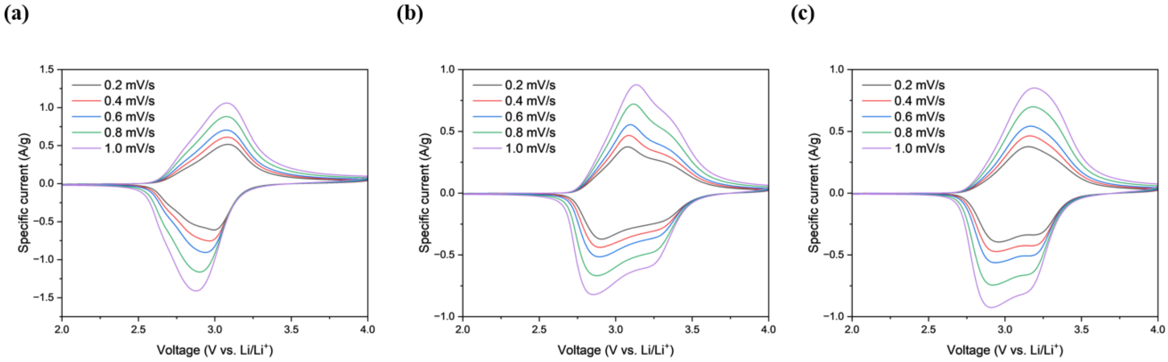

Fig. 4.15 CV curves at different scan rates (0.1 to 1.0 mV/s) between 2.0 and 4.0 V in dark conditions for (a) 90-second electro-deposition PB/CF electrode. (b) 60-second electro-deposition PB/CF electrode. (c) 30-second electro-deposition PB/CF electrode.

Cyclic voltammetry (CV) measurements were performed within the voltage range of 2.0 V to 4.0 V at scan rates ranging from 0.2 mV/s to 1.0 mV/s, as illustrated in Figure 4.15.

The results reveal a pair of distinct peaks, corresponding to the redox reactions of high-spin Fe^{3+}/Fe^{2+} couples coordinated with nitrogen, consistent with previous findings.[335]

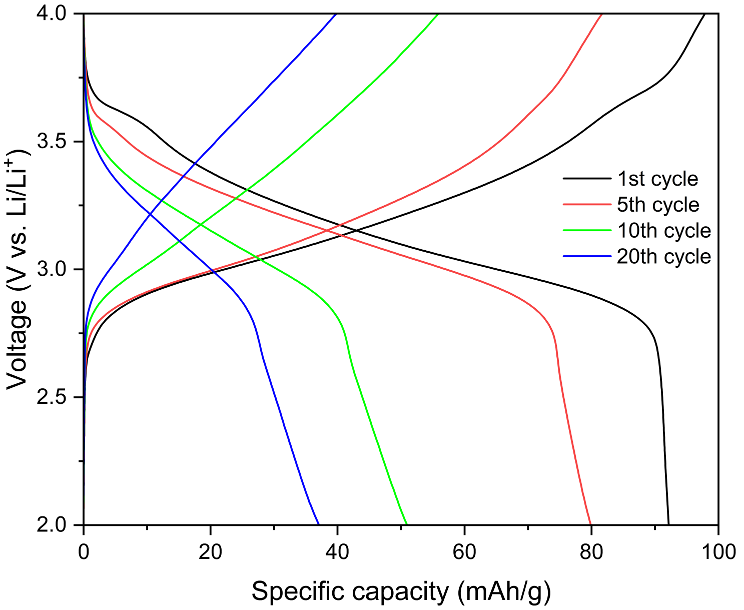

Fig. 4.16 GCD test of 30-second electro-deposition Fe-PB with the current density of 10 mA/g under blue LED.

The cell was then tested under illumination conditions with a current density of 10 mA/g by using a blue LED light source with $\lambda \approx 470$ nm and light intensity ≈ 128 mW/cm^2 as shown in Figure 4.16. The 30-second electro-deposition electrode is used in the light GCD measurement due to its highest stability under dark conditions. As shown in Figure 4.16, the cell shows a capacity of around 92 mAh/g for the first charge/discharge cycle under illumination, demonstrating a capacity enhancement of approximately 18 %. Even after 5 cycles, the capacity can still remain at around 80 mAh/g. However, after the 5th cycle, the capacity quickly decreased to 50 mAh/g in the 10th cycle and 37 mAh/g in the 20th cycle. This low capacity retention is possibly due to the instability of electroplating PB under elevation of temperature from the light source due to the photo-thermal effect. Here, I conclude that electroplating Fe-PB is also not suitable for photo-thermal enhanced batteries due to the large crack presented during the electrode fabrication process, the crack can lead to the degradation of active material, especially under illumination.

4.2.3 Na-PB by a facile hydrolytic precipitation method

As shown in Figure 4.17, the Na-PB has been successfully coated on the carbon felt. The photoelectrode was developed using a slow solution-growth method, distinct from the traditional co-precipitation method. This approach facilitated the uniform growth of nano-sized Prussian blue cubes, ranging from 500nm to 600nm, on the fibres of carbon felt as shown in the SEM images from Figure 4.17. This uniform growth enhances the electrical contact and transportation of phonons between the active material and the current collector. However, there is still cracking presented in Figure 4.17 (d) which could be influential to the electrochemical performance of the battery.

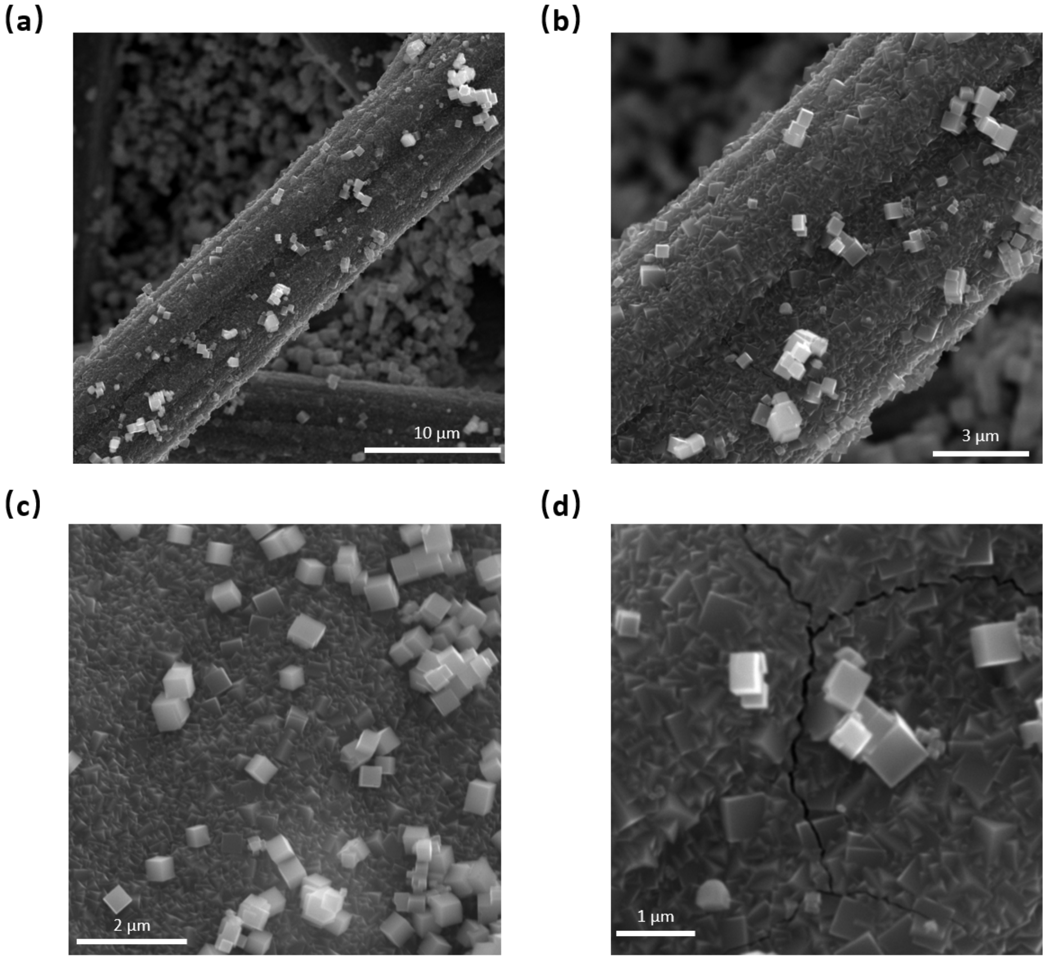

Fig. 4.17 SEM images at different magnifications of Na-PB from hydrolytic precipitation method.

The X-ray diffraction (XRD) plot of the Na-PB/CF electrode from the hydrolytic precipitation method is presented in Figure 4.18, revealing a distinct face-centred cubic phase (FCC, space group $Fm\overline{m}3m$). The large peak at around 25 degrees belongs to the carbon felt.

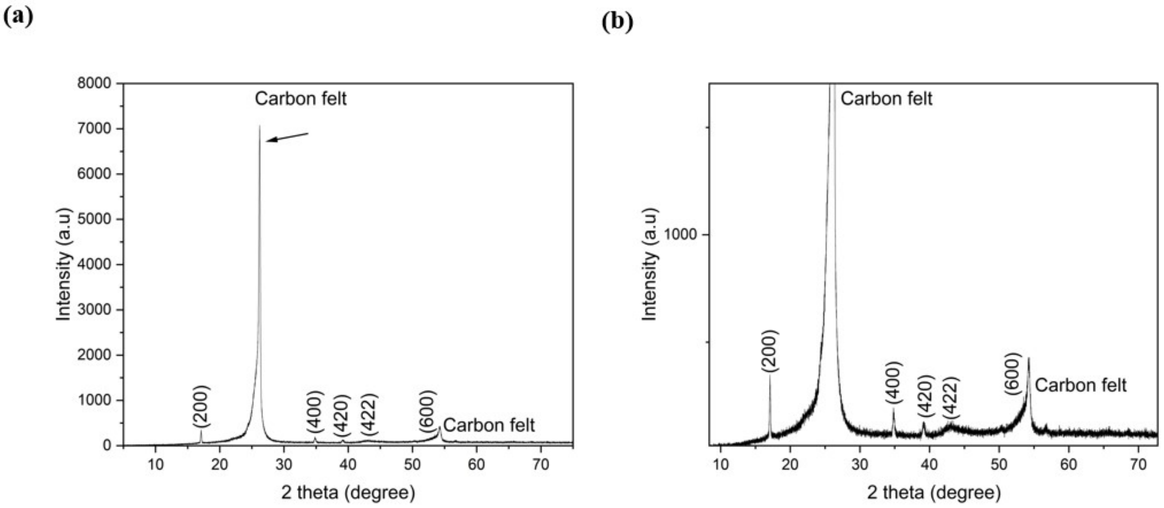

Fig. 4.18 XRD pattern of Na-PB/CF electrode from hydrolytic precipitation method, zoomed version on the left.

Figure 4.19 (a) displays the UV-vis absorption spectrum alongside bandgap determination, the UV-vis absorbance spectrum shows a high absorbance below 475 nm. By using the Tauc plot, the bandgap is estimated at approximately 2.77 eV as shown in Figure 4.19 (b).

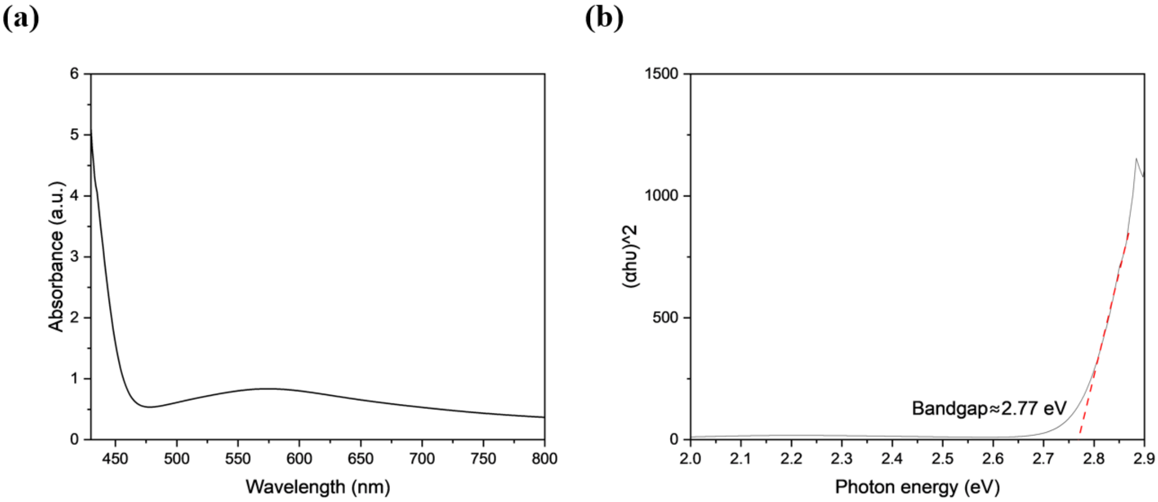

Fig. 4.19 (a) UV-VIS spectra of Na-PB/CF electrode from hydrolytic precipitation method. (b) Tauc plot of Na-PB/CF electrode from hydrolytic precipitation method.

The photothermal response of PBAs was evaluated using a planar Au-PB-Au interdigital electrode (IDE) configuration. Compared to the PDs I fabricated previously for g-C_3N_4, these simple devices are easy to synthesise and more applicable in evaluating the photo-thermal response. The IDE was created by drop-casting PB onto the centre of the device, as illustrated in Figure 4.20.

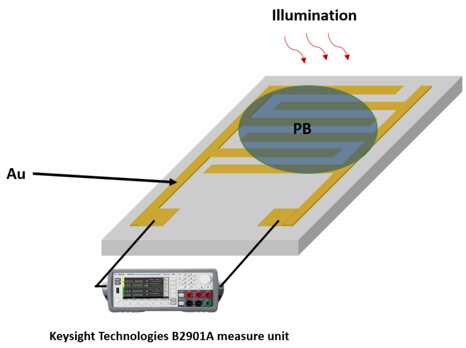

Fig. 4.20 Schematic diagram of the Au-PB-Au interdigital electrode.

Notably, as the bias voltages increased, a heightened response current was observed under illuminated conditions compared to dark conditions. In Figure 4.21, the current is presented under alternating dark and illuminated conditions at 20 mV to 80 mV bias voltage.

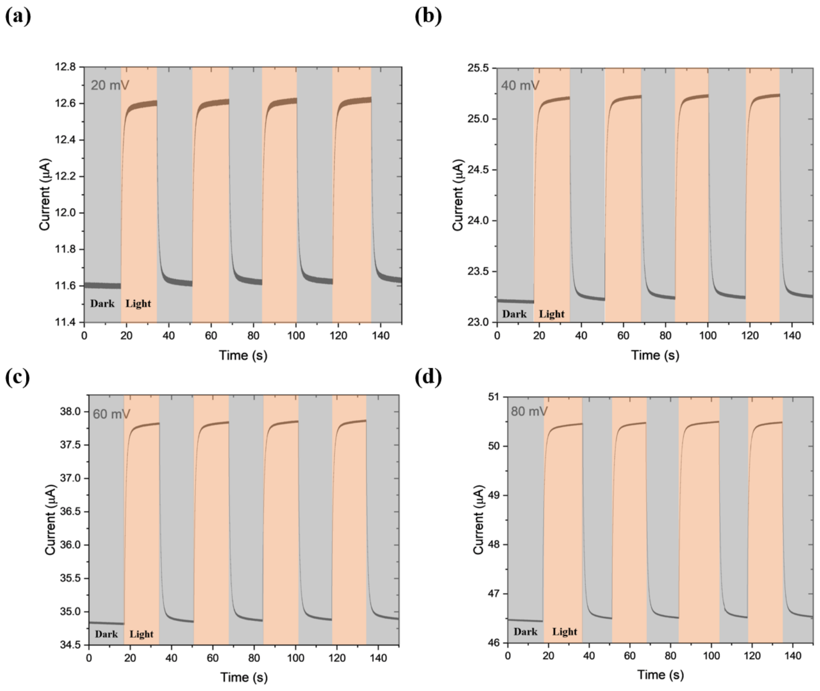

Fig. 4.21 Response current of the Au-PB-Au PD under alternating dark and illuminated conditions at (a) 0.2 V (b) 0.4 V (c) 0.6 V and (d) 0.8 V applied bias.

Figure 4.22 illustrates the average current under light and dark conditions as a function of bias voltage. Both currents under different conditions exhibit a linear increase with higher bias voltage. Additionally, as the absolute bias voltage increases, the difference between light and dark current also becomes more pronounced. Notably, at zero bias voltage, no current is observed. The results obtained from the interdigitated electrode configuration suggest that

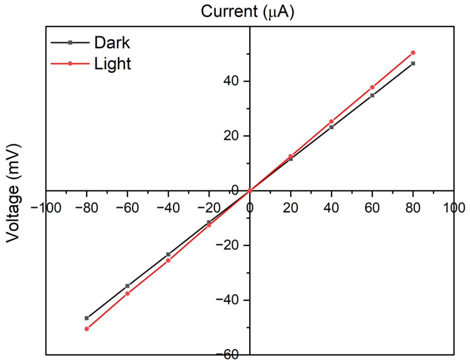

Fig. 4.22 Current-voltage curves of the planar Au-PB-Au PD in dark and illuminated conditions.

the magnitude of current flowing through the photo-detector can vary upon irradiation. This could be attributed to the reduction of resistance due to the heat generated on the device.

Galvanostatic discharge-charge curves were initially obtained within a potential window of 2.0 V to 4.0 V vs. Li/Li$^+$ at a current density of 10 mA/g. As depicted in Figure 4.23 (a), the galvanostatic discharge-charge (GCD) curves exhibit a two-plateau shape during charge and discharge cycles with no significant alterations observed over 100 cycles, indicating stable electrochemistry.

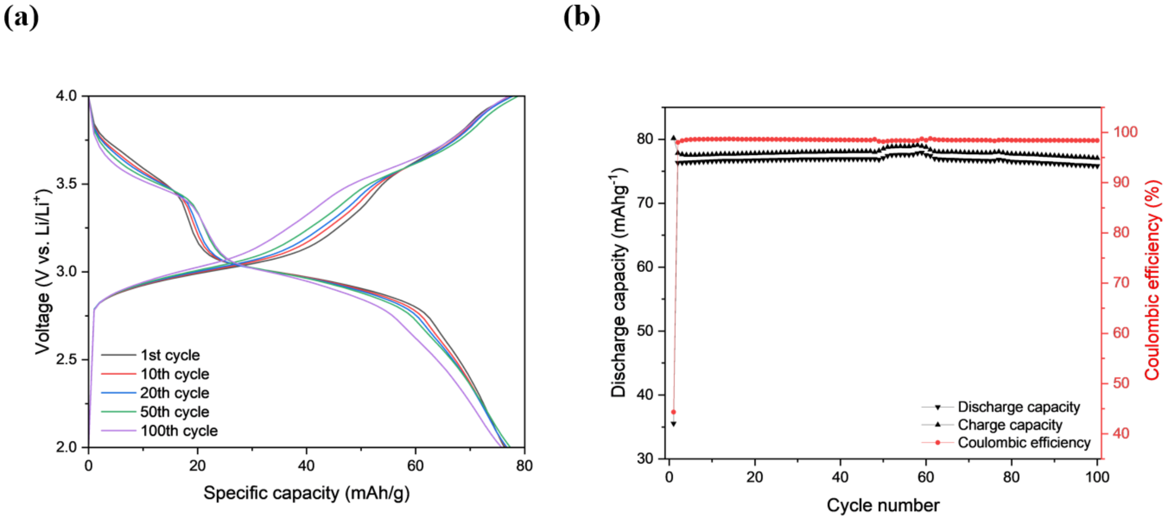

Fig. 4.23 (a) Galvanostatic discharge-charge curves at 10 mA/g for selected cycles. (b) Long-term cycling (100 cycles) stability of the LIB at 10 mA/g.

Furthermore, as shown in Figure 4.23 (b) the cell maintains continuous operation for over 100 cycles and displays a remarkable capacity retention of 99.4% in dark conditions. The Coulombic efficiency remains around 99%, highlighting the absence of side reactions and the overall robust performance of the system. Coulombic efficiency is defined as the ratio of the discharge capacity to the charge capacity of a battery in a single cycle.

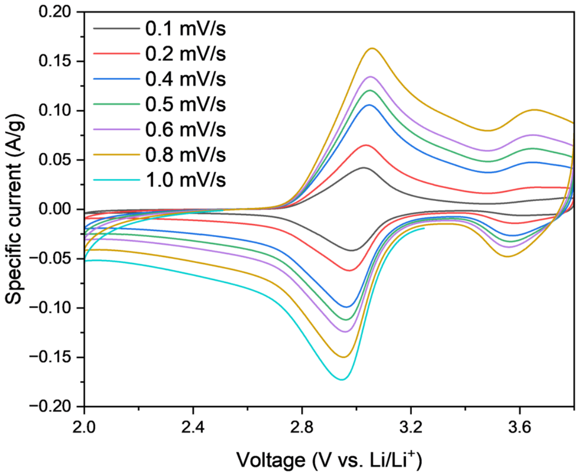

Fig. 4.24 CV curves at different scan rates (0.1 to 1.0 mVs^{-1}) between 2.0 and 3.8V in dark condition.

To further explore the electrochemical performance of the Na-PB by a facile hydrolytic precipitation method Li-ion batteries, and cyclic voltammograms (CV) were then conducted under dark conditions. The experiments involved scanning at a rate ranging from 0.1 mVs^{-1} to 1.0 mVs^{-1} over the potential window of 2.0 V to 3.8 V. As depicted in Figure 4.24, two distinct cathodic peaks are evident at approximately 3.5 V and 2.9 V, respectively. Additionally, two corresponding anodic peaks are observed at around 3.1 V and 3.7 V. These peaks correspond to subsequent two-step Li^+ insertion reactions:

$$Fe^{3+}[Fe^{3+}(CN)_6] + Li^+ + e^- \leftrightarrow LiFe^{3+}[Fe^{2+}(CN)_6] \tag{4.6}$$

$$LiFe^{3+}[Fe^{2+}(CN)_6] + Li^+ + e^- \leftrightarrow Li_2Fe^{2+}[Fe^{2+}(CN)_6] \tag{4.7}$$

For the investigation of the photothermal enhanced ability of the photocathode, galvanostatic discharge-charge curves were obtained at a current density of 10 mA/g under both dark and illuminated conditions as shown in Figure 4.25.

It can be observed that no capacity enhancement was observed under illumination. Apart from that, the shape of the curve has changed a lot during the light charge/discharge cycle. This is possibly due to the instability of Na-PB under illumination. The first plateau at around 3.8 V for the dark discharge cycle has disappeared compared to light conditions. A new plateau also appeared during the charging cycle above 3.7 V for the illuminated conditions.

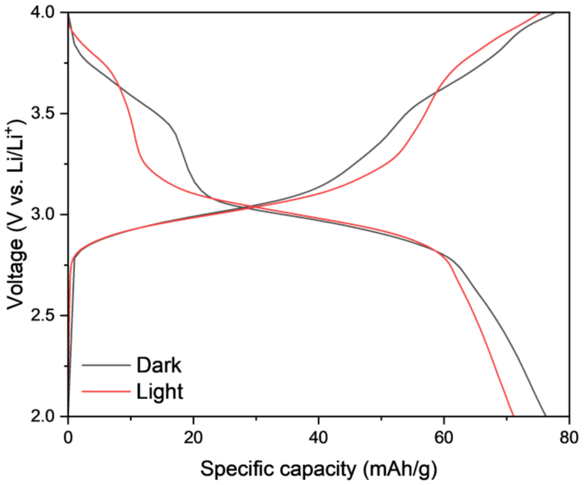

Fig. 4.25 Galvanostatic discharge-charge curves at 10 mA/g in dark and illuminated conditions.

This is possible due to the side reaction in the electrolyte from the heat generation from illumination and the degradation of the Na-PB active material.

In summary, the Na-PB synthesized through a facile hydrolytic precipitation method is not deemed a suitable cathode material for Li-ion batteries due to its instability under illumination conditions. Consequently, our focus shifted to a Fe-PB Prussian blue analogue with a hydrothermal growth method which is known for its stability under elevated temperatures.

4.2.4 Fe-PB by a facile hydrolytic precipitation method

The PBA was synthesized on the carbon current collector using a simple hydrolytic precipitation method by using $K_3Fe(CN)_6$ as a single iron source. Distinct from the rapid co-precipitation method, this approach allows for a uniform coating of nano-sized Prussian blue cubes of about 400 to 600 nm on the carbon felt, the SEM image of the bare carbon felt can be seen in Figure 4.26 (a). Only carbon fibres and flakes can be observed. The SEM images of CF/PB photo-cathodes are shown in Figure 4.26 (b)-(d). Compared to the bare CF images, PB nano-particles have been successfully grown on the fibres without any cracking compared to our previously synthesized electroplating PB electrodes. The size of the PB nano-cubes is around 400 to 600 nm.

The X-ray diffraction (XRD) plot of Prussian blue is presented in Figure 4.27, revealing a face-centred cubic phase (FCC, space group F$\overline{m}$3m) without any trace of impurities.[336] The XRD sample is prepared by sonicating the PB/CF electrode and later dried on the hot plate at 80°C for 12 hours.

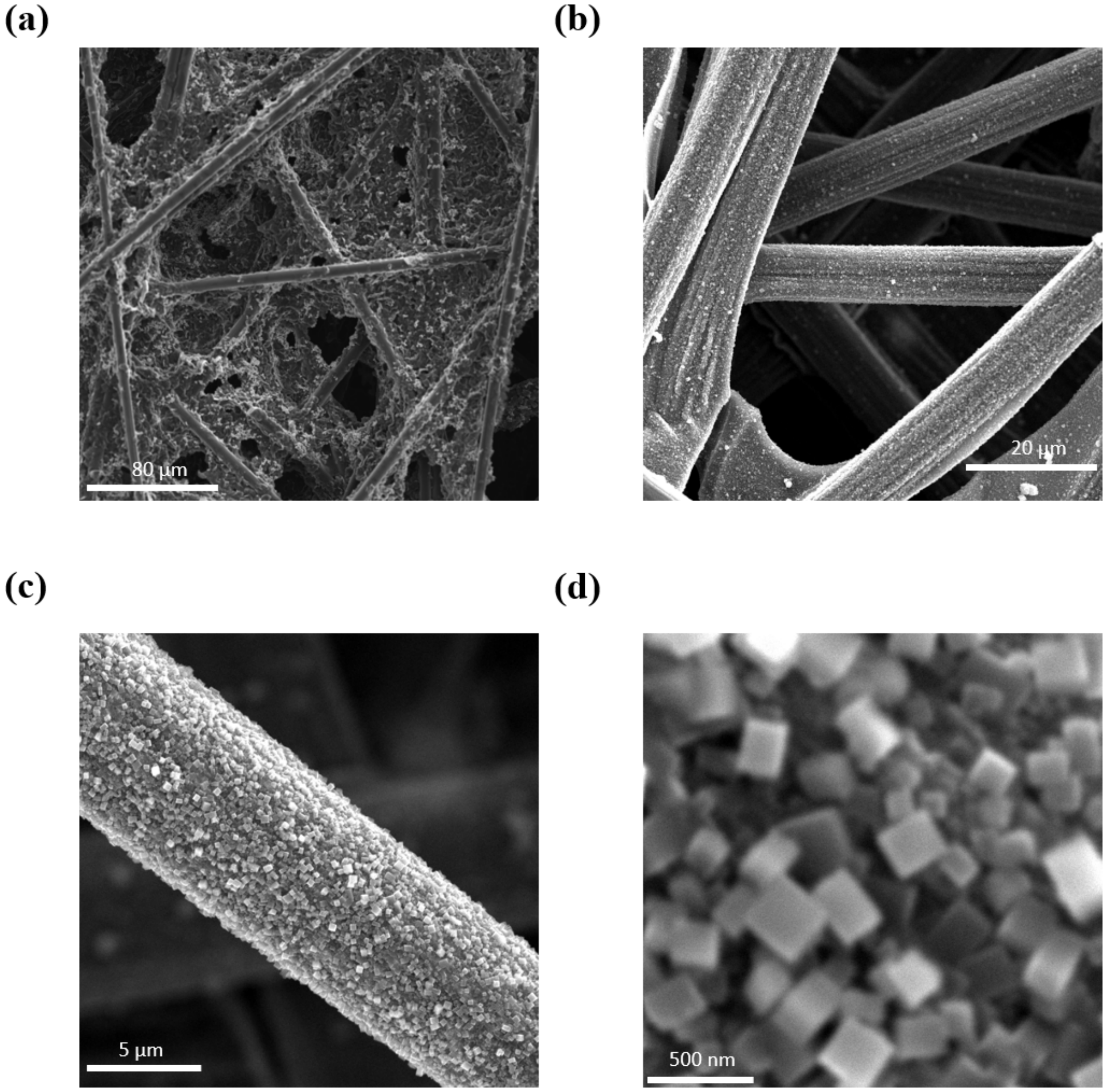

Fig. 4.26 SEM images of (a) Carbon felt, (b, c, d) PB/CF photocathode at low and high magnifications.

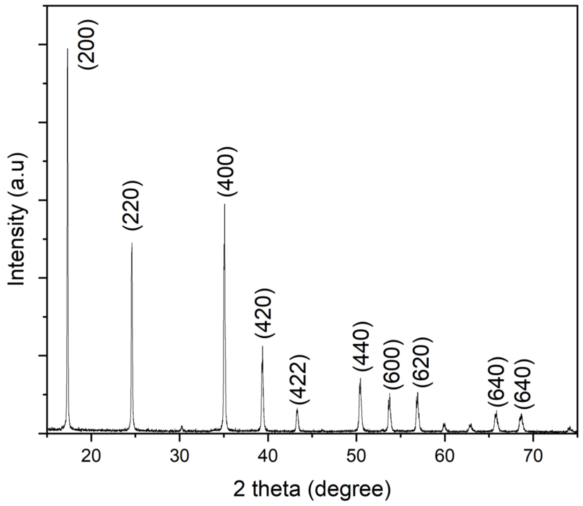

Fig. 4.27 XRD pattern of the Fe-PB by a facile hydrolytic precipitation method.

As shown in Figure 4.28 (a), the UV-VIS spectrum of Prussian blue shows a large absorbance peak at around 370 nm and from the Tauc plot, the bandgap is calculated at around 2.55 eV as shown in Figure 4.28 (b).

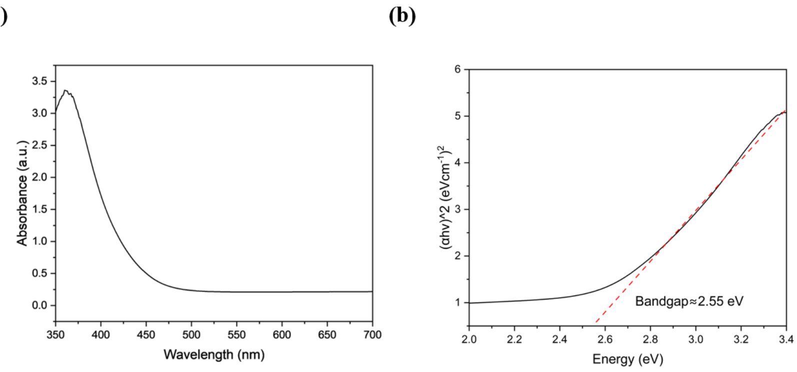

Fig. 4.28 (a) UV-VIS spectrum of Prussian blue. (b) Bandgap determination with 2.55 eV by using Tauc plot.

To explore the electrochemical performance of the photocathode, I first carry out cyclic voltammograms in light and dark conditions using CR2032 coin cells with a 10 mm diameter window. Scanning rates ranging from 0.1 mVs^{-1} to 1.0 mVs^{-1} over the potential window of 2.0 V to 4.2 V were tested first in dark and then light conditions. The light source employed had a wavelength of 470 nm with an intensity of 144 $mWcm^{-2}$.

As depicted in Figure 4.29 (a), two distinct cathodic peaks labelled Peak 1C and Peak 2C are evident at approximately 3.5 V and 2.9 V, respectively. Additionally, two corresponding anodic peaks labelled as Peak 1A and Peak 2A are observed at around 3.0 V and 3.7 V. These peaks correspond to subsequent two-step Li^+ insertion reactions reported previously in the literature.[337]

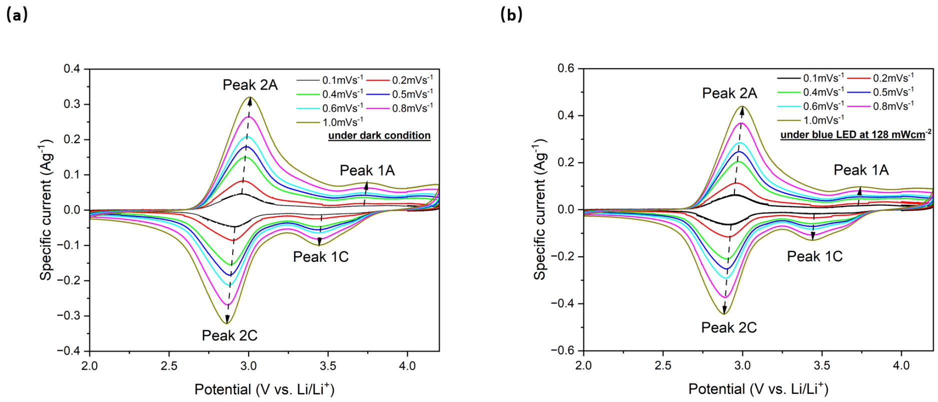

Fig. 4.29 CV curves at different scan rates (0.1 to 1.0 mVs^{-1}) between 2.0 and 4.2 V in both (a) dark and (b) illuminated conditions.

Take the CV curves at 1.0 mVs^{-1} as an example, in comparison to the dark condition, both cathodic peaks and anodic peaks exhibit slight shifts to higher and lower voltages, respectively, in the illuminated cyclic voltammetry (CV) curve, as illustrated in Figure 4.30 (a). The shifts are observed from 2.86 V to 2.89 V for the 2C cathodic peaks and from 3.01 V to 2.99 V for the 2A anodic peaks. Similar trends are evident at different scan rates of 0.4 mVs^{-1}, 0.5 mVs^{-1}, 0.6 mVs^{-1}, and 0.8 mVs^{-1} as shown in Figure 4.31. As shown in Figure 4.30 (b), The Li^+ diffusion constant under both dark and illuminated conditions was investigated by utilizing the peak current densities at the cathodic peak of ~2.9 V and the anodic peak of ~3.00 V, spanning a scan rate range from 0.1 mVs^{-1} to 1.0 mVs^{-1}. The Li^+ diffusion constant (D) is calculated using the formula provided below:

$$i_p = 0.4463F(\frac{F}{RT})^{0.5}C \times \vartheta^{0.5}AD^{0.5} = K\vartheta^{0.5}D^{0.5} \tag{4.8}$$

Where,

$$K = 0.4463F(\frac{F}{RT})^{0.5}C \times A \tag{4.9}$$

Here i_p, F, T, C, ϑ, A, D represent peak current, Faraday constant, absolute temperature, initial concentration in $molcm^{-3}$, scan rate in Vs^{-1}, electrode area in cm^2 and diffusion constant in cm^2s^{-1}, respectively. The equation is given by the Randles–Sevcik equation in a reversible reaction. [338] Based on the linear fitting slope between the square root of different scan rates and peak currents under both dark and illuminated conditions, as shown in

Figure 4.30 (b), the Li^{+} diffusion constants exhibited an increase of approximately ≈52.7% for anodic reactions and ≈52.1% for cathodic reactions.

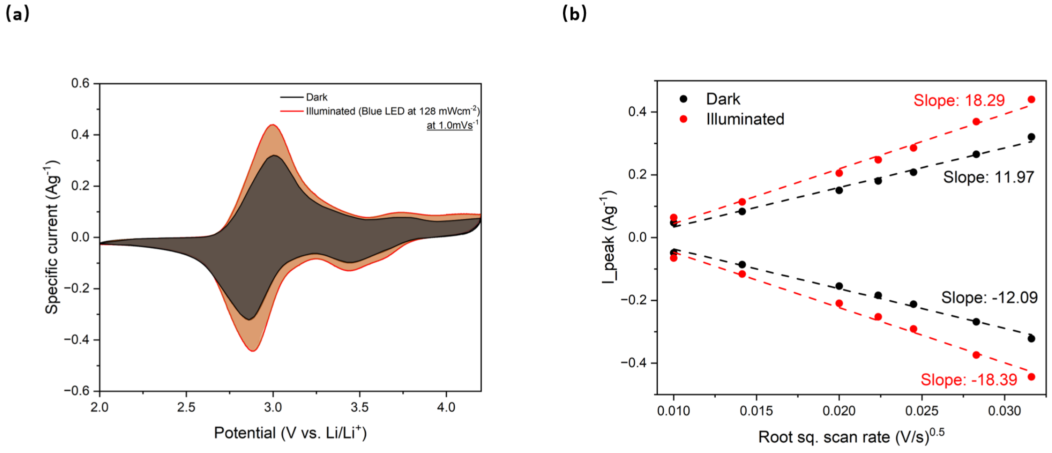

Fig. 4.30 (a) CV curves at 1.0 mVs^{-1} in dark and illuminated conditions. (b) Diffusion constant analysis in dark and illuminated conditions.

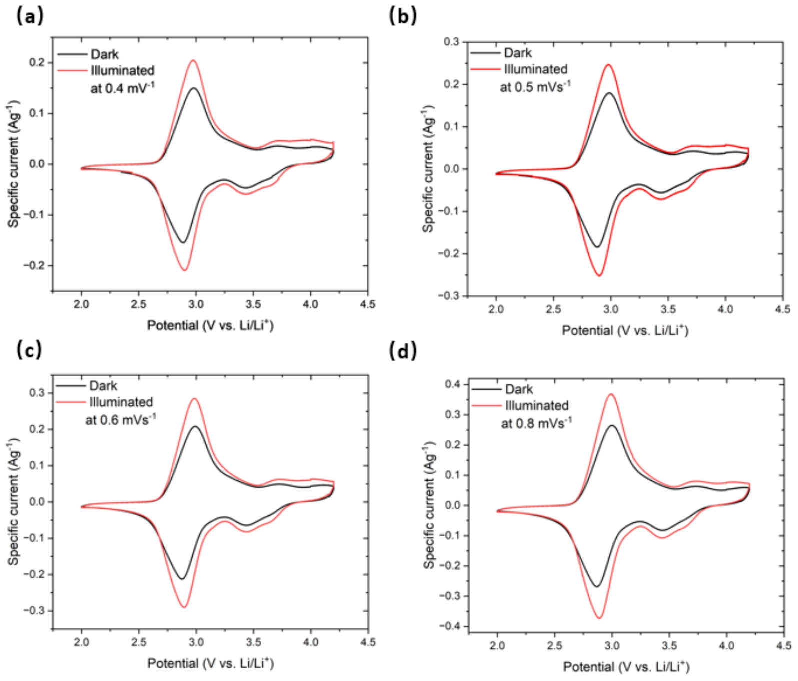

Fig. 4.31 CV scans at rate of (a) 0.4 mVs^{-1}, (b) 0.5 mVs^{-1}, (c) 0.6 mVs^{-1} and (d) 0.8 mVs^{-1} in dark and illuminated conditions.

To further explore the electrochemical performance of the photothermal-assisted lithium-ion Batteries, galvanostatic discharge-charge curves were obtained at a current density ranging from 100 to 1600 mAg^{-1} under both dark and illuminated conditions. Figure 4.32

shows the Galvanostatic charge-discharge curves at the specific current density from 200 to 800 mAg^{-1}. I can see that the capacity was enhanced under illumination.

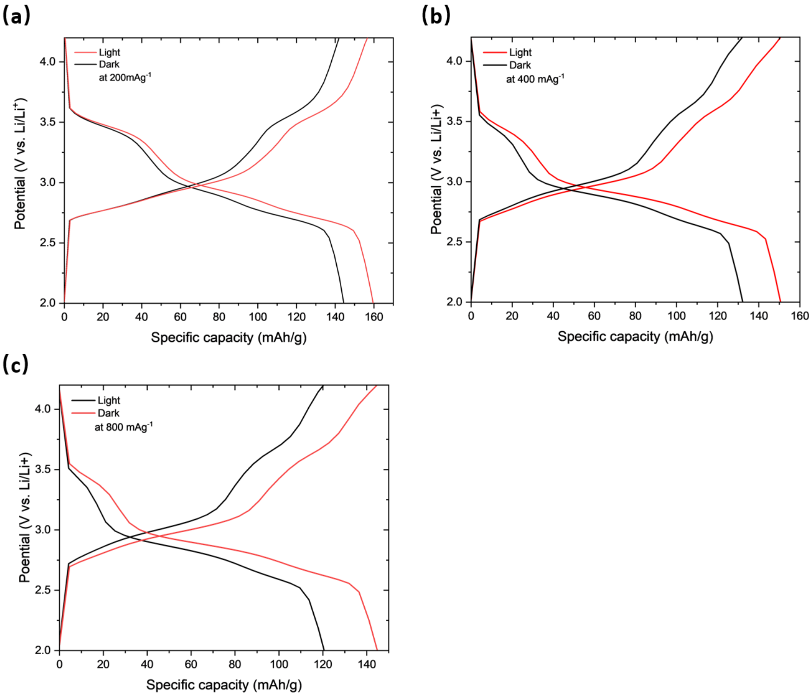

Fig. 4.32 Galvanostatic charge-discharge curves at the specific current density of (a) 200 mAg^{-1}, (b) 400 mAg^{-1} and (c) 800 mAg^{-1} under light and dark conditions.

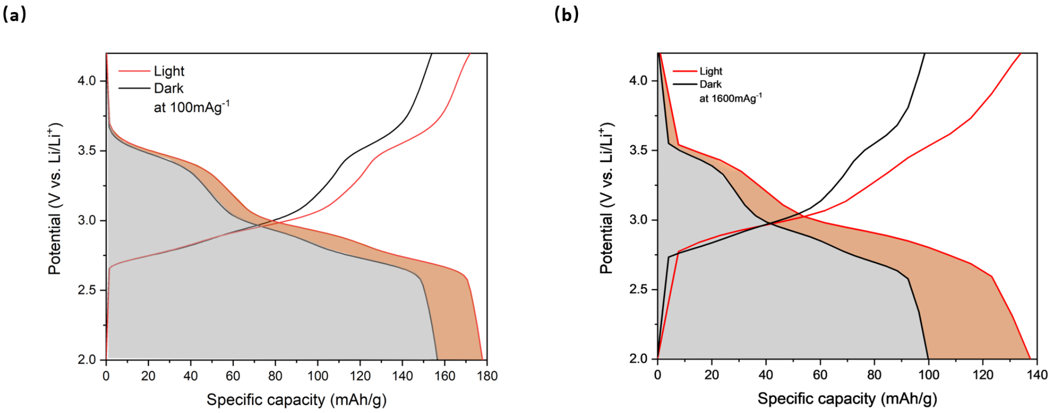

Fig. 4.33 (a, b) Galvanostatic discharge-charge curves at 100 mAg^{-1} and 1600 mAg^{-1} in dark and illuminated conditions.

The galvanostatic charge-discharge curves at specific current densities of 100 mAg^{-1} and 1600 mAg^{-1} were analyzed, as shown in Figure 4.33. Under illumination, the capacity increased from 161.0 to 183.5 $mAhg^{-1}$, representing a 14.0% increment, at a current density of 100 mAg^{-1}. At a higher current density of 1600 mAg^{-1}, the capacity rose from 99.8 to 137.6 $mAhg^{-1}$, indicating a substantial 37.9% increment.

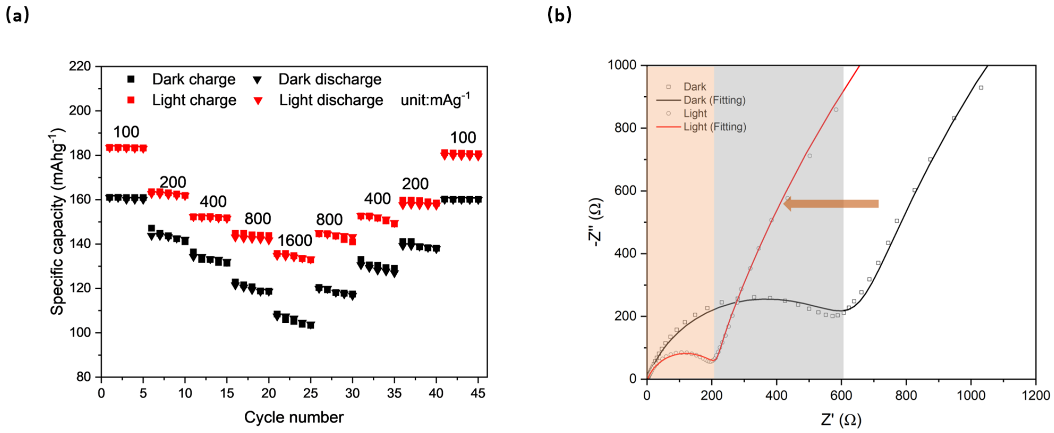

Fig. 4.34 (a) Rate performance tests of the Photo-LIBs in dark and illuminated conditions. (b) EIS measurement of photo-LIB obtained after the 2nd galvanostatic discharge cycle to 3.0V (50% SoC) in the frequency range of 10 mHz-100 kHz at 10 mV amplitude with dark and illuminated conditions.

The photo-LIB demonstrates excellent rate performance under both dark and light conditions, as shown in Figure 4.34 (a). The battery remains stable during charge and discharge cycles at various specific current densities. Electrochemical Impedance Spectroscopy (EIS) measurements were conducted in the frequency range of 10 mHz to 100 kHz with a voltage amplitude of 10 mV at a 50% state of charge (SOC), as illustrated in Figure 4.34 (b). Under illumination, the charge transfer resistance showed a 65% reduction, decreasing from 715 Ω to 250 Ω. The equivalent circuit corresponding to the EIS plot is presented in Figure 4.35.

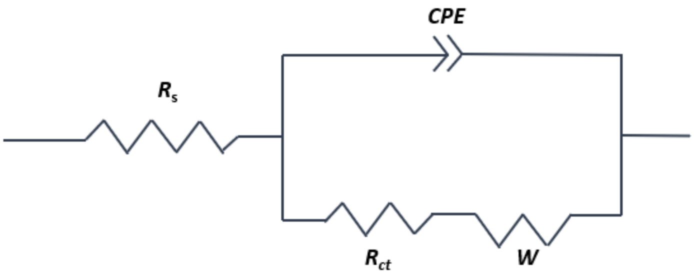

Fig. 4.35 Equivalent circuit for Nyquist plots for the EIS measurement, where R_s corresponds to the total resistance of the electrode, electrolyte, and separator, R_{ct} refers to the charge transfer resistance, CPE represents constant phase element corresponding to the semicircles, and W refers to the Warburg impedance.

The cycling stability under illumination was assessed and is presented in Figure 4.36. The photothermal-assisted battery underwent an initial test under dark conditions with a current density of 200 mAg^{-1} for 100 cycles. Subsequently, a rest period was implemented because during the dark cycle, there may be residual ionic movements or reactions within the battery, especially after charging or discharging. A rest period allows these processes to settle, ensuring that the start of the light cycle doesn't carry over any artefacts from ongoing reactions, such as incomplete charge redistribution or residual polarization effects. After the rest period, the photobattery is followed by cycling under illumination at the same current density for another 100 cycles.

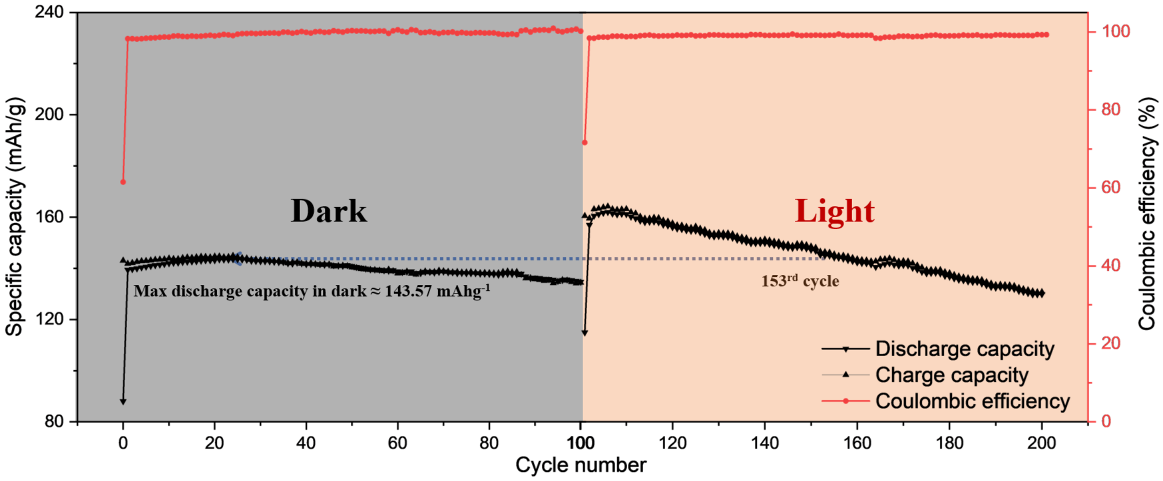

Fig. 4.36 Long-term cycling stability of the photo-LIBs in dark and light conditions at $200mAg^{-1}$.

The results showed that 94.0% and 81.5% of the capacity is retained after 100 cycles under dark and light, respectively. Moreover, the specific capacity remains higher than the maximum discharge capacity for another 53 cycles under illuminated conditions. However, it is still worth noticing that the stability under illumination is reduced, which still requires further improvement.

Post-mortem SEM images of the photocathodes after lithiation and de-lithiation are presented in Figure 4.37, showing no evidence of cracking or significant structural changes in the material. Figures 4.37 (a) and (b) display the lithiated CF/PB photocathode, where lithium plating on the PB nanoparticles is clearly visible when the cell is discharged to 2.0 V. In contrast, Figures 4.37 (c) and (d) illustrate the de-lithiated CF/PB photocathode after charging to 4.2 V, revealing a shape that closely resembles the pristine electrode. These findings further confirm the reversible nature of the CF/PB photocathode during cycling.

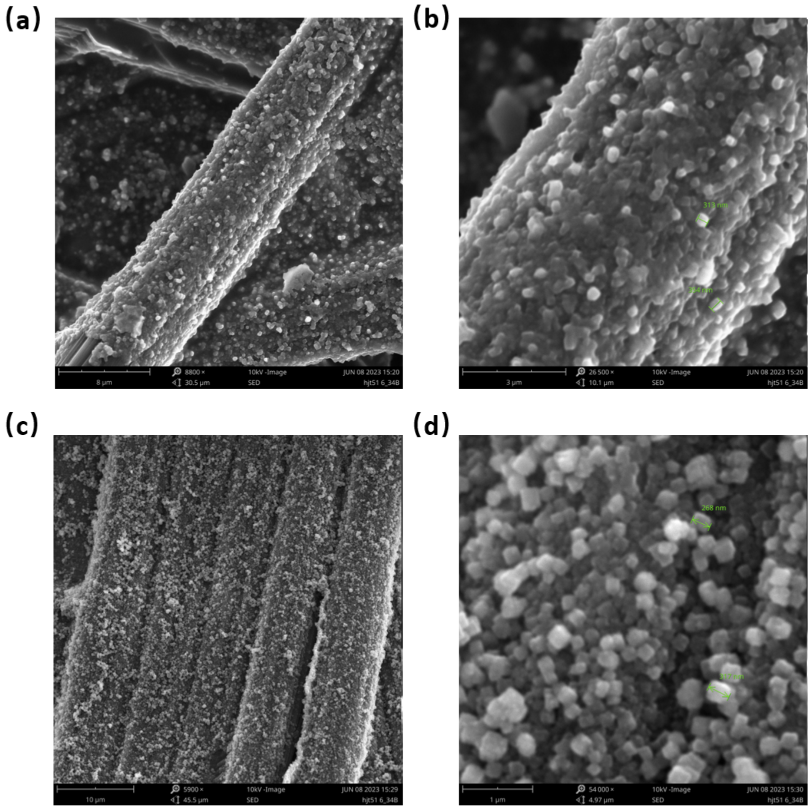

Fig. 4.37 SEM images of (a, b) photocathode after lithiation (discharged to 2.0 V) at different magnifications (c, d) after de-lithiation (charged to 4.2 V) at different magnifications.

Next, the effect of light on the cell temperature is analyzed. Since embedding temperature probes inside batteries is challenging, an impedance-based temperature measurement method was implemented [1]. As is well-known, temperature significantly influences the performance of Li-ion batteries. At lower temperatures, batteries may exhibit reduced capacity or even internal short circuits, while at higher temperatures, aging issues may arise, significantly shortening cell lifespan. Therefore, determining the internal temperature of the cells is crucial for ensuring efficient device operation.

In the context of this experiment, understanding the internal temperature of the photo-LIBs is particularly important to assess how the photo-thermal effect impacts the batteries. As shown in Figure 4.38, based on literature data, the impedance of the cell strongly depends on three factors: state of charge (SOC), frequency, and temperature. For instance, in the low-frequency region, even when tested at the same temperature, impedance varies significantly with SOC [1]. Thus, to analyze changes in impedance caused by temperature or light-induced temperature variations, focusing on the high-frequency region is ideal. In this region, impedance is primarily related to the conductivity of the electrode and the ionic conductivity of the electrolyte.

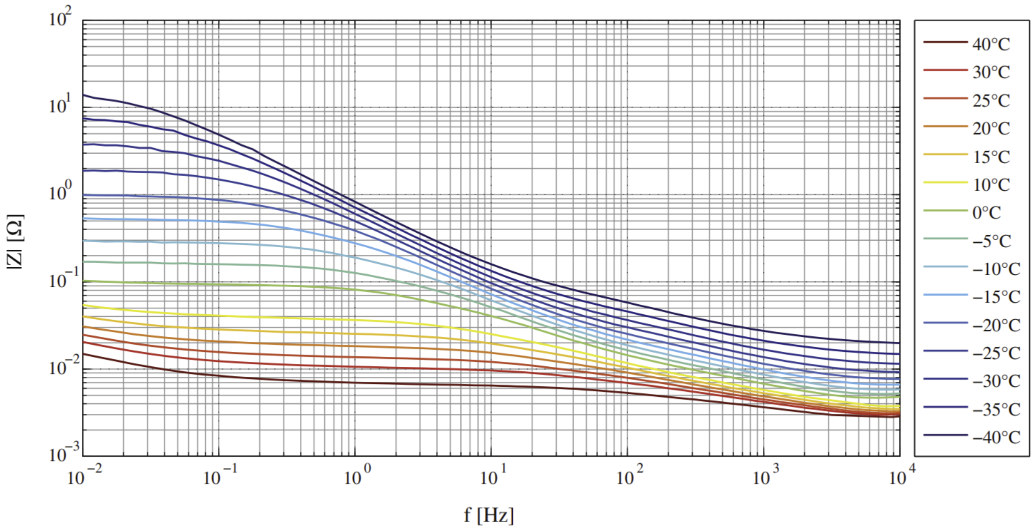

Fig. 4.38 Amplitude of the impedance of the investigated Li-ion battery cell at different SOC (10%-90%) and temperatures (15 °C, 20 °C, 25 °C).[1]

In this approach, the battery was first equilibrated in an autoclave at temperatures ranging from 18 °C to 38 °C, followed by Electrochemical Impedance Spectroscopy (EIS) measurements at 50% State of Charge (SOC). Subsequently, the same measurements were conducted on the same cell under varying light intensities. The real part of the impedance at a frequency of 100 kHz is plotted as a function of both temperature and light intensity, as illustrated in Figure 4.39.

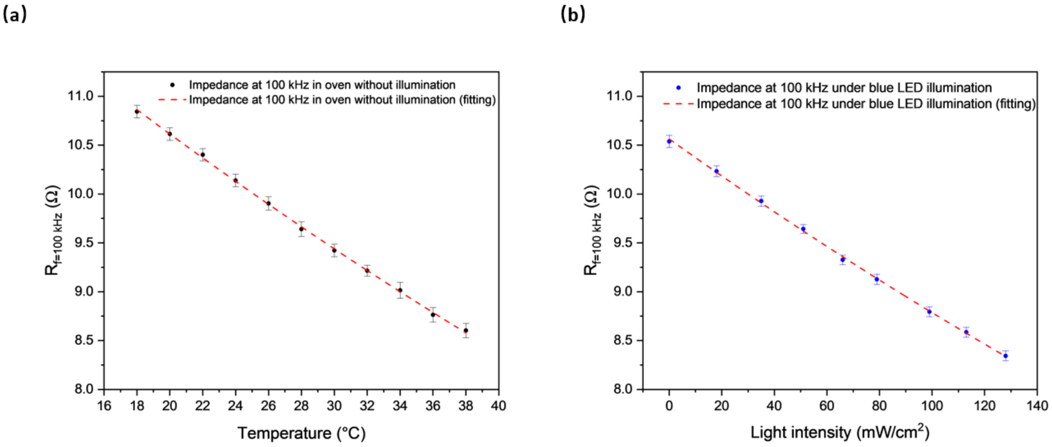

Fig. 4.39 (a) Impedance at 100 kHz as a function of temperature. (b) Impedance at 100 kHz as a function of light intensity (Blue LED). (Fit: Arrhenius + R)

As expected, the real part of the impedance at $f_m = 100kHz$ decreases with increasing temperature as shown in Figure 4.39 (a). Furthermore, the real part of the impedance at $f_m = 100kHz$ as a function of light intensity also shows a similar trend. This suggests that the photo-LIB based on PB NPs has the ability to convert light to heat and lead to temperature increase within the internal device. Both curves were attempted to fit with a conventional Arrhenius relation. The fitting equation is described as:

$$R(f_m, T) = k \times e^{\frac{E_A}{RT}} \tag{4.10}$$

Where the equation consists of a typical Arrhenius characteristic part. [339]

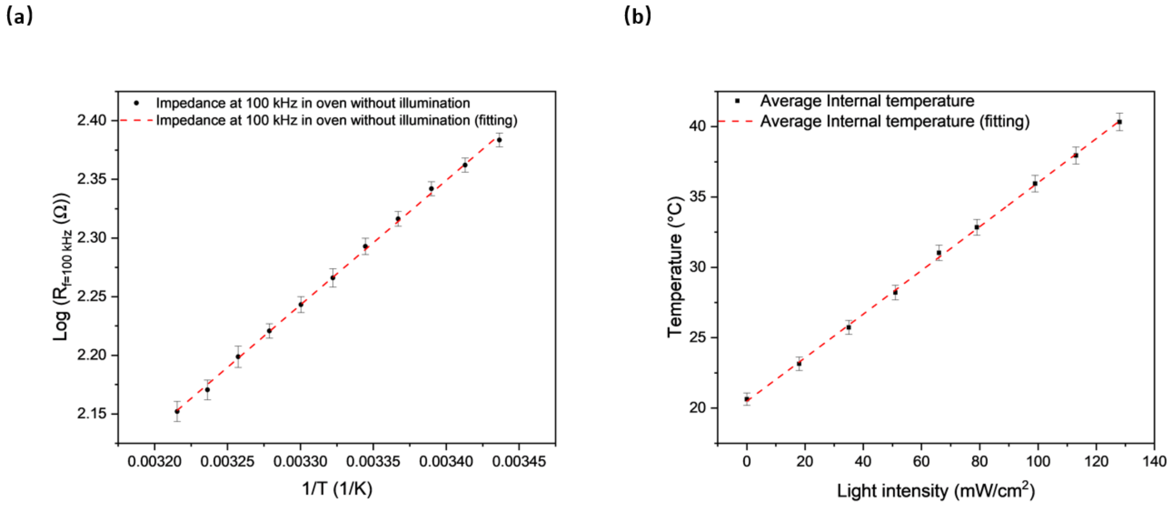

Fig. 4.40 (a) The real part of the impedance at 100 kHz (Log) as a function of the inverse of oven temperature with no illumination. (b) Average internal temperature from EIS as a function of light intensity (Blue LED).

The results were then analyzed using a logarithmic scale, as shown in Figure 4.40 (a). The real part of impedance at 100 kHz (log scale) increased with increasing inverse temperature, displaying a roughly linear trend, consistent with previous studies. [340, 341] Subsequently, the real part of impedance at $f_m = 100$ kHz at different light intensities was used to estimate the internal temperature corresponding to each light intensity. This was achieved by substituting the impedance at $f_m = 100$ kHz into the fitting curve obtained from impedance measurements at a range of temperatures in the autoclave. The average internal temperature of the battery was then plotted as a function of light intensity, as shown in Figure 4.40 (b). In our experiment, the internal temperature increased linearly with light intensity, which aligns with previous findings. [321]

To further analyze the effect of light on cells' performance, chronoamperometry tests were then conducted at various temperatures and light intensities as shown in Figure 4.41.

Under both increasing temperature and light intensity, a higher initial charging current is observed. I then integrated the area below the current-time curves in Figure 4.41, these values correspond to the charge during the constant voltage hold at 3.2 V vs. Li/Li$^+$ sequence. The charge was then divided by the time interval and mass loading in order to obtain the charge rate during the charging process.

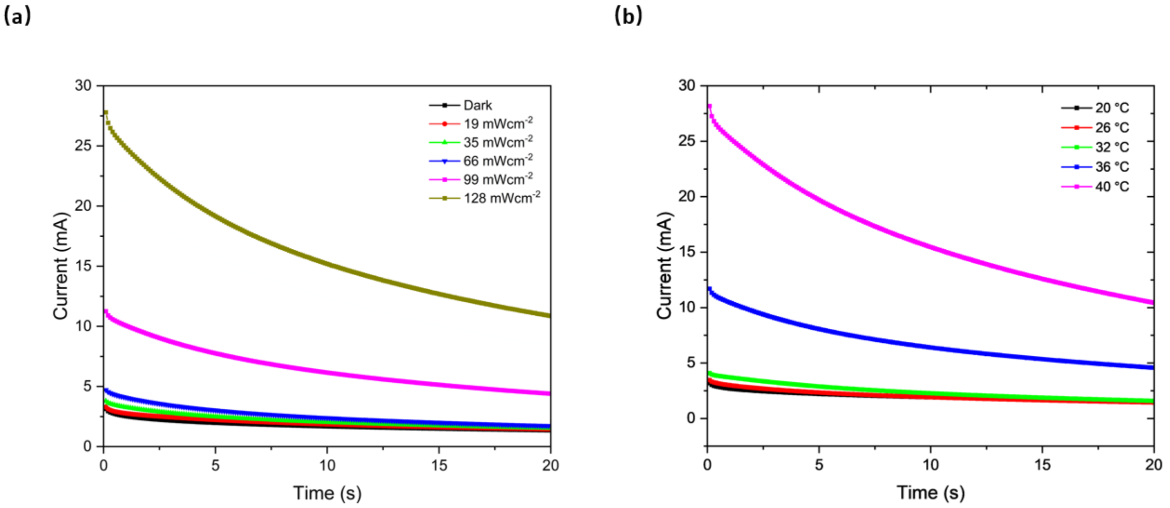

Fig. 4.41 (a) Chronoamperometry curves at different light intensities (Blue LED) during constant voltage hold charging at 3.2 V vs. Li/Li$^+$. (b) Chronoamperometry curves at different temperature during constant voltage hold charging at 3.2 V vs. Li/Li$^+$.

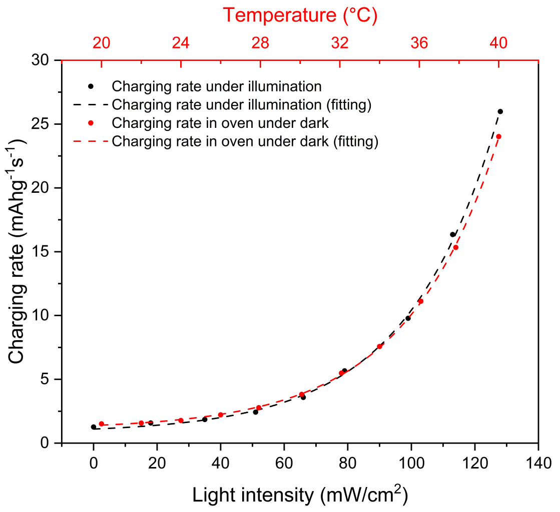

Fig. 4.42 Charging rate calculated from integration of chronoamperometry curves as a function of light intensity (Blue LED) and measured surface temperature fitted using the Arrhenius law.

As depicted in Figure 4.42, the charging rate exhibits an exponential increase with both light intensity and the estimated internal temperature at the corresponding light intensity. To explain that, like a battery system, the temperature dependence of a chemical reaction is often described by the Arrhenius equation as shown below:

$$K = A \times exp^{\frac{E\alpha}{RT}} \tag{4.11}$$

Where K is the rate constant of a chemical reaction, A is the pre-exponential constant factor, E_α is the molar activation energy and R is the gas constant. The very similar changes in chronoamperometry under elevated temperature and illumination again suggest that photothermal heating is a dominating effect in these cells. [342] The small differences between the temperature and illuminated cells could be due to measurement errors as well as localized inhomogeneous cell temperature.

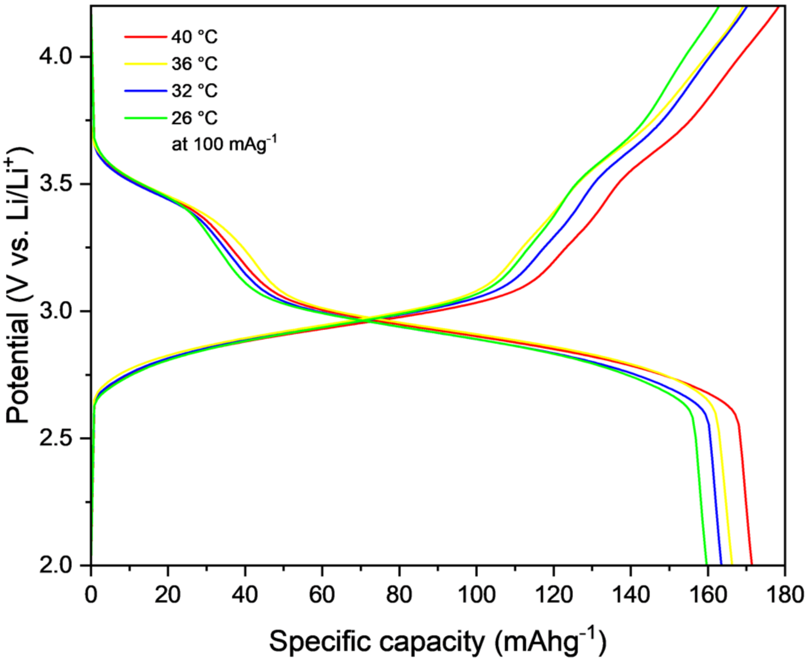

Fig. 4.43 Galvanostatic discharge-charge curves at 100 mAg^{-1} at a range of temperatures.

Next, galvanostatic tests at different temperatures were performed in temperature-controlled incubators, as shown in Figure 4.43. The results indicate that both charge and discharge capacities increase with rising temperature.

Subsequently, batteries were tested under a 128 $mWcm^{-2}$ blue LED and at 40 °C (the temperature corresponding to EIS measurements in Figure 4.40 (b)), as depicted in Figure 4.44 (a). Under light illumination and elevated temperature, the specific capacities were observed to be higher than those under dark conditions. However, based on Figure 4.40

(b), if the internal temperature at 128 $mWcm^{-2}$ is accurately estimated, the capacity should theoretically remain the same. A small capacity difference was noted between the light condition and its corresponding internal temperature, but this variation aligns with the charging rate shown in Figure 4.42.

This suggests that the capacity difference between temperature and light intensity comparison may be attributed to localized inhomogeneous cell temperature or slight degradation during testing at 40 °C. Notably, the capacity difference is less than 10 mAh/g and decreases further under lower light intensities, indicating that the temperature estimation remains relatively accurate.

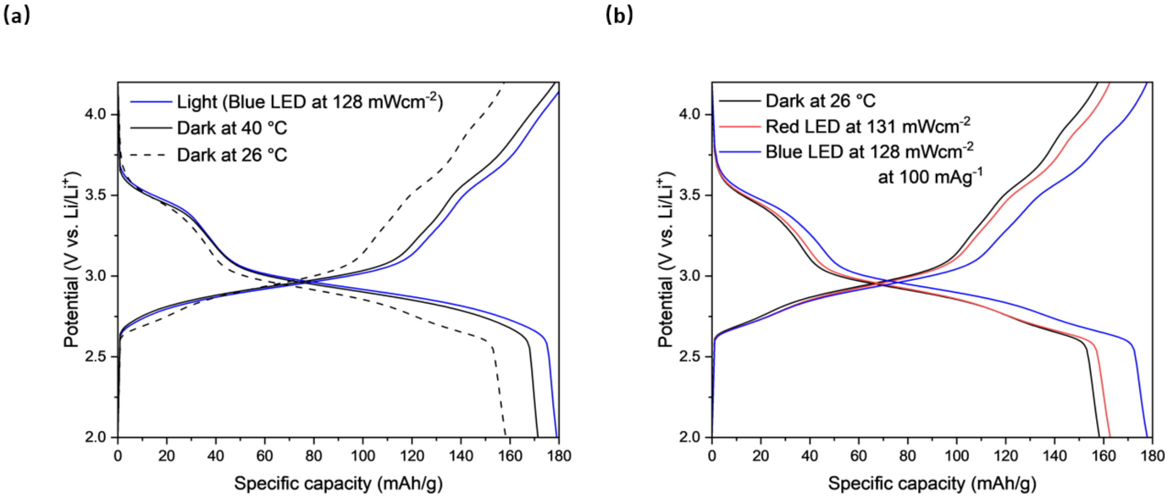

Fig. 4.44 (a) Galvanostatic discharge-charge curves at 100 mAg^{-1} under dark, blue LED with a light intensity of 128 $mWcm^{-2}$ and dark with the corresponding temperature derived from EIS measurement. (b) Galvanostatic discharge-charge curves at 100 mAg^{-1} under blue and red LED.

Under illumination with both red (630 nm) and blue (470 nm) LEDs at an intensity of approximately 130 $mWcm^{-2}$ and a current density of 100 mA/g, the cell demonstrated increased specific capacity compared to dark conditions, as depicted in Figure 4.44 (b). The enhancement under blue LED was more pronounced, with the specific capacity being 11.6% higher than under red LED illumination.

To investigate the internal changes in the photo-LIB during red LED illumination, impedance measurements at 100 kHz were conducted over a range of temperatures and light intensities, as presented in Figure 4.45. The impedance data collected under red LED illumination were substituted into the fitting equation from temperature-controlled autoclave measurements to estimate the internal temperature. The average internal temperature as a function of red LED light intensity is shown in Figure 4.45 (b).

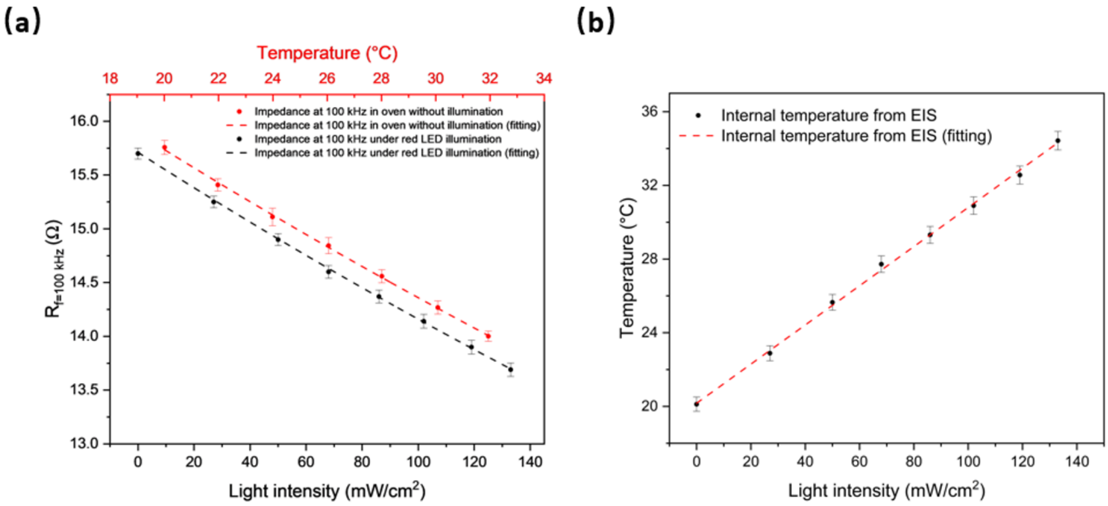

Fig. 4.45 (a) Impedance at 100 kHz as a function of light intensity (Red LED) and measured oven temperature. (fit: Arrhenius + R) (b) Estimated internal temperature as a function of light intensity (red LED).

The temperature changes under blue and red illumination were compared, as shown in Figure 4.46. The results indicate that the temperature rise is more pronounced under blue LED illumination at the same intensity, as represented by the fitting line. Additionally, the temperature increase during a light-on/off cycle was evaluated by continuously measuring the impedance at 100 kHz, as depicted in Figure 4.47.

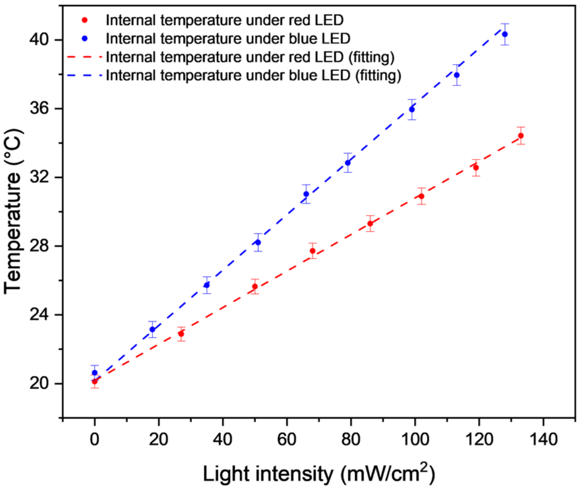

Fig. 4.46 Estimated internal temperature from EIS measurement as a function of light intensity for both red and blue LED.

Under both blue and red LED illumination, the impedance at 100 kHz decreased over time during the light-on cycle, while during the light-off cycle, the impedance returned to its original values. By substituting the impedance values into the fitting equations obtained from the temperature-controlled autoclave measurements, the corresponding temperature changes during the light-on/off cycle were determined, as illustrated in Figure 4.48.

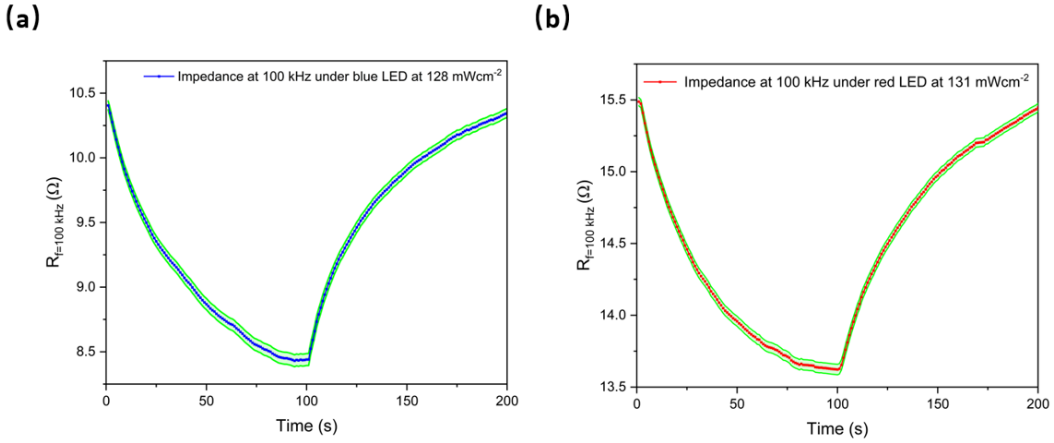

Fig. 4.47 (a) The impedance at 100 kHz during a continuous light-on/off cycle for blue LED at 128 $mWcm^{-2}$. (b) The impedance at 100 kHz during a continuous light-on/off cycle for red LED at 131 $mWcm^{-2}$.

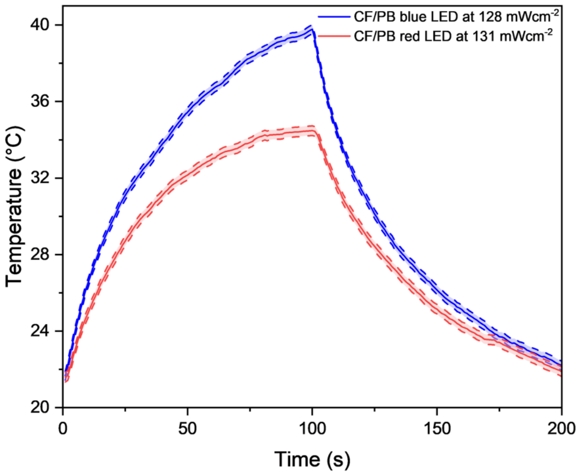

Fig. 4.48 Heating and cooling curves of CF/PB under blue and red LED.

By comparing the electrodes with PB under both blue and red LED illumination, a higher temperature is recorded under blue LED, which again demonstrates that the CF with Prussian blue nano-particles under blue LED can convert light to heat more efficiently than under red LED with similar light intensity. This may correspond to the blue LED being above the band gap energy, leading to more efficient photo-thermal heating compared to using a red LED. In order to further understand the importance of PB regarding photo-thermal conversion, a dummy photo-LIB was assembled with only carbon felt as the cathode. Then, the same EIS-temperature measurement was done under the same conditions as shown in Figure 4.49.

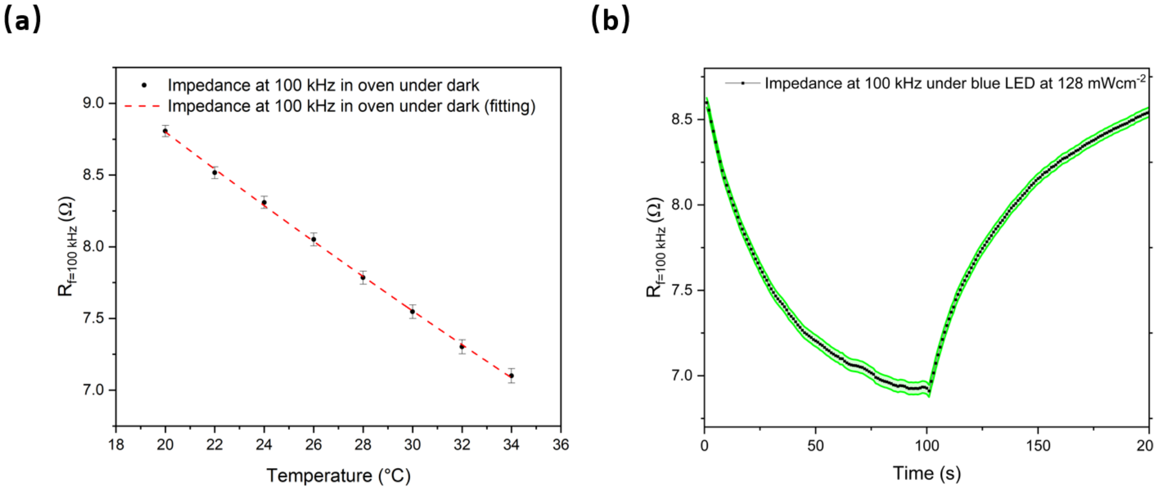

Fig. 4.49 (a) Impedance at 100 kHz as a function of temperature for CF/Li half-cell. (fit: Arrhenius + R) (d) The impedance at 100 kHz during a continuous light-on/off cycle for blue LED at 128 $mWcm^{-2}$ with CF/Li half-cell.

Following the previous characterization approach, impedance was initially measured at 100 kHz as a function of temperature in a temperature-controlled autoclave. The results were well-fitted using the Arrhenius+R equation, as previously discussed. Subsequently, the impedance at 100 kHz was measured during light-on/off cycles under blue LED illumination at an intensity of 128 $mWcm^{-2}$.

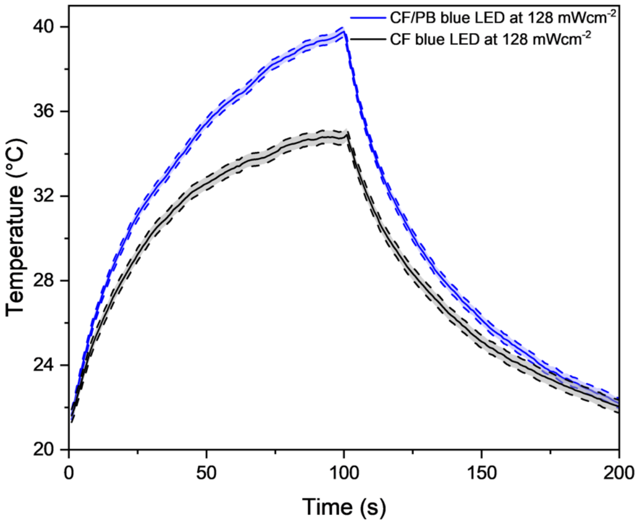

Fig. 4.50 Heating and cooling curves of bare CF and CF/PB electrodes under blue LED.

The impedance at 100 kHz during the light-on/off cycle under blue LED illumination at a light intensity of 128 $mWcm^{-2}$ was converted to temperature using the fitting equation from Figure 4.50. By comparing the temperature difference between CF and CF/PB electrodes under identical illumination conditions, it is evident that the presence of PB nanoparticles (NPs) in the cathode significantly influences the temperature, with higher temperatures observed in the electrodes with PB NPs, as shown in Figure 4.50.

To further investigate how PB NPs affect the reflectance spectra of bare CF, a UV–vis spectrometer paired with an integrating sphere was used for precise measurements of diffuse reflectance spectra for both bare CF and CF/PB NPs, as illustrated in Figure 4.51.

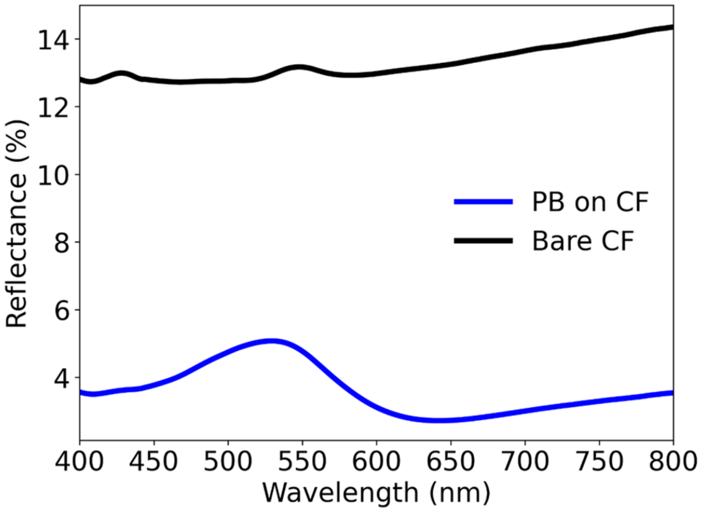

Fig. 4.51 Reflectance spectra of bare CF and CF/PB electrode.

It has been shown that, after PB NPs grown on CF, the reflectance has been largely reduced by around 10% under the same wavelength as shown in Figure 4.51. Apart from that, the reflectance spectra for CF/PB NPs present a semiconducting property. When combined with carbon materials, carbon-semiconductor composites offer additional structures for efficient electron transfer, promoting nonrelaxation processes, enhancing light absorption, and accelerating photothermal conversion. [343–345] In addition, more light is converted to heat with PB grown on CF leading to a higher recorded temperature under illumination.

In order to analyse the working mechanism of our CF/PB electrode, the spectra of our light sources are measured as shown in Figure 4.52. The peak intensity for the blue LED is around 470 nm and 630 nm for the red LED, respectively. It is worth noticing that the intensity for the red LED ends before 700 nm, therefore, NIR is not responsible for the temperature rise. So I can conclude the working mechanism of the CF/PB electrode solely results from the photo-thermal effect in the visible light region. For the bare CF electrode, the temperature rise is due to the photo-thermal effect within the CF. Previous research has already shown that carbon-based material can exhibit the photo-thermal effect.[346] The photo-thermal effect for the bare CF under the red LED is slightly lower than the blue LED due to the phonon energy of the blue LED being higher than the red LED. The CF/PB under blue LED results from a combination of photo-thermal effects from both CF and PB.

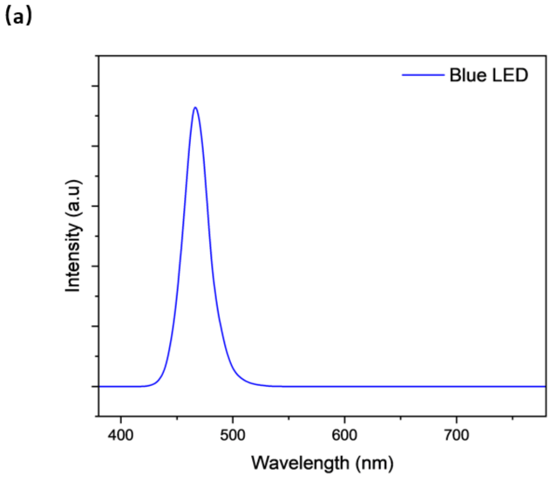

Fig. 4.52 Spectrum of the (a) blue and (b) red LED.

The CF/PB electrode was also tested under various illumination conditions using a traditional temperature probe in ambient air. The probe was connected to the back side of the CF/PB electrode with silver paste to ensure stable contact, while the front side was illuminated with LEDs.

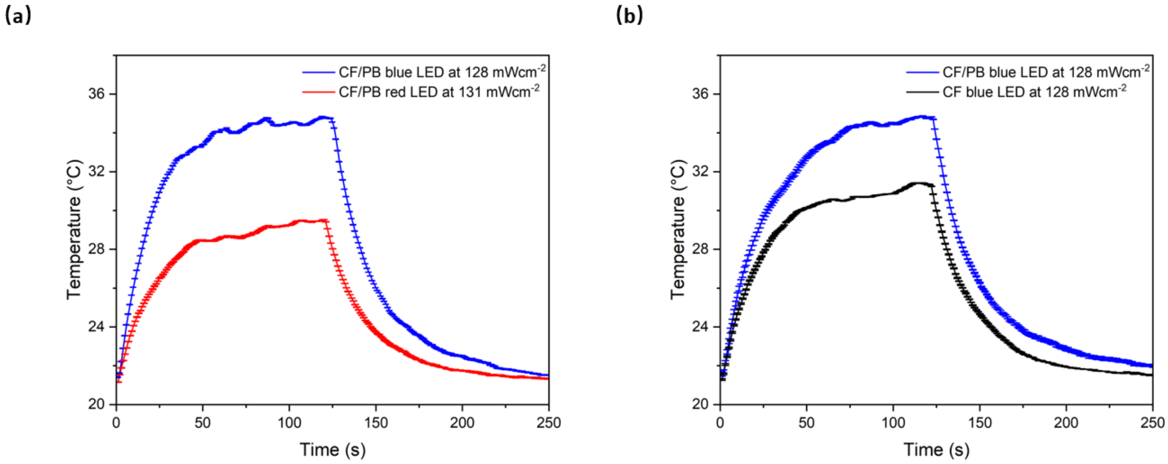

Fig. 4.53 (a) Heating and cooling curves of CF/PB under blue and red LED. (b) Heating and cooling curves of bare CF and CF/PB electrodes under blue LED. (Both were measured from a temperature probe)

As shown in Figure 4.53 (a), the heating and cooling curves of CF/PB under both blue and red LEDs confirm the results I obtained from the EIS measurement. The CF/PB under blue LED shows a much higher temperature rise compared to the red LED. More importantly, the temperature change was again compared by using bare CF and CF/PB electrodes as shown in Figure 4.53 (b). Very similar to our previous EIS measurement, by growing PB on CF, the photo-thermal conversion is much more distinct under the blue LED. It is worth noticing that even though the trends for both results are the same as the EIS measurement, the maximum temperatures for the temperature probe tests under various illumination conditions are quite different from the EIS measurement. This is possibly due to the ambient environment because the EIS tests undergone in the coin-cell configuration, but this experiment only used the temperature probe and the temperature can be affected by the surroundings, most of the heat is dissipated to the air. Moreover, the temperature probe was connected to the CF/PB electrode physically by using a silver paste, even though the silver paste has excellent thermal conduction between the CF and probe, there is still heat loss during the transportation. As shown in both figures in Figure 4.53, the initial temperature recorded for the first 50 seconds is very stable but the temperature started to fluctuate. This is possibly due to the connection between the temperature probe and our CF/PB electrode. In our experiment condition, there is an air conditioner operating, possibly leading to inaccurate results. Our CF/PB electrode is very light and the wind from the air conditioner may lead to a disconnection between the temperature probe and the CF/PB electrodes.

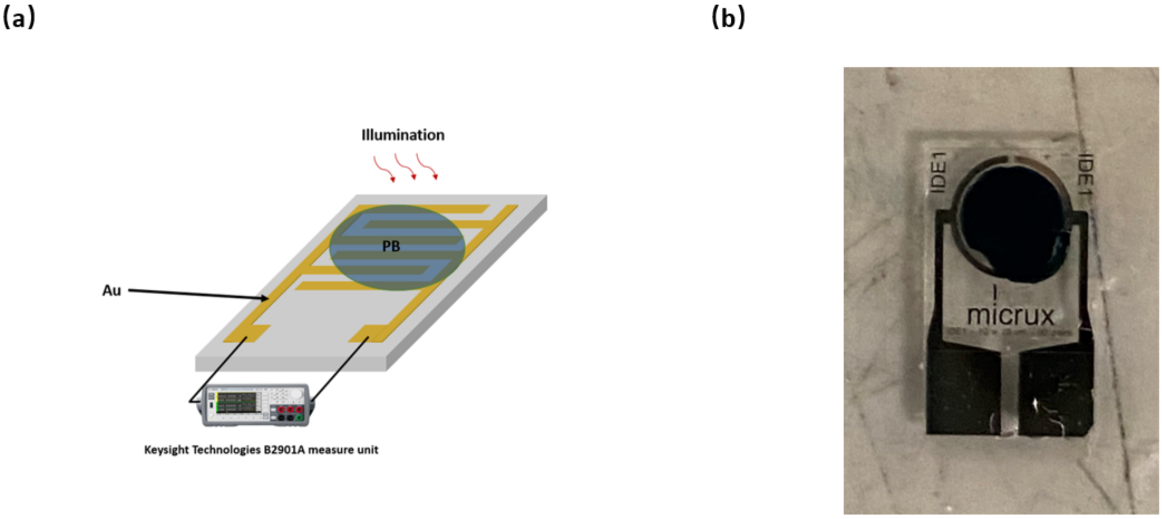

Fig. 4.54 (a) Schematic diagram of the Au-PB-Au interdigital electrode. (b) Digital images of the Au-PB-Au interdigitated electrode.

The photo response of Prussian blue (PB) was evaluated using a planar Au-PB-Au interdigital electrode (IDE) configuration. The IDE was created by drop-casting PB onto the centre of the device, as illustrated in Figure 4.54 (a). The current response under different illumination conditions is recorded by using the Keysight Technologies B2901A measure unit. The digital image of the dropcasted Au-PB-Au IDE is shown in Figure 4.54 (b). I can clearly see the centre is covered with PB with a dark blue colour.

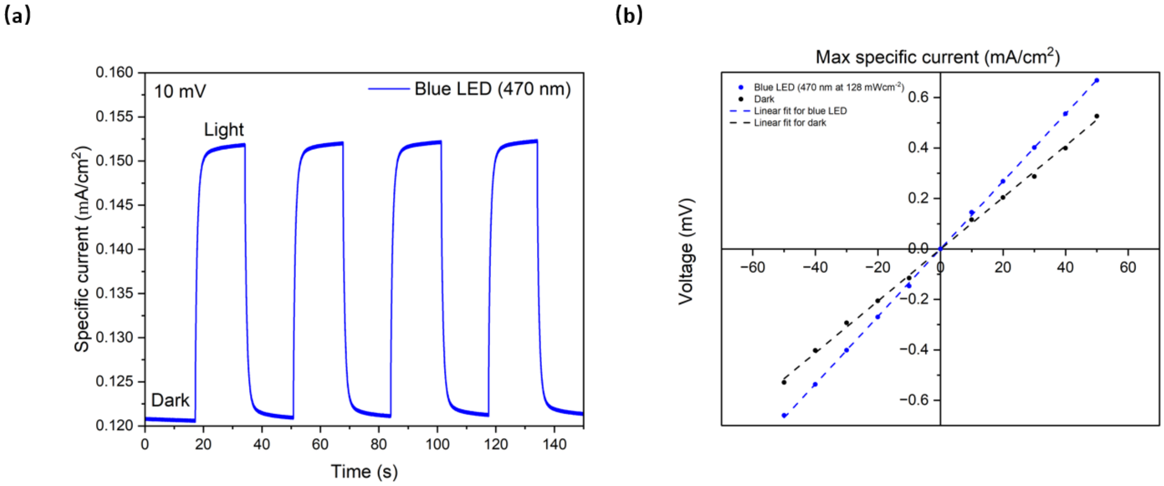

Fig. 4.55 (a) Response current of the Au-PB-Au PD under alternating dark and illuminated conditions at 10 mV. (b) Current-voltage curves of the planar Au-PB-Au PD in dark and illuminated conditions.

In Figure 4.55 (a), an increased response current was observed under illuminated conditions compared to dark conditions as bias voltages increased. The rise in response current under illumination is attributed to heat generation from the photo-thermal effect, in contrast to the response under dark conditions. At a bias voltage of 10 mV, the specific current increased from approximately 0.12 $mAcm^{-2}$ to 0.15 $mAcm^{-2}$ under blue LED illumination at an intensity of 128 $mWcm^{-2}$. This measurement was repeated at different bias voltages, as depicted in Figure 4.55 (b). No response current was detected at 0 V bias under either dark or illuminated conditions.

Additionally, the results indicated that with increasing bias voltage, a greater enhancement in current was observed under illuminated conditions. The findings from the interdigitated electrode setup suggest that the current flow through the photodetector varied upon irradiation, likely due to heat generation from the photo-thermal effect. This underscores the photoresponsive behavior of the Prussian blue material in the interdigital electrode photodetector.

To further explore the light absorption ability of the Prussian blue (PB) cathode material during the lithiation and de-lithiation process, ex-situ UV-vis measurements of the PB/CF photocathode were conducted at different states of charge to understand the change in bandgap during discharge and charge. The test samples were prepared by sonicating the photocathodes in 1M HCl for 30 minutes. As I discussed before, the photo-thermal effect strongly depends on the absorption of light at a certain wavelength, the shift in bandgap can lead to lower photo-thermal conversion efficiency. As illustrated in Figure 4.56 (a), the photo-batteries were disassembled at five points during the state of charge, labelled from a to e. The absorbance spectra at each stage of charge are presented in Figure 4.56 (b). During full discharge from the Open Circuit Potential (OCP) at 3.7 V to 2.0 V, the absorption peak shifts toward shorter wavelengths, and the bandgap increases from 2.40 eV to 2.71 eV. Conversely, during charging from 2.0 V to 4.2 V, the bandgap decreases from 2.71 eV to 2.33 eV. This bandgap shift is likely attributed to phase changes in the material, where Li^+ ions insert into the cathode, effectively "doping" the Prussian blue with Li^+ ions [347]. The measured bandgap corresponds to $E_g+\Delta E$, where E_g represents the intrinsic bandgap of Prussian blue and ΔE represents the Moss-Burstein shift. These observations suggest that the material maintains a bandgap between 2.3 and 2.7 eV throughout cycling, though further operando studies are required for confirmation.

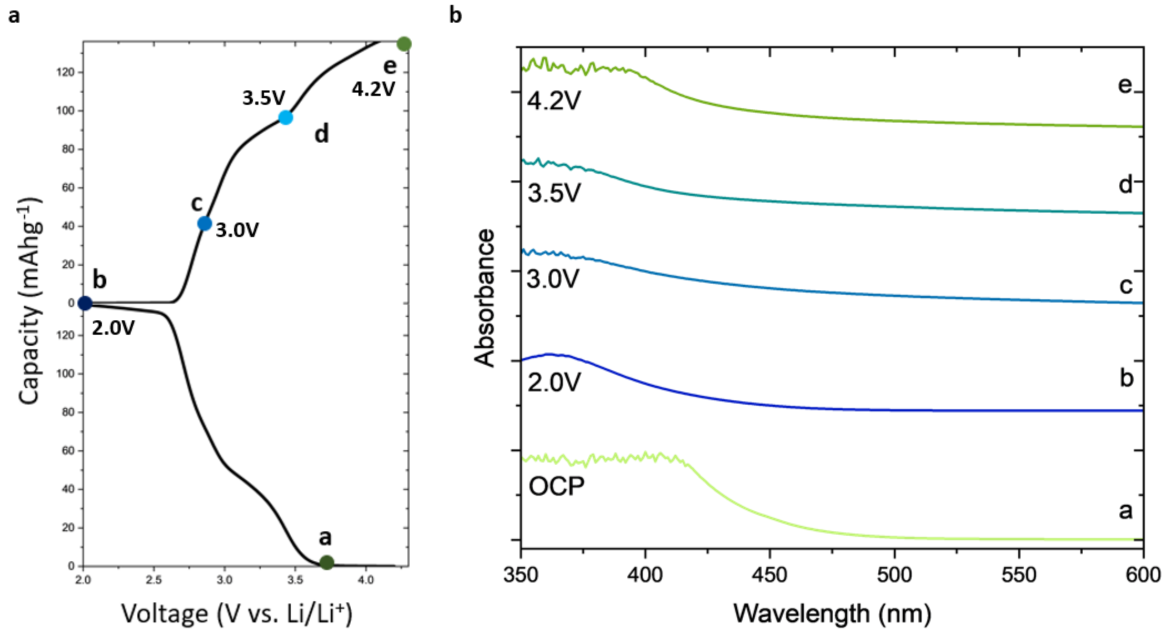

Fig. 4.56 (a) Galvanostatic discharge-charge curves at 200 mAg^{-1} from photo-cell with labelled at different states of charge. (b) Ex-situ absorbance spectra of the sonicated photo-cathode samples.

To evaluate the effect of photo-thermal heating on the lifetime of photo batteries, three PB/Li half cells were cycled under three different conditions: room temperature in dark conditions, 40 °C in dark conditions, and room temperature under illuminated conditions. Each cell was cycled at 200 mA/g for 100 cycles, and the galvanostatic charge-discharge (GCD) results were compared.

As shown in Figure 4.57 (a), the GCD curves at a specific current density of 200 mA/g under dark conditions at 26 °C across selected cycles exhibit no significant change in shape, indicating the stable electrochemical performance of the synthesized PB/CF photo-electrode. The cell demonstrated excellent long-term stability with a capacity retention of 96.6%. Some of the poor initial Coulombic efficiency observed during cycling may be attributed to side reactions occurring in the carbon felt [348].

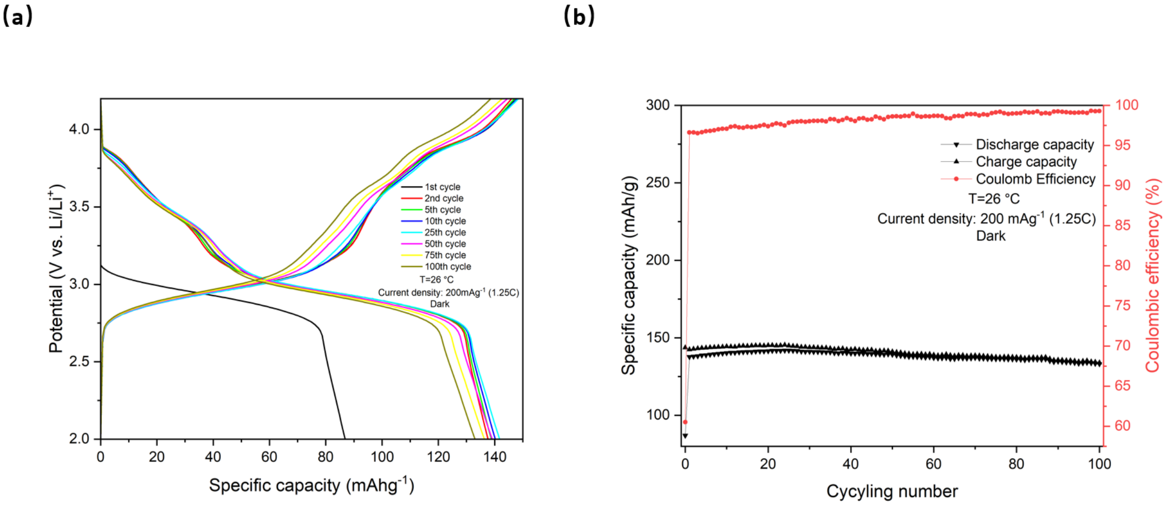

Fig. 4.57 (a) Galvanostatic charge-discharge curves at the specific current density of 200 mA/g under dark conditions at 26 °C at selected cycles. (b) Long-term cycling stability of the photo-LIBs under dark conditions at 26 °C at 200mA/g.

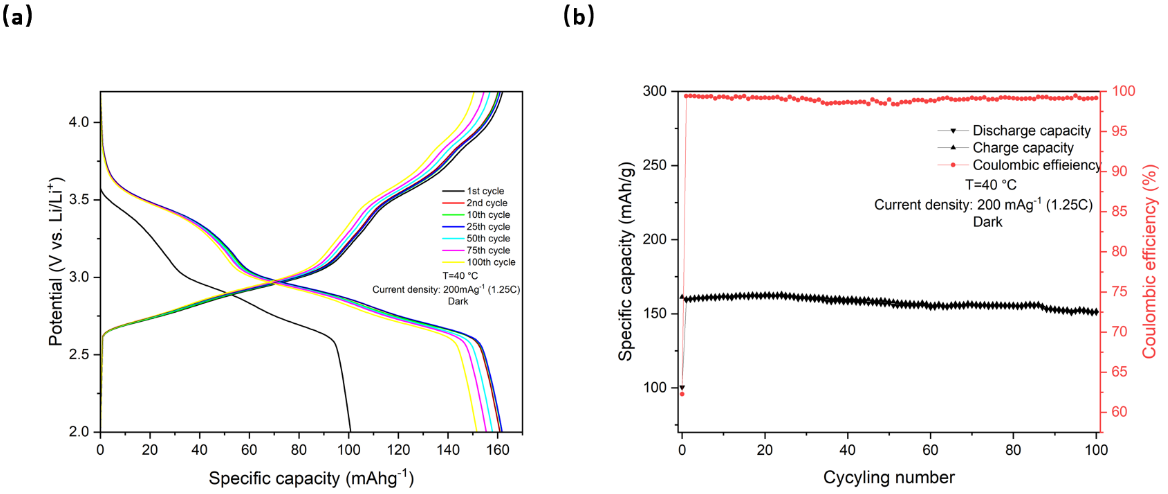

Fig. 4.58 (a) Galvanostatic charge-discharge curves at the specific current density of 200 mA/g under dark conditions at 40 °C at selected cycles. (b) Long-term cycling stability of the photo-LIBs under dark conditions at 40 °C at 200mA/g.

Another PB/Li half cell was tested at an elevated temperature of 40 °C under the same conditions, current density, and number of cycles. As shown in Figure 4.58 (a), the galvanostatic charge-discharge (GCD) curves at a specific current density of 200 mA/g under dark conditions at 40 °C exhibit no noticeable change in shape when comparing the 100th cycle to the first cycle. Furthermore, the long-term cycling stability of the photo-LIBs under dark conditions at 40 °C at 200 mA/g shows a capacity retention of 95.4%, which is consistent with the previous GCD results obtained at 26 °C.

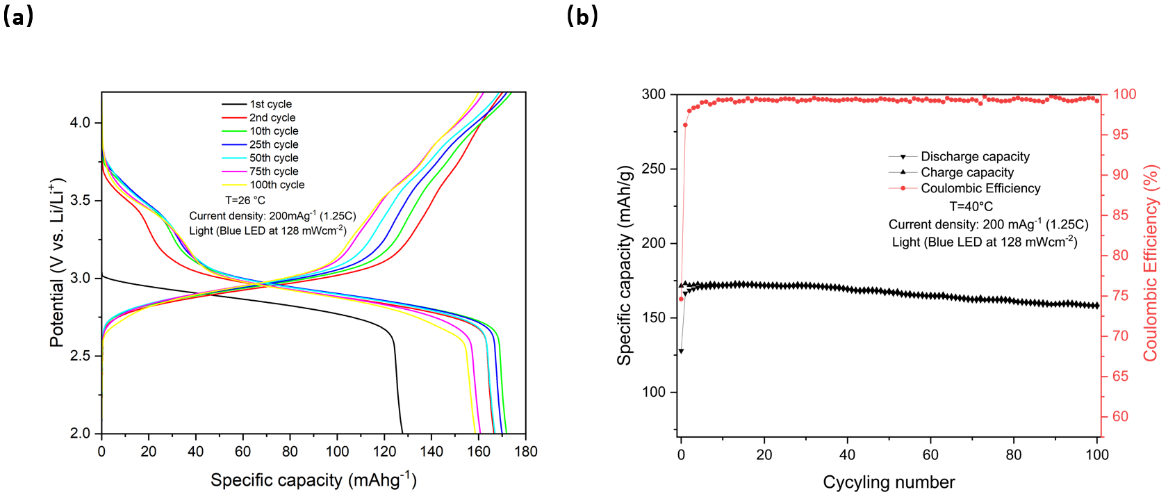

Fig. 4.59 (a) Galvanostatic charge-discharge curves at the specific current density of 200 mA/g under light conditions at 26 °C at selected cycles. (b) Long-term cycling stability of the photo-LIBs under light conditions at 26 °C at 200mA/g.

Lastly, the same galvanostatic charge-discharge (GCD) measurement was conducted for the photobatteries under illumination using a blue LED at a light intensity of 128 mW/cm^2. This light intensity was selected based on previous impedance-based measurements, which indicated that the internal temperature of the photo-battery at this intensity is approximately 40 °C, facilitating a direct comparison with prior results.

The GCD curves at a specific current density of 200 mA/g under light conditions at 26 °C, shown in Figure 4.59 (a), exhibit no significant change in shape between the first charge-discharge cycle and the 100th cycle, consistent with the results obtained under dark conditions at 26 °C and 40 °C. Additionally, the coin cell demonstrated excellent cycling stability with a capacity retention of 94.8%, as shown in Figure 4.59 (b), which is comparable to the performance observed at the elevated temperature.

Even though no notable change of the shape of the GCD curves can be observed from our results in 26 °C in dark conditions, 40 °C in dark conditions and 26 °C in illuminated conditions, I can still observe a little drop in the capacity retention from the long-term cycling test. Therefore, I analysed the differences between nominal charge and discharge voltage (Δ) for each condition at the selected cycles and the Δ V is plotted as a function of cycle number as shown in Figure 4.60.

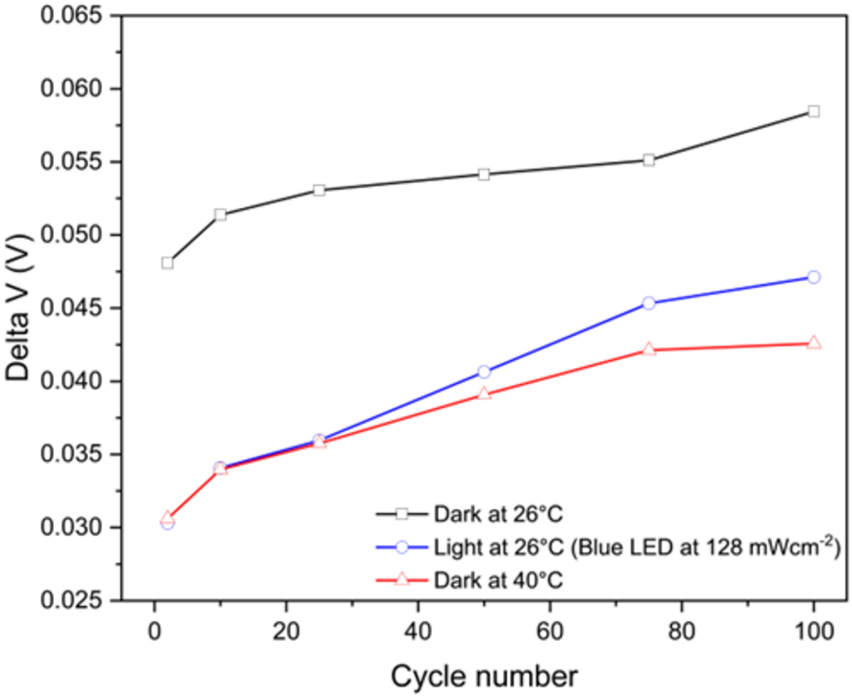

Fig. 4.60 The differences between nominal charge and discharge voltage (Δ) as a function of cycle number under dark at 26 °C, dark at 40 °C and light at 26 °C.

Here, Delta V can be used to study the impedance and polarization in the cell during long-term cycling. As expected, the values of Δ V are lower under elevated temperature and illumination as temperature increases improve ion transfer. I can also see that the value of Δ V for each condition increases during cycling with cell ageing. The cell under illumination shows an increase of Δ V values with 55.6% compared to 39% at 40 °C, which suggests that light might lead to slight degradation processes over long-term cycling that do not take place in control experiments at the same temperature.

In order to fully understand what might lead to the degradation that appeared in our Δ V vs. cycle number results. I first performed XPS for the photocathode before and after 100 cycles for each condition as shown in Figure 4.61. The XPS analysis was performed using a Thermo Scientific Escalab 250Xi fitted with a monochromated Al kα X-ray source (1486.7 eV). All data was recorded with an X-ray beam size of 650 μm, a pass energy of 20 eV at a step size of 0.1 eV. Electronic charge neutralization was achieved using an ion source. Ion gun current = 100 μA. Ion gun voltage = 40 V. All sample data was recorded at a pressure below 10-8 Torr and a room temperature of 294 K. Data was analysed using

CasaXPS v2.3.26rev1.0N. The high-resolution XPS spectra show the distinguishable Fe 2p peaks, the peak which is located at a binding energy of 727.5 eV corresponds to the $Fe^{III}2p_{1/2}$. The peak which is located at the binding energy of 722.2 eV corresponds to the $Fe^{II}2p_{1/2}$. The peak which is located at the binding energy of 713.0 eV corresponds to the $Fe^{II}2p_{3/2}$ and last, the peak which is located at the binding energy of 708.4 eV corresponds to the $Fe^{II}2p_{3/2}$. The XPS spectra show no clear shifts of peak positions and maintain a consistent shape for the Fe 2P peaks, which means high reversibility after long-term cycling under both illuminated and elevated temperature conditions.

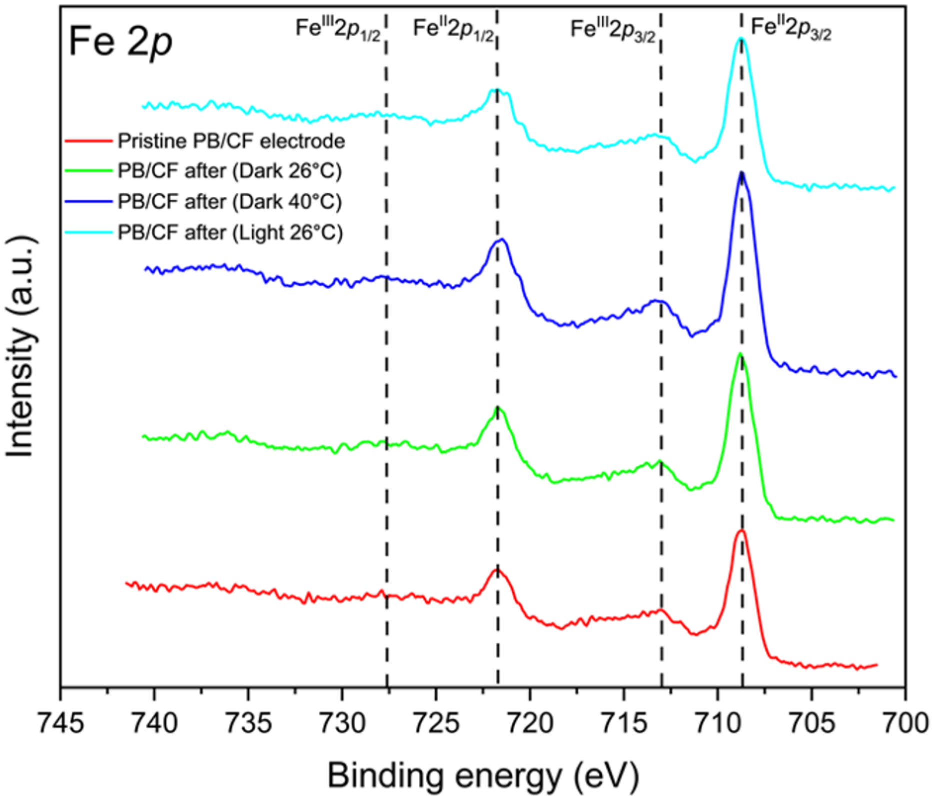

Fig. 4.61 XPS spectra of the characteristic Fe 2P peaks under Dark at 26 °C, Dark at 40 °C and Light at 26 °C before and after cycling.

To further evaluate the stability of the designed photocathode, XRD analysis was conducted for the PB/CF electrode before and after 100 cycles under each condition, as shown in Figure 4.62. The XRD patterns exhibited minimal differences, even after 100 cycles under each condition. Unlike the previous XRD results of PBAs, the image on the right presents a zoomed-in version of the XRD data. Since the analysis was conducted on PB coated on the CF electrode, prominent peaks were observed at around 27 degrees, corresponding to the (002) plane of CF, and at around 54 degrees, corresponding to the (004) plane of CF.

Again, minimal changes were observed in the XRD patterns, suggesting that the increased cell polarization observed under illumination is more likely due to electrolyte decomposition caused by photochemical reactions, rather than decomposition of the PBA material.

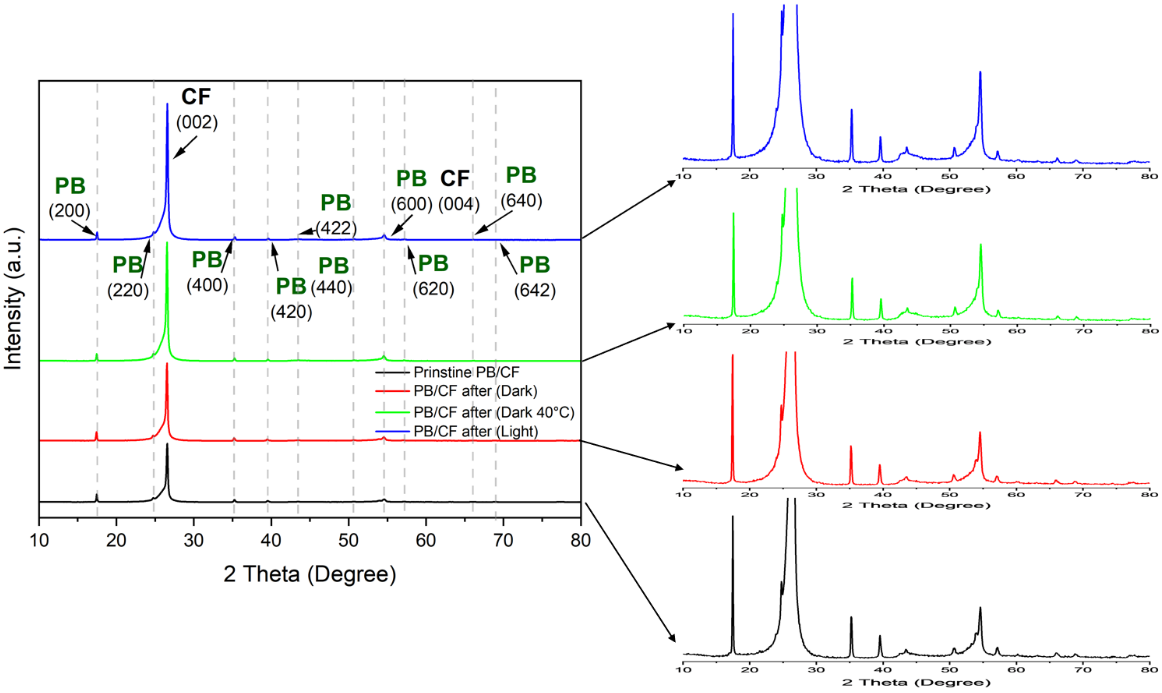

Fig. 4.62 XRD pattern of PB/CF electrodes under Dark at 26 °C, Dark at 40 °C and Light at 26 °C before and after cycling.

The additional stability characterization provides deeper insights into the light-driven interactions on the PB/CF photocathode. To examine the effect of photo-thermal heating on battery lifetime, three PBA cells were cycled for 100 cycles at 200 mA/g under three conditions: room temperature, 40 °C, and illumination with a blue LED at 128 mW/cm^2. The cells demonstrated similar capacity retentions of 96.6%, 95.4%, and 94.8%, respectively. The poor initial Coulombic efficiency observed during cycling may be attributed to side reactions in the carbon felt.

Analysis of the difference in nominal charge and discharge voltage (polarization) over 100 cycles revealed that heating the cell reduces impedance, consistent with EIS data. However, polarization in the illuminated cell increased more rapidly over time (a total increase of 55.6%) compared to the control cell heated to 40 °C (a total increase of 39%). This suggests that illumination induces additional degradation processes, which were further investigated using XPS and XRD post-mortem analyses. These studies revealed no significant differences in the PBA cathodes cycled under different conditions, indicating that the observed increase in polarization may stem from light-induced reactions with the electrolyte.

4.3 Conclusion

This investigation focuses on the photothermal effects observed in Prussian blue analogues (PBAs) when used as cathodes in lithium-ion batteries. The study highlights the significant role of light-induced heating in enhancing the electrochemical performance of PBAs, providing insights into the synergy between photothermal effects and battery functionality. Leveraging the high photothermal efficiency of PBAs, attributed to their superior light absorption in the visible and near-infrared regions, the research identifies non-radiative relaxation processes such as Shockley-Read-Hall and Auger recombination as the primary mechanisms leading to localized temperature increases within the lattice structure.

Four types of PBAs were synthesized using different methods, including co-precipitation, electroplating, and solution growth. Among these, electrodes prepared via the solution growth method exhibited superior electrochemical performance. Comprehensive characterization of the PBAs was conducted, with the bandgap emerging as a critical parameter due to its direct relationship with photo-induced effects and the energy required to activate photothermal processes. UV-Vis spectroscopy revealed that the bandgap of all PBAs lies within the visible light range. To study light-induced effects, active materials were deposited on interdigitated electrodes (IDEs) and subjected to chronoamperometry under alternating dark and light conditions. Surface temperature measurements demonstrated coherence between current and temperature changes, indicating a strong correlation between current variations and heat generation from illumination.

Electrochemical experiments demonstrated that PBAs maintained stable performance as cathodes in lithium-ion batteries under dark conditions. Under illumination, only Fe-PB prepared by the solution growth method showed enhanced electrochemical performance. Further electrochemical investigations revealed cathodic and anodic peak shifts in cyclic voltammetry, indicating improved charge transfer kinetics. Light exposure increased Li-ion diffusion constants, highlighting enhanced ion transport. Galvanostatic cycling at various current densities confirmed augmented capacity under illumination, underscoring the beneficial impact of photothermal heating on charge/discharge processes. Integration of Electrochemical Impedance Spectroscopy (EIS) with temperature sensors provided detailed insights into the reduction of charge transfer resistance and the exponential rise in charging rates with increased light intensity. EIS-based temperature estimates proved more accurate than temperature probe measurements, aligning with galvanostatic charge-discharge and chronoamperometry results. By comparing charging rates under light-induced and temperature-induced conditions, the study confirmed that the observed light enhancement was primarily thermal in nature. Additionally, the impedance-based method was validated for evaluating the internal temperature of battery cells under different light sources. Using red light, which has photon energy below the PBA bandgap, demonstrated a reduced photothermal effect and a lower temperature rise compared to blue LEDs. These findings emphasize the importance of precise temperature control and measurement to understand the complex interactions between photothermal and photo-charging effects in light-enhanced batteries. Furthermore, ex-situ UV-Vis spectroscopy revealed shifts in bandgap during charge and discharge cycles, which may lead to inconsistent photothermal enhancements. Overall, this study advances understanding of the mechanisms governing light-battery interactions, paving the way for next-generation photo-enhanced energy storage devices.

The study also examined the impact of photothermal heating on the lifespan of photo batteries. Three PB/Li half cells were cycled under different conditions: room temperature in the dark, 40 °C in the dark, and room temperature under illumination (blue LED, 128 mW/cm²). Each cell underwent 100 cycles at 200 mA/g, with galvanostatic charge-discharge results compared. Stable electrochemical performance was observed across all conditions, with capacity retention rates of 96.6%, 95.4%, and 94.8%, respectively. Initial poor Coulombic efficiency was likely due to side reactions with the carbon felt current collector. Analysis of nominal charge and discharge voltage differences revealed reduced impedance with heating, but faster polarization growth under illumination suggested additional light-induced degradation processes. XPS and XRD analyses showed consistent electrode characteristics before and after cycling, indicating largely reversible behaviour. However, slight degradation observed under illumination pointed to potential light-induced reactions with the electrolyte. These findings provide valuable insights into light-driven interactions in PB/CF photocathodes and highlight the need for further research to optimize the performance and durability of photo-enhanced batteries.

Chapter 5

Distinguishing between Photothermal and Photoelectric Effects in Li-ion Batteries

5.1 Motivation

Over the past decades, photo-enhanced batteries where light is used to improve the rate performance or recharge batteries have received increased attention in the academic community. However, the underlying mechanisms that contribute to performance enhancement in several photo-enhanced batteries are still under debate. For instance, photothermal effects, resulting from light absorption and subsequent conversion to heat through non-radiative relaxation, and photoelectric effects, involving the generation, separation and transport of electron-hole pairs under illumination, can be challenging to disentangle. This study aims to distinguish between the photothermal and photoelectric effects in TiO_2 and Fe_2O_3 as model systems because of their photo-activity and ability to store Li-ions. Using ultraviolet photoelectron spectroscopy (UPS) and UV-vis spectroscopy, we measure the band positions of these materials, and by a combination of different electrochemical processes, we demonstrate the transition from photothermal dominated to photoelectric effects in these materials. These results further illustrate the fact that different processes take place in photo-batteries and this work provides a workflow to investigate these complex interactions. As mentioned previously, transition metal oxides (TMOs) have been widely investigated in energy storage and photo-thermal applications due to their high photothermal conversion efficiency, chemical stability, suitable bandgap and photoactivity under illumination. In the context of energy storage, titanium oxide-based materials have found widespread use in lithium-ion batteries, thanks to their attributes such as cost-effectiveness, low toxicity, safety, and extended cycling life. Different polymorphs of titanium oxide, including rutile, anatase, brookite, and bronze B as depicted in Figure 5.1, offer diverse structural variations. Among these, rutile stands out for its thermodynamically stable structure and efficient scattering of white light. However, it has been noted that rutile can only accommodate a limited number of lithium ions at room temperature[145], rendering it unsuitable for certain energy storage applications. In contrast, anatase, another polymorph of titanium oxide, exhibits a higher capacity to store lithium ions within its lattice structure. Notably, anatase possesses superior surface chemistry and a higher conduction band value, rendering it well-suited for a range of applications, including energy storage and photocatalysis. The advantageous combination of photocatalytic activity and charge storage properties positions titanium oxide as a promising candidate for deployment as a photoelectrode material in photo-rechargeable batteries. The subsequent sections will delve into the various aspects of titanium oxide, shedding light on its role in advancing the development of next-generation photo-rechargeable energy storage devices.

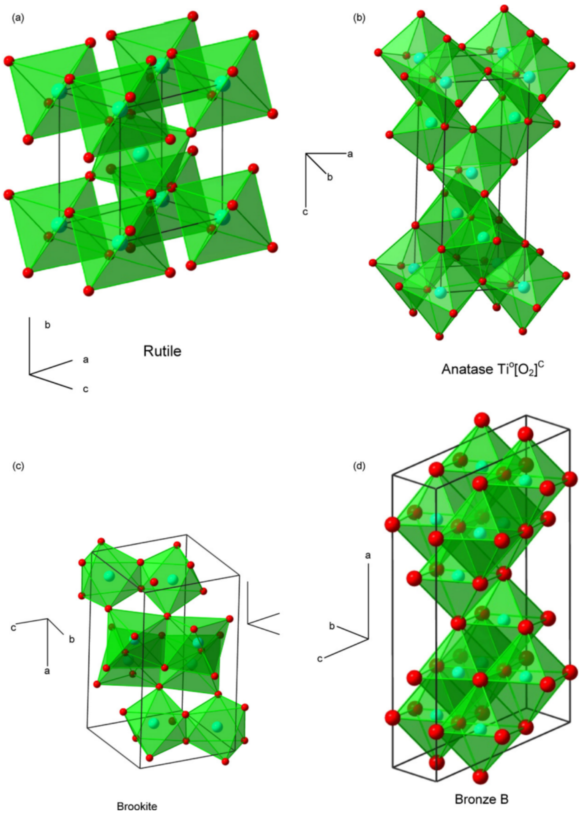

Fig. 5.1 (a) Rutile, (b) anatase, (c) brookite, and (d) bronze(B) of TiO_2.[145]

In 2017, Nguyen et al. introduced a novel light-driven Li-ion battery featuring a Li-rich TiO_2 mesoporous film, as depicted in Figure 5.2 (a). The photoelectrode is composed of three layers of mesoporous TiO_2 structures. The top layer, situated at the FTO interface, exhibits a pore size of 12 nm in diameter, while the bottom layer, located on the electrode surface, has a pore size of 17 nm in diameter. This electrode architecture is specifically tailored to facilitate the separation and transfer of photogenerated charges, contributing to enhanced high-rate capacity.

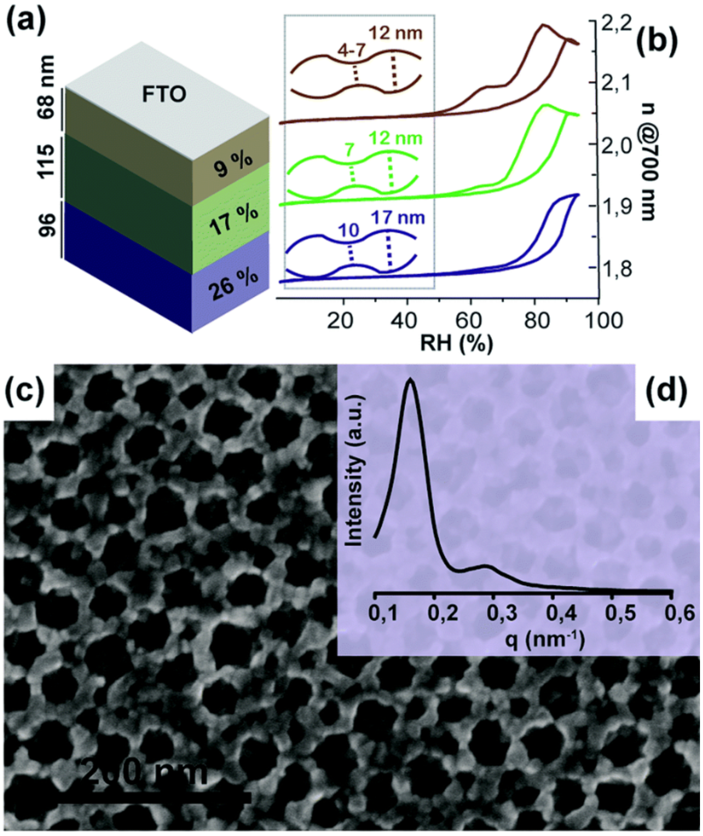

Fig. 5.2 (a) Scheme of the film architecture, presenting the porosity (%) and the thickness (nm) of each constitutive layer, determined by ellipsometry. (b) Isotherms of environmental ellipsometric porosimetry of the 3 different layers and (inset) the corresponding pore morphology. (c) SEM-FEG image of the top of the film. (d) GI-SAXS line scan of the corresponding film.[183]

Figure 5.3 illustrates the distinctive three-phase transformations experienced by anatase TiO_2 during the charge and discharge cycles. In the I phase, voltage exhibits rapid changes with discharge or charge current, accompanied by the insertion of a small amount of Lithium ions into anatase TiO_2, resulting in the formation of $Li_{0.1}TiO_2$. The II phase reveals a prominent plateau at approximately 1.75 V, attributed to the generation of tetragonal $Li_{\alpha}TiO_2$ and orthorhombic $Li_{0.5}TiO_2$. Transitioning to the III region, voltage undergoes swift changes following the plateau, leading to the formation of $Li_{0.5+\beta}TiO_2$ with additional inserted Lithium ions. Under the influence of illumination, a noteworthy enhancement of 33% is observed, elevating the capacity from 180 $mAhg^{-1}$ to 240 $mAhg^{-1}$.

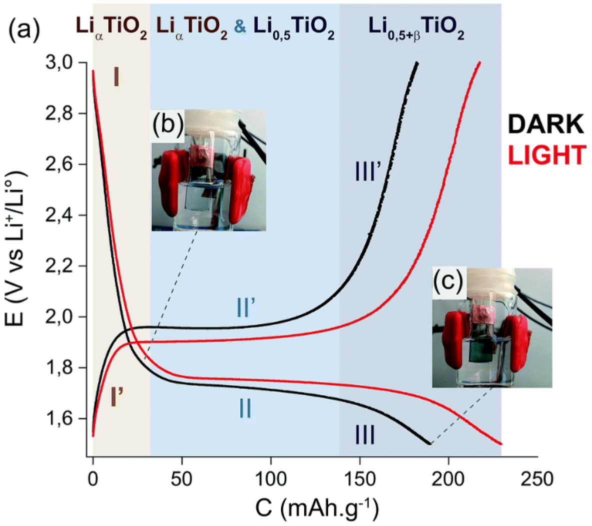

Fig. 5.3 (a) Potential versus capacity evolution (discharge–charge at a C-rate) of TiO_2 mesoporous films under dark conditions and under light. (b and c) Pictures of the cell at the beginning of zone II and at the end of zone III. $Li_{0.5}TiO_2$ corresponds to a capacity of 168 $mAhg^{-1}$.[183]

In conclusion, the exploration of titanium oxide (titania) in the context of photo-rechargeable batteries unveils a promising avenue for advancing the field of light-induced energy storage. Titanium oxide, with its intrinsic semiconducting properties and well-established applications in solar cells, demonstrates considerable potential for enhancing the efficiency and sustainability of rechargeable battery technologies. The unique bandgap structure of titanium oxide allows it to absorb light across the visible spectrum, making it an effective material for harnessing solar energy in various devices, including photo-rechargeable batteries. Its ability to generate and separate charge carriers under illumination contributes to improved electrochemical performance, enabling efficient energy storage and release. As evidenced by research endeavors, the integration of titanium oxide into photo-rechargeable batteries holds the promise of addressing the growing demand for clean and renewable energy solutions. The material's compatibility with light-driven processes, coupled with its stability and abundance, positions it as a valuable asset in the quest for developing environmentally friendly energy storage technologies. Despite these promising attributes, challenges such as optimizing charge carrier mobility, addressing potential degradation issues, and improving overall battery performance must be addressed in future research. Additionally, exploring novel architectures and engineering approaches can further unlock the full potential of titanium oxide in photo-rechargeable batteries. Hence, the journey of titanium oxide in the realm of photo-rechargeable batteries marks a significant stride toward sustainable energy solutions. Continued research and innovation in this domain have the potential to pave the way for the integration of titanium oxide into practical and efficient photo-induced energy storage devices, contributing to a cleaner and greener energy future.

In a groundbreaking study conducted in 2019, Liu et al. unveiled a revolutionary sunlight-promoted Zinc-air battery featuring $\alpha - Fe_2O_3$ as the photoelectrode. This innovative system showcased a remarkable reduction in charge potential, approximately 0.5 V lower than the conventional charge voltage of approximately 2.0 V for Zinc-air batteries [178].

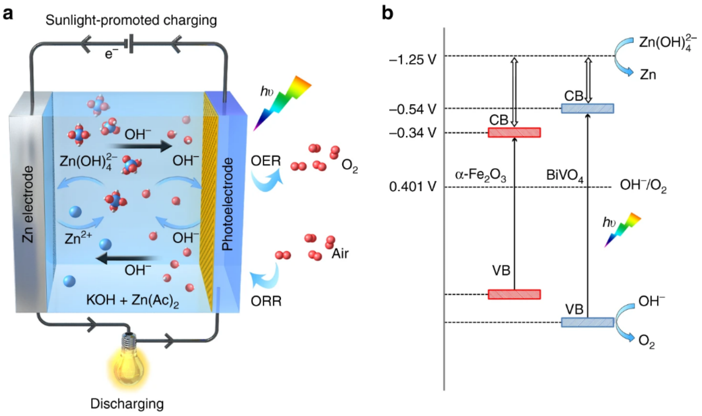

Fig. 5.4 (a)The scheme of the basic structure and working principle of the sunlight-promoted rechargeable zinc–air battery. (b) The proposed mechanism of the sunlight-promoted charging process under solar light illumination.[178]

The intricacies of the working mechanism are elucidated in Figure 5.4. In the sunlight-promoted charging mode, the $\alpha - Fe_2O_3$ photoelectrode serves as the focal point, generating electron-hole pairs upon exposure to light. These excited electrons are subsequently propelled into the conduction band, embarking on a journey to the Zn electrode through the external circuit. Within this journey, the electrons actively engage in the reduction reaction of $Zn(OH)_4^{2-}$ to Zn and OH^-. Simultaneously, the photo-generated holes at the photoelectrode play a pivotal role in oxidizing water to produce oxygen. By leveraging the light-promoted electron-hole pairs, this innovative design achieves a substantial reduction in charge potential, effectively addressing the challenges posed by the typically sluggish kinetics of the oxygen evolution reaction [349].

In summary, ferric oxide, particularly hematite, holds promise for application in photo-rechargeable batteries, contributing to the development of sustainable energy storage technologies. However, there is still work needed to address the problems. First, Hematite has a relatively wide bandgap, limiting its absorption of light in the visible spectrum. This can result in lower efficiency in converting sunlight into electrical energy. Strategies such as doping or coupling with other materials are explored to overcome these challenges. Second, In its pristine form, Fe_2O_3 exhibits low electrical conductivity, leading to challenges in efficient charge transport and overall performance in photo-rechargeable batteries. Third, Rapid recombination of electron-hole pairs within hematite can reduce the efficiency of charge separation, impacting the overall photoconversion efficiency of the battery. Last, Fe_2O_3 may undergo corrosion and degradation over extended cycling, affecting the long-term stability and performance of the photo-rechargeable battery. Ongoing research efforts seek to address challenges and unlock the full potential of hematite in this context.

The development of compact energy solutions that can simultaneously operate as a solar cell and a battery, goes back to the 70s. With the emergence of smart off-grid sensor networks and Internet of things devices, there has been a renewed interest in these so-called photo-batteries during the past decade. In particular, two-electrode systems where a photo-active cathode is simultaneously used as a Li-ion battery (LIB) cathode material and photo-active component have gained popularity, particularly because of their compact design. However, the interaction of light and battery electrodes is complicated and in particular, the effects of heat generation as a result of exposing the electrodes to light is very difficult to eliminate. In particular, LIB electrodes are typically mixed with carbon additives to enhance the electrical conductivity of electrodes which results in high emissivity coatings that are prone to heating by radiative heat transfer. Furthermore, the active materials used in photo-batteries are often photothermally active, and change bandgap with their stage of charge, which further complicates the analysis of photo-charging effects. Finally, the operation of these batteries are complicated by side reactions with the electrolyte and capacitive effects.

In this experiment, commercially available anatase TiO_2, rutile TiO_2, and Fe_2O_3 were selected due to their well-documented photocatalytic properties and suitable bandgaps for specific wavelength ranges. These materials have also been extensively studied in the context of Li-ion batteries. The inclusion of two different forms of TiO_2 was based on their distinct properties: rutile TiO_2 has a narrower bandgap, potentially enabling more efficient photothermal conversion, while anatase TiO_2 is reported to exhibit superior photocatalytic activity.[350]

Structurally, anatase and rutile differ in their oxygen ion arrangements. Rutile features a slightly distorted hexagonal close-packed (HCP) sublattice, whereas anatase has a cubic close-packed sublattice. Both structures are composed of titanium-oxygen octahedra, with rutile sharing two edges and anatase sharing four. Their bandgaps are indirect, though rutile also includes a direct forbidden transition. The valence band is derived from O 2p orbitals, while the conduction band originates from Ti 3d orbitals. The crystal field created by six oxygen atoms causes the 3d states to split into t2g and eg components. This field, along with slight oxygen deficiencies, contributes to n-type doping in the semiconductor material, despite the lack of perfect octahedral symmetry.

Iron oxide (Fe_2O_3), with its narrow bandgap of approximately 2.2 eV in the visible light region, has been reported for applications in both energy storage and photothermal-induced processes. By incorporating these active materials into a single electrode, this study explores whether photo-induced effects can occur in a device configuration and assesses their impact on battery performance.

5.2 Results and discussion

5.2.1 Material characterisation

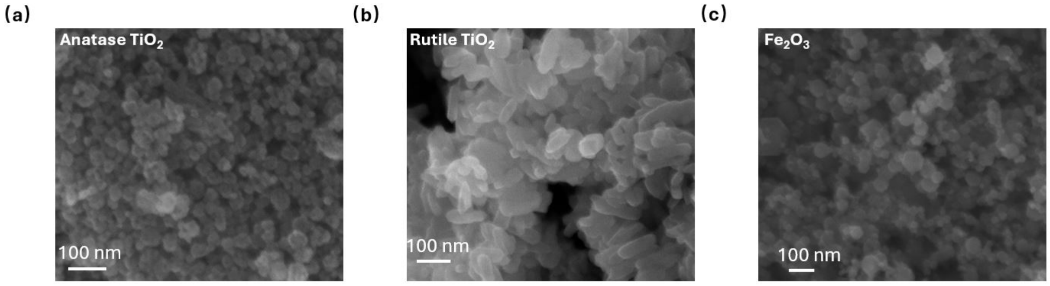

Fig. 5.5 SEM images of commercial (a) anatase TiO_2. (b) Rutile TiO_2. (c) Fe_2O_3 nanoparticles.

Figure 5.5 presents the SEM images of commercial anatase, rutile TiO_2, and Fe_2O_3 nanoparticles. The images reveal clusters of nanoparticles connected together, forming large secondary particles with a porous structure. This morphology is observed consistently across all the commercially acquired samples.

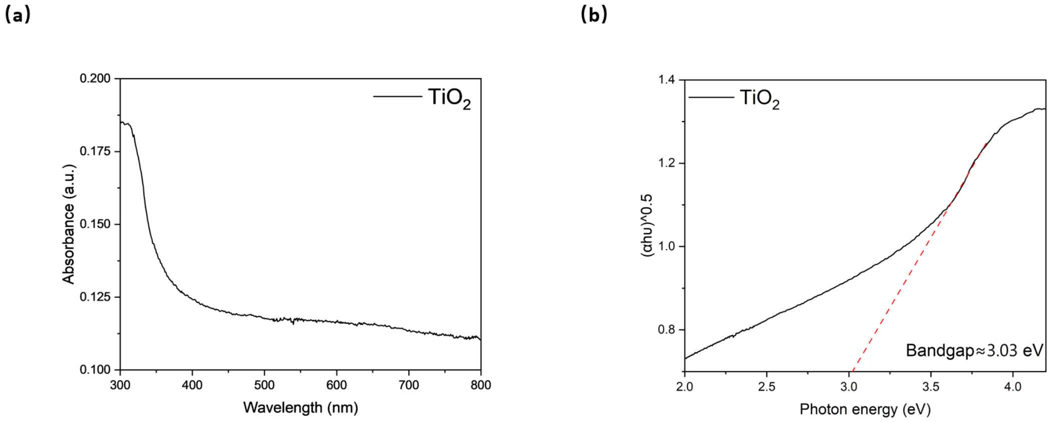

Fig. 5.6 (a) Absorbance spectrum of anatase TiO_2 nanoparticles. (b) Tauc plot of anatase TiO_2 nanoparticles from absorbance spectrum, which an indirect bandgap of $\approx$ 3.03 eV

As shown in Figure 5.6 (a), the UV-Vis spectrum of the anatase TiO_2 shows an elevated absorbance at 300-400 nm wavelength. Moreover, the bandgap is estimated by using a Tauc plot as shown in Figure 5.6 (b). The results report an indirect bandgap of around 3.03 eV, which is similar to literature values.[351]

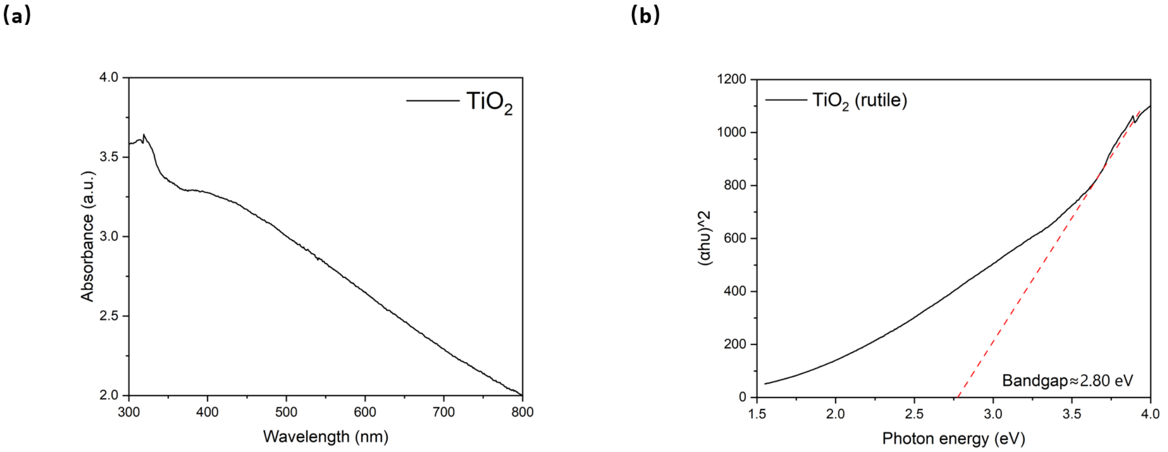

Fig. 5.7 (a) Absorbance spectrum of rutile TiO_2 nanoparticles. (b) Tauc plot of rutile TiO_2 nanoparticles from absorbance spectrum, which a direct bandgap of ≈ 2.80 eV

As shown in Figure 5.7 (a), the UV-Vis spectrum of the rutile TiO_2 shows the highest absorbance at 320 nm wavelength. Apart from that, the bandgap is estimated by using a Tauc plot as shown in Figure 5.7 (b). The results report a direct bandgap of around 2.80 eV, the value agrees with the literature.[351]

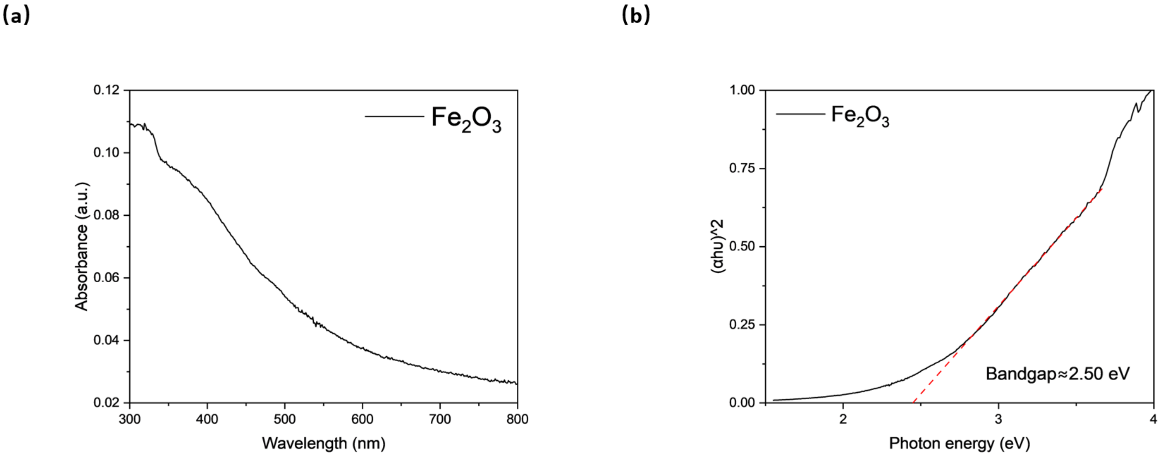

Fig. 5.8 (a) Absorbance spectrum of Fe_2O_3 nanoparticles. (b) Tauc plot of Fe_2O_3 nanoparticles from absorbance spectrum, which an indirect bandgap of ≈ 2.5 eV

As depicted in Figure 5.8 (a), the UV-Vis spectrum of Fe_2O_3 exhibits absorbance across the wavelength range of 300 to 800 nm with the highest absorbance at around 300 nm.

Furthermore, the estimation of the bandgap, depicted in Figure 5.8 (b) using a Tauc plot, reveals a direct bandgap of approximately 2.5 eV, which is close to literature values.[352]

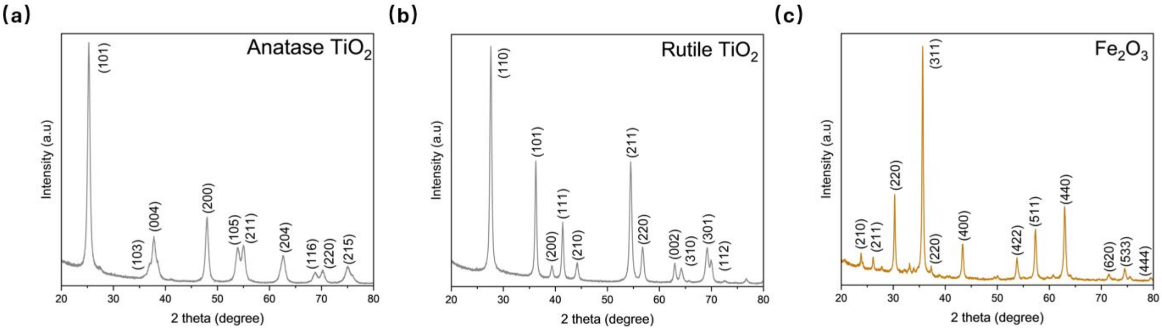

Fig. 5.9 XRD of (a) anatase TiO_2. (b) Rutile TiO_2. (c) γ-Fe_2O_3 nanoparticles.

The XRD pattern of anatase TiO_2, as shown in Figure 5.9 (a), displays characteristic diffraction peaks consistent with its crystal structure. Anatase TiO_2 has a tetragonal crystal structure with space group I41/amd (D4h). The prominent peaks observed correspond to the (101), (004), (200), and (105) crystallographic planes of anatase TiO_2. The intense and narrow peaks indicate the high crystallinity of the sample. Additionally, no significant peaks associated with other phases are observed, confirming the purity of the anatase TiO_2 sample. The XRD pattern of rutile is presented in Figure 5.9 (b), rutile TiO_2 has a tetragonal crystal structure with space group P42/mnm (D4h). There are mainly four characteristic sharp peaks corresponding to the interatomic distances within the crystal lattice including the (110) peak at around 27.5°, the (101) peak at around 36.1°, the (111) peak at around 41.2° and the (211) peak at around 54.3°. These peaks are corresponding to its tetragonal structure. The sharp shape and high intensity also show that the rutile TiO_2 has no major defects with high purity. The XRD pattern of γ-Fe_2O_3, presented in Figure 5.9 (c), exhibits characteristic diffraction peaks indicative of its crystal structure. Notable peaks are observed at 2θ angles corresponding to the (311), (400), (511), and (440) crystallographic planes of γ-Fe_2O_3. These sharp and well-defined peaks signify the high crystallinity of the sample. Furthermore, no discernible peaks associated with other phases are detected, affirming the purity of the γ-Fe_2O_3 sample.

The interdigitated electrode(IDE) was first scanned between a voltage window from -2V to 2V at 10 mV/s under different types of illumination. By simply dropcasting the active material on the IDEs, measuring the current shifts vs. scanned potential under both dark and light conditions can help us solely understand the photothermal effect of metal oxides without the additives (e.g. Super-P carbon black, PVDF) or the current collector. Based on the working principle of the photo-thermal effect, the energy of the incident photon must exceed the bandgap of anatase TiO_2 which is 3.03 eV. Therefore, only wavelength lower than approximately 410 nm can generate photocharge carriers. As shown in Figure 5.10 (a), the current profiles showed increments for both blue LED and solar simulators with 1 SUN illumination. Surprisingly, the blue LED shows a moderate shift compared to the dark conditions even though the peak wavelength of the photons is 470 nm (2.64 eV).

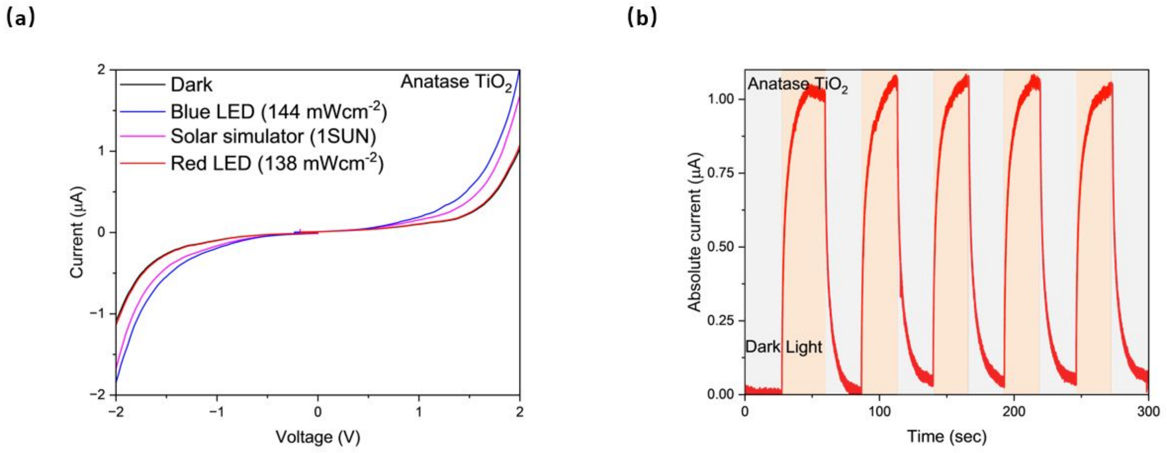

Fig. 5.10 (a) Current-voltage curves of the planar Au-Anatase TiO_2-Au IDE in dark and illuminated conditions. (b) Response current of the Au-Anatase TiO_2-Au IDE under alternating dark and illuminated conditions at 2V under the blue LED.

In order to understand this, we analysed the spectral power for both the solar simulator and the blue LED at the same light intensity as shown in Figure 5.11.

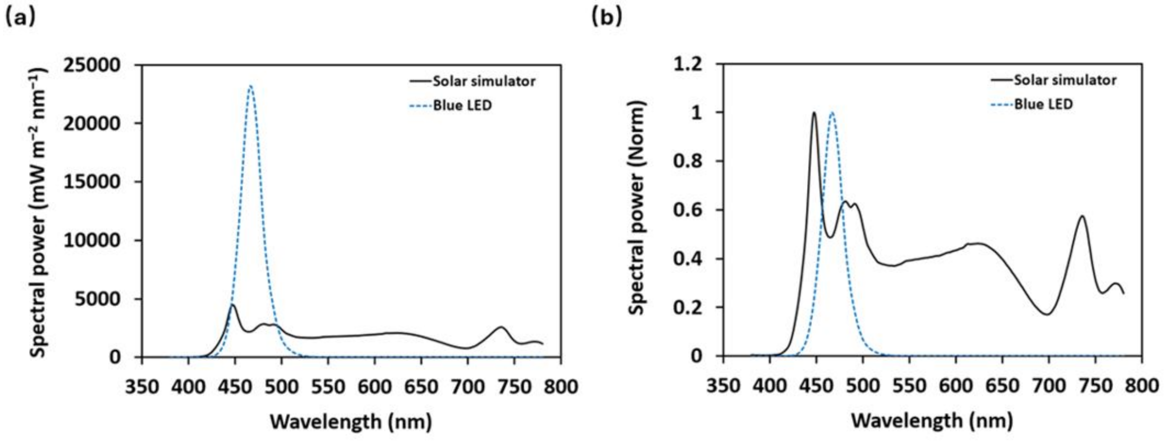

Fig. 5.11 (a) Spectral power for both solar simulator and blue LED as a function of wavelength. (b) Normalized Spectral power for both solar simulator and blue LED as a function of wavelength. (66.4 mW cm^{-2} for solar simulator and 69.2 mW cm^{-2} for blue LED)

As shown in Figure 5.11 (a), it is worth noticing that the light intensity at the short wavelength region is much higher with blue LED than that of the solar simulator at a similar total light intensity. By normalizing the spectral power as shown in Figure 5.11 (b), The peak wavelength of the blue LED is around 470 nm which is slightly red-shifted than that of the solar simulator but the overall photon energy input is high for the blue LED light source. Hence, there are two possible reasons for causing a larger shift in the I-V curve for blue LED: first, the blue LED can also emit photons with shorter wavelengths but with a much higher intensity than the solar simulator. Second, the defect in anatase TiO_2 introduce electronic states that fall within the bandgap. Both effects can contribute to the photothermal effect, leading to heat generation and the reduction of resistance in the device. The chronoamperometry test was done as shown in Figure 5.10 (b), a bias voltage of 2V is applied at the IDE and the current is measured under alternating dark and light conditions. Under different durations of the blue LED, the elevated current can be observed. The current curve looks very thermal-dominated because the current is reduced very slowly with illumination and the current with longer illumination for the first two cycles keeps increasing, possibly due to the heat accumulation. This heat accumulation is mainly due to the photo-thermal effect of anatase TiO_2. In our experiment, only the solar simulator and the blue LED can lead to a positive current response. The higher enhancement from the solar simulator compared to the blue LED also results from the IR heating of the IDE.

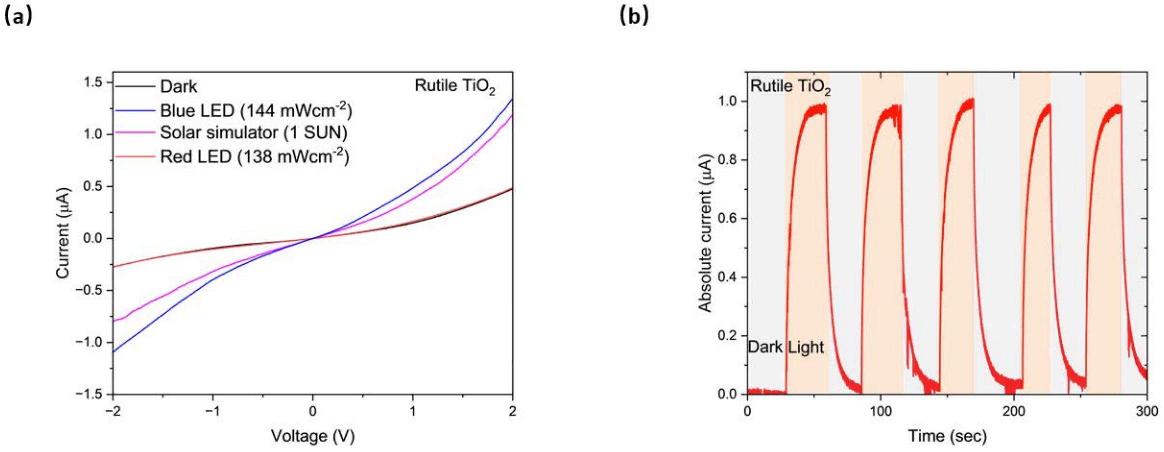

Fig. 5.12 (a) Current-voltage curves of the planar Au-rutile TiO_2-Au IDE in dark and illuminated conditions. (b) Response current of the Au-rutile TiO_2-Au IDE under alternating dark and illuminated conditions at 2V under blue LED.

As shown in Figure 5.12 (a), the CV profiles for rutile TiO_2 show various shifts under different types of illumination. Under red LED, the curve has no shift, this is due to the photon energy of the LED being relatively lower than the bandgap. In comparison, the curve shifts the most under blue LED due to the higher photon energy. Surprisingly, the solar simulator shows a moderate curve shift even though these light sources have a broad spectrum. The reason is possible because the intensity of the solar simulator at a shorter wavelength is low compared to the blue LED. Therefore, the overall photon energy input is high for the blue LED light source. The CA test was then performed under blue LED as shown in Figure 5.12 (b) with a 2V bias voltage applied, the current shows an increase under blue LED illumination. Again the shape of the curve is mainly thermal-dominated due to the slow reduction of the current without illumination.

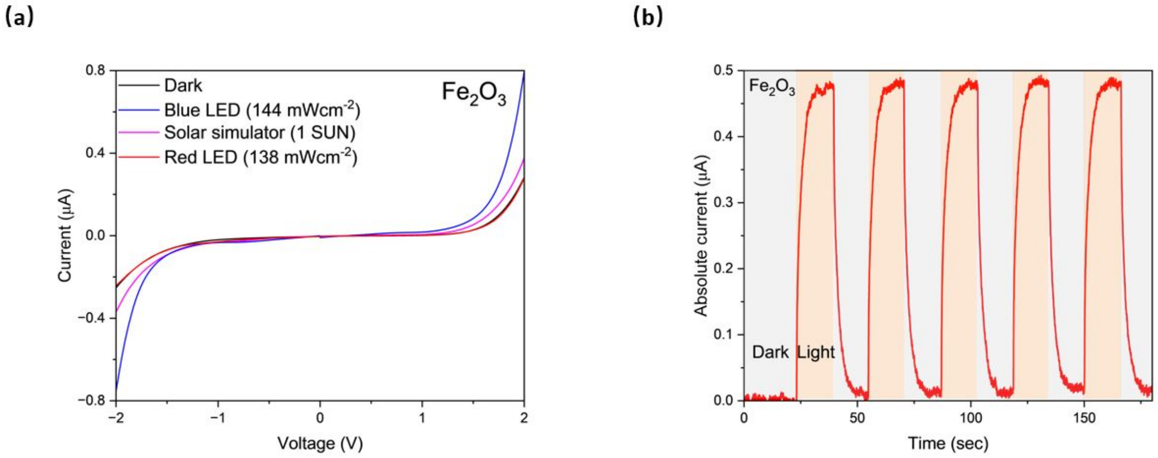

Fig. 5.13 (a) Current-voltage curves of the planar Au-Fe_2O_3-Au IDE in dark and illuminated conditions. (b) Response current of the Au-Fe_2O_3-Au IDE under alternating dark and illuminated conditions at 2V under blue LED.

As shown in Figure 5.13 (a), the Fe_2O_3-based IDE was tested by sweeping the voltage between -2V and 2V at a scan rate of 10 mV/s under various light sources. Among the three types of light sources, the red LED, with a photon energy of approximately 1.85 eV, has energy lower than the bandgap of Fe_2O_3. This is reflected in the current-voltage curve, where the magnitude of the CV curve remains roughly identical to the dark CV curve, and no enhancement is observed. In contrast, under blue LED and solar simulator illumination, the CV curve magnitudes increase. The enhancement under the blue LED and solar simulator is greater than that under the white LED. However, it is worth noting that the solar simulator also emits IR radiation, which can heat the IDE.

The IDE was then tested under a bias voltage of 2V with alternating blue LED illumination, as shown in Figure 5.13 (b). The results indicate a clear increase in current under illumination. In dark conditions, the current decreases very slowly, suggesting that these effects are predominantly thermally driven. Compared to TiO_2, the current curves for Fe_2O_3 appear more stable, possibly due to its narrower bandgap.

Overall, the I-V results indicate that all three metal oxides exhibit photoactivity, as evidenced by the shift in magnitude under illumination. The current-time curves suggest that the photo-induced effects are predominantly thermally driven. Further electrochemical testing is necessary to evaluate the impact of the photothermal effect on battery performance and to explore the potential contribution of photo-generated charge effects.

5.2.2 Electrochemical performance measurement for anatase, rutile TiO_2 and Fe_2O_3

Anatase TiO_2

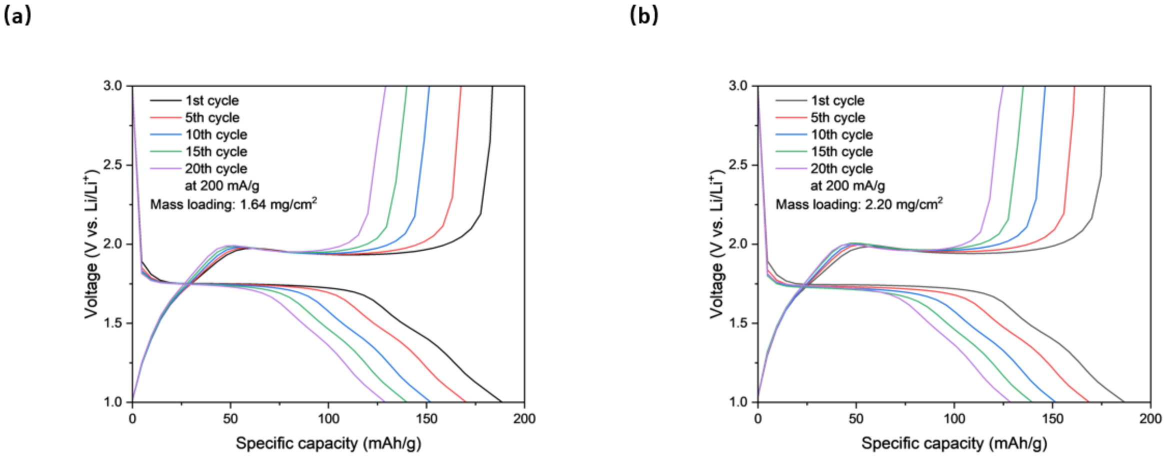

Fig. 5.14 GCD tests of anatase TiO_2/Li half cell at a current density of 200 mA/g (a) With a mass loading of 1.64 mg/cm^2. (b) With a mass loading of 2.20 mg/cm^2.

First, GCD tests are done in order to investigate the electrochemical performance of the anatase TiO_2/Li half cells. As shown in Figure 5.14, both batteries are measured at the same current density of 200 mA/g for 20 cycles but the mass loading for each cell is different. Both cells show similar capacity and voltage profiles with an initial capacity of approximately 185 mAh/g and a flat plateau at around 1.7 V vs. Li/Li$^+$. However, the capacity fades quickly after 20 cycles with a capacity retention of 68.1%. This stability can be problematic for further photo-enhanced measurement, therefore I will need to solve the degradation issue of the batteries. Here are a few methods I intended to do improve the capacity retention:

1. Decreasing the mass loading to 1 mg/cm^2 or 0.5 mg/cm^2. Some small cracks can be observed on the surface of the drop-casting electrodes after drying.

2. Decreasing the current density slightly to 50 mA/g or 100 mA/g.

3. Changing the voltage to a smaller region, for example, 1.1 V to 2.5 V.

I then applied those changes and performed another GCD test with a potential window between 1.1V and 2.5V under the current density of 50 mA/g. As shown in Figure 5.15

(a) and (b), two coin cells were fabricated with mass loading around 0.5 mg/cm^2 and 1 mg/cm^2, respectively. I can clearly see an improvement in capacity retention. The capacity is maintained at around 88 % for the 0.527 mg/cm^2 electrode and 85% for the 0.980 mg/cm^2 after 20 cycles. However, lower mass loading does not seem to have a large impact on cycling performance but decreases the specific capacity. Therefore, I controlled the mass loading of the active material at 1 mg/cm^2.

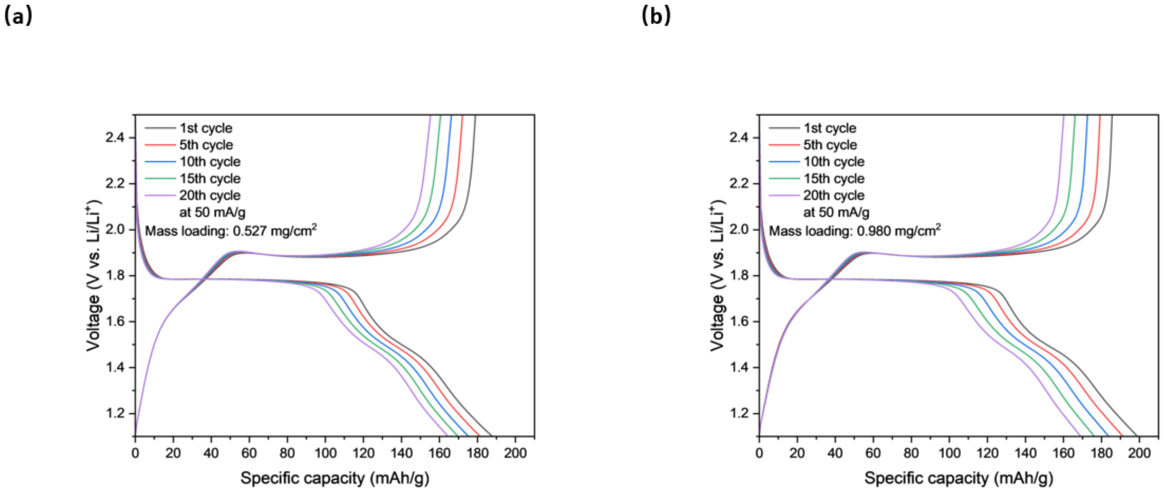

Fig. 5.15 GCD tests of anatase TiO_2/Li half cell at a current density of 50 mA/g (a) With a mass loading of 0.527 mg/cm^2. (b) With a mass loading of 0.980 mg/cm^2.

In order to further improve the stability of the anatase TiO_2/Li half cells, I tested the cell at other voltage windows from 1.5V to 2.5 V and 1.7 V to 2.5 V as shown in Figure 5.16 (a) and (b).

With an increased cut-off voltage, the cycling performance of the cell shows significant improvement. In the voltage window ranging from 1.5 V to 2.5 V, the capacity retention over 20 cycles is approximately 92.6%, with an initial capacity of 123.1 mAh/g. Narrowing the voltage window further to 1.7 V to 2.5 V results in an improved capacity retention of 95.7%, with an initial capacity of 134.1 mAh/g. These findings suggest that a stable voltage window from 1.7 V to 2.5 V is optimal for the designed anatase TiO_2 Li-ion battery. However, the specific capacity observed is lower compared to literature values, possibly due to the higher lower-cutoff voltage allowing only partial lithium insertion. Given the primary focus on stability in investigating the photothermal effect, this voltage window will be used for further electrochemical characterization.

Cyclic voltammetry was performed within the specified voltage window across a range of scan rates, as shown in Figure 5.17. Figure 5.17 (a) presents the cyclic voltammogram for anatase TiO_2, measured within a voltage range of 1.7 to 2.5 V at a sweep rate of 0.1

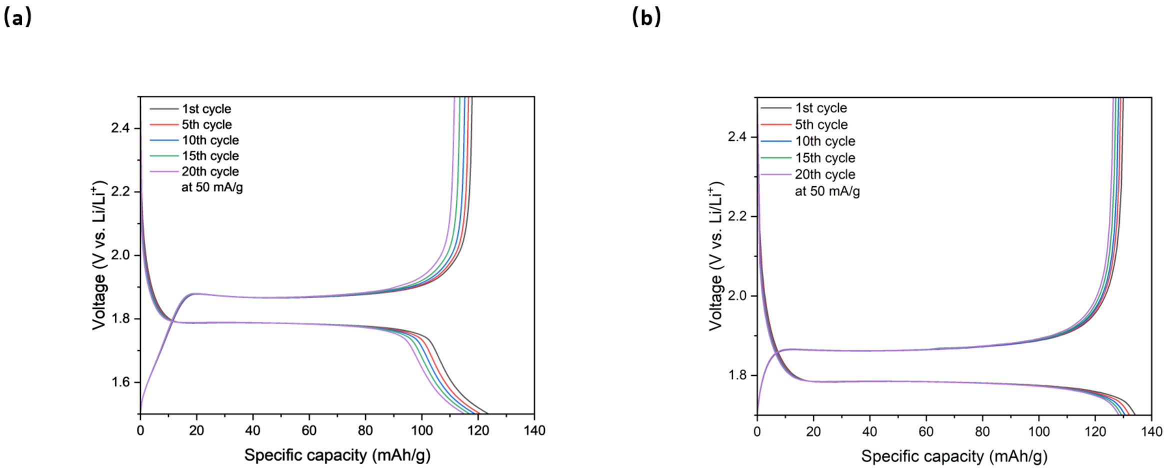

Fig. 5.16 GCD tests of anatase TiO_2/Li half cell at a current density of 50 mA/g (a) With voltage window from 1.5V to 2.5V vs. Li/Li$^+$. (b) With voltage window from 1.7V to 2.5V vs. Li/Li$^+$.

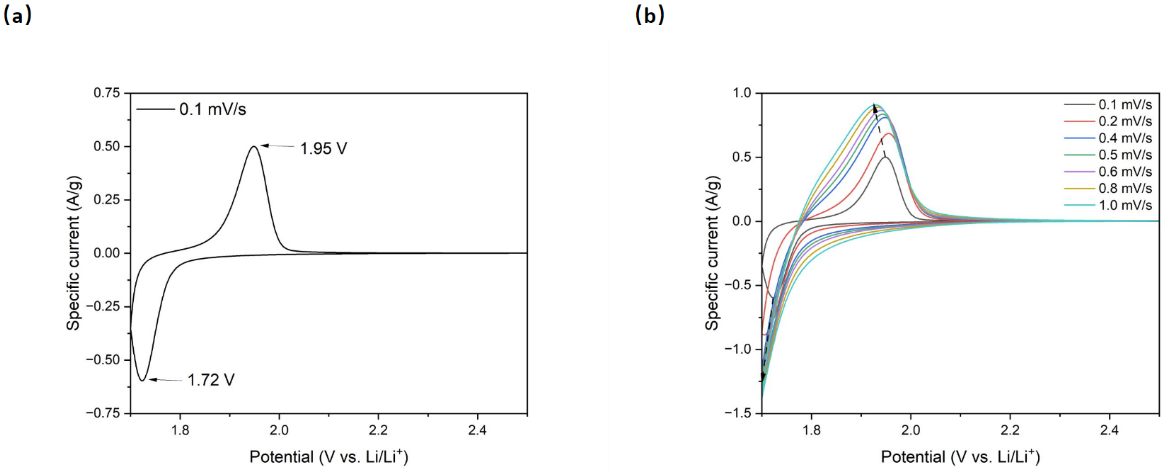

Fig. 5.17 (a) CV measurement for anatase TiO_2 Li-ion half cell at 0.1 mV/s (b) CV measurement at other scan rates.

mV/s. During the first cathodic sweep, a peak at 1.72 V is observed, corresponding to the insertion of lithium ions into the TiO_2 matrix and the structural transition of TiO_2 from a tetragonal to an orthorhombic Li_xTiO_2 phase, where x represents the degree of lithium insertion. Conversely, the anodic peak at 1.95 V is associated with the extraction of lithium from the TiO_2 matrix.

Additional CV scans were conducted at higher scan rates ranging from 0.2 mV/s to 1.0 mV/s, as shown in Figure 5.17 (b). The CV curves align with the plateaus observed in the GCD tests, and no changes in the peak shapes were detected, indicating consistent electrochemical behavior across varying scan rates.

In regards to long-term stability, the cells were tested under a higher current density of 100 mA/g over 200 cycles under dark conditions. As shown in Figure 5.18, the capacity retention for the voltage window between 1.1 and 2.5 V is around 35.2% over 200 cycles. With a lower voltage window between 1.5 V and 2.5 V, the capacity retention is approximately 35.3%. However, at the voltage window between 1.7 V and 2.5 V, the capacity retention is largely improved to 68.5% over 200 cycles. The low Coulombic efficiency for the first few cycles is due to the side reaction on the carbon felt as we discussed previously.

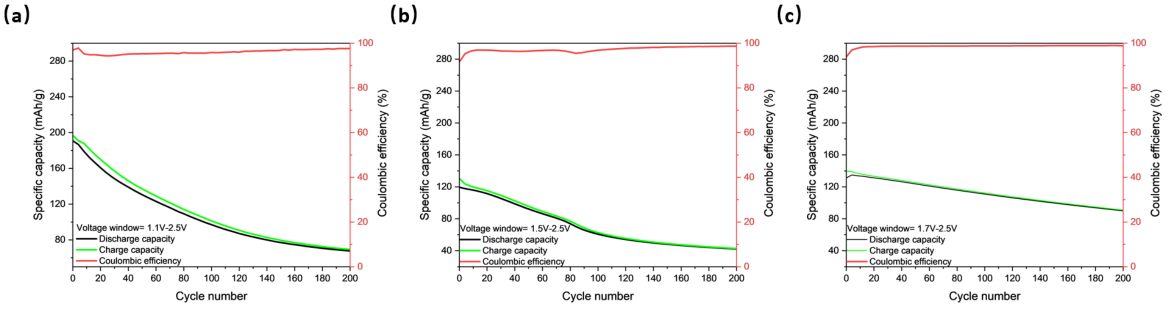

Fig. 5.18 (a) Long-term cycling test over 200 cycles at 100 mA/g for voltage window from 1.1 V to 2.5V. (b) Long-term cycling test over 200 cycles at 100 mA/g for voltage window from 1.5 V to 2.5V. (c) Long-term cycling test over 200 cycles at 100 mA/g for voltage window from 1.7 V to 2.5V.

Rutile TiO_2

For rutile TiO_2, a voltage window of 1.0 V to 3.0 V was first selected and the GCD tests were done at a current density of 25 mA/g as shown in Figure 5.19 (a). The voltage window is selected because it is most commonly used in the literature.[353] The mass loading of the active material is controlled at 1 mg/cm^2 The cells showed an initial capacity of 63.4 mAh/g and stayed very stable at around 60.0 mAh/g after 50 cycles. The GCD tests were also done at a range of current density as shown in Figure 5.19 (b) from 25 mA/g to 200 mA/g. At

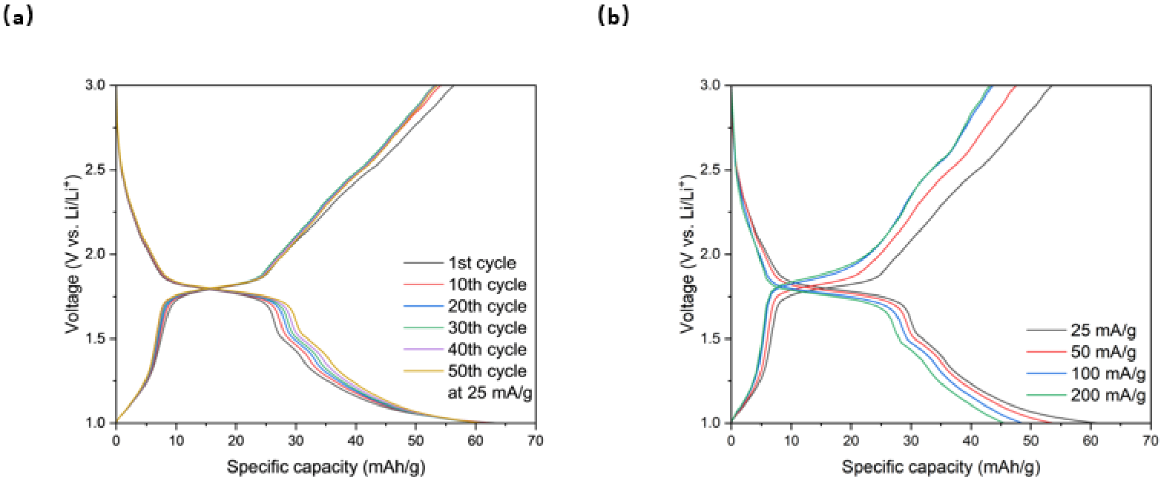

Fig. 5.19 (a) GCD tests of rutile TiO_2/Li half cell at a current density of 25 mA/g at selected cycles. (b) GCD tests of rutile TiO_2/Li half cell at a range of current densities.

the highest current density of 200 mA/g, the cells showed a specific capacity of around 45.0 mAh/g. The difference in lithium-ion storage capacities between rutile and anatase forms of TiO_2 is attributed to their crystal structures and electronic properties. Both rutile and anatase are polymorphs of TiO_2, meaning they have the same chemical composition but different crystal structures. This structural difference leads to varied electrochemical performance. Compared to anatase TiO_2, rutile can only accommodate a limited amount of Li-ions due to the low insertion coefficient.[354] Apart from that, surface Area, porosity and particle size can also affect the capacity, the commercial-bought anatase TiO_2 has an average particle size < 25 nm and the commercial-bought rutile TiO_2 has an average particle size < 100 nm. Therefore, the anatase TiO_2 has higher specific surface areas and porosities compared to rutile TiO_2. A higher surface area allows for more lithium-ion interaction sites, enhancing the lithium storage capacity.

After that, the CV measurements were done at a range of voltage scan rates between 1.0 V to 3.0 V as shown in Figure 5.20. At the lowest scan rate of 0.1 mV/s in Figure 5.20 (a), two peaks can be observed in the cathodic reaction at 1.75 V and 1.25 V. The peak at 1.25 V disappeared in the following scans due to the irreversible reaction in rutile TiO_2. One anodic peak can be observed at 1.80 V. The peaks at 1.75 V and 1.80 V correspond to the insertion and de-insertion of the Li ions within the rutile TiO_2 crystal structure. The CV measurements were also done at higher scan rates from 0.2 mV/s to 1.0 mV/s as shown in Figure 5.20 (b), the cell shows stable electrochemistry and the peak shifts due to the magnitude of the scan rate. When the scan rate is low, the ions in the electrolyte and the active components of your prepared samples have sufficient time to interact. This enhanced interaction raises the

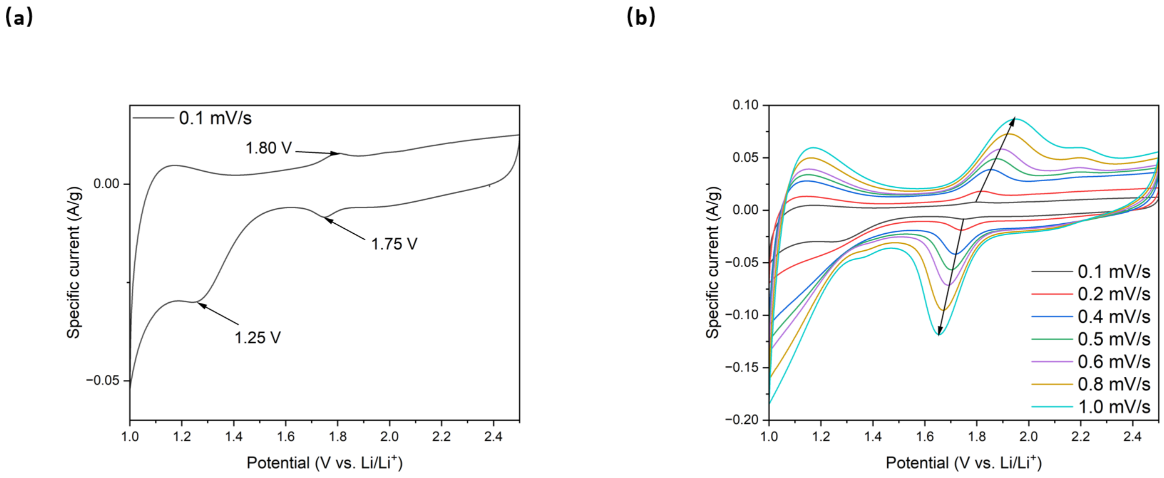

Fig. 5.20 (a) CV measurement for rutile TiO_2 Li-ion half cell at 0.1 mV/s (b) CV measurement at other scan rates.

likelihood of redox reactions occurring. However, at high scan rates, the interaction between these components is limited due to the shorter duration of contact, which in turn hampers the various reactions that could otherwise take place between them.

Overall, the rutile TiO_2 Li-ion batteries show good capacity retention of 94.6% over 50 cycles. Despite the low specific capacity recorded, rutile TiO_2 has great potential in photothermal-induced batteries as the heat generation can improve the sluggish Li-ion de-/insertion and low electric conductivity.

Fe_2O_3

The GCD measurement was initially conducted for the Fe_2O_3/Li-ion half cell within a voltage range of 0.5 V to 3.0 V at a current density of 100 mA/g. As shown in Figure 5.21 (a), the cell exhibited a high initial capacity of approximately 700 mAh/g. However, the specific capacity declined rapidly and stabilized after around 50 cycles, maintaining a capacity of approximately 90 mAh/g after 400 cycles, as illustrated in Figure 5.21 (b). Overall, the cell demonstrated a long-term capacity retention of approximately 8.7

The significant capacity loss can be attributed to several factors, including the formation of the solid electrolyte interphase (SEI) layer, the irreversible breakdown of the electrolyte, and the partial extraction of lithium from the active material [355]. This capacity loss appears inevitable; however, as previously discussed, when the potential vs. Li/Li^+ drops below 1.0 V, the contribution of carbon felt to the overall capacity becomes significant. To address this issue and improve stability and formation cycles, the cut-off voltage was increased to 0.8-2.5 V, and the GCD measurement was repeated under the same current density.

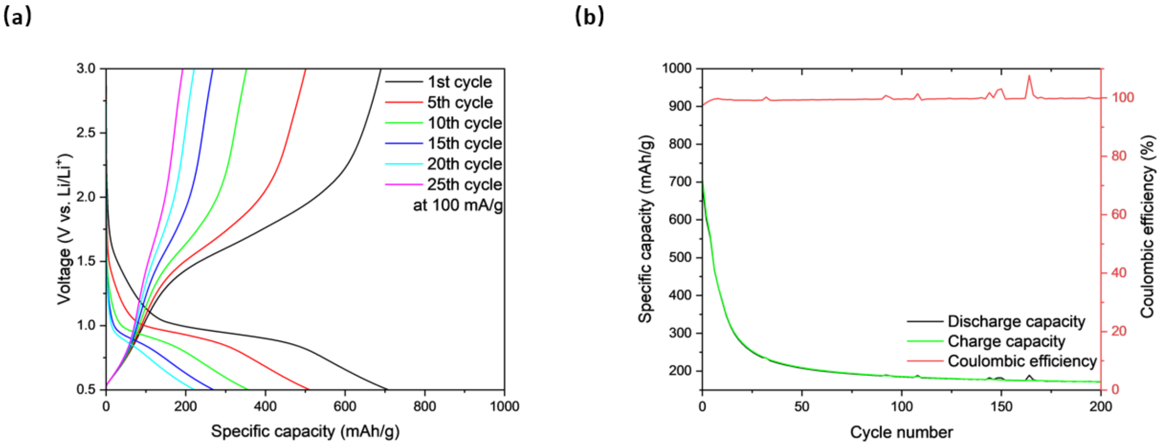

Fig. 5.21 (a) GCD tests of Fe_2O_3/Li half cell at a current density of 100 mA/g at selected cycles. (b) Long-term cycling performance of Fe_2O_3/Li half cell at a current density of 100 mA/g.

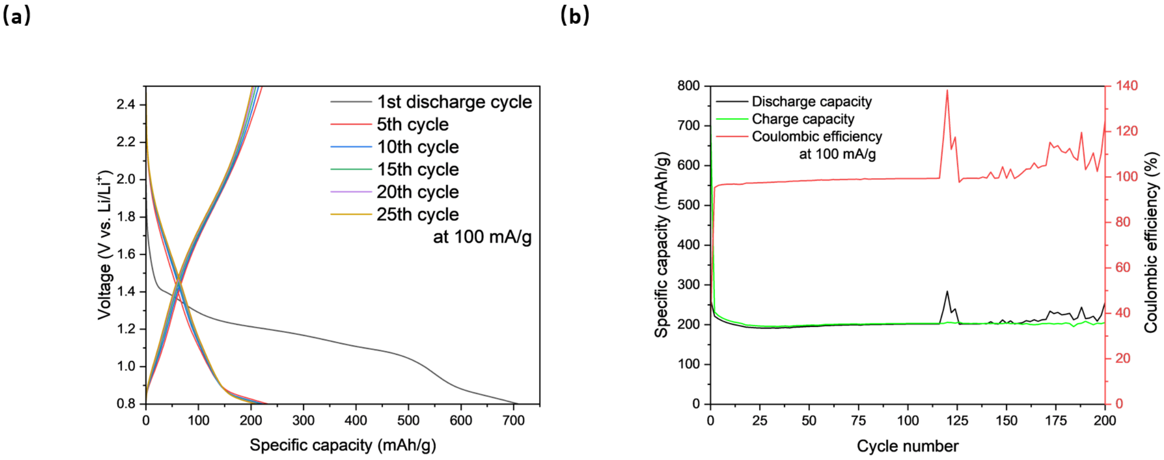

Fig. 5.22 (a) GCD tests of Fe_2O_3/Li half cell at a current density of 100 mA/g at selected cycles. (b) Long-term cycling performance of Fe_2O_3/Li half cell at a current density of 100 mA/g.

As shown in Figure 5.22 (a), the formation cycles are much shorter by using a smaller voltage window. After the initial discharge cycle, both the charge and discharge capacity remain at a stable value of around 200 mAh/g. The cell also showed excellent long-term stability over 200 cycles as shown in Figure 5.22 (b) with a capacity retention of 88.6% from the 2nd cycle. However, I noticed some sharp increase in the Coulombic efficiency after 150 cycles, this is possibly due to the instability of the electrolyte.

5.2.3 Investigation on photo-thermal effect for TiO_2 and Fe_2O_3 Li-ion batteries

To investigate how light interacts with the photocathode inside the battery, an impedance-based method was employed to determine the internal temperature of the devices. The cells were tested under various light intensities, and the real part of the impedance at 100 kHz was recorded. This frequency was chosen as it represents the highest measurable frequency on the VMP-3 Multichannel Potentiostat and minimizes the impact of the state of charge on the results, allowing the observed trends to be attributed solely to temperature effects [1].

After testing the coin cells under light, they were placed in a temperature-controlled oven and subjected to measurements across a range of temperatures. To ensure accuracy, the cells were stabilized in the oven for 1 hour after each temperature adjustment before beginning the measurement. Using the derived fitting equation for the relationship between temperature and the real part of the impedance at 100 kHz, the internal temperature under various light intensities was calculated.

Additionally, efforts were made to distinguish between photothermal and photocharging effects by analyzing the band alignment of each battery system. By applying a bias voltage, it was possible to transition the photothermal effect into a photo-assisted charging effect, providing further insights into the mechanisms at play.

Anatase TiO_2

As shown in Figure 5.23, the impedance at 100 kHz is measured as a function of light intensity and oven temperature, both datasets were fitted in order to calculate the correction between.

As previously discussed, the impedance measured at 100 kHz under varying light intensities was incorporated into the fitted equation from the impedance-temperature relationship presented in Figure 5.23 (b). The error bars were calculated based on three repeated impedance measurements for the same cell. As depicted in Figure 5.24, the internal temperature of the anatase TiO_2 coin cell under blue LED illumination was estimated. The results

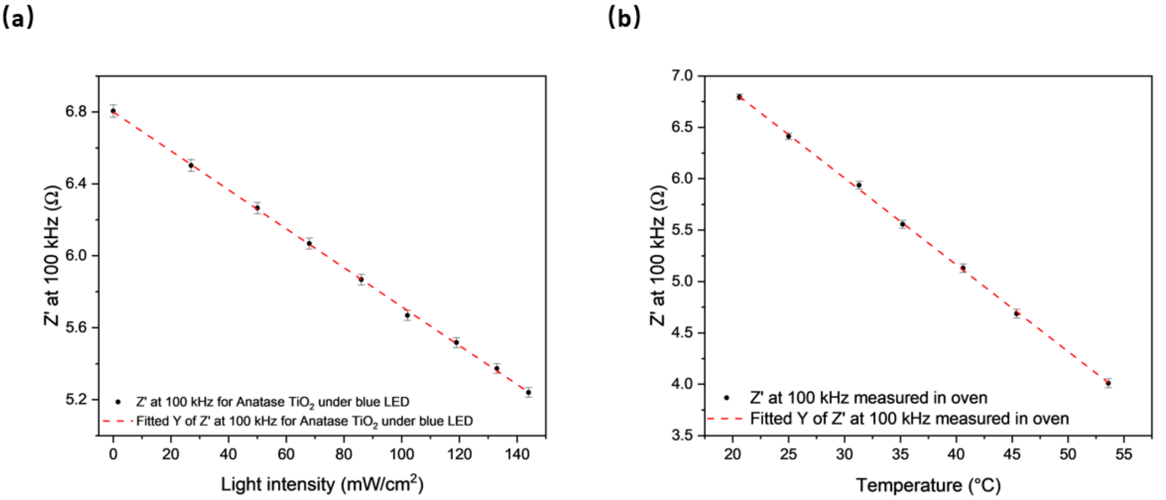

Fig. 5.23 (a) Impedance at 100 kHz as a function of light intensity (Blue LED). (b) Impedance at 100 kHz as a function of oven temperature at 50% SOC.

indicate that the temperature increases approximately linearly with increasing light intensity, with a maximum estimated internal temperature of around 39.1 °C at a light intensity of 144 mW/cm^2.

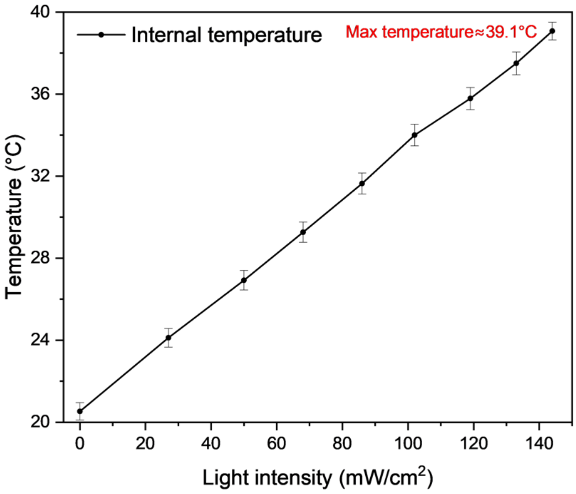

Fig. 5.24 Internal temperature as a function of light intensity for anatase TiO_2 under blue LED

A chronoamperometry test was conducted for the anatase TiO_2 Li-ion battery under varying light intensities. The cell was initially discharged at a constant current of 100 mA/g to 1.0 V vs. Li/Li$^+$. Subsequently, a constant voltage hold of 1.0 V was applied until the discharge current exceeded -5.0 μA. Finally, a constant charging voltage of 2.0 V was applied for 60 seconds. As shown in Figure 5.25 (a), the current was recorded every 0.1 seconds

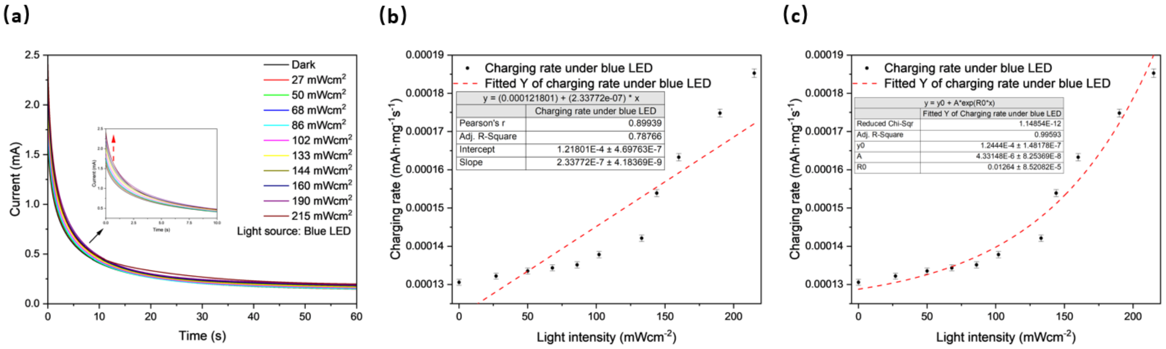

y = (0.000121801) + (2.33772e-07) * x	
	Charging rate under blue LED
Pearson's r	0.89939
Adj. R-Square	0.78766
Intercept	1.21801E-4 ± 4.69763E-7
Slope	2.33772E-7 ± 4.18369E-9

y = y0 + A*exp(R0*x)	
	Fitted Y of Charging rate under blue LED
Reduced Chi-Sqr	1.14854E-12
Adj. R-Square	0.99593
y0	1.2444E-4 ± 1.48178E-7
A	4.33148E-6 ± 8.25369E-8
R0	0.01264 ± 8.52082E-5

Fig. 5.25 (a) Chronoamperometry curves at different light intensities (Blue LED) during constant voltage hold charging at 2.0 V vs. Li/Li$^+$. Charging rate calculated from integration of chronoamperometry curves as a function of light intensity (Blue LED) fitted by (b) linear function. (c) Arrhenius-type.

during the constant voltage charging period. The current decreased rapidly over time for each light intensity, with a clear shift in the curve and an increase in initial current as light intensity increased.

The area under the chronoamperometry curves for each light intensity was calculated and then divided by the mass loading and charging time to determine the charging rate. The charging rate was plotted as a function of light intensity, as illustrated in Figures 5.25 (b) and (c). By analyzing the trend, it is possible to discern whether the reaction is dominated by photothermal or photocharging effects. In photo-electrochemical reactions, a photothermal-dominated reaction follows an Arrhenius-type curve, while a photocharging-dominated reaction exhibits a linear relationship between reaction rate and light intensity [310].

The results clearly show that the charging rates increase exponentially with higher light intensity rather than linearly. This is further supported by the fitting analysis in Figures 5.25 (b) and (c), where the R-square value for the Arrhenius-type fitting is 0.97, significantly higher than the 0.79 obtained for the linear fitting. This confirms that the reaction is primarily photothermal-dominated.

Although the results indicate that the photothermal effect predominantly drives the observed phenomena in this experiment, the potential contribution of the photocharging effect remains a question. Previous studies have reported that lithiated TiO_2 exhibits enhanced charge separation and transfer, attributed to lattice distortion-induced internal electric fields [356]. Furthermore, several reports have noted a reduction in the bandgap of anatase TiO_2 during the lithiation process, which may influence its photoelectrochemical behavior [357].

To further investigate the possible contributions of the photocharging effect, Ultraviolet Photoelectron Spectroscopy (UPS) and UV-vis spectroscopy were conducted on commercial anatase TiO_2 nanoparticles discharged to 1.0 V vs. Li/Li$^+$, as shown in Figure 5.26. The

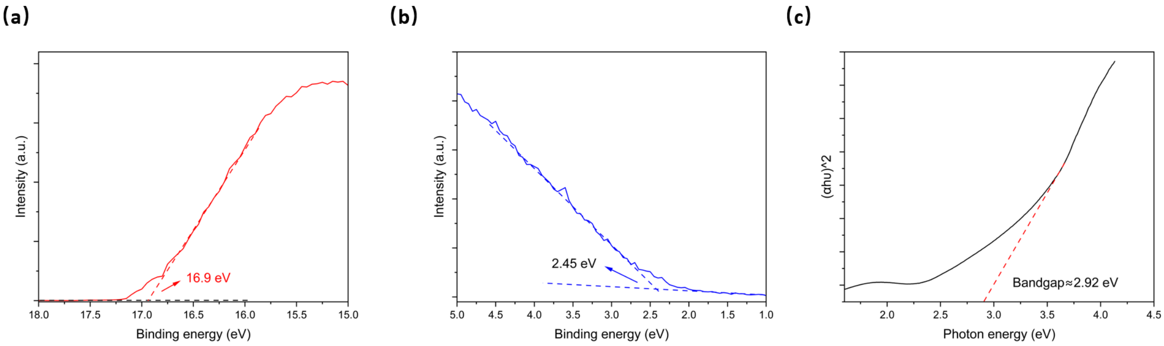

Fig. 5.26 (a) UPS spectra of the intersection to determine the work function. (b) UPS spectra of the intersection to determine the valence band edge. (c) UV-vis spectra of the lithiated anatase TiO_2 at 1.0 V vs. Li/Li$^+$.

combination of UPS and UV-vis spectroscopy provides valuable insights into the band alignment within the photobatteries, aiding in understanding the mechanisms underlying the photothermal and photocharging effects.

In a standard UPS spectrum, two intersections with the baseline typically define the binding energy width (ΔE). This width can be used to determine the valence band energy (E_v) of a semiconductor. Using He I (21.22 eV) as a reference, the valence band energy of lithiated anatase TiO_2 was calculated by subtracting the He I photon energy from the measured ΔE value (ΔE - 21.22 eV). The valence band position for lithiated anatase TiO_2 was determined to be -6.77 eV relative to the vacuum level.

The conduction band position was calculated by adding the determined valence band position (-6.77 eV) to the bandgap of lithiated anatase TiO_2 (2.92 eV), which was derived from the UV-vis spectroscopy results shown in Figure 5.26 (c). This places the conduction band position at -3.85 eV relative to the vacuum level. These findings provide a comprehensive understanding of the band alignment and its implications for photothermal and photocharging effects in the photobattery system.

Based on the comparison with the standard reduction potential of the Li metal anode, the band alignment for lithiated anatase TiO_2 was constructed. This alignment corresponds to the point when the photobattery was discharged to 1.0 V vs. Li/Li$^+$, just before the application of the constant charging voltage, as depicted in Figure 5.27.

The band position for anatase TiO_2 is converted from the physical scale vs. vacuum level to the electrochemical sale vs. standard hydrogen electrode. The conversion is shown in the equation below,

$$E_{SHE} = -(E_{abs} + 4.44) \tag{5.1}$$

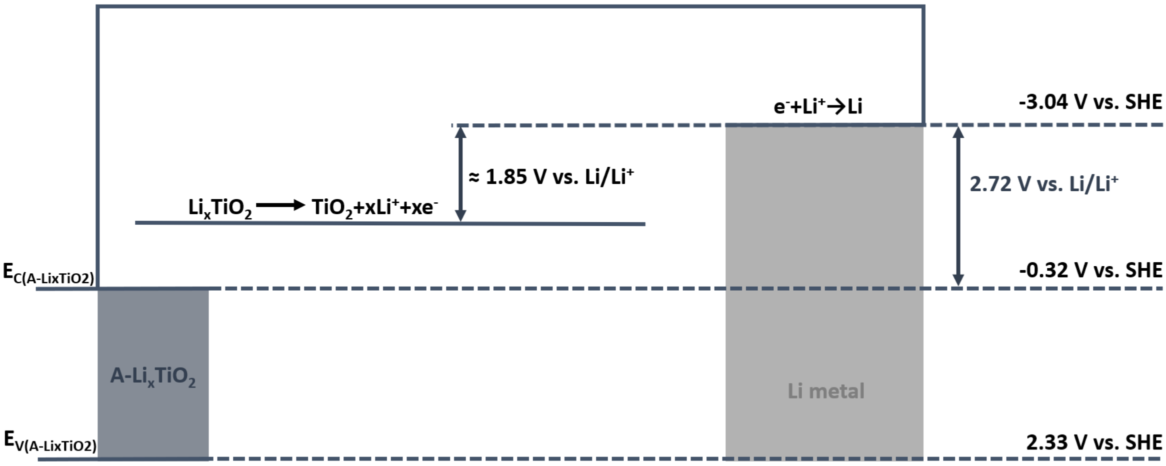

Fig. 5.27 Band alignment between the lithiated anatase TiO_2 photocathode and the Li metal anode.

First, it is important to note the potential of 1.85 V vs. Li/Li$^+$, as shown in Figure 5.27, which corresponds to the main delithiation potential in anatase TiO_2 Li-ion batteries. When a potential higher than this value is applied, charging occurs. In a typical photo-rechargeable battery, this potential is generally lower than the conduction band of the photocathode, allowing photo-generated electrons to spontaneously participate in the photo-charging process. However, in the present case, an energy gap of 2.72 V vs. Li/Li$^+$ exists between the conduction band of anatase TiO_2 and its main delithiation potential. This energy gap must be overcome for photo-generated charges to participate in the electrochemical process. Even when charge separation occurs in the anatase TiO_2/CF photocathode, the energy of photo-generated electrons is insufficient for efficient transport to the anode, limiting their involvement in the reduction of Li ions.

In the scenario of constant voltage charging at 2.0 V vs. Li/Li$^+$, as depicted in Figure 5.28, the charging electrons are derived solely from the delithiation of TiO_2 because the applied potential is insufficient to overcome the energy gap. Consequently, the photo-generated charge carriers undergo recombination, resulting in heat generation, which corresponds to the observed photothermal effect in previous experiments. For anatase TiO_2, the charging rate versus light intensity curve demonstrates an exponential increase with increasing light intensity, indicating that the photothermal effect dominates the charge transfer in the photo-battery, as discussed in Figure 5.25. However, if an external voltage is applied that sufficiently reduces or eliminates the energy gap, it becomes possible for photo-generated electrons to contribute to the reduction of Li ions accumulating at the Li metal anode.

Based on this band alignment, photo-generated charges can be transferred if a potential which is higher than 2.72 vs. Li/Li$^+$ is applied, for example, 3.0 V vs. Li/Li$^+$ is applied to

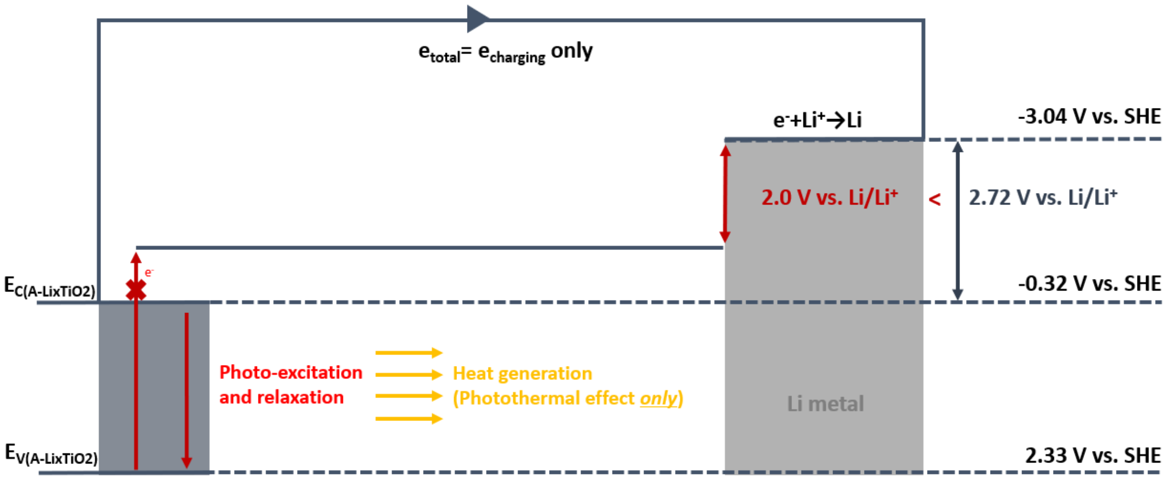

Fig. 5.28 Band alignment between the lithiated anatase TiO_2 photocathode and the Li metal anode at 2.0 V vs. Li/Li$^+$.

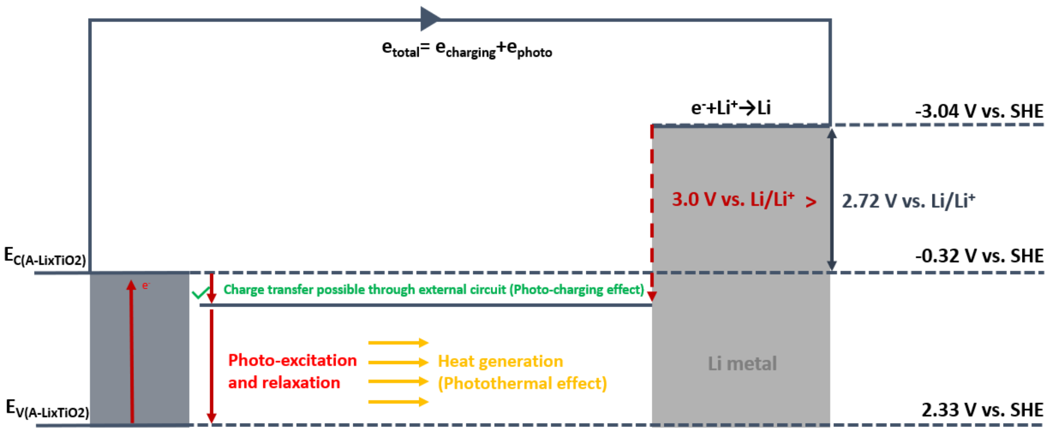

Fig. 5.29 Band alignment between the lithiated anatase TiO_2 photocathode and the Li metal anode at 3.0 V vs. Li/Li$^+$.

the photobattery as shown in Figure 5.29. In this scenario, the photo-generated electrons gained enough energy from the applied external voltage and therefore, the total amount of electrons transferred includes the charging electrons from the delithiation of Li_xTiO_2 and photo-generated electrons.

The chronoamperometry (CA) test was repeated with a modified protocol to validate the hypothesis. The cell was initially discharged at a constant current of 100 mA/g to 1.0 V vs. Li/Li$^+$. A constant voltage hold at 1.0 V was then applied until the discharging current exceeded -5.0 μA. Finally, a constant charging voltage of 3.0 V was applied for 60 seconds. The charging voltage of 3.0 V was selected as it exceeds the potential gap between the conduction band edge and the standard reduction potential of Li metal, while also ensuring safe delithiation of Li_xTiO_2.

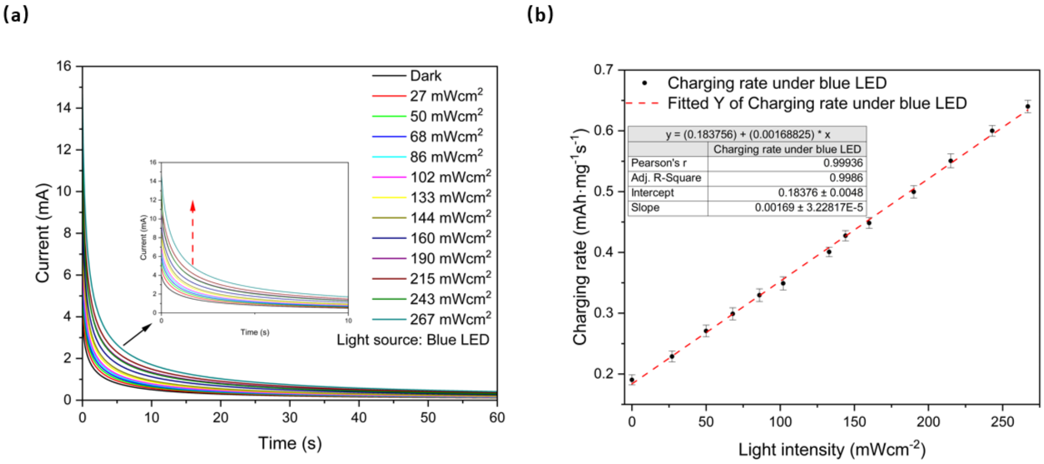

Fig. 5.30 (a) Chronoamperometry curves at different light intensities (Blue LED) during constant voltage hold charging at 3.0 V vs. Li/Li$^+$. (b) Charging rate calculated from integration of chronoamperometry curves as a function of light intensity (Blue LED) fitted by a linear function.

The results were notably distinct, as anticipated, with higher applied voltages more effectively driving photo-generated electrons to the Li metal anode. In Figure 5.30 (a), a similar decay trend in the current curves was observed when a 3.0 V vs. Li metal potential was applied. However, the initial current was significantly higher than in the previous results obtained with a 2.0 V vs. Li metal potential.

The charging rate was then plotted as a function of light intensity, as shown in Figure 5.30 (b). A linear trend was observed, indicating that the charging process under increasing light intensity is dominated by the photo-charge effect rather than the photo-thermal effect. This finding aligns with predictions based on the band alignment of anatase TiO_2 and the Li metal anode. When the applied bias voltage exceeded the potential gap between the conduction band of anatase TiO_2 and the reduction potential of Li metal, photo-generated charge carriers were able to transfer to the Li metal anode. This enabled the reduction of Li ions, bypassing recombination and heat generation, which would otherwise lead to a photothermal effect. This behavior confirms the influence of band alignment and applied voltage on the dominance of the photo-charge effect.

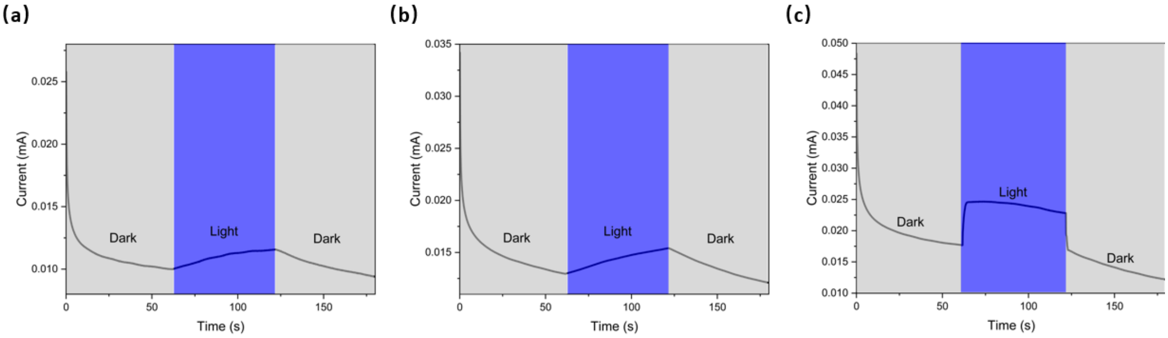

Fig. 5.31 Chronoamperometry curves under pulsed light (Blue LED) during constant voltage hold charging at (a) 2.0 V vs. Li/Li$^+$. (b) 2.5 V vs. Li/Li$^+$. (c) 3.0 V vs. Li/Li$^+$.

To further distinguish between the photo-charge and photothermal effects, a controlled chronoamperometry (CA) test was conducted under pulsed light conditions, as shown in Figure 5.31. The protocol was similar to the previous test, with the only difference being in the last constant voltage charging step, where the cells were charged under constant voltage hold at 2.0 V, 2.5 V, and 3.0 V vs. Li/Li$^+$. During this step, the blue LED was alternately switched off for 60 seconds and on for the next 60 seconds.

At 2.0 V and 2.5 V vs. Li/Li$^+$, as shown in Figures 5.31 (a) and (b), the charging current initially decreased rapidly under dark conditions. When the light was turned on, the charging current gradually increased, attributed to the photothermal effect raising the device's internal temperature and reducing its impedance. Upon switching off the light, the charging current slowly returned to its original value. This gradual increase and decrease in current under illumination is consistent with the heat generation and temperature rise associated with the photothermal effect.

After allowing the cell to rest for 2 hours, the same test was repeated at 3.0 V vs. Li/Li$^+$, as shown in Figure 5.31 (c). Under dark conditions, the charging current decreased rapidly, similar to the lower voltage tests, but the overall charging current was higher at 3.0 V vs. Li/Li$^+$. When the light was switched on, the charging current exhibited a rapid increase, followed by a gradual decline to a lower current. Upon turning off the light, the current quickly dropped and continued to decay, following the initial trend observed in the dark.

These results highlight the distinct behaviors of the photothermal and photo-charge effects. At 2.0 V vs. Li/Li$^+$, the photo-generated charge carriers lack sufficient energy to participate in the reduction of Li ions at the anode. As a result, the recombination of photo-generated charge carriers in the photocathode releases heat, leading to the photothermal effect. The heat generation and associated temperature rise occur slowly, resulting in a gradual, linear increase in charging current under illumination.

In contrast, at 3.0 V vs. Li/Li^+, the photo-generated charge carriers have sufficient energy to overcome the barrier between the conduction band and the reduction potential of Li ions, enabling their participation in the electrochemical process. This results in a markedly different charging current profile under illumination. Unlike the gradual increase seen with the photothermal effect, the charging current under the photo-charge effect increases rapidly, displaying a sharp rise that appears nearly linear. This distinct behavior confirms the role of applied voltage in determining the dominance of the photothermal or photo-charge effect.

Rutile TiO_2

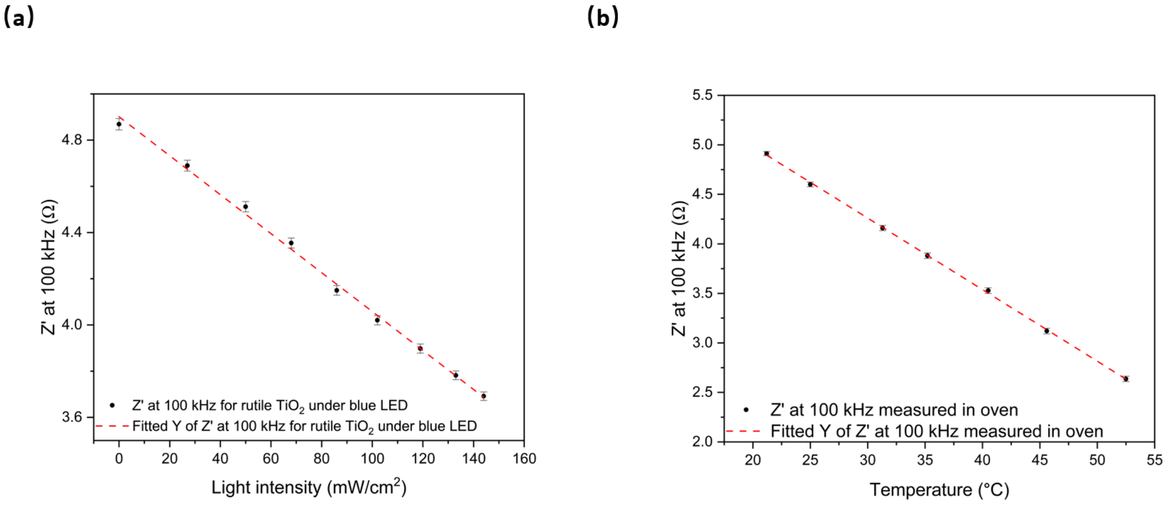

Fig. 5.32 (a) Impedance at 100 kHz as a function of light intensity (Blue LED). (b) Impedance at 100 kHz as a function of oven temperature.

The measurement was then repeated for the rutile TiO_2/CF photocathode. To estimate the photothermal effect, the impedance-based method was employed to calculate the relationship between light intensity and internal temperature, as shown in Figure 5.32. Consistent with previous findings, the impedance decreased with both increasing light intensity and temperature, highlighting the photothermal effect's impact on the internal temperature of the photocathode.

By using the fitting equation from the oven, we were able to calculate the internal temperature of the coin cell under different light intensities of the blue LED light source.

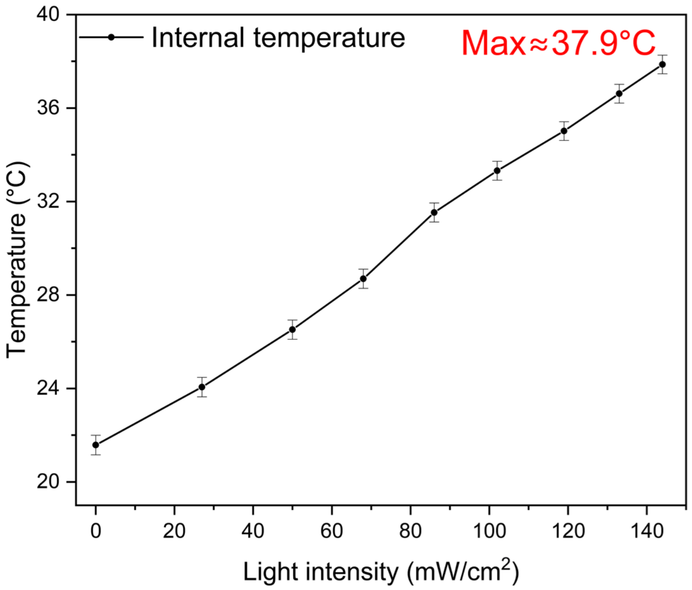

Fig. 5.33 Internal temperature as a function of light intensity for rutile TiO_2 under blue LED

As shown in Figure 5.33, the internal temperature roughly increases linearly with higher light intensity and I recorded a maximum temperature of 37.9 °C. Compared to anatase TiO_2, rutile TiO_2 seems to exhibit a weaker photothermal effect due to lower estimated internal temperature with the same light source and light intensity. This possibly results from the distinct difference in electronic structures and surface properties of anatase and rutile TiO_2. First, it has been reported that anatase TiO_2 has an indirect band gap, which is smaller than its direct band gap. In contrast, rutile TiO_2's indirect bandgap is close to its direct bandgap. Semiconductors with smaller indirect band gaps tend to have longer lifetimes for charge carriers compared to those with direct band gaps. This means that electron-hole pairs last longer in anatase than in rutile TiO_2, making it more likely for them to engage in surface reactions. Furthermore, the commercial rutile TiO_2 has a larger particle size than the anatase TiO_2, making it less effective to take part in any photocatalytic reactions.

Chronoamperometry (CA) tests were conducted to determine whether the photothermal effect predominantly influences the electrochemical process during charging and discharging under illumination for rutile TiO_2. The CA test protocol for rutile TiO_2 was identical to that used for anatase TiO_2.

As shown in Figure 5.34 (a), when the cell was charged at a constant voltage of 2.0 V vs. Li/Li$^+$, a significant initial current was observed, followed by a gradual decrease in charging current over time. The area under each current-time curve for different light intensities was calculated, then normalized by the mass loading and charging time to determine the charging rate of the rutile TiO_2 Li-ion photo-batteries under varying light intensities.

The charging rate was plotted against light intensity, as shown in Figures 5.34 (b) and (c). By fitting the data using both linear and Arrhenius models, it was observed that the R-square values were significantly higher for the Arrhenius model, as shown in Figure 5.34 (c). This indicates that the electrochemical process under increasing light intensities is primarily governed by heat generated from the photocathode, confirming that the photothermal effect is the dominant mechanism.

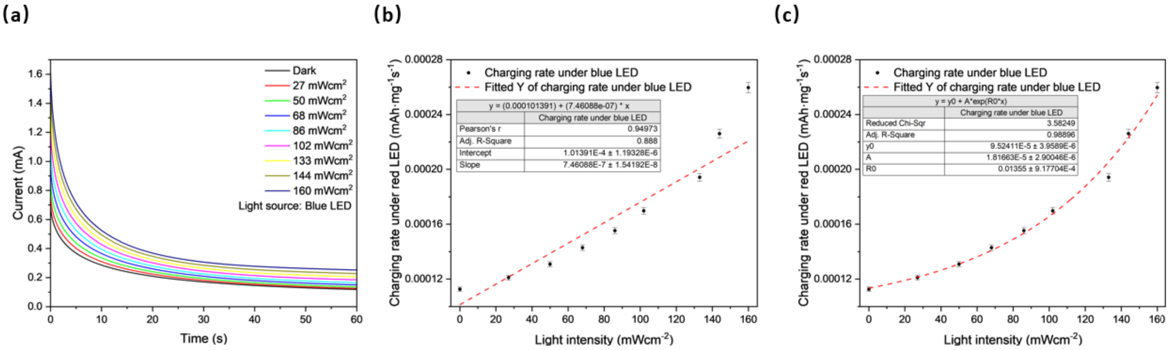

Fig. 5.34 (a) Chronoamperometry curves at different light intensities (Blue LED) during constant voltage hold charging at 2.0 V vs. Li/Li$^+$. Charging rate calculated from integration of Chronoamperometry curves as a function of light intensity (Blue LED) fitted by (b) linear function. (c) Arrhenius-type.

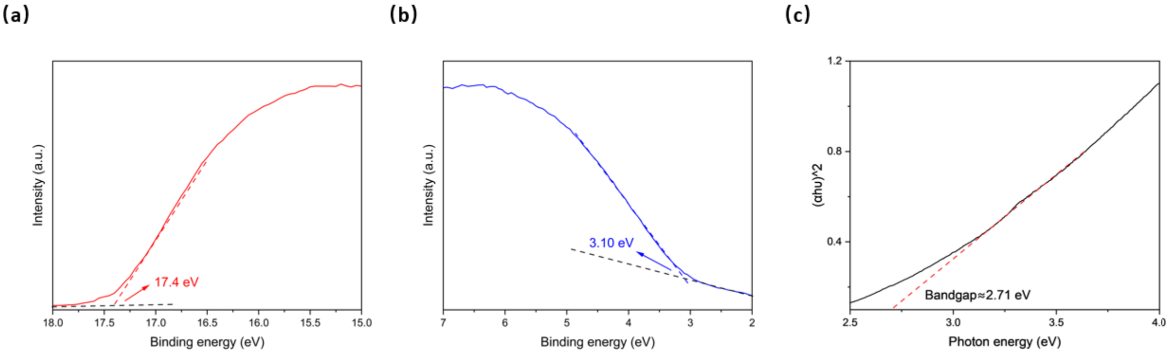

Fig. 5.35 (a) UPS spectra of the intersection to determine the work function. (b) UPS spectra of the intersection to determine the valence band edge.

To explore the potential for the photo-charge effect in rutile TiO_2, Ultraviolet Photoelectron Spectroscopy (UPS) was conducted to estimate the valence band maximum (VBM) and conduction band minimum (CBM). As shown in Figure 5.35, the VBM was calculated using the UPS data as follows: (17.4 eV - 3.10 eV) - 21.2 eV = -6.9 eV. The CBM was then determined by adding the bandgap energy to the VBM: -6.9 eV + 2.8 eV = -4.1 eV.

The bandgap of lithiated rutile TiO_2 was measured using the Tauc plot, which yielded a value of 2.71 eV, as shown in Figure 5.35 (c). Using these data, the band alignment for the rutile TiO_2 photocathode and Li metal anode was constructed, as depicted in Figure 5.36. This alignment provides insights into the potential for photo-generated charge carriers to participate in the electrochemical process.

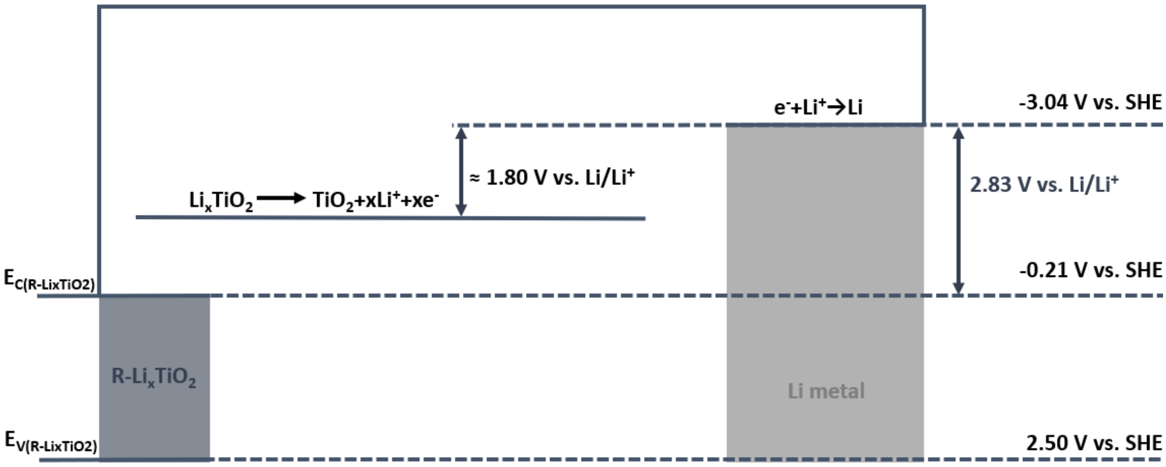

Fig. 5.36 Band alignment between the rutile TiO_2 photocathode and the Li metal anode.

The energy level vs. vacuum is changed to electrochemical potential vs. standard hydrogen electrode for the rutile TiO_2 photocathode for better comparison. Compared to anatase TiO_2, rutile TiO_2 has a higher valence band maximum and lower conduction band minimum. Hence, the potential gap between the conduction band minimum and the reduction potential of the Li metal anode is slightly higher than lithiated anatase TiO_2, which is 2.83 V vs. Li/Li$^+$. Also, it is worth noticing that the main delithiation potential is slightly lower in rutile TiO_2, which is 1.80 V vs. Li/Li$^+$ as labelled in Figure 5.36.

In the first case, when the rutile TiO_2 Li-ion battery was charged at 2.0 V vs. Li/Li$^+$, the band alignment is shown in Figure 5.37. Similar to anatase TiO_2, the applied voltage of 2.0 V vs. Li/Li$^+$ is lower than the potential gap between the conduction band of lithiated rutile TiO_2 and the reduction potential of Li metal. Under these conditions, photo-generated charges cannot transfer through the external circuit. Instead, they undergo photo-excitation and relaxation processes, with the energy ultimately being released as heat, resulting in a photothermal effect.

On the other hand, when the applied voltage exceeds 2.83 V vs. Li/Li$^+$, this potential gap can theoretically be overcome, enabling photo-generated charges to gain sufficient energy to transfer to the Li metal anode. The band alignment for the lithiated rutile TiO_2 photocathode and the Li metal anode at 3.0 V vs. Li/Li$^+$ is depicted in Figure 5.38. While the potential gap is overcome with the applied voltage, the low conduction band position of rutile TiO_2 makes photo-generated electrons less likely to transfer efficiently to the Li metal through the external circuit, especially when compared to anatase TiO_2. This difference highlights the influence of band alignment and conduction band positioning on the effectiveness of photo-charge processes.

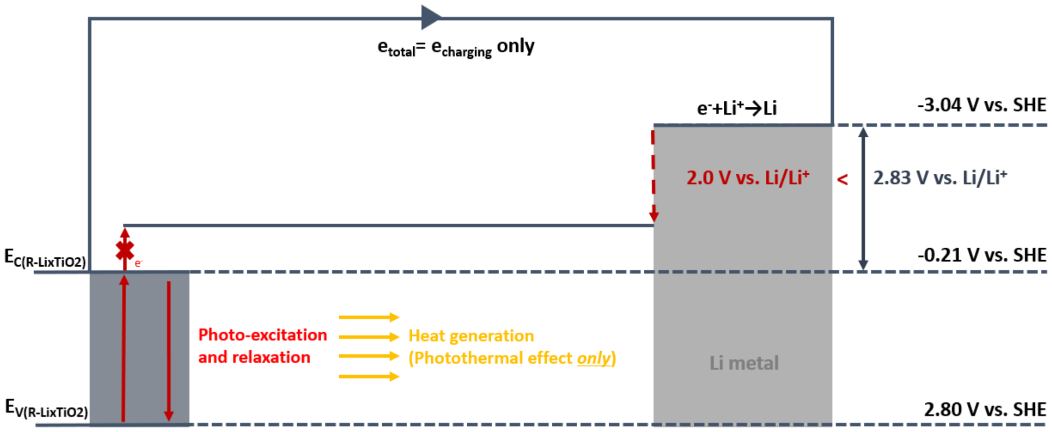

Fig. 5.37 Band alignment between the lithiated rutile TiO_2 photocathode and the Li metal anode at 2.0 V vs. Li/Li$^+$.

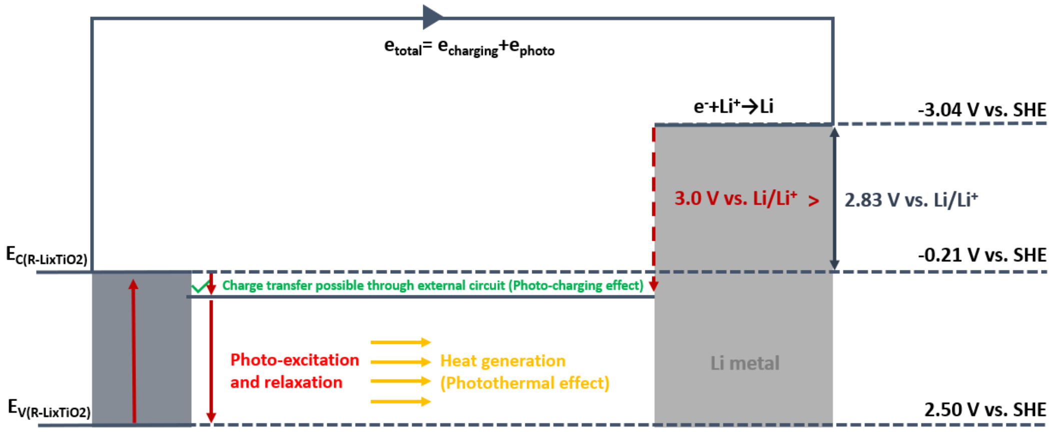

Fig. 5.38 Band alignment between the lithiated rutile TiO_2 photocathode and the Li metal anode at 3.0 V vs. Li/Li$^+$.

To validate the predictions derived from the band diagram, another chronoamperometry (CA) test was conducted under a constant voltage hold of 3.0 V vs. Li/Li$^+$, following a discharge at 0.5 C and a voltage hold at 1.0 V vs. Li/Li$^+$, as shown in Figure 5.39. Similar to the previous CA test at 2.0 V vs. Li/Li$^+$, a significant initial charging current was observed, which gradually decreased over time. However, the overall magnitude of the charging current was notably higher compared to the test under 2.0 V vs. Li/Li$^+$.

The charging rate was calculated by integrating the area under the current-time curve and normalizing it by the mass and charging time. As shown in Figure 5.39 (b), the charging rate was plotted as a function of light intensity. The data were fitted with a linear function, yielding an excellent R-square value of 0.999, indicating a strong fit.

This linear relationship suggests that the photo-charge effect dominates the electrochemical process in the device under light irradiation at 3.0 V vs. Li/Li$^+$. These results confirm the theoretical predictions from the band diagram, where sufficient applied voltage enables photo-generated charge carriers to overcome the potential barrier and participate actively in the electrochemical process.

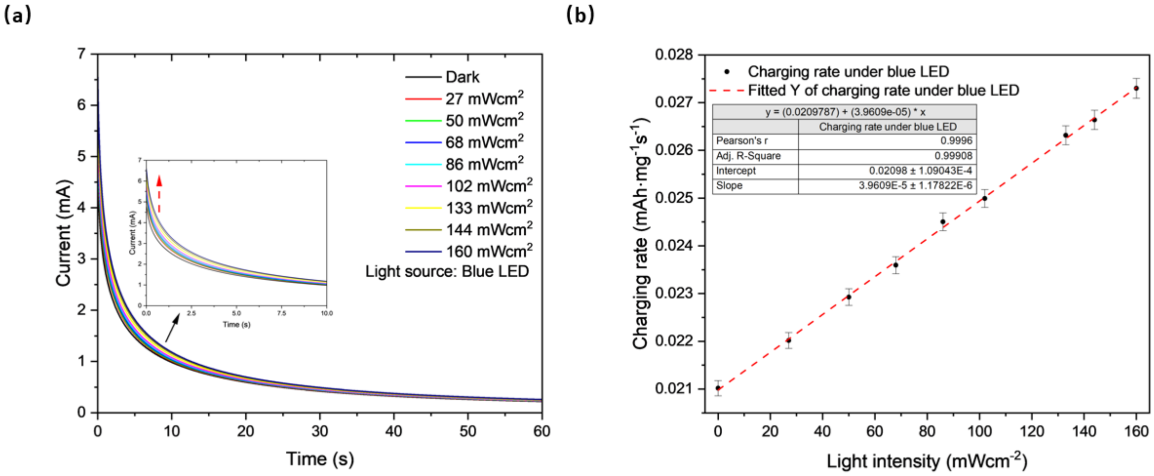

Fig. 5.39 (a) Chronoamperometry curves at different light intensities (Blue LED) during constant voltage hold charging at 3.0 V vs. Li/Li$^+$. (b) Charging rate calculated from integration of chronoamperometry curves as a function of light intensity (Blue LED) fitted by a linear function.

To further investigate the photo-charge effect during the charging process, a chronoamperometry (CA) test was performed under pulsed light conditions, as shown in Figure 5.40. The cell was initially discharged at 1 C to 1.0 V and held at 1.0 V until the current decreased below 5 μA. Subsequently, a constant voltage of 2.0 V was applied, and the charging current was recorded, as shown in Figure 5.40 (a). During the constant voltage charging phase, the blue LED was intermittently switched on and off for 60 seconds.

The charging current initially decreased rapidly but began to increase when the light was turned on. Similar to the behavior observed with anatase TiO_2, this increase in current was primarily attributed to the heat generated by the photothermal effect, which reduced the impedance within the device. The gradual rise in current is consistent with the slow increase in internal temperature driven by the photothermal effect.

A similar trend was observed in Figure 5.40 (b), where a higher charging voltage of 2.5 V vs. Li/Li$^+$ was applied. After resting the photo-battery for 2 hours, it was discharged again at

1 C to 1.0 V, held at 1.0 V until the current decreased below 5 μA, and subsequently charged under a constant voltage of 3.0 V, as shown in Figure 5.40 (c).

At 3.0 V, the charging current exhibited a rapid increase when the blue LED was switched on. However, this increase was less pronounced compared to anatase TiO_2. This behavior is likely due to the lower photocatalytic activity and lower conduction band minimum of rutile TiO_2, which limits photo-charge generation and the transfer of charges between the cathode and anode [358]. When the light source was removed, the charging current experienced a sharp drop and continued to decay, highlighting the distinct response of rutile TiO_2 compared to anatase TiO_2.

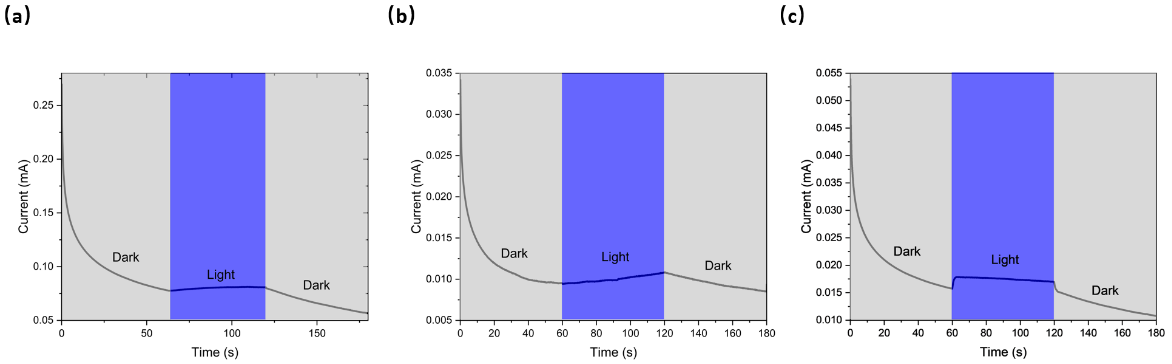

Fig. 5.40 Chronoamperometry curves under pulsed light (Blue LED) during constant voltage hold charging at (a) 2.0 V vs. Li/Li$^+$. (b) 2.5 V vs. Li/Li$^+$. (c) 3.0 V vs. Li/Li$^+$.

Fe_2O_3

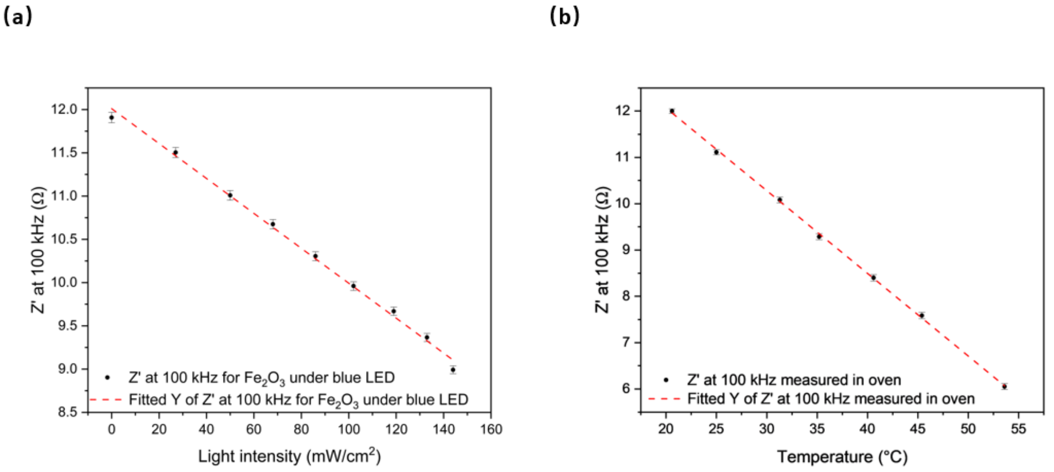

Fig. 5.41 (a) Impedance at 100 kHz as a function of light intensity (Blue LED). (b) Impedance at 100 kHz as a function of oven temperature.

For Fe_2O_3, impedance-based measurements were conducted to establish the relationship between the light intensity and the internal temperature of the photo-device. As shown in Figure 5.41 (a), the impedance at 100 kHz for the Fe_2O_3 Li-ion photo-battery was measured under varying light intensities using a blue LED as the light source. The distance between the light source and the center of the cell's glass window was maintained at approximately 5 cm. As the light intensity increased, a reduction in impedance at 100 kHz was observed, which can be attributed to heat generation from the photothermal effect.

Subsequently, the same cell was used to establish a thermal baseline for the impedance at 100 kHz to determine the internal temperature of the Fe_2O_3 Li-ion photo-battery. As shown in Figure 5.41 (b), a similar trend was observed under controlled oven temperatures, where the impedance at 100 kHz decreased with increasing temperature. The impedance at 100 kHz as a function of oven temperature was then fitted with a linear function, and the resulting equation was used to calculate the internal temperature of the device under different light intensities, as shown in Figure 5.42. This approach provides insights into the internal thermal behavior of the Fe_2O_3 Li-ion photo-battery under varying illumination conditions.

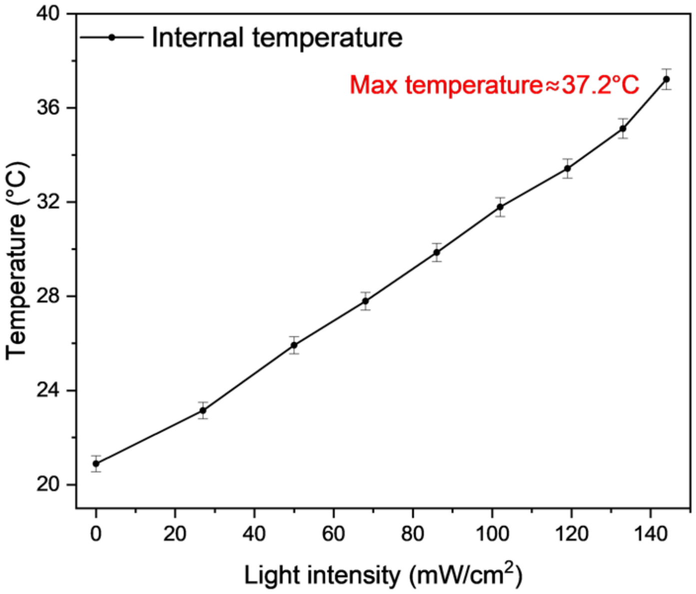

Fig. 5.42 Internal temperature as a function of light intensity for Fe_2O_3 under blue LED

For Fe_2O_3 Li-ion photo-battery, the maximum internal temperature reached under the light intensity of 144 mW/cm^2 is around 37.2 °C. This calculated internal temperature is lower than both anatase and rutile TiO_2 despite the lower bandgap than them. This is possibly due to several reasons, first, from our UV-vis spectroscopy results, the Fe_2O_3 nanopowder has a bandgap of 2.50 eV, which is lower than both anatase and rutile TiO_2, in theory, this makes Fe_2O_3 photocathode more responsive to a wider spectrum of light including visible light. However, it suffers from higher rates of recombination of electron-hole pairs before they can relax non-radiatively, reducing the amount of heat generated. Secondly, Hematite has lower thermal conductivity compared to anatase and rutile TiO_2. This reduced thermal conductivity means that any generated heat is not as effectively distributed, resulting in a lower overall photothermal effect. Lastly, the commercial Fe_2O_3 nanopowder has a larger particle size and less effective surface properties for photocatalytic reactions, which limits the amount of heat generated from light absorption.

To further explore the mechanism of the photothermal effect in the Fe_2O_3 Li-ion photo-battery, a chronoamperometry (CA) test was conducted, and the charging rate during the constant voltage charging step was calculated. The testing protocol consisted of a constant current discharging step at 1C, followed by a constant voltage hold at 1.0 V vs. Li/Li$^+$ until the discharging current dropped below 5 μA. Subsequently, a constant voltage hold at 2.0 V vs. Li/Li$^+$ was applied, during which the charging current was recorded.

The charging rate was plotted as a function of light intensity to analyze the interaction between light and the Fe_2O_3 photocathode within the device. As shown in Figure 5.43 (a), the charging current during the final constant voltage hold charging step at 2.0 V vs. Li/Li$^+$ was measured over a period of 60 seconds. With increasing light intensities, a clear shift in the charging current was observed, with the overall magnitude of the charging current increasing under higher light intensities. This trend reflects the influence of light intensity on the charging process, suggesting a dominant photothermal contribution to the behavior of the Fe_2O_3 photocathode.

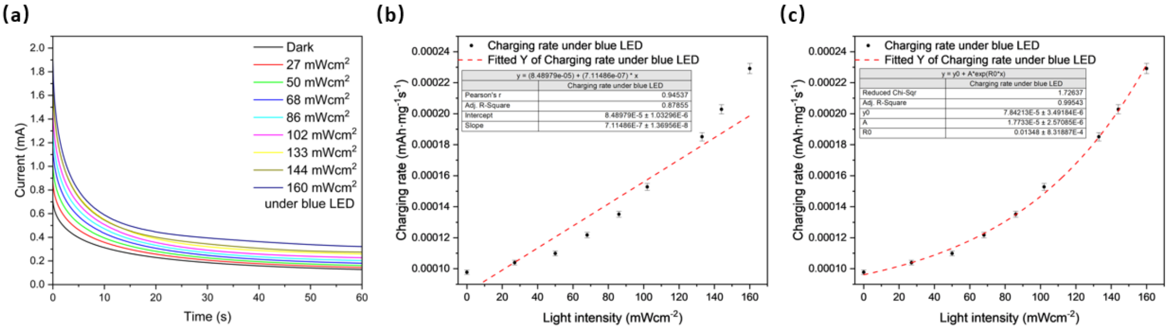

Fig. 5.43 (a) Chronoamperometry curves at different light intensities (Blue LED) during constant voltage hold charging at 2.0 V vs. Li/Li$^+$. Charging rate calculated from integration of Chronoamperometry curves as a function of light intensity (Blue LED) fitted by (b) linear function. (c) Arrhenius-type.

To quantify the charging rate of the Fe_2O_3 Li-ion photo-battery during the constant voltage hold charging at 2.0 V vs. Li/Li$^+$, the area under the current-time curves for the 60-second charging period was integrated. The integrated area was then normalized by the mass loading and charging time to calculate the charging rate. This charging rate was plotted against the corresponding light intensities, as shown in Figures 5.43 (b) and (c).

Initially, the data were fitted with a linear function; however, the fit was poor, with an R-square value of 0.88. The curve was subsequently fitted using the Arrhenius law, resulting in a significantly better fit with an R-square value approaching 1.00. These results indicate that the enhancement mechanism of the Fe_2O_3 Li-ion photo-battery under illumination during the constant voltage hold charging at 2.0 V vs. Li/Li$^+$ is predominantly driven by the photothermal effect and is heat-dominated. This finding underscores the critical role of photothermal heating in the observed electrochemical behavior of the device.

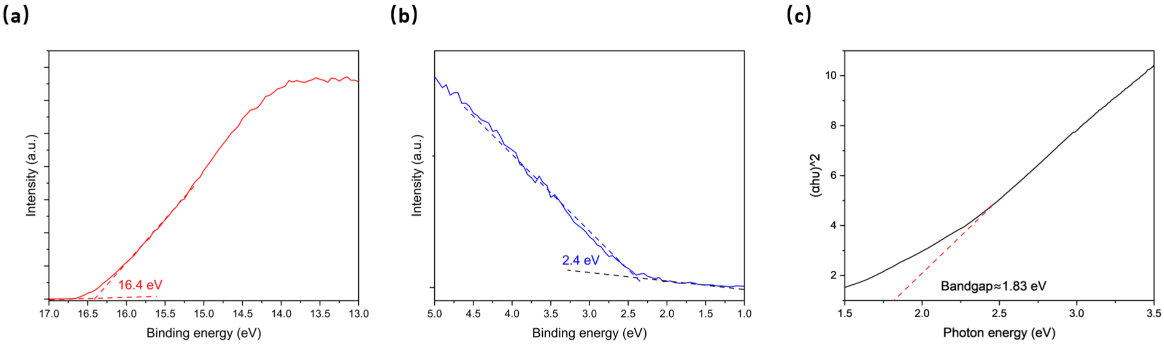

Fig. 5.44 (a) UPS spectra of the intersection to determine the work function. (b) UPS spectra of the intersection to determine the valence band edge. (c) Tauc plot of the Fe_2O_3 electrode at 1.0 V vs. Li/Li$^+$.

To investigate the photocharge potential of the Fe_2O_3 Li-ion photo-battery, Ultraviolet Photoelectron Spectroscopy (UPS) measurements were conducted on the Fe_2O_3 electrode at 1.0 V vs. Li/Li$^+$ to determine its valence band maximum and conduction band minimum values. From the UPS spectrum, the valence band maximum was calculated based on the two intersections, as shown in Figure 5.44. The valence band maximum was determined to be (16.4 eV -2.4 eV)- 21.2 eV = -7.2 eV vs. the vacuum level. The conduction band minimum was then calculated by adding the bandgap of Fe_2O_3 to the valence band maximum: -7.2 eV + 1.8 eV = -5.4 eV. These values provide critical insights into the electronic structure of Fe_2O_3, aiding in the understanding of its photocharging capability in the photo-battery system.

The band alignment of the Fe_2O_3 photocathode and the Li metal anode, along with their corresponding electrochemical potentials, was plotted as shown in Figure 5.45. To facilitate understanding, the energy levels of Fe_2O_3 were converted from the vacuum level to the standard hydrogen electrode (SHE) scale. Compared to anatase and rutile TiO_2, Fe_2O_3 exhibits an even lower conduction band minimum, which significantly hinders the extraction of photo-generated charges. Theoretically, an external voltage exceeding 4.04 V vs. Li/Li$^+$

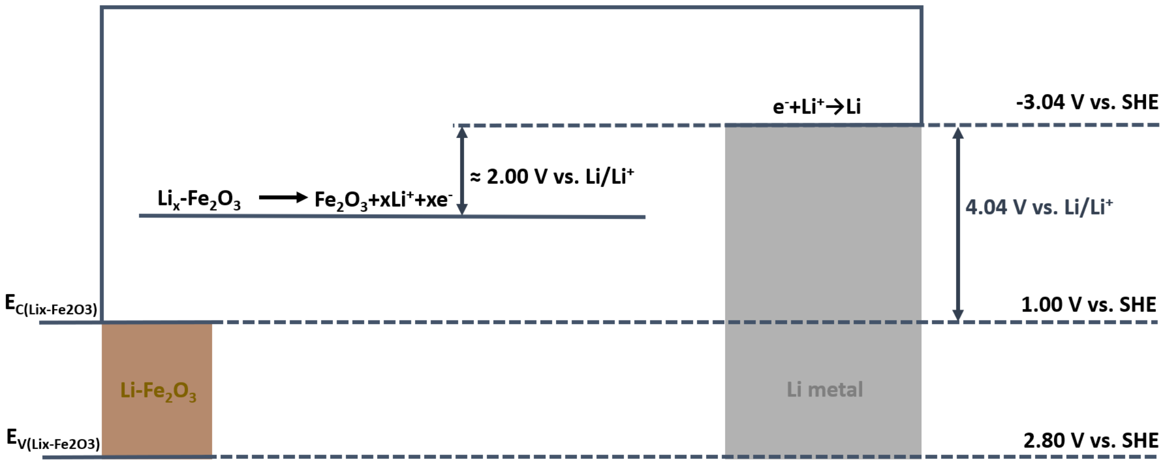

Fig. 5.45 Band alignment between the Fe_2O_3 photocathode and the Li metal anode.

would be required to move photo-electrons to the anode. Such a high potential is impractical for Fe_2O_3 Li-ion photo-batteries and could potentially damage the cell.

To further explore this behavior, a series of chronoamperometry (CA) tests were conducted. Initially, a CA test was performed under constant voltage hold charging at 2.0 V vs. Li/Li$^+$ with pulsed dark and light conditions. After resting the cell for 2 hours, another CA test was conducted under constant voltage hold charging at 3.5 V vs. Li/Li$^+$ under similar pulsed dark and light conditions. Subsequently, a third CA test was performed under continuous constant voltage hold charging at 3.5 V vs. Li/Li$^+$. The results are presented in Figure 5.46.

The charging current behavior at 2.0 V vs. Li/Li$^+$ exhibited a distinct pattern compared to anatase and rutile TiO_2. When the light was switched on, the charging current remained nearly flat instead of rising linearly, as observed for anatase and rutile TiO_2. Upon switching the light off, the charging current decayed normally. These findings indicate that the photothermal effect in the Fe_2O_3 photocathode is less pronounced than in anatase and rutile TiO_2, leading to less efficient heat generation and a correspondingly lower gradient in the charging current under illumination.

Surprisingly, the chronoamperometry results under pulsed light (Blue LED) during constant voltage hold charging at 3.5 V vs. Li/Li$^+$ were consistent with the behavior observed at 2.0 V vs. Li/Li$^+$. Unlike anatase and rutile TiO_2, no sudden increase in charging current was observed when the light was switched on. Instead, the current curve closely resembled the previous result at 2.0 V vs. Li/Li$^+$, further confirming that Fe_2O_3 lacks a significant photocharge effect and that the photothermal effect is the primary driver in this system.

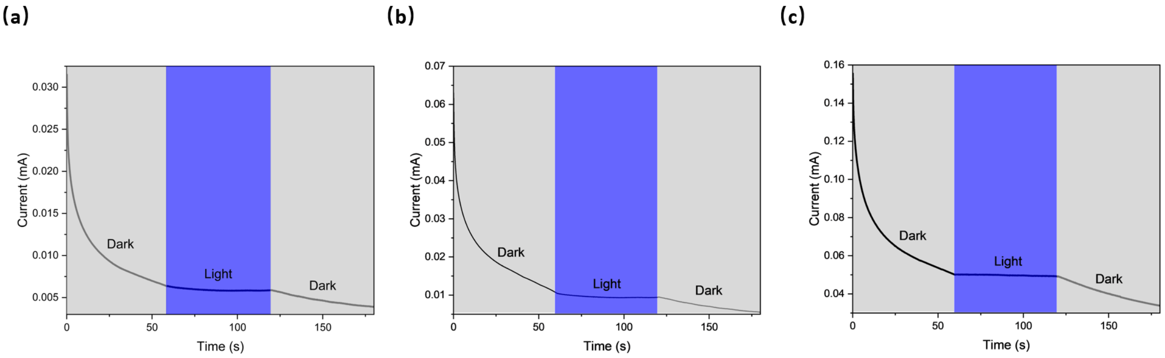

Fig. 5.46 Chronoamperometry curves under pulsed light (Blue LED) during constant voltage hold charging at (a) 2.5 V vs. Li/Li$^+$. (b) 3.0 V vs. Li/Li$^+$. (c) 3.5 V vs. Li/Li$^+$.

During discharge, lithium ions move from the anode to the cathode (Fe_2O_3/CF) through the electrolyte. The associated electrochemical reactions can be summarized as follows:

$$Fe_2O_3 + 6Li^+ 6e^- \rightarrow 2Fe + 3Li_2O \tag{5.2}$$

The Fe_2O_3 is essentially converted to metallic Fe with the formation of lithium oxide. When the Fe_2O_3 Li-ion photo-battery is charged under constant voltage hold charging at 3.5 V vs. Li/Li$^+$, the metallic Fe shows a very limited photothermal effect and no photo-charge effect, therefore, no matter what external potential is applied to the device, no photo-generated charge carriers can appear in the metallic Fe.

5.2.4 Investigation on the stability of photo-thermal effect for TiO_2 and Fe_2O_3 Li-ion batteries

Anatase TiO_2

To evaluate the long-term stability of the anatase TiO_2 Li-ion photo-battery, galvanostatic charge-discharge (GCD) tests were performed under alternating dark and light conditions at a current density of 50 mA/g, as shown in Figure 5.47 (a). A significant capacity increase was observed under blue LED illumination compared to dark conditions during the selected first cycle of each condition. Specifically, the specific capacity increased by 69.2%, rising from 172.5 mAh/g to 291.8 mAh/g. The low initial Coulombic efficiency can be attributed to side reactions involving the carbon felt current collector.[359]

The battery exhibited excellent overall capacity retention over 100 cycles, as depicted in Figure 5.47 (b). The photobattery was first cycled under dark conditions with a constant current of 50 mA/g for 50 cycles. Afterward, the cell was rested for 2 hours and then cycled

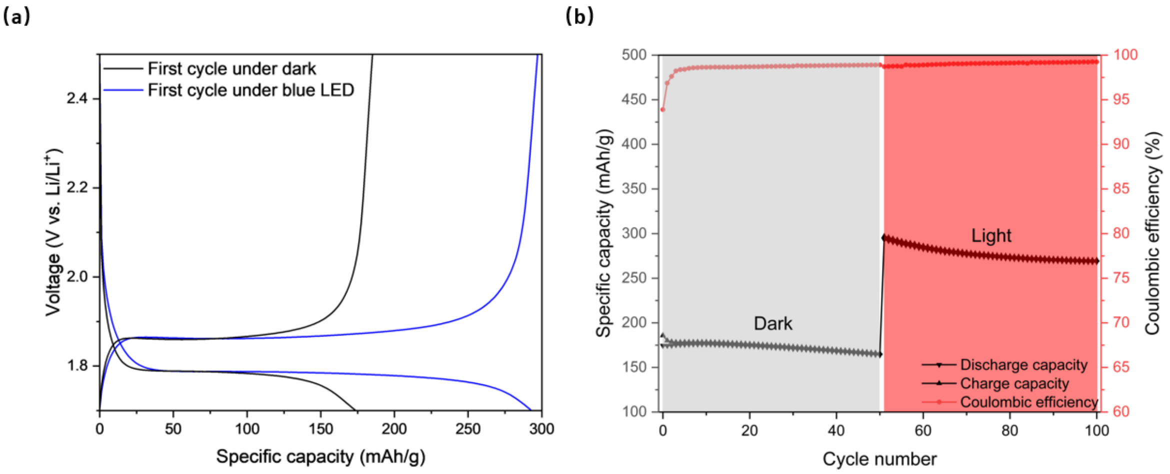

Fig. 5.47 (a) Galvanostatic charge-discharge curves at the specific current density of 50 mA/g under dark and light conditions at 26 °C at the first cycle. (b) Long-term cycling stability of the photo-LIBs under dark and light conditions at 50mA/g.

for an additional 50 cycles under blue LED illumination with a light intensity of 144 mW/cm^2. During the first 50 cycles in the dark, the battery demonstrated a capacity retention of 95.0%. Under illuminated conditions, the capacity retention was slightly lower at 91.0%, indicating a reduction of approximately 4.0% in retention under illumination.

Additionally, a minor drop in Coulombic efficiency was observed during the initial cycles under light conditions, which may be attributed to light-induced decomposition of the electrolyte or the solid electrolyte interphase (SEI). To investigate the underlying causes of this behavior, the X-ray diffraction (XRD) patterns of the anatase TiO_2 carbon felt photoelectrode were analyzed, as shown in Figure 5.48. This analysis provides insights into potential structural changes or degradation of the photoelectrode during cycling.

Unlike the XRD pattern from our previous measurement on anatase TiO_2 nanoparticles, the XRD pattern of the anatase TiO_2 carbon felt photoelectrode also shows some characteristic peaks of the carbon felt which are labelled in Figure 5.48 (a) at around 25 degrees, 43 degrees and 54 degrees two theta. By comparing the zoomed version of the XRD patterns for the anatase TiO_2 carbon felt photoelectrode before and after the cycling test, I can tell the peaks at (103), (104), (200), (204), (116), (200). (215) remain at their original positions without a significant change of the shapes. Our XRD results show that the TiO_2 carbon felt photoelectrode does not contribute to the lower capacity retention in the long-term cycling performance under light conditions.

To investigate the slight capacity loss during the 50 cycles under illuminated conditions, the differences between the nominal charge and discharge voltage (ΔV) were analyzed and plotted as a function of cycle number, as shown in Figure 5.49. The nominal voltage for each

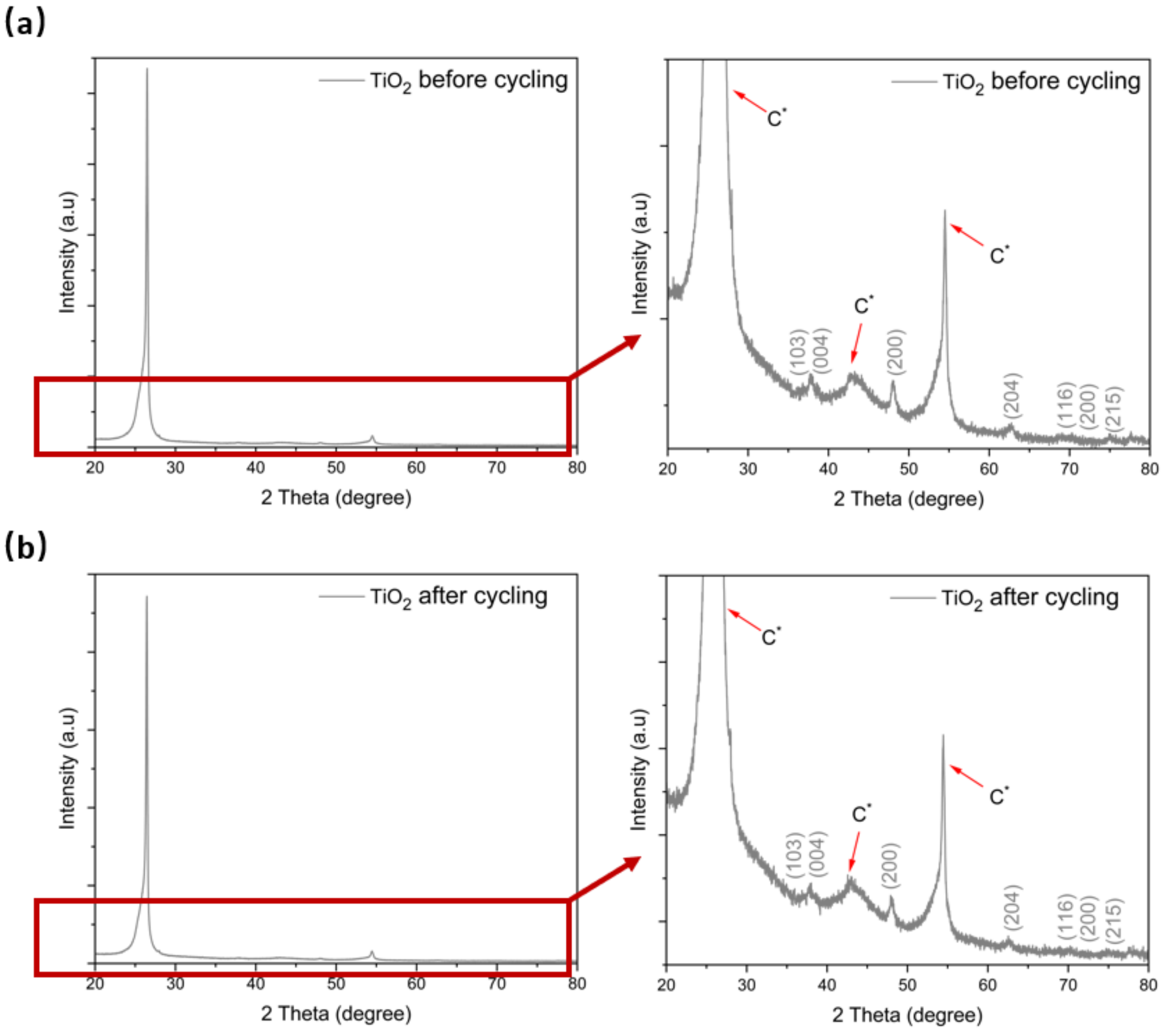

Fig. 5.48 (a) XRD pattern of anatase TiO_2/CF electrodes before cycling. (b) XRD pattern of anatase TiO_2/CF electrodes after 100 cycles.

charge and discharge condition was calculated by dividing the energy density by the specific capacity. The energy density was obtained by integrating the area below the Q_{spec} vs. voltage curve, measured using the VMP-3. The trend of ΔV versus cycle number provides further insights into the performance and degradation of lithium-ion batteries over time. Under both dark and illuminated conditions, ΔV was found to increase with increasing cycle numbers, which is generally attributed to the rise in the battery's internal resistance. Specifically, the increase in ΔV was 1.61% under dark conditions and 4.0% under illuminated conditions. Overall, the value of ΔV was lower under illuminated conditions compared to dark cycles, which can be explained by reduced internal resistance and improved Li-ion transfer due to heat generation from the photo-thermal effect.

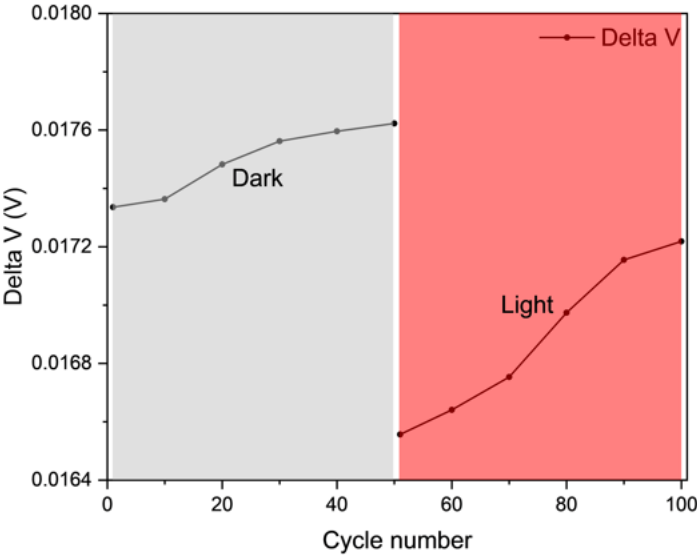

Fig. 5.49 The differences between nominal charge and discharge voltage (Δ V) as a function of cycle number under both dark and light conditions.

This higher increase of ΔV shows that the degradation process happens faster within the device under illumination. Since anatase TiO_2 is a famous photocatalyst and therefore the electrolyte might be decomposed under light due to the photocatalytic activity, which is the reason why I found the capacity loss is much higher under blue LED compared to dark.

The rate performance of anatase TiO_2 Li-ion photo-LIBs was subsequently evaluated under both dark and illuminated conditions using a new cell. Illumination was provided by a blue LED at a light intensity of 144 mW/cm^2. The rate performance protocol included charge/discharge tests across a range of current densities, from 50 mA/g to 400 mA/g, as shown in Figure 5.50 (a). The anatase TiO_2 Li-ion photo-LIBs were first tested under dark conditions, followed by blue LED illumination before resuming the GCD tests. After testing

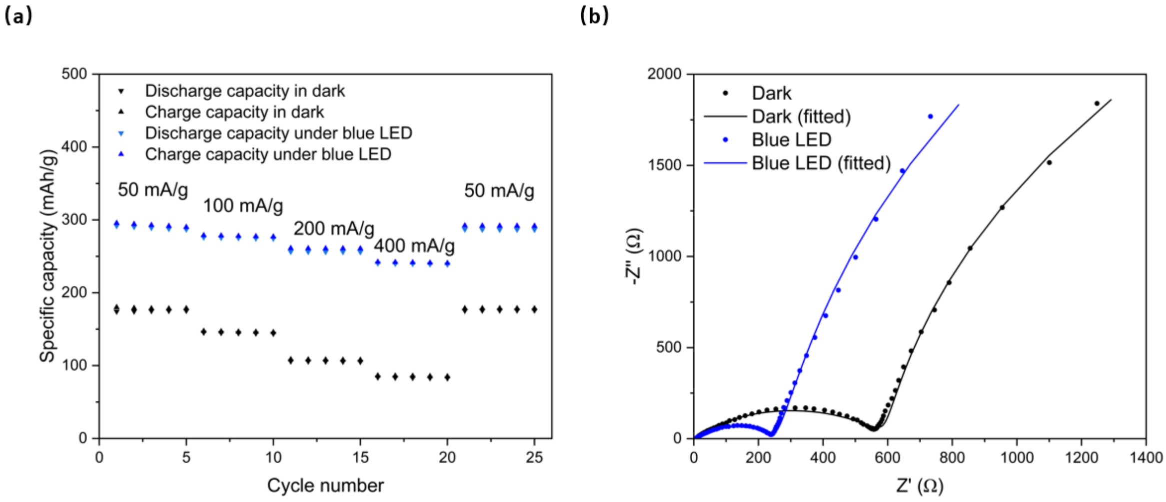

Fig. 5.50 (a) Rate performance tests of the anatase TiO_2 Photo-LIBs in dark and illuminated conditions. (b) EIS measurement of photo-LIB obtained after the 2nd galvanostatic discharge cycle to 1.85V (50% SoC) in the frequency range of 10 mHz-100 kHz at 10 mV amplitude with dark and illuminated conditions.

at 400 mA/g, the cell was retested at the initial current density of 50 mA/g to evaluate the rate stability of the anatase TiO_2 carbon felt photoelectrode.

The anatase TiO_2 Li-ion photo-LIBs demonstrated excellent rate stability over 25 cycles under both dark and illuminated conditions. In dark conditions, the device exhibited average specific discharge capacities of 175.2 mAh/g at 50 mA/g, 144.7 mAh/g at 100 mA/g, 105.6 mAh/g at 200 mA/g, and 83.4 mAh/g at 400 mA/g. Notably, the specific capacity at 50 mA/g returned to its initial value after testing at 400 mA/g, indicating good rate stability.

Under blue LED illumination, the anatase TiO_2 Li-ion photo-LIBs achieved significantly enhanced performance, with average specific discharge capacities of 289.3 mAh/g at 50 mA/g, 275.2 mAh/g at 100 mA/g, 256.2 mAh/g at 200 mA/g, and 239.7 mAh/g at 400 mA/g. By comparing capacities under dark and illuminated conditions, the following capacity enhancements were observed: 65.1% at 50 mA/g, 90.2% at 100 mA/g, 142.6% at 200 mA/g, and 187.4% at 400 mA/g.

To further understand the observed capacity enhancement, Electrochemical Impedance Spectroscopy (EIS) measurements were performed after the second galvanostatic discharge cycle at 50% state of charge (1.85 V) in the frequency range of 10 mHz to 100 kHz with a 10 mV amplitude, as shown in Figure 5.50 (b). The results clearly show a reduction in both series resistance and charge transfer resistance under illumination, which supports the observed capacity enhancements and highlights the significant contribution of the photothermal effect under blue LED illumination.

rutile TiO_2

The long-term stability test was also done for rutile TiO_2 Li-ion photobatteries. Similar to the anatase TiO_2 Li-ion photobatteries, I first performed a GCD test under pulsed dark and light conditions over 100 cycles. The coin cell was first cycled under dark conditions at room temperature for 50 cycles, the blue LED light source with light intensity 144 mW/cm^2 was then switched on and the GCD test was resumed for another 50 cycles as shown in Figure 5.51. I can notice that the rutile TiO_2 Li-ion photobattery shows a capacity enhancement of 113.0% from 56.2 mAh/g to 119.7 mAh/g. There is also a small increase in the specific capacity in the first few cycles under dark conditions. This is generally due to the activation process in Li-ion batteries, where a protective layer called the SEI (Solid Electrolyte Interphase) forms on the electrodes. This layer usually comes from the decomposition products of the electrolyte. In general, the SEI layer is crucial for stabilizing battery performance, it can prevent further decomposition of the electrolyte and lead to longer battery life.

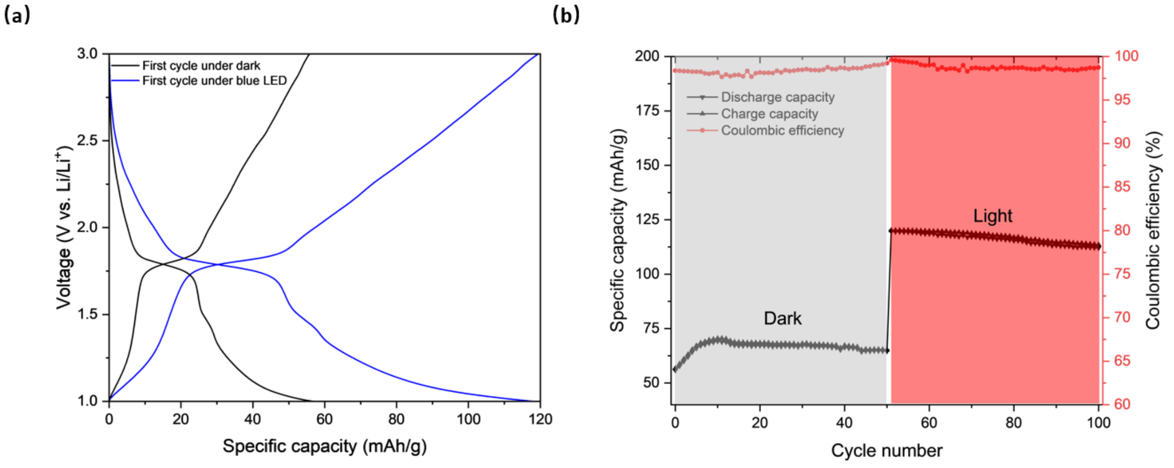

Fig. 5.51 (a) Galvanostatic charge-discharge curves at the specific current density of 50 mA/g under dark and light conditions at 26 °C at the first cycle. (b) Long-term cycling stability of the photo-LIBs under dark and light conditions at 50mA/g.

The long-term cycling performance of the photo-LIBs under dark and illuminated conditions at 50 mA/g was compared, as shown in Figure 5.51 (b). Both specific charge and discharge capacities increased significantly under blue LED illumination. During the final 40 cycles under dark conditions, the photo-LIBs exhibited a capacity retention of 92.5%. For the subsequent sequence of 50 cycles under light conditions, a slightly higher capacity retention of 93.7% was achieved, surpassing the retention observed under dark conditions in rutile TiO_2 and illuminated conditions in anatase TiO_2.

Several factors may account for the superior capacity retention of rutile TiO_2 compared to anatase TiO_2: firstly, rutile TiO_2 is more thermodynamically stable at elevated temperatures than anatase TiO_2, making it less susceptible to structural changes under prolonged cycling. Secondly, rutile TiO_2 may exhibit better thermal conductivity, allowing it to dissipate heat more effectively. This can help in maintaining the cell's overall stability and reducing thermal-induced degradation.[360] Thirdly, while anatase TiO_2 has superior photocatalytic properties, this can lead to faster degradation of the electrolyte under light conditions, adversely affecting capacity retention over time. Lastly, the solid electrolyte interphase (SEI) layer on anatase TiO_2 is known to be less stable and more prone to decomposition at elevated temperatures compared to that on rutile TiO_2. The more stable SEI layer on rutile TiO_2 contributes to its better cycling performance under illuminated conditions.[361]

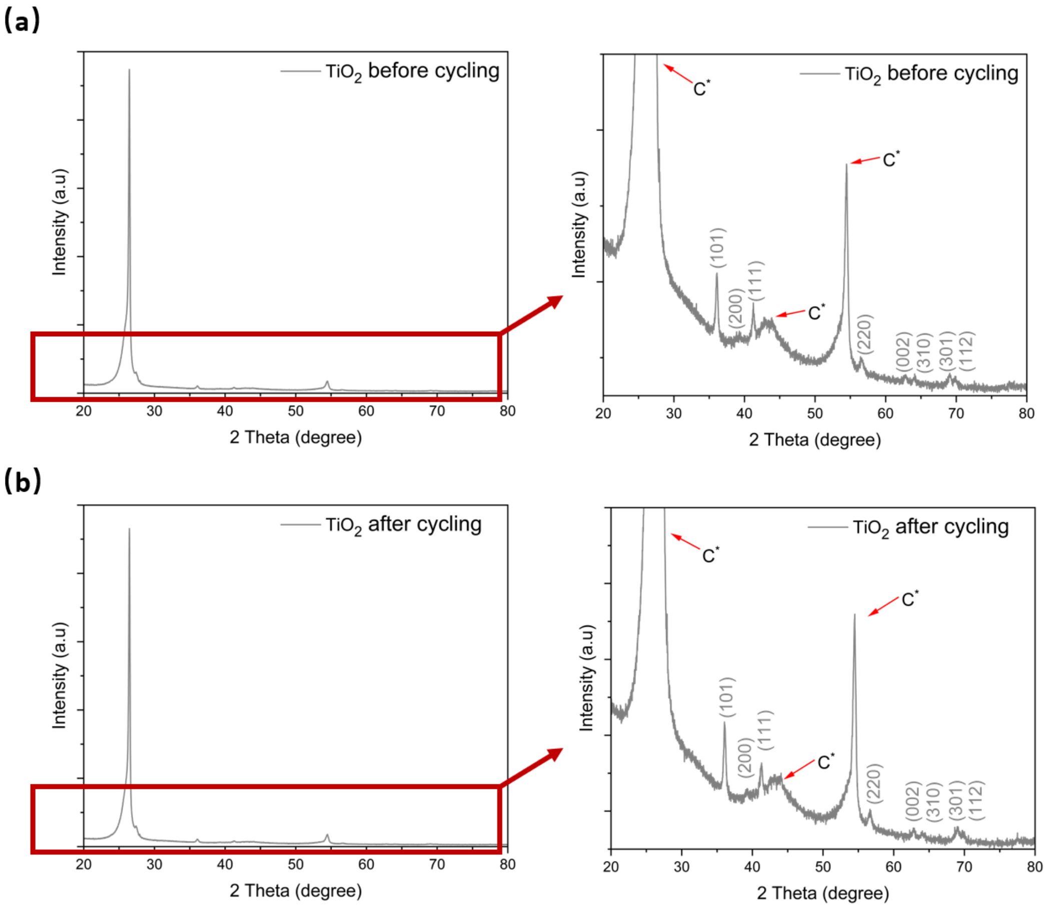

Fig. 5.52 (a) XRD pattern of rutile TiO_2/CF electrodes before cycling. (b) XRD pattern of rutile TiO_2/CF electrodes after 100 cycles. (zoomed pattern on the right)

To evaluate the structural integrity of the rutile TiO_2 carbon felt photoelectrode, XRD analysis was conducted before and after the long-term cycling test, as shown in Figure

5.52. The zoomed-in XRD patterns provide further insights into potential structural changes. Before cycling, characteristic peaks corresponding to rutile TiO_2 were observed, including (101) at 36°, (200) at 39°, (111) at 42°, (220) at 56°, (002) at 63°, (310) at 64°, (301) at 69°, and (112) at 70°. Additionally, prominent peaks at 25°, 43°, and 54°—attributed to the carbon current collector—were also visible, consistent with the anatase TiO_2 carbon felt photoelectrode.

After 100 cycles, the XRD pattern of the rutile TiO_2/CF electrode, shown in Figure 5.52 (b), exhibited no significant changes compared to the pre-cycling results. Each peak in the zoomed XRD pattern retained a similar position and shape, indicating that the rutile TiO_2 carbon felt photoelectrode maintained its structural integrity after extended cycling.

Based on these findings, the capacity fade observed in earlier results is unlikely to be caused by structural degradation of the rutile TiO_2 photoelectrode. Instead, the capacity loss must arise from other factors, such as side reactions in the electrolyte, SEI formation, or material/electrolyte interactions during cycling.

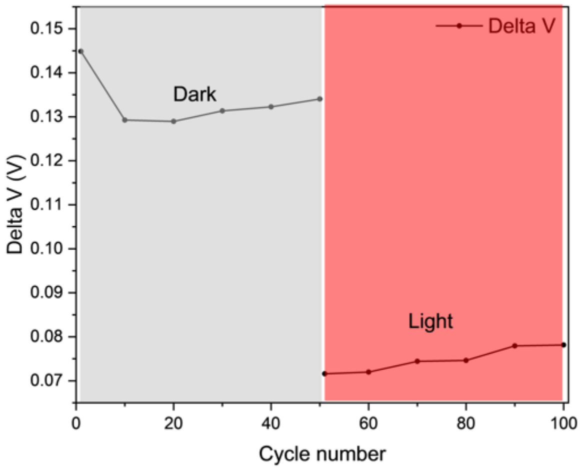

Fig. 5.53 The differences between nominal charge and discharge voltage (Δ V) as a function of cycle number under both dark and light conditions.

To further understand the performance differences, the nominal charge and discharge voltage differences (ΔV) were analyzed and plotted as a function of cycle number, as shown in Figure 5.53. During the dark cycles, a slight reduction in ΔV was observed over the first 10 cycles. This decrease is attributed to the activation process, which reduces the internal resistance of the battery. This activation effect also correlates with the capacity increase observed in the earlier long-term cycling measurements. Following the initial 10 cycles, ΔV began to increase gradually with the number of cycles, showing a total increase of 3.88% from the 10th to the 50th cycle under dark conditions.

Under illuminated conditions, ΔV displayed an overall reduction due to the photothermal effect. However, as the cycle number increased, ΔV gradually rose, culminating in a total increase of 9.16%. This higher ΔV under light conditions is likely due to photo-degradation or heat-induced degradation of the electrolyte, both of which can contribute to increased internal resistance and polarization within the battery. These results underscore the potential trade-offs associated with illumination, highlighting the importance of mitigating light-induced or heat-related degradation for improved long-term stability.

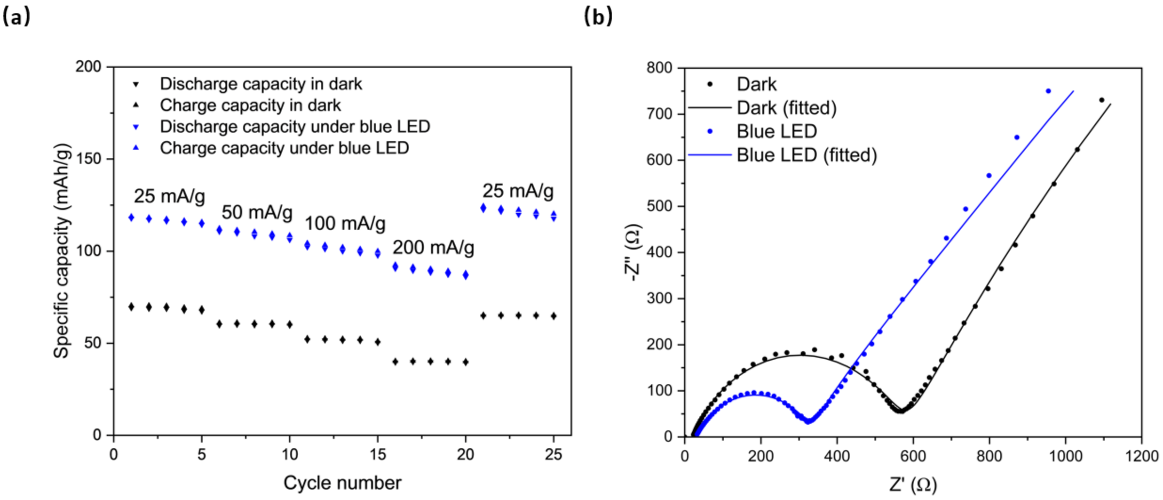

Fig. 5.54 (a) Rate performance tests of the rutile TiO_2 Photo-LIBs in dark and illuminated conditions. (b) EIS measurement of photo-LIB obtained after the 2nd galvanostatic discharge cycle to 1.80V (50% SoC) in the frequency range of 10 mHz-100 kHz at 10 mV amplitude with dark and illuminated conditions.

The rate performance was later done for the rutile TiO_2 Photo-LIBs under both dark and light conditions using a cell which has been cycled for 10 times to avoid the activation process. As shown in Figure 5.54 (a), the GCD test was first performed in the dark from 25 mAh/g to 200 mAh/g and repeated under blue LED with a light intensity of 144 mW/cm^2. The rutile TiO_2 Li-ion Photo-LIBs demonstrated good rate stability over 25 cycles under dark but slightly worse in light conditions. Under dark conditions, the device achieved an average specific discharge capacity of 68.8 mAh/g at the current density of 25 mA/g, 61.0 mAh/g at the current density of 50 mA/g and 48.3 mAh/g at the current density of 100 mA/g and 39.8 mAh/g at the current density of 200 mA/g. The specific capacity at 25 mA/g went back to the original specific capacity after the GCD test with 200 mA/g current density. Under blue LED, the rutile TiO_2 Li-ion Photo-LIBs obtained an average specific discharge capacity of 117.4 mAh/g at the current density of 25 mA/g, 108.2 mAh/g at the current density of 50 mA/g, 102.1 mAh/g at the current density of 100 mA/g and 88.4 mAh/g at the current density of 200 mA/g. Overall, the rutile TiO_2 shows a capacity enhancement of 70.6% at the current density of 25 mA/g, 77.4% at the current density of 50 mA/g, 111.4% at the current density of 100 mA/g and 122.1% at the current density of 200 mA/g. As shown in Figure 5.54 (b), the EIS measurement was done for the rutile TiO_2 Photo-LIB after the 2nd galvanostatic discharge cycle to 1.80V (50% SoC) in the frequency range of 10 mHz-100 kHz at 10 mV amplitude with dark and illuminated conditions. Under illumination, I can clearly see the shift of the impedance results, which indicates the reduction of series and charge transfer resistance.

Fe_2O_3

To assess the long-term stability of the Fe_2O_3 Li-ion photo-batteries, galvanostatic charge-discharge (GCD) measurements were performed at a current density of 100 mA/g under both dark and illuminated conditions for 100 cycles, as shown in Figure 5.55. In Figure 5.55 (a), a comparison of the first cycle GCD curves for each condition shows a capacity enhancement of 27.4% under illumination at 100 mA/g.

Regarding long-term stability, as depicted in Figure 5.51 (b), the Fe_2O_3 Li-ion photo-batteries were initially tested in the dark at a current density of 100 mA/g for 50 cycles, achieving a capacity retention of 91.8%. This relatively low capacity retention is attributed to irreversible reactions during the conversion of Fe_2O_3 in the Li-ion battery. Subsequently, the cell was cycled again under the same current density but with blue LED illumination at a light intensity of 144 mW/cm^2. Under illuminated conditions, an increase in capacity was observed, resulting in a capacity retention of 96.7%. Notably, the Fe_2O_3 Li-ion photo-batteries did not exhibit the significant capacity fade seen in anatase and rutile TiO_2, but instead demonstrated higher capacity retention, which could be attributed to the stable solid electrolyte interphase (SEI) formation that tends to be more resilient under elevated temperature conditions.

A rate performance test was conducted for the Fe_2O_3 Li-ion Photo-LIBs across a range of current densities from 100 mA/g to 800 mA/g under both dark and illuminated conditions after the long-term cycling test, as shown in Figure 5.56. The Fe_2O_3 Li-ion Photo-LIBs demonstrated excellent rate stability under both conditions, with specific capacity returning to its initial value at a current density of 100 mA/g after testing at 800 mA/g. Under dark conditions, the device achieved an average specific discharge capacity of 206.7 mAh/g at 100 mA/g, 186.4 mAh/g at 200 mA/g, 178.5 mAh/g at 400 mA/g, and 169.5 mAh/g at 800 mA/g. The specific capacity returned to the original value after testing again at 100 mA/g.

Under blue LED illumination, the Fe_2O_3 Li-ion Photo-LIBs achieved an average specific discharge capacity of 283.1 mAh/g at 100 mA/g, 266.2 mAh/g at 200 mA/g, 253.2 mAh/g at 400 mA/g, and 240.2 mAh/g at 800 mA/g. Overall, the Fe_2O_3 Li-ion Photo-LIBs exhibited

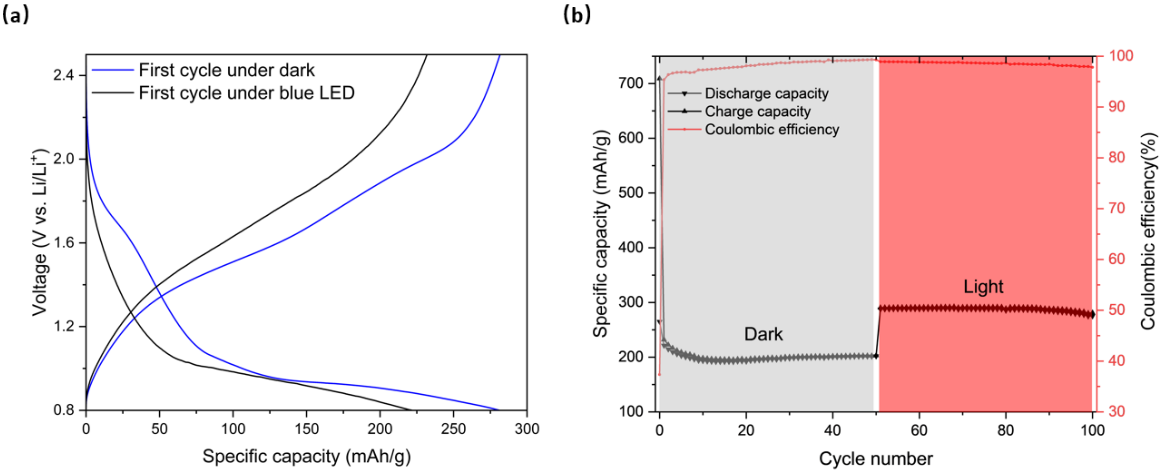

Fig. 5.55 (a) Galvanostatic charge-discharge curves at the specific current density of 100 mA/g under dark and light conditions at 26 °C at the first cycle. (b) Long-term cycling stability of the photo-LIBs under dark and light conditions at 100mA/g.

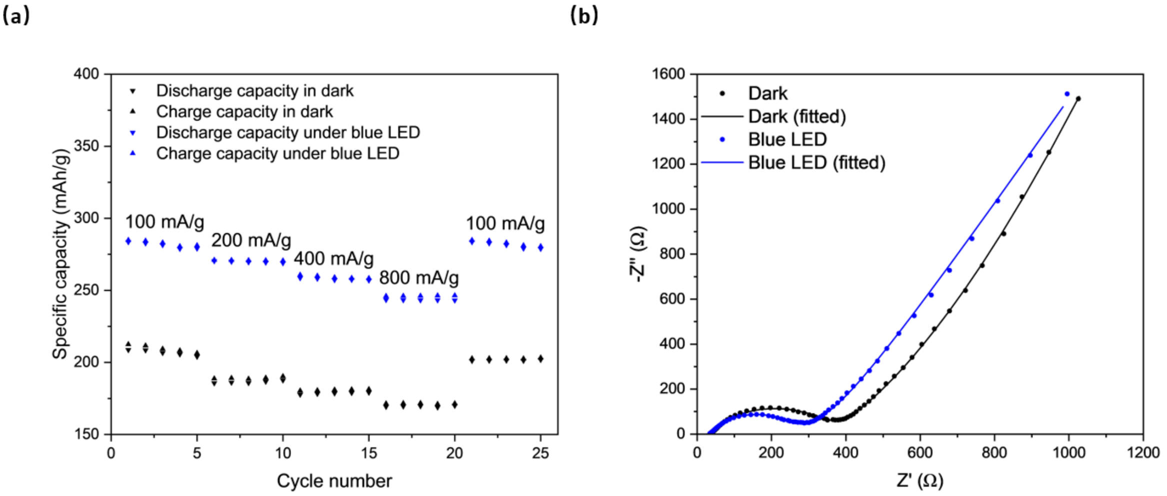

Fig. 5.56 (a) Rate performance tests of the Fe_2O_3 Photo-LIBs in dark and illuminated conditions. (b) EIS measurement of photo-LIB obtained after the 2nd galvanostatic discharge cycle to 1.0V (50% SoC) in the frequency range of 10 mHz-100 kHz at 10 mV amplitude with dark and illuminated conditions.

a capacity enhancement of 37.0% at 100 mA/g, 42.8% at 200 mA/g, 41.8% at 400 mA/g, and 41.7% at 800 mA/g under illumination. However, a reduction in Coulombic efficiency was observed under illumination, potentially due to photocatalytic reactions between the electrolyte and the photoelectrode, or degradation of the electrolyte from heat.

Electrochemical Impedance Spectroscopy (EIS) measurements were performed for the Fe_2O_3 Li-ion Photo-LIBs after the second galvanostatic discharge cycle to 1.0V (50% state of charge) in the frequency range of 10 mHz to 100 kHz, with an amplitude of 10 mV under both dark and illuminated conditions. Compared to rutile and anatase TiO_2, the shift in the impedance curve was smaller, possibly due to the lower photo-thermal effect as indicated in previous measurements. Despite this, a reduction in impedance under illumination was still observed.

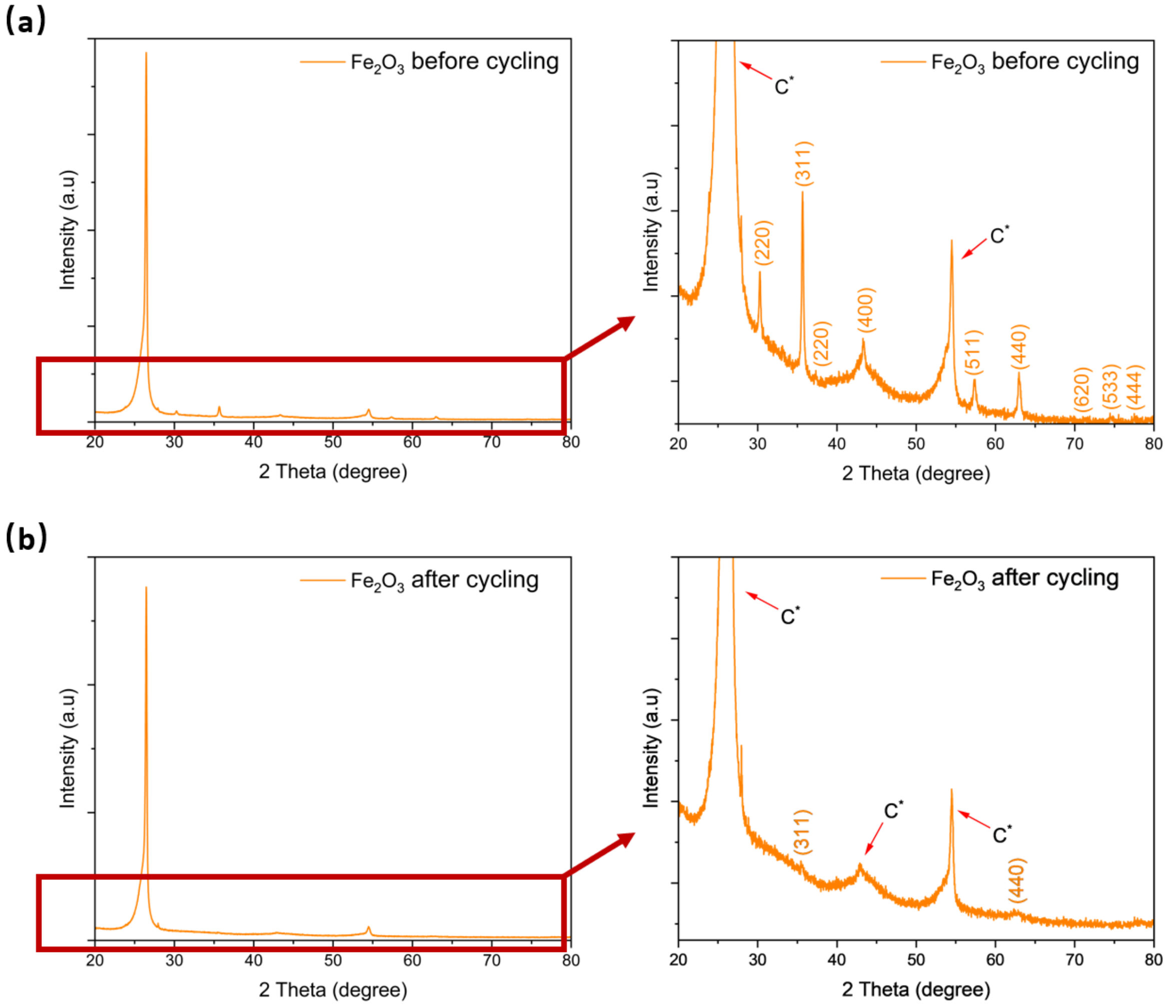

Fig. 5.57 (a) XRD pattern of Fe_2O_3/CF electrodes before cycling. (b) XRD pattern of Fe_2O_3/CF electrodes after 100 cycles. (zoomed pattern on the right)

In order to further investigate the cycling stability of the Fe_2O_3 carbon felt photoelectrode, we disassembled the coin cell and performed XRD for the previously cycled photobattery electrodes after 100 cycles. As shown in Figure 5.57 (a), the zoomed version of the XRD of Fe_2O_3 carbon felt photoelectrode before cycling shows the characteristic peaks of Fe_2O_3 including (220) at 30°, (311) at 36°, (220) at 37°, (400) at 43°, (511) at 57°, (440) at 63°, (620) at 71°, (533) at 75° and (444) at 78°. Compared to the pure Fe_2O_3 nanopowder which we measured previously, most of the peaks are identical. Like the anatase and rutile TiO_2 carbon felt electrode, I can still observe the strong carbon peak as labelled in the zoomed version of the XRD pattern. After 100 cycles, the XRD pattern shows a weak signal of Fe_2O_3 as shown in Figure 5.57 (b) including the (311) peak at 35° and the (440) peak at 63°, indicating a low reversibility of the structural change during the discharge/charge process due to the conversation reaction of Fe_2O_3.

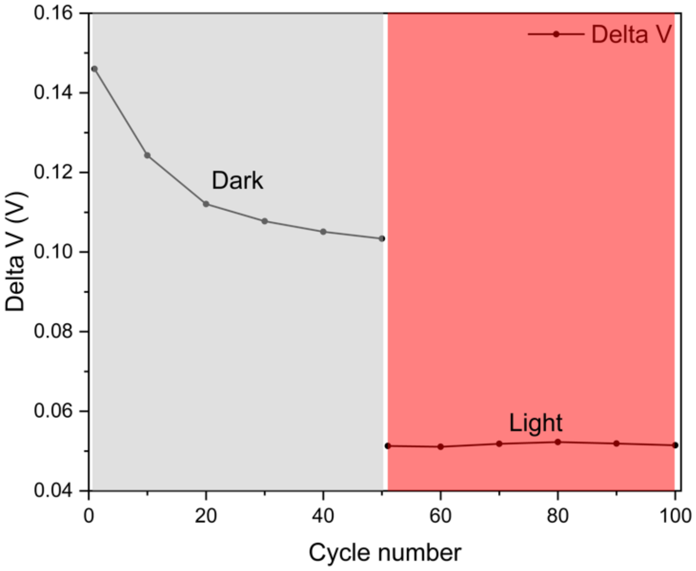

Fig. 5.58 The differences between nominal charge and discharge voltage (delta V) as a function of cycle number under both dark and light conditions.

To further evaluate the stability of the Fe_2O_3 Li-ion photobattery under illumination, the galvanostatic charge-discharge (GCD) curves from the previous long-term cycling test were analyzed. The nominal voltages of the charging and discharging curves were calculated, and the difference between them (ΔV) was plotted as a function of cycle number, as shown in Figure 5.58.

Under dark conditions, a sharp reduction in ΔV was observed during the initial 25 cycles. This reduction is likely attributed to the irreversible conversion reactions occurring at the Fe_2O_3 sites. Despite some capacity loss, as noted in the previous long-term cycling test, the impedance of the cell decreased over cycling and eventually stabilized, indicating improved conductivity over time.

Under illuminated conditions, a significant reduction in ΔV was observed due to the temperature increase driven by the photothermal effect. Notably, ΔV remained stable over time, demonstrating consistent electrochemical performance even at elevated temperatures. This result highlights the ability of the Fe_2O_3 Li-ion photobattery to maintain stable operation under illumination, suggesting that the photothermal effect can enhance performance without introducing additional degradation.

5.3 Conclusion

In conclusion, photothermal-enhanced photobatteries based on metal oxides, including anatase TiO_2, rutile TiO_2, and Fe_2O_3, were successfully fabricated and evaluated. By adjusting parameters such as mass loading, voltage, and current density, stable electrochemical performance was achieved for all three materials. The photothermal and photocharging effects were thoroughly analyzed, providing valuable insights into the interaction of light with photocathodes within batteries. An impedance-based method was utilized to measure the internal temperature of the cells under varying light intensities and controlled temperatures, revealing a linear rise in internal temperature with increasing light intensity, indicative of a significant photothermal effect. Chronoamperometry tests demonstrated that the charging rate increased exponentially with light intensity, further confirming the dominance of the photothermal effect. When a higher bias voltage was applied, photo-generated electrons bridged the gap between the conduction band of anatase TiO_2 and the reduction potential of Li metal, causing the charging rate to follow a linear trend. This transition suggested a shift from a photothermal to a photocharge effect. Ultraviolet photoelectron spectroscopy (UPS) provided deeper insights into the band alignment, showing that a higher voltage facilitated more effective participation of photo-generated electrons in reducing Li ions. At a charging voltage of 3.0 V, a more efficient charge transfer process was observed compared to lower voltages. These findings emphasize the importance of voltage control in photo-batteries to transition from photothermal to photocharge effects, potentially enhancing device performance.

To assess the long-term stability of anatase TiO_2 Li-ion photobatteries, galvanostatic charge-discharge (GCD) tests were conducted under alternating dark and light conditions at a current density of 50 mA/g. The battery's capacity increased by 69.2%, from 172.5 mAh/g in the dark to 291.8 mAh/g under blue LED illumination. Capacity retention over 100 cycles was also examined. After 50 cycles in the dark, the battery retained 95.0% of its capacity, while illuminated conditions for the subsequent 50 cycles showed 91.0% retention, indicating a minor 4.0% reduction. XRD analysis of anatase TiO_2 carbon felt photoelectrodes before and after cycling revealed no significant structural changes, suggesting that the observed lower capacity retention under illumination was not due to electrode degradation. Rate performance tests under both dark and illuminated conditions showed excellent stability across current densities (50 to 400 mA/g) over 25 cycles. Electrochemical impedance spectroscopy (EIS) measurements after 100 cycles indicated reduced series and charge transfer resistance under light conditions, supporting the observed capacity enhancement attributed to the photothermal effect. These results demonstrate that anatase TiO_2 Li-ion photobatteries exhibit substantial capacity increases under illumination and excellent long-term stability with minimal structural degradation of the photoelectrode.

For rutile TiO_2, a series of experiments investigated its photothermal effects and compared its performance to anatase TiO_2. Impedance-based measurements showed a linear increase in internal temperature with light intensity, though the rise was less pronounced compared to anatase TiO_2, indicating a weaker photothermal effect due to differences in electronic structure and surface properties. Chronoamperometry tests demonstrated that the charging rate under light predominantly followed the Arrhenius law, further confirming the dominance of the photothermal effect. At a charging voltage of 3.0 V, the charging rate displayed a linear relationship with light intensity, suggesting a shift towards a photocharge effect. UPS analysis revealed that rutile TiO_2 had a higher valence band maximum and a lower conduction band minimum compared to anatase TiO_2, resulting in a potential gap of 2.83 V between the conduction band minimum and the reduction potential of the Li metal anode. Pulsed light tests showed a noticeable but less significant increase in charging current compared to anatase TiO_2, attributed to rutile TiO_2's lower photocatalytic ability and conduction band minimum. A capacity boost of 113.0% under illumination compared to dark conditions was observed, demonstrating the advantages of photo-enhancement. Long-term cycling tests showed 92.5% capacity retention in the dark and 93.7% under light, with XRD analysis confirming structural stability after cycling. Voltage difference (ΔV) analysis indicated faster degradation under illumination, aligning with higher capacity loss. Rate performance tests showed good stability across current densities, though slight degradation was observed under light. EIS results confirmed reduced resistance under light, correlating with the capacity enhancement.

In the study of Fe_2O_3 as a cathode material for Li-ion photobatteries, the effects of light intensity and temperature were explored. Impedance-based measurements showed a decrease in impedance with increasing light intensity due to the photothermal effect, with the internal temperature reaching a maximum of 37.2°C under blue LED illumination at 144 mW/cm². However, Fe_2O_3 exhibited a weaker photothermal effect compared to TiO_2, likely due to its lower thermal conductivity, poor electron mobility, shorter carrier lifetimes, and suboptimal surface properties. Chronoamperometry tests confirmed that charging current increased with light intensity, driven primarily by the photothermal effect. UPS analysis indicated that photo-generated charge extraction from Fe_2O_3 required an external voltage exceeding 4.04 V, limiting its applicability for photocharge-driven processes. Pulsed light tests revealed no significant photocharge effects, consistent with Fe_2O_3's conversion-type charge-discharge mechanism, where it forms metallic Fe and lithium oxide during discharge. Long-term cycling tests showed 91.8% capacity retention in the dark over 50 cycles, while illuminated conditions resulted in 96.7% retention over the next 50 cycles. Rate performance tests demonstrated high stability across current densities, with impedance measurements indicating reduced resistance under illumination. XRD analysis suggested partial structural reversibility after cycling, consistent with the conversion reaction of Fe_2O_3. Voltage difference analysis showed stable performance with minimal fluctuation under light, potentially due to the formation of a stable SEI or conversion of Fe_2O_3 to Fe.

Overall, the study demonstrated that the light response of the three materials is a combination of photothermal and photoelectric effects, with shifts depending on applied voltage bias and bandgap changes with state of charge. These effects are further influenced by side reactions with the electrolyte and capacitive contributions. The findings provide new electrochemical protocols and techniques to gain deeper insights into the mechanisms governing light-battery interactions, advancing the development of photo-enhanced energy storage devices.

Chapter 6

Summary and outlook

This PhD project focused on advancing photo-rechargeable and photothermal batteries by integrating innovative materials to optimize their performance. The research explored three main areas: the use of g-C_3N_4 and $BiVO_4$ in photo-rechargeable batteries, photothermal enhancements through Prussian Blue analogues (PBAs), and the integration of transition metal oxides into photobattery systems.

6.1 Summary of Key Findings

In the first phase, g-C_3N_4 and $BiVO_4$ were investigated as potential photoactive materials for photo-rechargeable batteries. Challenges were identified, including low specific capacity and photo-instability during the charge/discharge process. Analysis of band alignment revealed that the low potential of Li metal prevents effective photocharging. This limitation highlighted the need to shift focus toward alternative photo-induced effects, such as photothermal enhancement.

The second phase leveraged the exceptional photothermal efficiency of PBAs, which exhibit strong light absorption in the visible and near-infrared regions. By utilizing their non-radiative relaxation processes, including Shockley-Read-Hall and Auger recombination, localized temperature increases in the cathode were achieved. PBAs demonstrated significant electrochemical performance enhancements under illumination, with improved charge transfer kinetics, higher Li-ion diffusion rates, and increased battery capacity. Long-term cycling stability was also confirmed, with minimal structural degradation observed. However, challenges such as limited absorption spectra, heat dissipation, and structural changes during cycling were identified as areas requiring further investigation.

In the final phase, transition metal oxides, including anatase TiO_2, rutile TiO_2, and Fe_2O_3, were integrated into battery systems to evaluate their photothermal and photocharge effects. While all materials showed positive photo responses, their photothermal efficiencies and mechanisms varied. Anatase TiO_2 exhibited the highest internal temperature rise and significant photocharge activity. In contrast, rutile TiO_2 displayed moderate photothermal enhancement and excellent cycling stability, and Fe_2O_3 showed limited photothermal effects but the highest cycling stability under illumination. These findings provided valuable insights into the interplay between photothermal effects and electrochemical performance in different materials.

6.2 Future Directions

6.2.1 Optimizing Existing Systems

g-C$_3$N$_4$ and BiVO$_4$:

Efforts should focus on optimizing g-C$_3$N$_4$ photo-rechargeable batteries by refining mass loading, voltage windows, and current densities to improve specific capacity and stability. Band engineering techniques, such as employing anodes with higher potentials relative to Li plating, could help overcome limitations in band alignment and facilitate photocharging.

PBAs:

Investigating the absorption spectra of various PBAs to harness a broader range of light frequencies is crucial for enhancing photothermal effects. Additionally, optimizing the thermal management of PBAs is necessary to prevent overheating and degradation, ensuring consistent performance under illumination.

Transition Metal Oxides:

Further optimization of device configurations, such as electrode architecture and electrolyte compatibility, could improve the photocharging efficiency of metal oxides. Exploring strategies to enhance their light absorption and thermal management could also unlock their full potential.

6.2.2 Exploring New Systems

Future work should explore novel approaches to photothermal and photocharging enhancements:

Solar Simulators:

Replacing LED-based systems with solar simulators could provide a more representative spectrum of natural sunlight, improving the relevance of laboratory findings to real-world applications.

Unique Materials:

Investigating other photothermal-active materials, such as transition metal dichalcogenides, two-dimensional materials, or hybrid composites, could lead to breakthroughs in light absorption and thermal management.

6.2.3 Practical Applications and Thermal Effects

The integration of photothermal effects into practical systems presents both opportunities and risks.

Advantages:

Photothermal effects can accelerate reaction kinetics, enhance ion diffusion, and improve power output. These effects are particularly valuable in environments with challenging temperature conditions.

Challenges:

Risks such as thermal runaway, overheating, and material degradation must be mitigated. Advanced thermal management strategies, including phase-change materials, thermally conductive layers, and adaptive cooling mechanisms, could address these issues and ensure safety and stability in scaled-up systems.

6.2.4 Solid-State Systems

Exploring the application of photothermal effects in solid-state batteries could address challenges such as interfacial resistance and limited ion transport. By optimizing thermal distribution and reducing solid-solid interface barriers, photothermal effects could improve the safety, capacity, and efficiency of solid-state energy storage systems.

6.3 Conclusion

This work has highlighted the intricate interplay between photothermal and photocharge effects in enhancing battery performance. While significant progress has been made, further research is essential to optimize these systems for practical applications. By addressing current limitations and exploring innovative materials and methodologies, photothermal-enhanced batteries have the potential to become a cornerstone of next-generation energy storage technologies.

References

[1] J. P. Schmidt, S. Arnold, A. Loges, D. Werner, T. Wetzel, and E. Ivers-Tiffée, “Measurement of the internal cell temperature via impedance: Evaluation and application of a new method,” *Journal of Power Sources*, vol. 243, pp. 110–117, 2013.

[2] H.-W. Schiffer, “Wec energy policy scenarios to 2050,” *Energy Policy*, vol. 36, no. 7, pp. 2464–2470, 2008.

[3] R. Haight, W. Haensch, and D. Friedman, “Solar-powering the internet of things,” *Science*, vol. 353, no. 6295, pp. 124–125, 2016.

[4] X. Cao, X. Dai, and J. Liu, “Building energy-consumption status worldwide and the state-of-the-art technologies for zero-energy buildings during the past decade,” *Energy and Buildings*, vol. 128, pp. 198–213, 2016.

[5] D. R. Criswell, “Energy from space for sustainable commercial power for earth,” *Engineering Response to Climate Change*, p. 369, 2013.

[6] A. Gurung and Q. Qiao, “Solar charging batteries: Advances, challenges, and opportunities,” *Joule*, vol. 2, no. 7, pp. 1217–1230, 2018.

[7] V. Badescu, “Dynamic model of a complex system including pv cells, electric battery, electrical motor and water pump,” *Energy*, vol. 28, pp. 1165–1181, 10 2003.

[8] Z. Yang, L. Li, Y. Luo, R. He, L. Qiu, H. Lin, and H. Peng, “An integrated device for both photoelectric conversion and energy storage based on free-standing and aligned carbon nanotube film,” *J. Mater. Chem. A*, vol. 1, pp. 954–958, 2013.

[9] A. W. Bayeh, D. M. Kabtamu, Y.-C. Chang, T. H. Wondimu, H.-C. Huang, and C.-H. Wang, “Carbon and metal-based catalysts for vanadium redox flow batteries: a perspective and review of recent progress,” *Sustainable Energy Fuels*, vol. 5, pp. 1668–1707, 2021.

[10] M. Al Hassan, A. Sen, T. Zaman, and M. Mostari, “Emergence of graphene as a promising anode material for rechargeable batteries: a review,” *Materials Today Chemistry*, vol. 11, pp. 225–243, 2019.

[11] H.-J. Peng, J.-Q. Huang, and Q. Zhang, “A review of flexible lithiumulfur and analogous alkali metalhalcogen rechargeable batteries,” *Chem. Soc. Rev.*, vol. 46, pp. 5237–5288, 2017.

[12] X.-B. Cheng, R. Zhang, C.-Z. Zhao, and Q. Zhang, “Toward safe lithium metal anode in rechargeable batteries: A review,” *Chemical Reviews*, vol. 117, no. 15, pp. 10403–10473, 2017. PMID: 28753298.

[13] K. Lourenssen, J. Williams, F. Ahmadpour, R. Clemmer, and S. Tasnim, “Vanadium redox flow batteries: A comprehensive review,” *Journal of Energy Storage*, vol. 25, p. 100844, 2019.

[14] M. Maksoud, R. Amer Fahim, A. Shalan, M. Abd El-Kodous, O. Samuel Oluwaseun, A. Osman, C. Farrell, A. Al-Muhtaseb, A. Awed, A. Ashour, and D. Rooney, “Advanced materials and technologies for supercapacitors used in energy conversion and storage: a review,” *Environmental Chemistry Letters*, 08 2020.

[15] P. Forouzandeh, V. Kumaravel, and S. Pillai, “Electrode materials for supercapacitors: A review of recent advances,” *Catalysts*, vol. 10, p. 969, 08 2020.

[16] H. Liu, X. Liu, S. Wang, H.-K. Liu, and L. Li, “Transition metal based battery-type electrodes in hybrid supercapacitors: A review,” *Energy Storage Materials*, vol. 28, pp. 122–145, 2020.

[17] M. Grtzel, “Dye-sensitized solar cells,” *Journal of Photochemistry and Photobiology C: Photochemistry Reviews*, vol. 4, no. 2, pp. 145–153, 2003.

[18] M. Jot, L. Kegelmann, L. Korte, and S. Albrecht, “Monolithic perovskite tandem solar cells: A review of the present status and advanced characterization methods toward 30% efficiency,” *Advanced Energy Materials*, vol. 10, no. 26, p. 1904102, 2020.

[19] F. Babar, U. Mehmood, H. Asghar, M. H. Mehdi, A. U. H. Khan, H. Khalid, N. ul Huda, and Z. Fatima, “Nanostructured photoanode materials and their deposition methods for efficient and economical third generation dye-sensitized solar cells: A comprehensive review,” *Renewable and Sustainable Energy Reviews*, vol. 129, p. 109919, 2020.

[20] R. Cariou, J. Benick, F. Feldmann, O. Höhn, H. Hauser, P. Beutel, N. Razek, M. Wimplinger, B. Bläsi, D. Lackner, M. Hermle, G. Siefer, S. Glunz, A. Bett, and D. Frank, “Iii–v-on-silicon solar cells reaching 33

[21] S. Yu, A. J. Wilson, G. Kumari, X. Zhang, and P. K. Jain, “Opportunities and challenges of solar-energy-driven carbon dioxide to fuel conversion with plasmonic catalysts,” *ACS Energy Letters*, vol. 2, no. 9, pp. 2058–2070, 2017.

[22] H. Badenhorst, “A review of the application of carbon materials in solar thermal energy storage,” *Solar Energy*, 2018.

[23] F. Brunetti, A. Operamolla, S. Castro-Hermosa, G. Lucarelli, V. Manca, G. M. Farinola, and T. M. Brown, “Printed solar cells and energy storage devices on paper substrates,” *Advanced Functional Materials*, vol. 29, no. 21, p. 1806798, 2019.

[24] M. M. A. Khan, N. I. Ibrahim, I. Mahbubul, H. Muhammad. Ali, R. Saidur, and F. A. Al-Sulaiman, “Evaluation of solar collector designs with integrated latent heat thermal energy storage: A review,” *Solar Energy*, vol. 166, pp. 334–350, 2018.

[25] A. Dahash, F. Ochs, M. B. Janetti, and W. Streicher, “Advances in seasonal thermal energy storage for solar district heating applications: A critical review on large-scale hot-water tank and pit thermal energy storage systems,” *Applied Energy*, vol. 239, pp. 296–315, 2019.

[26] N. S. Bentsen and I. M. MÃ¸ller, “Solar energy conserved in biomass: Sustainable bioenergy use and reduction of land use change,” *Renewable and Sustainable Energy Reviews*, vol. 71, pp. 954–958, 2017.

[27] C. Bie, B. Zhu, F. Xu, L. Zhang, and J. Yu, “In situ grown monolayer n-doped graphene on cds hollow spheres with seamless contact for photocatalytic co2 reduction,” *Advanced Materials*, vol. 31, no. 42, p. 1902868, 2019.

[28] L. Wang, Y. Tong, J. Feng, J. Hou, J. Li, X. Hou, and J. Liang, “G-c3n4-based films: A rising star for photoelectrochemical water splitting,” *Sustainable Materials and Technologies*, vol. 19, p. e00089, 2019.

[29] L. Wang, W. Si, Y. Tong, F. Hou, D. Pergolesi, J. Hou, T. Lippert, S. X. Dou, and J. Liang, “Graphitic carbon nitride (g-c3n4)-based nanosized heteroarrays: Promising materials for photoelectrochemical water splitting,” *Carbon Energy*, vol. 2, no. 2, pp. 223–250, 2020.

[30] Q. Li, Y. Liu, S. Guo, and H. Zhou, “Solar energy storage in the rechargeable batteries,” *Nano Today*, vol. 16, 10 2017.

[31] M. Peng, B. Dong, and D. Zou, “Three dimensional photovoltaic fibers for wearable energy harvesting and conversion,” *Journal of Energy Chemistry*, vol. 27, no. 3, pp. 611–621, 2018.

[32] S. Pang, H. Meng, and G. Cui, “Photo-supercapacitors based on third-generation solar cells,” *ChemSusChem*, vol. 12, 04 2019.

[33] S. Yun, Y. Qin, A. R. Uhl, N. Vlachopoulos, M. Yin, D. Li, X. Han, and A. Hagfeldt, “New-generation integrated devices based on dye-sensitized and perovskite solar cells,” *Energy Environ. Sci.*, vol. 11, pp. 476–526, 2018.

[34] V. Vega-Garita, L. Ramirez-Elizondo, N. Narayan, and P. Bauer, “Integrating a photovoltaic storage system in one device: A critical review,” *Progress in Photovoltaics: Research and Applications*, vol. 27, no. 4, pp. 346–370, 2019.

[35] E. Ogunniyi and H. Pienaar, “Overview of battery energy storage system advancement for renewable (photovoltaic) energy applications,” 04 2017.

[36] N. A. Ludin, N. I. Mustafa, M. M. Hanafiah, M. A. Ibrahim, M. Asri Mat Teridi, S. Sepeai, A. Zaharim, and K. Sopian, “Prospects of life cycle assessment of renewable energy from solar photovoltaic technologies: A review,” *Renewable and Sustainable Energy Reviews*, vol. 96, pp. 11–28, 2018.

[37] C. Rodríguez-Seco, Y.-S. Wang, K. Zaghib, and D. Ma, “Photoactive nanomaterials enabled integrated photo-rechargeable batteries,” *Nanophotonics*, vol. 11, no. 8, pp. 1443–1484, 2022.

[38] Q. Li, Y. Liu, S. Guo, and H. Zhou, "Solar energy storage in the rechargeable batteries," *Nano Today*, vol. 16, pp. 46–60, 2017.

[39] H. Meng, S. Pang, and G. Cui, "Photo-supercapacitors based on third-generation solar cells," *ChemSusChem*, vol. 12, no. 15, pp. 3431–3447, 2019.

[40] V. Vega-Garita, L. Ramirez-Elizondo, N. Narayan, and P. Bauer, "Integrating a photovoltaic storage system in one device: A critical review," *Progress in Photovoltaics: Research and Applications*, vol. 27, no. 4, pp. 346–370, 2019.

[41] N. K. and C. S. Rout, "Photo-powered integrated supercapacitors: a review on recent developments, challenges and future perspectives," *J. Mater. Chem. A*, vol. 9, pp. 8248–8278, 2021.

[42] A. Paolella, A. Vijh, A. Guerfi, K. Zaghib, and C. Faure, "Review—li-ion photo-batteries: Challenges and opportunities," *Journal of The Electrochemical Society*, vol. 167, p. 120545, sep 2020.

[43] Z. Fang, X. Hu, and D. Yu, "Integrated photo-responsive batteries for solar energy harnessing: Recent advances, challenges, and opportunities," *ChemPlusChem*, vol. 85, no. 4, pp. 600–612, 2020.

[44] A. Das, S. Deshagani, R. Kumar, and M. Deepa, "Bifunctional photo-supercapacitor with a new architecture converts and stores solar energy as charge," *ACS Applied Materials & Interfaces*, vol. 10, no. 42, pp. 35932–35945, 2018.

[45] C. Ng, H. Lim, S. Hayase, I. Harrison, A. Pandikumar, and N. Huang, "Potential active materials for photo-supercapacitor: A review," *Journal of Power Sources*, vol. 296, pp. 169–185, 2015.

[46] Poonam, K. Sharma, A. Arora, and S. Tripathi, "Review of supercapacitors: Materials and devices," *Journal of Energy Storage*, vol. 21, pp. 801–825, 2019.

[47] W. Li and S. Jin, "Design principles and developments of integrated solar flow batteries," *Accounts of Chemical Research*, vol. 53, no. 11, pp. 2611–2621, 2020. PMID: 33085467.

[48] P. Lu, P. Leung, H. Su, W. Yang, and Q. Xu, "Materials, performance, and system design for integrated solar flow batteries – a mini review," *Applied Energy*, vol. 282, p. 116210, 2021.

[49] L. Cao, M. Skyllas-Kazacos, and D.-W. Wang, "Solar redox flow batteries: Mechanism, design, and measurement," *Advanced Sustainable Systems*, vol. 2, no. 8-9, p. 1800031, 2018.

[50] D. Aurbach, B. Mccloskey, L. Nazar, and P. Bruce, "Advances in understanding mechanisms underpinning lithium–air batteries," *Nature Energy*, vol. 1, p. 16128, 09 2016.

[51] F. Jiao and P. Bruce, "Mesoporous crystalline -mno2—a reversible positive electrode for rechargeable lithium batteries," *Advanced Materials*, vol. 19, pp. 657 – 660, 02 2007.

[52] H. Sun, X. Xiang, X. Wang, H.-S. Tsai, and W. Feng, “Advanced photo-rechargeable lithium-and zinc-ion batteries: Progress and prospect,” *Journal of Power Sources*, vol. 598, p. 234204, 2024.

[53] C. Sanchez, P. Belleville, M. Popall, and L. Nicole, “Cheminform abstract: Applications of advanced hybrid organic-inorganic nanomaterials: From laboratory to market,” *Chemical Society reviews*, vol. 40, pp. 696–753, 02 2011.

[54] Y. Yang, C. Zhang, C. Lai, G. Zeng, D. Huang, M. Cheng, J. Wang, F. Chen, C. Zhou, and W. Xiong, “Biox (x=cl, br, i) photocatalytic nanomaterials: Applications for fuels and environmental management,” *Advances in Colloid and Interface Science*, vol. 254, pp. 76–93, 2018.

[55] R. Leary and A. Westwood, “Carbonaceous nanomaterials for the enhancement of tio2 photocatalysis,” *Carbon*, vol. 49, no. 3, pp. 741–772, 2011.

[56] J. Wang, Y. Wang, C. Zhu, and B. Liu, “Photoinduced rechargeable lithium-ion battery,” *ACS Applied Materials & Interfaces*, vol. 14, no. 3, pp. 4071–4078, 2022. PMID: 35012312.

[57] B. D. Boruah, B. Wen, and M. De Volder, “Light rechargeable lithium-ion batteries using v2o5 cathodes,” *Nano Letters*, vol. 21, no. 8, pp. 3527–3532, 2021. PMID: 33856814.

[58] B. Deka Boruah, A. Mathieson, S. K. Park, X. Zhang, B. Wen, L. Tan, A. Boies, and M. De Volder, “Vanadium dioxide cathodes for high-rate photo-rechargeable zinc-ion batteries,” *Advanced Energy Materials*, vol. 11, no. 13, p. 2100115, 2021.

[59] G. Hodes, J. Manassen, and D. Cahen, “Photoelectrochemical energy-conversion and storage using polycrystalline chalcogenide electrodes,” *Nature*, vol. 261, no. 5559, p. 2, 1976.

[60] P. Liu, H. Yang, X. Ai, G. Li, and X. Gao, “A solar rechargeable battery based on polymeric charge storage electrodes,” *Electrochemistry Communications*, vol. 16, no. 1, pp. 69–72, 2012.

[61] M. Yu, X. Ren, L. Ma, and Y. Wu, “Integrating a redox-coupled dye-sensitized photoelectrode into a lithium-oxygen battery for photoassisted charging,” *Nature communications*, vol. 5, p. 5111, 10 2014.

[62] Y. Zhong, X. Xia, W. Mai, J. Tu, and H. J. Fan, “Integration of energy harvesting and electrochemical storage devices,” *Advanced Materials Technologies*, vol. 2, no. 12, p. 1700182, 2017.

[63] J. Xu, Y. Chen, and L. Dai, “Efficiently photo-charging lithium-ion battery by perovskite solar cell,” *Nature Communications*, vol. 6, 2015.

[64] J. Lv, Y.-X. Tan, J. Xie, R. Yang, M. Yu, S. Sun, M.-D. Li, D. Yuan, and Y. Wang, “Direct solar-to-electrochemical energy storage in a functionalized covalent organic framework,” *Angewandte Chemie International Edition*, vol. 57, no. 39, pp. 12716–12720, 2018.

[65] A. Gurung, K. Chen, R. Khan, S. S. Abdulkarim, G. Varnekar, R. Pathak, R. Naderi, and Q. Qiao, “Highly efficient perovskite solar cell photocharging of lithium ion battery using dcâ€“dc booster,” *Advanced Energy Materials*, vol. 7, no. 11, p. 1602105, 2017.

[66] S. Ahmad, C. George, D. J. Beesley, J. J. Baumberg, and M. De Volder, “Photo-rechargeable organo-halide perovskite batteries,” *Nano Letters*, vol. 18, no. 3, pp. 1856–1862, 2018. PMID: 29425044.

[67] B. D. Boruah, B. Wen, and M. De Volder, “Light rechargeable lithium-ion batteries using v2o5 cathodes,” *Nano Letters*, vol. 21, no. 8, pp. 3527–3532, 2021. PMID: 33856814.

[68] B. Deka Boruah and M. De Volder, “Vanadium dioxide–zinc oxide stacked photocathodes for photo-rechargeable zinc-ion batteries,” *J. Mater. Chem. A*, vol. 9, pp. 23199–23205, 2021.

[69] B. D. Boruah, A. Mathieson, B. Wen, C. Jo, F. Deschler, and M. De Volder, “Photo-rechargeable zinc-ion capacitor using 2d graphitic carbon nitride,” *Nano Letters*, vol. 20, no. 8, pp. 5967–5974, 2020. PMID: 32589038.

[70] U. Gangopadhyay, S. Jana, and S. Das, “State of art of solar photovoltaic technology,” *Journal of Energy*, vol. 764132, 01 2013.

[71] N. K. Abd Hamed, M. K. Ahmad, N. Urus, F. Mohamad, N. Nayan, N. Ahmad, C. Soon, A. Ameruddin, F. Abu Bakar, M. Shimomura, and K. Murakami, “Performance comparison between silicon solar panel and dye-sensitized solar panel in malaysia,” vol. 1883, p. 020029, 09 2017.

[72] M. Jamal, M. Bashar, A. M. Hasan, Z. A. Almutairi, H. F. Alharbi, N. H. Alharthi, M. R. Karim, H. Misran, N. Amin, K. B. Sopian, and M. Akhtaruzzaman, “Fabrication techniques and morphological analysis of perovskite absorber layer for high-efficiency perovskite solar cell: A review,” *Renewable and Sustainable Energy Reviews*, vol. 98, pp. 469–488, 2018.

[73] B. O’regan and M. Grätzel, “A low-cost, high-efficiency solar cell based on dye-sensitized colloidal tio2 films,” *nature*, vol. 353, no. 6346, pp. 737–740, 1991.

[74] C. Cavallo, F. Pascasio, A. Latini, M. Bonomo, and D. Dini, “Nanostructured semiconductor materials for dye-sensitized solar cells,” *Journal of Nanomaterials*, vol. 2017, pp. 1–31, 01 2017.

[75] M. K. Nazeeruddin, E. Baranoff, and M. Grätzel, “Dye-sensitized solar cells: A brief overview,” *Solar Energy*, vol. 85, no. 6, pp. 1172–1178, 2011. Organic photovoltaics and dye sensitized solar cells.

[76] A. Hagfeldt, G. Boschloo, L. Sun, L. Kloo, and H. Pettersson, “Dye-sensitized solar cells,” *Chemical Reviews*, vol. 110, no. 11, pp. 6595–6663, 2010. PMID: 20831177.

[77] B. Hardin, H. Snaith, and M. Mcgehee, “The renaissance of dye-sensitized solar cells,” *Nature Photonics*, vol. 6, pp. 162–169, 02 2012.

[78] S. Ferrere, A. Zaban, and B. A. Gregg, “Dye sensitization of nanocrystalline tin oxide by perylene derivatives,” *The Journal of Physical Chemistry B*, vol. 101, no. 23, pp. 4490–4493, 1997.

[79] G. Oskam, B. Bergeron, G. Meyer, and P. Searson, “Pseudohalogens for dye-sensitized tio 2 photoelectrochemical cells,” *Journal of Physical Chemistry B - J PHYS CHEM B*, vol. 105, pp. 6867–6873, 07 2001.

[80] H. Nusbaumer, J.-E. Moser, S. Zakeeruddin, M. Nazeeruddin, and M. Graetzel, “Co ii (dbbip) 2 2+ complex rivals triiodide/iodide redox mediator in dye-sensitized photovoltaic cells,” *Journal of Physical Chemistry B - J PHYS CHEM B*, vol. 105, pp. 10461–10464, 11 2001.

[81] K. Sharma, V. Sharma, and S. S. Sharma (Dr. S. S Sharma), “Dye-sensitized solar cells: Fundamentals and current status,” *Nanoscale Research Letters*, vol. 13, 12 2018.

[82] H. Nagai and H. Segawa, “Energy-storable dye-sensitized solar cell with a polypyrrole electrode,” *Chem. Commun.*, pp. 974–975, 2004.

[83] A. J. Carrillo, J. González-Aguilar, M. Romero, and J. M. Coronado, “Solar energy on demand: A review on high temperature thermochemical heat storage systems and materials,” *Chemical Reviews*, vol. 119, no. 7, pp. 4777–4816, 2019.

[84] B.-M. Kim, M.-H. Lee, V. S. Dilimon, J. S. Kim, J. S. Nam, Y.-G. Cho, H. K. Noh, D.-H. Roh, T.-H. Kwon, and H.-K. Song, “Indoor-light-energy-harvesting dye-sensitized photo-rechargeable battery,” *Energy Environ. Sci.*, vol. 13, pp. 1473–1480, 2020.

[85] H. Wells, “Über die cäsium- und kalium-bleihalogenide,” *Zeitschrift für anorganische Chemie*, vol. 3, pp. 195 – 210, 11 2004.

[86] A. Kojima, K. Teshima, Y. Shirai, and T. Miyasaka, “Organometal halide perovskites as visible-light sensitizers for photovoltaic cells,” *Journal of the American Chemical Society*, vol. 131, no. 17, pp. 6050–6051, 2009. PMID: 19366264.

[87] J. Shamsi, A. S. Urban, M. Imran, L. De Trizio, and L. Manna, “Metal halide perovskite nanocrystals: Synthesis, post-synthesis modifications, and their optical properties,” *Chemical Reviews*, vol. 119, no. 5, pp. 3296–3348, 2019. PMID: 30758194.

[88] H. Huang, B. Pradhan, J. Hofkens, M. B. J. Roeffaers, and J. A. Steele, “Solar-driven metal halide perovskite photocatalysis: Design, stability, and performance,” *ACS Energy Letters*, vol. 5, no. 4, pp. 1107–1123, 2020.

[89] C. Li, K. C. K. Soh, and P. Wu, “Formability of abo3 perovskites,” *Journal of Alloys and Compounds*, vol. 372, no. 1, pp. 40–48, 2004.

[90] J. Jeong, M. Kim, J. Seo, H. Lu, P. Ahlawat, A. Mishra, Y. Yang, M. Hope, F. Eickemeyer, M. Kim, Y. Yoon, I. Choi, B. Darwich, S. Choi, Y. Jo, J. Lee, B. Walker, S. Zakeeruddin, L. Emsley, and J. Y. Kim, “Pseudo-halide anion engineering for -fapbi3 perovskite solar cells,” *Nature*, vol. 592, pp. 1–5, 04 2021.

[91] N. Marinova, S. Valero, and J. L. Delgado, “Organic and perovskite solar cells: Working principles, materials and interfaces,” *Journal of Colloid and Interface Science*, vol. 488, pp. 373–389, 2017.

[92] J. Xu, Y. Chen, and L. Dai, “Efficiently photo-charging lithium-ion battery by perovskite solar cell,” *Nature communications*, vol. 6, no. 1, p. 8103, 2015.

[93] J. Xu, Y. Chen, and L. Dai, “Efficiently photo-charging lithium-ion battery by perovskite solar cell,” *Nature communications*, vol. 6, no. 1, p. 8103, 2015.

[94] S. Ahmad, C. George, D. J. Beesley, J. J. Baumberg, and M. De Volder, “Photo-rechargeable organo-halide perovskite batteries,” *Nano Letters*, vol. 18, no. 3, pp. 1856–1862, 2018. PMID: 29425044.

[95] J. A. Dawson, A. J. Naylor, C. Eames, M. Roberts, W. Zhang, H. J. Snaith, P. G. Bruce, and M. S. Islam, “Mechanisms of lithium intercalation and conversion processes in organicâ€“inorganic halide perovskites,” *ACS Energy Letters*, vol. 2, no. 8, pp. 1818–1824, 2017.

[96] T. Ishihara, “Optical properties of pbi-based perovskite structures,” *Journal of Luminescence*, vol. 60-61, pp. 269–274, 1994.

[97] H. Tsai, W. Nie, J.-C. Blancon, C. Stoumpos, R. Asadpour, B. Harutyunyan, A. Neukirch, R. Verduzco, J. Crochet, S. Tretiak, L. Pedesseau, J. Even, M. Alam, G. Gupta, J. Lou, P. Ajayan, M. Bedzyk, M. Kanatzidis, and A. Mohite, “High-efficiency two-dimensional ruddlesden-popper perovskite solar cells,” *Nature*, vol. 536, 07 2016.

[98] R. L. Milot, R. J. Sutton, G. E. Eperon, A. A. Haghighirad, J. Martinez Hardigree, L. Miranda, H. J. Snaith, M. B. Johnston, and L. M. Herz, “Charge-carrier dynamics in 2d hybrid metalâ€“halide perovskites,” *Nano Letters*, vol. 16, no. 11, pp. 7001–7007, 2016. PMID: 27689536.

[99] M. Martos and L. Sánchez, “Lead-based systems as suitable anode materials for li-ion batteries,” *Electrochimica Acta - ELECTROCHIM ACTA*, vol. 48, pp. 615–621, 02 2003.

[100] F. Cao, L. Bian, and L. Li, “Perovskite solar cells with high-efficiency exceeding 25

[101] N. Tewari, D. Lam, C. H. A. Li, and J. E. Halpert, “Recent advancements in batteries and photo-batteries using metal halide perovskites,” *APL Materials*, vol. 10, no. 4, 2022.

[102] J. Büttner, T. Berestok, S. Burger, M. Schmitt, M. Daub, H. Hillebrecht, I. Krossing, and A. Fischer, “Are halide-perovskites suitable materials for battery and solar-battery applications–fundamental reconsiderations on solubility, lithium intercalation, and photo-corrosion,” *Advanced Functional Materials*, vol. 32, no. 49, p. 2206958, 2022.

[103] S. Ahmad, C. George, D. J. Beesley, J. J. Baumberg, and M. De Volder, “Photo-rechargeable organo-halide perovskite batteries,” *Nano letters*, vol. 18, no. 3, pp. 1856–1862, 2018.

[104] N. Tewari, S. B. Shivarudraiah, and J. E. Halpert, “Photorechargeable lead-free perovskite lithium-ion batteries using hexagonal cs3bi2i9 nanosheets,” *Nano Letters*, vol. 21, no. 13, pp. 5578–5585, 2021.

[105] S. Meher, “6 - transition metal oxide-based materials for visible-light-photocatalysis,” in *Nanostructured Materials for Visible Light Photocatalysis* (A. K. Nayak and N. K. Sahu, eds.), Micro and Nano Technologies, pp. 153–183, Elsevier, 2022.

[106] L. V. Bora and R. K. Mewada, “Visible/solar light active photocatalysts for organic effluent treatment: Fundamentals, mechanisms and parametric review,” *Renewable and Sustainable Energy Reviews*, vol. 76, pp. 1393–1421, 2017.

[107] Y. Sun, J. Zhang, T. Huang, Z. Liu, and A. Yu, “Fe2o3/cnts composites as anode materials for lithium-ion batteries,” *International Journal of Electrochemical Science*, vol. 8, pp. 2918–2931, 02 2013.

[108] L. Noerochim, M. A. Taimiyah Indra, H. Purwaningsih, and A. Subhan, “Porous fe 2 o 3 microspheres as anode for lithium-ion batteries,” *IOP Conference Series: Materials Science and Engineering*, vol. 367, p. 012038, 05 2018.

[109] M. Ashraf, I. Khan, M. Usman, A. Khan, S. S. Shah, A. Z. Khan, K. Saeed, M. Yaseen, M. F. Ehsan, M. N. Tahir, and N. Ullah, “Hematite and magnetite nanostructures for green and sustainable energy harnessing and environmental pollution control: A review,” *Chemical Research in Toxicology*, vol. 33, no. 6, pp. 1292–1311, 2020. PMID: 31884781.

[110] Y. Xue and Y. Wang, “A review of the -fe2o3 (hematite) nanotube structure: recent advances in synthesis, characterization, and applications,” *Nanoscale*, vol. 12, pp. 10912–10932, 2020.

[111] C. Wu, P. Yin, X. Zhu, C. OuYang, and Y. Xie, “Synthesis of hematite (-fe2o3) nanorods:?diameter-size and shape effects on their applications in magnetism, lithium ion battery, and gas sensors,” *The Journal of Physical Chemistry B*, vol. 110, no. 36, pp. 17806–17812, 2006. PMID: 16956266.

[112] S. Chamola and S. Ahmad, “High performance photorechargeable li-ion batteries based on nanoporous fe2o3 photocathodes,” *Advanced Sustainable Systems*, vol. 7, no. 6, p. 2300043, 2023.

[113] R. Khan, J. Banerjee, G. P. Sharma, A. Nagendra, D. Bhattacharyya, and S. Sivakumar, “Vanadium doping enhances the photo-capacity of fe2o3 nanoflowers: A promising photo-battery electrode material for iron-ion batteries,” *Available at SSRN 4510190*.

[114] S. Chamola and S. Ahmad, “High performance photorechargeable li-ion batteries based on nanoporous fe2o3 photocathodes,” *ADVANCED SUSTAINABLE SYSTEMS*, vol. 7, JUN 2023.

[115] C. Tomon, S. Sarawutanukul, S. Duangdangchote, A. Krittayavathananon, and M. Sawangphruk, “Photoactive zn–air batteries using spinel-type cobalt oxide as a bifunctional photocatalyst at the air cathode,” *Chem. Commun.*, vol. 55, pp. 5855–5858, 2019.

[116] C. Tomon, S. Sarawutanukul, S. Duangdangchote, A. Krittayavathananon, and M. Sawangphruk, “Photoactive zn–air batteries using spinel-type cobalt oxide as a bifunctional photocatalyst at the air cathode,” *Chemical communications*, vol. 55, no. 42, pp. 5855–5858, 2019.

[117] Y. Fan, N. Zhang, L. Zhang, H. Shao, J. Wang, J. Zhang, and C. Cao, “Co3o4-coated tio2 nanotube composites synthesized through photo-deposition strategy with enhanced performance for lithium-ion batteries,” *Electrochimica Acta*, vol. 94, pp. 285–293, 2013.

[118] Y. Zhao, X. Wang, H. Li, B. Qian, Y. Zhang, and Y. Wu, “Synthesis of co3o4 nanospheres for enhanced photo-assisted supercapacitor,” *Chemical Engineering Journal*, vol. 431, p. 133981, 2022.

[119] L. Bai, H. Huang, S. Zhang, L. Hao, Z. Zhang, H. Li, L. Sun, L. Guo, H. Huang, and Y. Zhang, “Photocatalysis-assisted co3o4/g-c3n4 p–n junction all-solid-state supercapacitors: A bridge between energy storage and photocatalysis,” *Advanced science*, vol. 7, no. 22, p. 2001939, 2020.

[120] H. Ren, S. Sun, J. Cui, and X. Li, “Synthesis, functional modifications, and diversified applications of molybdenum oxides micro-/nanocrystals: A review,” *Crystal Growth & Design*, vol. 18, no. 10, pp. 6326–6369, 2018.

[121] A. Khademi, R. Azimirad, A. A. Zavarian, and A. Z. Moshfegh, “Growth and field emission study of molybdenum oxide nanostars,” *The Journal of Physical Chemistry C*, vol. 113, no. 44, pp. 19298–19304, 2009.

[122] Y. Zhang, P. Chen, Q. Wang, Q. Wang, K. Zhu, K. Ye, G. Wang, D. Cao, J. Yan, and Q. Zhang, “High-capacity and kinetically accelerated lithium storage in moo3 enabled by oxygen vacancies and heterostructure,” *Advanced Energy Materials*, vol. 11, no. 31, p. 2101712, 2021.

[123] Y. Zhu, Y. Yao, Z. Luo, C. Pan, J. Yang, Y. Fang, H. Deng, C. Liu, Q. Tan, F. Liu, *et al.*, “Nanostructured moo3 for efficient energy and environmental catalysis,” *Molecules*, vol. 25, no. 1, p. 18, 2019.

[124] E. Avigad and L. Etgar, “Studying the effect of moo3 in hole-conductor-free perovskite solar cells,” *ACS Energy Letters*, vol. 3, no. 9, pp. 2240–2245, 2018.

[125] G. Sun, D. Yang, Z. Zhang, Y. Wang, W. Lu, and M. Feng, “Oxygen vacancy-rich moo 3 nanorods as photocatalysts for photo-assisted li-o 2 batteries.,” *Journal of Advanced Ceramics*, vol. 12, no. 4, 2023.

[126] Z. Xue, Z. Wang, Q. Li, D. Wang, L. Xiang, Z. Mai, P. Du, H. Sun, and G. Xing, “Tailored plasmonic ru/ov-moo2 on tio2 catalysts via solid-phase interface engineering: Toward highly efficient photoassisted li–o2 batteries with enhanced cycling reliability,” *ACS Applied Materials & Interfaces*, vol. 14, no. 39, pp. 44251–44260, 2022.

[127] L. Ren, M. Zheng, F. Kong, Z. Yu, N. Sun, M. Li, Q. Liu, Y. Song, J. Dong, J. Qiao, *et al.*, “Light enables the cathodic interface reaction reversibility in solid-state lithium-oxygen batteries,” *Angewandte Chemie*, vol. 136, no. 17, p. e202319529, 2024.

[128] Z. Zhang, W. Fang, G. Fang, M. Bai, and X. Hu, “Construct heterostructures of moo3 nanorods modified with fe2o3 rice grains to improve the performance of light-involved li-o2 battery,” *Available at SSRN 4844279*.

[129] S. N. Lou, N. Sharma, D. Goonetilleke, W. H. Saputera, T. M. Leoni, P. Brockbank, S. Lim, D.-W. Wang, J. Scott, R. Amal, *et al.*, “An operando mechanistic evaluation of a solar-rechargeable sodium-ion intercalation battery,” *Advanced Energy Materials*, vol. 7, no. 19, p. 1700545, 2017.

[130] N. T. Narayanan, A. Kumar, P. Thakur, R. Sharma, A. Puthirath, and A. Pulickel, “Photo rechargeable li-ion batteries using nanorod heterostructure electrodes,” 2021.

[131] S. N. Lou, N. Sharma, D. Goonetilleke, W. H. Saputera, T. M. Leoni, P. Brockbank, S. Lim, D.-W. Wang, J. Scott, R. Amal, and Y. H. Ng, “An operando mechanistic evaluation of a solar-rechargeable sodium-ion intercalation battery,” *Advanced Energy Materials*, vol. 7, no. 19, p. 1700545, 2017.

[132] M. Spahr, P. NovÃ¡k, O. Haas, and R. Nesper, “Electrochemical insertion of lithium, sodium, and magnesium in molybdenum(vi) oxide,” *Journal of Power Sources*, vol. 54, no. 2, pp. 346–351, 1995. Proceedings of the Seventh International Meeting on Lithium Batteries.

[133] B. Yebka, B. Pecquenard, C. Julien, and J. Livage, “Electrochemical li+ insertion in wo3â€“xtio2 mixed oxides,” *Solid State Ionics*, vol. 104, no. 3, pp. 169–175, 1997.

[134] C. Wu and Y. Xie, “Promising vanadium oxide and hydroxide nanostructures: from energy storage to energy saving,” *Energy Environ. Sci.*, vol. 3, pp. 1191–1206, 2010.

[135] M. Liu, B. Su, Y. Tang, X. Jiang, and A. Yu, “Recent advances in nanostructured vanadium oxides and composites for energy conversion,” *Advanced Energy Materials*, vol. 7, no. 23, p. 1700885, 2017.

[136] B. D. Boruah, A. Mathieson, B. Wen, S. Feldmann, W. M. Dose, and M. De Volder, “Photo-rechargeable zinc-ion batteries,” *Energy Environ. Sci.*, vol. 13, pp. 2414–2421, 2020.

[137] B. Deka Boruah, A. Mathieson, S. K. Park, X. Zhang, B. Wen, L. Tan, A. Boies, and M. De Volder, “Vanadium dioxide cathodes for high-rate photo-rechargeable zinc-ion batteries,” *Advanced Energy Materials*, vol. 11, no. 13, p. 2100115, 2021.

[138] B. D. Boruah and M. De Volder, “Vanadium dioxide–zinc oxide stacked photocathodes for photo-rechargeable zinc-ion batteries,” *Journal of Materials Chemistry A*, vol. 9, no. 40, pp. 23199–23205, 2021.

[139] B. D. Boruah, A. Mathieson, B. Wen, S. Feldmann, W. M. Dose, and M. De Volder, “Photo-rechargeable zinc-ion batteries,” *Energy & Environmental Science*, vol. 13, no. 8, pp. 2414–2421, 2020.

[140] B. D. Boruah, B. Wen, and M. De Volder, “Light rechargeable lithium-ion batteries using v2o5 cathodes,” *Nano Letters*, vol. 21, no. 8, pp. 3527–3532, 2021.

[141] Y. Lu, H. Andersen, R. Wu, A. M. Ganose, B. Wen, A. Pujari, T. Wang, J. Borowiec, I. P. Parkin, M. De Volder, *et al.*, “Hydrogenated v2o5 with improved optical and electrochemical activities for photo-accelerated lithium-ion batteries,” *Small*, vol. 20, no. 14, p. 2308869, 2024.

[142] B. D. Boruah, B. Wen, S. Nagane, X. Zhang, S. D. Stranks, A. Boies, and M. De Volder, “Photo-rechargeable zinc-ion capacitors using v2o5-activated carbon electrodes,” *ACS Energy Letters*, vol. 5, no. 10, pp. 3132–3139, 2020.

[143] J. Schneider, M. Matsuoka, M. Takeuchi, J. Zhang, Y. Horiuchi, M. Anpo, and D. W. Bahnemann, “Understanding tio2 photocatalysis: mechanisms and materials,” *Chemical reviews*, vol. 114, no. 19, pp. 9919–9986, 2014.

[144] A. Fujishima and K. Honda, “Electrochemical photolysis of water at a semiconductor electrode,” *nature*, vol. 238, no. 5358, pp. 37–38, 1972.

[145] Z. Yang, D. Choi, S. Kerisit, K. M. Rosso, D. Wang, J. Zhang, G. Graff, and J. Liu, “Nanostructures and lithium electrochemical reactivity of lithium titanites and titanium oxides: A review,” *Journal of Power Sources*, vol. 192, no. 2, pp. 588–598, 2009.

[146] W. Yan, J. Wang, Q. Hu, J. Fu, M. K. Albolkany, T. Zhang, X. Lu, F. Ye, and B. Liu, “Approaching the theoretical capacity of tio2 anode in a photo-rechargeable lithium-ion battery,” *Nano Research*, vol. 17, no. 4, pp. 2655–2662, 2024.

[147] L. Long, Y. Ding, N. Liang, J. Liu, F. Liu, S. Huang, and Y. Meng, “A carbon-free and free-standing cathode from mixed-phase tio2 for photo-assisted li–co2 battery,” *Small*, vol. 19, no. 27, p. 2300519, 2023.

[148] H. Jiao, G. Sun, Y. Wang, Z. Zhang, Z. Wang, H. Wang, H. Li, and M. Feng, “Defective tio2 hollow nanospheres as photo-electrocatalysts for photo-assisted li-o2 batteries,” *Chinese Chemical Letters*, vol. 33, no. 8, pp. 4008–4012, 2022.

[149] X. Zou, N. Maesako, T. Nomiyama, Y. Horie, and T. Miyazaki, “Photo-rechargeable battery with tio2/carbon fiber electrodes prepared by laser deposition,” *Solar energy materials and solar cells*, vol. 62, no. 1-2, pp. 133–142, 2000.

[150] L. Kong, J. Qiao, Q. Ruan, H. Wang, X. Xi, W. Zha, Z. Zhou, W. He, W. Zhang, and Z. Sun, “A very low charge potential for zinc-air battery promoted by photochemical effect of triazine-based conjugated polymer nanolayer coated tio2,” *Journal of Power Sources*, vol. 536, p. 231507, 2022.

[151] L. Zhang, X. Bai, G. Zhao, X. Shen, Y. Liu, X. Bao, J. Luo, L. Yu, and N. Zhang, “A visible light illumination assistant li-o2 battery based on an oxygen vacancy doped tio2 catalyst,” *Electrochimica Acta*, vol. 405, p. 139794, 2022.

[152] C. Hu, L. Chen, Y. Hu, A. Chen, L. Chen, H. Jiang, and C. Li, “Light-motivated sno2/tio2 heterojunctions enabling the breakthrough in energy density for lithium-ion batteries,” *ADVANCED MATERIALS*, vol. 33, DEC 2021.

[153] T. Jayaraman, K. Karuppasamy, D. Govindarajan, A. u. H. Rana, P. Arunachalam, S. Kirubanandam, K. Parasuraman, and H.-S. Kim, "Recent advances in metal chalcogenides (mx; x = s, se) nanostructures for electrochemical supercapacitor applications: A brief review," *Nanomaterials*, vol. 8, p. 256, 04 2018.

[154] R. Ktz and M. Carlen, "Principles and applications of electrochemical capacitors," *Electrochimica Acta*, vol. 45, no. 15, pp. 2483–2498, 2000.

[155] Z. Peimanifard and S. Rashid-Nadimi, "Glassy carbon/multi walled carbon nanotube/cadmium sulphide photoanode for light energy storage in vanadium photoelectrochemical cell," *Journal of Power Sources*, vol. 300, pp. 395–401, 2015.

[156] C. Ren, Q. Zhou, W. Jiang, J. Li, C. Guo, L. Zhang, and J. Su, "Investigation of germanium selenide electrodes for the integrated photo-rechargeable battery," *International Journal of Energy Research*, vol. 44, 03 2020.

[157] B. D. Boruah, B. Wen, and M. De Volder, "Molybdenum disulfideinc oxide photocathodes for photo-rechargeable zinc-ion batteries," *ACS Nano*, vol. 15, no. 10, pp. 16616–16624, 2021. PMID: 34609134.

[158] D.-H. Guan, X.-X. Wang, M.-L. Li, F. Li, L.-J. Zheng, X.-L. Huang, and J.-J. Xu, "Light/electricity energy conversion and storage for a hierarchical porous in2s3@cnt/ss cathode towards a flexible li-co2 battery," *Angewandte Chemie International Edition*, vol. 59, no. 44, pp. 19518–19524, 2020.

[159] B. D. Boruah, B. Wen, and M. De Volder, "Molybdenum disulfideinc oxide photocathodes for photo-rechargeable zinc-ion batteries," *ACS Nano*, vol. 15, no. 10, pp. 16616–16624, 2021. PMID: 34609134.

[160] Y. Xu, M. Zhou, and Y. Lei, "Organic materials for rechargeable sodium-ion batteries," *Materials Today*, vol. 21, no. 1, pp. 60–78, 2018.

[161] Y. Chen and C. Wang, "Designing high performance organic batteries," *Accounts of Chemical Research*, vol. 53, no. 11, pp. 2636–2647, 2020. PMID: 32976710.

[162] J. Xie and Q. Zhang, "Recent progress in aqueous monovalent-ion batteries with organic materials as promising electrodes," *Materials Today Energy*, vol. 18, p. 100547, 2020.

[163] K. Kato, A. B. Puthirath, A. Mojibpour, M. Miroshnikov, S. Satapathy, N. K. Thangavel, K. Mahankali, L. Dong, L. M. R. Arava, G. John, P. Bharadwaj, G. Babu, and P. M. Ajayan, "Light-assisted rechargeable lithium batteries: Organic molecules for simultaneous energy harvesting and storage," *Nano Letters*, vol. 21, no. 2, pp. 907–913, 2021. PMID: 33416335.

[164] Q. Lv, Z. Zhu, S. Zhao, L. Wang, Q. Zhao, F. Li, L. A. Archer, and J. Chen, "Semiconducting metal–organic polymer nanosheets for a photoinvolved li–o2 battery under visible light," *Journal of the American Chemical Society*, vol. 143, no. 4, pp. 1941–1947, 2021. PMID: 33467851.

[165] Z. Yang, P. Zhu, Z. Ullah, S. Zheng, S. Yu, S. Zhu, L. Liu, and Q. Li, "Synchronous light harvesting and energy storing organic cathode material 1,4-dihydroxyanthraquinone for lithium-ion batteries," *Chemical Engineering Journal*, vol. 468, p. 143787, 2023.

[166] Z. Yang, P. Zhu, Z. Ullah, S. Zheng, S. Yu, S. Zhu, L. Liu, and Q. Li, "Synchronous light harvesting and energy storing organic cathode material 1,4-dihydroxyanthraquinone for lithium-ion batteries," *Chemical Engineering Journal*, vol. 468, p. 143787, 2023.

[167] W. Guo, X. Xue, S. Wang, C. Lin, and Z. L. Wang, "An integrated power pack of dye-sensitized solar cell and li battery based on double-sided tio2 nanotube arrays," *Nano Letters*, vol. 12, no. 5, pp. 2520–2523, 2012. PMID: 22519631.

[168] M. A. Mahmoudzadeh, A. Usgaocar, J. Giorgio, D. Officer, G. Wallace, and J. Madden, "A high energy density solar rechargeable redox battery," *J. Mater. Chem. A*, vol. 4, 02 2016.

[169] C. Xu, X. Zhang, L. Duan, X. Zhang, X. Li, and W. Lü, "A photo-assisted rechargeable battery: synergy, compatibility, and stability of a tio2/dye/cu2s bifunctional composite electrode," *Nanoscale*, vol. 12, pp. 530–537, 2020.

[170] J. Li, C. Ren, L. Zhang, W. Jiang, H. Liu, J. Su, and M. Li, "Hybridized s cathode with n719 dye for a photo-assisted charging li-s battery," *Journal of Energy Chemistry*, vol. 65, pp. 205–209, 2022.

[171] M.-H. Lee, B.-M. Kim, Y. Lee, H.-G. Han, M. Cho, T.-H. Kwon, and H.-K. Song, "Electrochemically induced crystallite alignment of lithium manganese oxide to improve lithium insertion kinetics for dye-sensitized photorechargeable batteries," *ACS Energy Letters*, vol. 6, no. 4, pp. 1198–1204, 2021.

[172] M. Yu, X. Ren, L. Ma, and Y. Wu, "Integrating a redox-coupled dye-sensitized photoelectrode into a lithium-oxygen battery for photoassisted charging," *Nature communications*, vol. 5, p. 5111, 10 2014.

[173] M. Yu, W. D. McCulloch, D. R. Beauchamp, Z. Huang, X. Ren, and Y. Wu, "Aqueous lithium–iodine solar flow battery for the simultaneous conversion and storage of solar energy," *Journal of the American Chemical Society*, vol. 137, no. 26, pp. 8332–8335, 2015. PMID: 26102317.

[174] Y.-Y. Gui, F.-X. Ai, J.-F. Qian, Y.-L. Cao, G.-R. Li, X.-P. Gao, and H.-X. Yang, "A solar rechargeable battery based on the sodium ion storage mechanism with fe2(moo4)3 microspheres as anode materials," *J. Mater. Chem. A*, vol. 6, pp. 10627–10631, 2018.

[175] R. Wang, K. Sun, H. Liu, C. Qian, M. Li, Y. Zhang, and W. Bao, "Integrating a redox-coupled fese2/n–c photoelectrode into potassium ion hybrid capacitors for photoassisted charging," *J. Mater. Chem. A*, vol. 10, pp. 11504–11513, 2022.

[176] J. Li, H. Liu, K. Sun, R. Wang, C. Qian, F. Yu, L. Zhang, and W. Bao, "Dual-functional iodine photoelectrode enabling high performance photo-assisted rechargeable lithium iodine batteries," *J. Mater. Chem. A*, vol. 10, pp. 7326–7332, 2022.

[177] C. Andriamiadamanana, I. Sagaidak, G. Bouteau, C. Davoisne, C. Laberty-Robert, and F. Sauvage, “Light-induced charge separation in mixed electronic/ionic semiconductor driving lithium-ion transfer for photo-rechargeable electrode,” *Advanced Sustainable Systems*, vol. 2, no. 5, p. 1700166, 2018.

[178] X. Liu, Y. Yuan, J. Liu, B. Liu, X. Chen, J. Ding, X. Han, D. Yida, C. Zhong, and W. Hu, “Utilizing solar energy to improve the oxygen evolution reaction kinetics in zinc–air battery,” *Nature Communications*, vol. 10, 10 2019.

[179] B. Deka Boruah, A. Mathieson, S. K. Park, X. Zhang, B. Wen, L. Tan, A. Boies, and M. De Volder, “Vanadium dioxide cathodes for high-rate photo-rechargeable zinc-ion batteries,” *Advanced Energy Materials*, vol. 11, no. 13, p. 2100115, 2021.

[180] B. D. Boruah, B. Wen, and M. De Volder, “Light rechargeable lithium-ion batteries using v2o5 cathodes,” *Nano Letters*, vol. 21, no. 8, pp. 3527–3532, 2021. PMID: 33856814.

[181] J. Wang, Y. Wang, C. Zhu, and B. Liu, “Photoinduced rechargeable lithium-ion battery,” *ACS Applied Materials & Interfaces*, vol. 14, no. 3, pp. 4071–4078, 2022. PMID: 35012312.

[182] M. Zhang, L. Pan, Z. Jin, X. Wang, H. Mei, L. Cheng, and L. Zhang, “Multiplying light harvest driven by hybrid-reflections 3d electrodes achieves high-availability photo-charging zinc-ion batteries,” *Advanced Energy Materials*, vol. 13, no. 15, p. 2204058, 2023.

[183] O. Nguyen, E. Courtin, F. Sauvage, N. Krins, C. Sanchez, and C. Laberty-Robert, “Shedding light on the light-driven lithium ion de-insertion reaction: towards the design of a photo-rechargeable battery,” *J. Mater. Chem. A*, vol. 5, pp. 5927–5933, 2017.

[184] R. Kumar, A. Kumar, P. S. Shukla, G. D. Varma, D. Venkataraman, and M. Bag, “Photorechargeable hybrid halide perovskite supercapacitors,” *ACS Applied Materials & Interfaces*, vol. 14, no. 31, pp. 35592–35599, 2022. PMID: 35903891.

[185] H. Liu, P. Wu, R. Wang, H. Meng, Y. Zhang, W. Bao, and J. Li, “A photo-rechargeable aqueous zinc–tellurium battery enabled by the janus-jointed perovskite/te photocathode,” *ACS Nano*, vol. 17, no. 2, pp. 1560–1569, 2023. PMID: 36622820.

[186] J. Han, S. Lee, C. Youn, J. Lee, Y. Kim, and T. Choi, “Hybrid photoelectrochemical-rechargeable seawater battery for efficient solar energy storage systems,” *Electrochimica Acta*, vol. 332, p. 135443, 2020.

[187] W. Yan, J. Wang, Q. Hu, J. Fu, M. K. Albolkany, T. Zhang, X. Lu, F. Ye, and B. Liu, “Approaching the theoretical capacity of tio2 anode in a photo-rechargeable lithium-ion battery,” *Nano Research*, 2023.

[188] Y. Feng, H. Xue, T. Wang, H. Gong, B. Gao, W. Xia, C. Jiang, J. Li, X. Huang, and J. He, “Enhanced li2o2 decomposition in rechargeable li-o-2 battery by incorporating wo3 nanowire array photocatalyst,” *ACS SUSTAINABLE CHEMISTRY & ENGINEERING*, vol. 7, pp. 5931–5939, MAR 18 2019.

[189] A. Lee, M. Voros, W. M. Dose, J. Niklas, O. Poluektov, R. D. Schaller, H. Iddir, V. A. Maroni, E. Lee, B. Ingram, L. A. Curtiss, and C. S. Johnson, "Photo-accelerated fast charging of lithium-ion batteries," *NATURE COMMUNICATIONS*, vol. 10, OCT 30 2019.

[190] Q. Zhang, M. Wei, Q. Dong, Q. Gao, X. Cai, S. Zhang, T. Yuan, F. Peng, Y. Fang, and S. Yang, "Photoinduced cu+/cu2+ interconversion for enhancing energy conversion and storage performances of cuo based li-ion battery," *Journal of Energy Chemistry*, vol. 79, pp. 83–91, 2023.

[191] Z. Peimanifard and S. Rashid-Nadimi, "Glassy carbon/multi walled carbon nanotube/cadmium sulphide photoanode for light energy storage in vanadium photoelectrochemical cell," *Journal of Power Sources*, vol. 300, pp. 395–401, 2015.

[192] D.-H. Guan, X.-X. Wang, M.-L. Li, F. Li, L.-J. Zheng, X.-L. Huang, and J.-J. Xu, "Light/electricity energy conversion and storage for a hierarchical porous in2s3@cnt/ss cathode towards a flexible li-co2 battery," *Angewandte Chemie International Edition*, vol. 59, no. 44, pp. 19518–19524, 2020.

[193] A. Kumar, P. Thakur, R. Sharma, A. B. Puthirath, P. M. Ajayan, and T. N. Narayanan, "Photo rechargeable li-ion batteries using nanorod heterostructure electrodes," *Small*, vol. 17, no. 51, p. 2105029, 2021.

[194] Q. Lv, Z. Zhu, S. Zhao, L. Wang, Q. Zhao, F. Li, L. A. Archer, and J. Chen, "Semiconducting metal–organic polymer nanosheets for a photoinvolved li–o2 battery under visible light," *Journal of the American Chemical Society*, vol. 143, no. 4, pp. 1941–1947, 2021. PMID: 33467851.

[195] K. Kato, A. B. Puthirath, A. Mojibpour, M. Miroshnikov, S. Satapathy, N. K. Thangavel, K. Mahankali, L. Dong, L. M. R. Arava, G. John, P. Bharadwaj, G. Babu, and P. M. Ajayan, "Light-assisted rechargeable lithium batteries: Organic molecules for simultaneous energy harvesting and storage," *Nano Letters*, vol. 21, no. 2, pp. 907–913, 2021. PMID: 33416335.

[196] D. Du, S. Zhao, Z. Zhu, F. Li, and J. Chen, "Photo-excited oxygen reduction and oxygen evolution reactions enable a high-performance zn–air battery," *Angewandte Chemie International Edition*, vol. 59, no. 41, pp. 18140–18144, 2020.

[197] S. Chu and A. Majumdar, "Opportunities and challenges for a sustainable energy future," *Nature*, vol. 488, pp. 294–303, 08 2012.

[198] C. Shih, T. Zhang, J. Li, and C. Bai, "Powering the future with liquid sunshine," *Joule*, vol. 2, 09 2018.

[199] J. Gong, C. Li, and M. Wasielewski, "Advances in solar energy conversion," *Chemical Society Reviews*, vol. 48, 04 2019.

[200] D. P. Almond and P. M. Patel, "Photothermal science and techniques," 1996.

[201] X. Liu, B. Li, F. Fu, K. Xu, R. Zou, Q. Wang, B. Zhang, Z. Chen, and J. Hu, “Facile synthesis of biocompatible cysteine-coated cus nanoparticles with high photothermal conversion efficiency for cancer therapy,” *Dalton Trans.*, vol. 43, pp. 11709–11715, 2014.

[202] H. Chen, L. Shao, T. Ming, Z. Sun, C. Zhao, B. Yang, and J. Wang, “Understanding the photothermal conversion efficiency of gold nanocrystals,” *Small*, vol. 6, no. 20, pp. 2272–2280, 2010.

[203] L. Jauffred, A. Samadi, H. Klingberg, P. M. Bendix, and L. B. Oddershede, “Plasmonic heating of nanostructures,” *Chemical Reviews*, vol. 119, no. 13, pp. 8087–8130, 2019. PMID: 31125213.

[204] X. Huang, W. Zhang, G. Guan, G. Song, R. Zou, and J. Hu, “Design and functionalization of the nir-responsive photothermal semiconductor nanomaterials for cancer theranostics,” *Accounts of Chemical Research*, vol. 50, no. 10, pp. 2529–2538, 2017. PMID: 28972736.

[205] N. Panwar, A. M. Soehartono, K. K. Chan, S. Zeng, G. Xu, J. Qu, P. Coquet, K.-T. Yong, and X. Chen, “Nanocarbons for biology and medicine: Sensing, imaging, and drug delivery,” *Chemical Reviews*, vol. 119, no. 16, pp. 9559–9656, 2019. PMID: 31287663.

[206] H. S. Jung, P. Verwilst, A. Sharma, J. Shin, J. L. Sessler, and J. S. Kim, “Organic molecule-based photothermal agents: an expanding photothermal therapy universe,” *Chem. Soc. Rev.*, vol. 47, pp. 2280–2297, 2018.

[207] X. Wang, Y. He, X. Liu, L. Shi, and J. Zhu, “Investigation of photothermal heating enabled by plasmonic nanofluids for direct solar steam generation,” *Solar Energy*, vol. 157, pp. 35–46, 2017.

[208] G. Ni, N. Miljkovic, H. Ghasemi, X. Huang, S. V. Boriskina, C.-T. Lin, J. Wang, Y. Xu, M. M. Rahman, T. Zhang, and G. Chen, “Volumetric solar heating of nanofluids for direct vapor generation,” *Nano Energy*, vol. 17, pp. 290–301, 2015.

[209] W. Zhao, H. Gong, Y. Song, B. Li, N. Xu, X. Min, G. Liu, B. Zhu, L. Zhou, X.-X. Zhang, and J. Zhu, “Hierarchically designed salt-resistant solar evaporator based on donnan effect for stable and high-performance brine treatment,” *Advanced Functional Materials*, vol. 31, no. 23, p. 2100025, 2021.

[210] Y. Wang, L. Zhang, and P. Wang, “Self-floating carbon nanotube membrane on macroporous silica substrate for highly efficient solar-driven interfacial water evaporation,” *ACS Sustainable Chemistry & Engineering*, vol. 4, no. 3, pp. 1223–1230, 2016.

[211] H. Ghasemi, G. Ni, A. Marconnet, J. Loomis, S. Yerci, N. Miljkovic, and G. Chen, “Solar steam generation by heat localization,” *Nature communications*, vol. 5, p. 4449, 07 2014.

[212] Y. Ito, Y. Tanabe, J. Han, T. Fujita, K. Tanigaki, and M. Chen, “Multifunctional porous graphene for high-efficiency steam generation by heat localization,” *Advanced Materials*, vol. 27, no. 29, pp. 4302–4307, 2015.

[213] H. Ren, M. Tang, B. Guan, K. Wang, J. Yang, F. Wang, M. Wang, J. Shan, Z. Chen, D. Wei, H. Peng, and Z. Liu, "Hierarchical graphene foam for efficient omnidirectional solar–thermal energy conversion," *Advanced Materials*, vol. 29, no. 38, p. 1702590, 2017.

[214] X. Li, W. Xu, M. Tang, L. Zhou, B. Zhu, S. Zhu, and J. Zhu, "Graphene oxide-based efficient and scalable solar desalination under one sun with a confined 2d water path," *Proceedings of the National Academy of Sciences*, vol. 113, no. 49, pp. 13953–13958, 2016.

[215] Q. Zhang, X. Xiao, G. Wang, X. Ming, X. Liu, H. Wang, H. Yang, W. Xu, and X. Wang, "Silk-based systems for highly efficient photothermal conversion under one sun: portability, flexibility, and durability," *J. Mater. Chem. A*, vol. 6, pp. 17212–17219, 2018.

[216] K.-K. Liu, Q. Jiang, S. Tadepalli, R. Raliya, P. Biswas, R. R. Naik, and S. Singamaneni, "Wood–graphene oxide composite for highly efficient solar steam generation and desalination," *ACS Applied Materials & Interfaces*, vol. 9, no. 8, pp. 7675–7681, 2017. PMID: 28151641.

[217] P. Yang, K. Liu, Q. Chen, J. Li, J. Duan, G. Xue, Z. Xu, W. Xie, and J. Zhou, "Solar-driven simultaneous steam production and electricity generation from salinity," *Energy Environ. Sci.*, vol. 10, pp. 1923–1927, 2017.

[218] Y. Liu, X. Wang, and H. Wu, "High-performance wastewater treatment based on reusable functional photo-absorbers," *Chemical Engineering Journal*, vol. 309, pp. 787–794, 2017.

[219] K. Bae, G. Kang, S. Cho, W. Park, K. Kim, and W. Padilla, "Flexible thin-film black gold membranes with ultrabroadband plasmonic nanofocusing for efficient solar vapour generation," *Nature communications*, vol. 6, p. 10103, 12 2015.

[220] X. Wu, Q. Jiang, D. Ghim, S. Singamaneni, and Y.-S. Jun, "Localized heating with a photothermal polydopamine coating facilitates a novel membrane distillation process," *J. Mater. Chem. A*, vol. 6, pp. 18799–18807, 2018.

[221] L. Zhou, Y. Tan, J. Wang, W. Xu, Y. Yuan, W. Cai, S. Zhu, and P. Jia, "3d self-assembly of aluminium nanoparticles for plasmon-enhanced solar desalination," *Nature Photonics*, vol. 10, 04 2016.

[222] Z. Hua, B. Li, L. Li, X. Yin, K. Chen, and W. Wang, "Designing a novel photothermal material of hierarchical microstructured copper phosphate for solar evaporation enhancement," *The Journal of Physical Chemistry C*, vol. 121, no. 1, pp. 60–69, 2017.

[223] H. Yao, P. Zhang, C. Yang, Q. Liao, X. Hao, Y. Huang, M. Zhang, X. Wang, T. Lin, H. Cheng, J. Yuan, and L. Qu, "Janus-interface engineering boosting solar steam towards high-efficiency water collection," *Energy Environ. Sci.*, vol. 14, pp. 5330–5338, 2021.

[224] Y. Shi, R. Li, Y. Jin, S. Zhuo, L. Shi, J. Chang, S. Hong, K.-C. Ng, and P. Wang, "A 3d photothermal structure toward improved energy efficiency in solar steam generation," *Joule*, vol. 2, no. 6, pp. 1171–1186, 2018.

[225] D. Ding, W. Huang, C. Song, M. Yan, C. Guo, and S. Liu, “Non-stoichiometric moo3x quantum dots as a light-harvesting material for interfacial water evaporation,” *Chem. Commun.*, vol. 53, pp. 6744–6747, 2017.

[226] F. Wang, N. Xu, W. Zhao, L. Zhou, P. Zhu, X. Wang, B. Zhu, and J. Zhu, “A high-performing single-stage invert-structured solar water purifier through enhanced absorption and condensation,” *Joule*, vol. 5, no. 6, pp. 1602–1612, 2021.

[227] C. Chen, L. Zhou, J. Yu, Y. Wang, S. Nie, S. Zhu, and J. Zhu, “Dual functional asymmetric plasmonic structures for solar water purification and pollution detection,” *Nano Energy*, vol. 51, pp. 451–456, 2018.

[228] M. Gao, C. K. Peh, H. T. Phan, L. Zhu, and G. W. Ho, “Solar absorber gel: Localized macro-nano heat channeling for efficient plasmonic au nanoflowers photothermic vaporization and triboelectric generation,” *Advanced Energy Materials*, vol. 8, no. 25, p. 1800711, 2018.

[229] L. Zhou, Y. Tan, D. Ji, B. Zhu, P. Zhang, J. Xu, Q. Gan, Z. Yu, and J. Zhu, “Self-assembly of highly efficient, broadband plasmonic absorbers for solar steam generation,” *Science Advances*, vol. 2, no. 4, p. e1501227, 2016.

[230] X. Wang, Q. Liu, S. Wu, B. Xu, and H. Xu, “Multilayer polypyrrole nanosheets with self-organized surface structures for flexible and efficient solar–thermal energy conversion,” *Advanced Materials*, vol. 31, no. 19, p. 1807716, 2019.

[231] S. Liu, T. Zhang, S. Li, Q. Wu, K. Wang, X. Xu, M. Lu, R. Shao, W. Zhao, and H. Liu, “Biomimetic nanobomb for synergistic therapy with inhibition of cancer stem cells,” *Small*, vol. 19, no. 12, p. 2206503, 2023.

[232] Z. Yu, K. Zheng, R. Yaguang, M. Wang, Q. Wu, F. Zhou, C. Liu, L. Liu, J. Song, and J. Qu, “Degradable mesoporous semimetal antimony nanospheres for near-infrared ii multimodal theranostics,” *Nature Communications*, vol. 13, 01 2022.

[233] W. Zhu, J. Mei, X. Zhang, J. Zhou, D. Xu, Z. Su, S. Fang, J. Wang, X. Zhang, and C. Zhu, “Photothermal nanozyme-based microneedle patch against refractory bacterial biofilm infection via iron-actuated janus ion therapy,” *Advanced Materials*, vol. 34, no. 51, p. 2207961, 2022.

[234] J. Wang, Z. Sun, S. Wang, C. Zhao, J. Xu, S. Gao, M. Yang, F. Sheng, S. Gao, and Y. Hou, “Biodegradable ferrous sulfide-based nanocomposites for tumor theranostics through specific intratumoral acidosis-induced metabolic symbiosis disruption,” *Journal of the American Chemical Society*, vol. 144, no. 43, pp. 19884–19895, 2022. PMID: 36183257.

[235] H. Zhao, Z. Liu, Y. Wei, L. Zhang, Z. Wang, J. Ren, and X. Qu, “Nir-ii light leveraged dual drug synthesis for orthotopic combination therapy,” *ACS Nano*, vol. 16, no. 12, pp. 20353–20363, 2022. PMID: 36398983.

[236] B. Yang, Y. Zhang, L. Sun, J. Wang, Z. Zhao, Z. Huang, W. Mao, R. Xue, R. Chen, J. Luo, T. Wang, J. Jiang, and Y. Qin, “Modulated ultrasmall -fe2o3 nanocrystal

assemblies for switchable magnetic resonance imaging and photothermal-ferroptotic-chemical synergistic cancer therapy," *Advanced Functional Materials*, vol. 33, no. 5, p. 2211251, 2023.

[237] W. Qin, J. Huang, C. Yang, Q. Yue, S. Chen, M. Wang, S. Gao, X. Zhou, X. Yang, and Y. Zhang, "Protease-activatable nanozyme with photoacoustic and tumor-enhanced magnetic resonance imaging for photothermal ferroptosis cancer therapy," *Advanced Functional Materials*, vol. 33, no. 4, p. 2209748, 2023.

[238] P. Xiao, W. Xie, J. Zhang, Q. Wu, Z. Shen, C. Guo, Y. Wu, F. Wang, B. Z. Tang, and D. Wang, "De novo design of reversibly ph-switchable nir-ii aggregation-induced emission luminogens for efficient phototheranostics of patient-derived tumor xenografts," *Journal of the American Chemical Society*, vol. 145, no. 1, pp. 334–344, 2023. PMID: 36575385.

[239] K. Wen, H. Tan, Q. Peng, H. Chen, H. Ma, L. Wang, A. Peng, Q. Shi, X. Cai, and H. Huang, "Achieving efficient nir-ii type-i photosensitizers for photodynamic/photothermal therapy upon regulating chalcogen elements," *Advanced Materials*, vol. 34, no. 7, p. 2108146, 2022.

[240] H. Bian, D. Ma, F. Pan, X. Zhang, K. Xin, X. Zhang, Y. Yang, X. Peng, and Y. Xiao, "Cardiolipin-targeted nir-ii fluorophore causes "avalanche effects" for re-engaging cancer apoptosis and inhibiting metastasis," *Journal of the American Chemical Society*, vol. 144, no. 49, pp. 22562–22573, 2022. PMID: 36445324.

[241] X. Guo, J. Yang, M. Li, F. Zhang, W. Bu, H. Li, Q. Wu, D. Yin, L. Jiao, and E. Hao, "Unique double intramolecular and intermolecular exciton coupling in ethene-bridged aza-bodipy dimers for high-efficiency near-infrared photothermal conversion and therapy," *Angewandte Chemie International Edition*, vol. 61, no. 44, p. e202211081, 2022.

[242] Y. Bai, P. Huang, N. Feng, Y. Li, J. Huang, H. Jin, M. Zhang, J. Sun, N. Li, H. Zhang, X. Xia, B. Z. Tang, and H. Wang, "Treat the "untreatable" by a photothermal agent: Triggering heat and immunological responses for rabies virus inactivation," *Advanced Science*, vol. 10, no. 2, p. 2205461, 2023.

[243] C. Xu, Y. Jiang, Y. Han, K. Pu, and R. Zhang, "A polymer multicellular nanoengager for synergistic nir-ii photothermal immunotherapy," *Advanced Materials*, vol. 33, no. 14, p. 2008061, 2021.

[244] Y. Xu, C. Li, X. Wu, M.-X. Li, Y. Ma, H. Yang, Q. Zeng, J. L. Sessler, and Z.-X. Wang, "Sheet-like 2d manganese(iv) complex with high photothermal conversion efficiency," *Journal of the American Chemical Society*, vol. 144, no. 41, pp. 18834–18843, 2022. PMID: 36201849.

[245] W. Chen, C. Liu, X. Ji, J. Joseph, Z. Tang, J. Ouyang, Y. Xiao, N. Kong, N. Joshi, O. C. Farokhzad, W. Tao, and T. Xie, "Stanene-based nanosheets for -elemene delivery and ultrasound-mediated combination cancer therapy," *Angewandte Chemie International Edition*, vol. 60, no. 13, pp. 7155–7164, 2021.

[246] Q. Zhang, Q. Guo, Q. Chen, X. Zhao, S. J. Pennycook, and H. Chen, “Highly efficient 2d nir-ii photothermal agent with fenton catalytic activity for cancer synergistic photothermal–chemodynamic therapy,” *Advanced Science*, vol. 7, no. 7, p. 1902576, 2020.

[247] Y. Zhao, T. Zhao, Y. Cao, J. Sun, Q. Zhou, H. Chen, S. Guo, Y. Wang, Y. Zhen, X.-J. Liang, and S. Zhang, “Temperature-sensitive lipid-coated carbon nanotubes for synergistic photothermal therapy and gene therapy,” *ACS Nano*, vol. 15, no. 4, pp. 6517–6529, 2021. PMID: 33749240.

[248] J. Ye, W. Lv, C. Li, S. Liu, X. Yang, J. Zhang, C. Wang, J. Xu, G. Jin, B. Li, Y. Fu, and X. Liang, “Tumor response and nir-ii photonic thermal co-enhanced catalytic therapy based on single-atom manganese nanozyme,” *Advanced Functional Materials*, vol. 32, no. 47, p. 2206157, 2022.

[249] Y. Feng, X. Ning, J. Wang, Z. Wen, F. Cao, Q. You, J. Zou, X. Zhou, T. Sun, J. Cao, and X. Chen, “Mace-like plasmonic au-pd heterostructures boost near-infrared photoimmunotherapy,” *Advanced Science*, vol. 10, no. 6, p. 2204842, 2023.

[250] G. Zhou, Y. Chen, W. Chen, H. Wu, Y. Yu, C. Sun, B. Hu, and Y. Liu, “Renal clearable catalytic 2d au–porphyrin coordination polymer augmented photothermal-gas synergistic cancer therapy,” *Small*, vol. 19, no. 14, p. 2206749, 2023.

[251] H. Arami, S. Kananian, L. Khalifehzadeh, C. Patel, E. Chang, Y. Tanabe, Y. Zeng, S. Madsen, M. Mandella, A. Natarajan, E. Peterson, R. Sinclair, A. Poon, and S. Gambhir, “Remotely controlled near-infrared-triggered photothermal treatment of brain tumours in freely behaving mice using gold nanostars,” *Nature Nanotechnology*, vol. 17, 08 2022.

[252] A. Fluksman, A. Lafuente, Z. Li, J. Sort, S. Lope-Piedrafita, M. J. Esplandiu, J. Nogues, A. G. Roca, O. Benny, and B. Sepulveda, “Efficient tumor eradication at ultralow drug concentration via externally controlled and boosted metallic iron magnetoplasmonic nanocapsules,” *ACS Nano*, vol. 17, no. 3, pp. 1946–1958, 2023. PMID: 36468629.

[253] Y. Ye, J. He, H. Wang, W. Li, Q. Wang, C. Luo, X. Tang, X. Chen, X. Jin, K. Yao, and M. Zhou, “Cell wall destruction and internal cascade synergistic antifungal strategy for fungal keratitis,” *ACS Nano*, vol. 16, no. 11, pp. 18729–18745, 2022. PMID: 36278973.

[254] W. Liu, Y. Wang, Y. Wang, X. Li, K. Qi, J. Wang, and H. Xu, “Black silver nanocubes@amino acid-encoded highly branched gold shells with efficient photothermal conversion for tumor therapy,” *ACS Applied Materials & Interfaces*, vol. 15, no. 1, pp. 236–248, 2023. PMID: 36538335.

[255] H. Li, K. Yang, L. Hai, Z. Wang, Y. Luo, L. He, W. Yi, J. Li, C. Xu, L. Deng, and D. He, “Photothermal-triggered release of alkyl radicals and cascade generation of hydroxyl radicals via a versatile hybrid nanocatalyst for hypoxia-irrelevant synergistic antibiofilm therapy,” *Chemical Engineering Journal*, vol. 455, p. 140903, 2023.

[256] M. Wang, Y. Liang, F. Liao, M. R. Younis, Y. Zheng, X. Zhao, X. Yu, W. Guo, and D.-Y. Zhang, “Iridium tungstate nanozyme-mediated hypoxic regulation and anti-inflammation for duplex imaging guided photothermal therapy of metastatic breast tumors,” *ACS Applied Materials & Interfaces*, vol. 14, no. 51, pp. 56471–56482, 2022. PMID: 36519432.

[257] H. Yan, J. Dong, X. Luan, C. Wang, Z. Song, Q. Chen, J. Ma, and X. Du, “Ultrathin porous nitrogen-doped carbon-coated cuse heterostructures for combination cancer therapy of photothermal therapy, photocatalytic therapy, and logic-gated chemotherapy,” *ACS Applied Materials & Interfaces*, vol. 14, no. 50, pp. 56237–56252, 2022. PMID: 36472929.

[258] A. Pujari, B.-M. Kim, F. N. Sayed, K. Sanders, W. M. Dose, A. Mathieson, C. P. Grey, N. C. Greenham, and M. De Volder, “Does heat play a role in the observed behavior of aqueous photobatteries?,” *ACS Energy Letters*, vol. 8, no. 11, pp. 4625–4633, 2023.

[259] S. Zheng, M. Chen, K. Chen, Y. Wu, J. Yu, T. Jiang, and M. Wu, “Solar-light-responsive zinc–air battery with self-regulated charge–discharge performance based on photothermal effect,” *ACS Applied Materials & Interfaces*, vol. 15, no. 2, pp. 2985–2995, 2023. PMID: 36622791.

[260] P.-F. Wang, X. He, Z.-C. Lv, H. Song, X. Song, T.-F. Yi, N. Xu, P. He, and H. Zhou, “Light-driven polymer-based all-solid-state lithium-sulfur battery operating at room temperature,” *Advanced Functional Materials*, vol. 33, no. 5, p. 2211074, 2023.

[261] B. Bann and S. A. Miller, “Melamine and derivatives of melamine,” *Chemical Reviews*, vol. 58, no. 1, pp. 131–172, 1958.

[262] B. D. Boruah, A. Mathieson, B. Wen, C. Jo, F. Deschler, and M. De Volder, “Photo-rechargeable zinc-ion capacitor using 2d graphitic carbon nitride,” *Nano Letters*, vol. 20, no. 8, pp. 5967–5974, 2020. PMID: 32589038.

[263] S. Wang, Y. Shi, C. Fan, J. Liu, Y. Li, X.-L. Wu, H. Xie, J. Zhang, and H. Sun, “Layered g-c3n4@reduced graphene oxide composites as anodes with improved rate performance for lithium-ion batteries,” *ACS Applied Materials & Interfaces*, vol. 10, no. 36, pp. 30330–30336, 2018. PMID: 30117734.

[264] G. Wang, J. Zhang, and S. Hou, “g-c3n4/conductive carbon black composite as pt-free counter electrode in dye-sensitized solar cells,” *Materials Research Bulletin*, vol. 76, pp. 454–458, 2016.

[265] B. Boruah, A. Mathieson, L. Wen, C. Jo, F. Deschler, and M. Volder, “Photo-rechargeable zinc-ion capacitor using 2d graphitic carbon nitride,” *Nano Letters*, vol. XXXX, 06 2020.

[266] R. Senthil, J. Theerthagiri, J. Madhavan, K. Murugan, P. Arunachalam, and A. Arof, “Enhanced performance of dye-sensitized solar cells based on organic dopant incorporated pvdf-hfp/peo polymer blend electrolyte with g-c3n4/tio2 photoanode,” *Journal of Solid State Chemistry*, vol. 242, pp. 199–206, 2016.

[267] D. Wu, K. Cao, F. Wang, H. Wang, Z. Gao, F. Xu, Y. Guo, and K. Jiang, “Two dimensional graphitic-phase c3n4 as multifunctional protecting layer for enhanced short-circuit photocurrent in zno based dye-sensitized solar cells,” *Chemical Engineering Journal*, vol. 280, pp. 441–447, 2015.

[268] Q. Gao, S. Sun, X. Li, X. Zhang, L. Duan, and W. Lü, “Enhancing performance of cds quantum dot-sensitized solar cells by two-dimensional g-c3n4 modified tio2 nanorods,” *Nanoscale Research Letters*, vol. 11, 12 2016.

[269] Z.-L. Yang, Z.-Y. Zhang, W.-L. Fan, C. sheng Hu, L. Zhang, and J.-J. Qi, “High-performance g-c3n4 added carbon-based perovskite solar cells insulated by al2o3 layer,” *Solar Energy*, vol. 193, pp. 859–865, 2019.

[270] X. Wei, X. Liu, H. Liu, S. Yang, H. Zeng, F. Meng, X. Lei, and J. Liu, “Exfoliated graphitic carbon nitride self-recognizing ch3nh3pbi3 grain boundaries by hydrogen bonding interaction for improved perovskite solar cells,” *Solar Energy*, vol. 181, pp. 161–168, 2019.

[271] L.-L. Jiang, Z.-K. Wang, M. Li, C.-C. Zhang, Q.-Q. Ye, K.-H. Hu, D.-Z. Lu, P.-F. Fang, and L.-S. Liao, “Passivated perovskite crystallization via g-c3n4 for high-performance solar cells,” *Advanced Functional Materials*, vol. 28, no. 7, p. 1705875, 2018.

[272] J. Chen, H. Dong, L. Zhang, J. Li, F. Jia, B. Jiao, J. Xu, X. Hou, J. Liu, and Z. Wu, “Graphitic carbon nitride doped sno2 enabling efficient perovskite solar cells with pces exceeding 22

[273] Y. Liu, N. Li, S. Wu, K. Liao, K. Zhu, J. Yi, and H. Zhou, “Reducing the charging voltage of a li2 battery to 1.9 v by incorporating a photocatalyst,” *Energy Environ. Sci.*, vol. 8, pp. 2664–2667, 2015.

[274] Y. Liu, N. Li, K. Liao, Q. Li, M. Ishida, and H. Zhou, “Lowering the charge voltage of li–o2 batteries via an unmediated photoelectrochemical oxidation approach,” *J. Mater. Chem. A*, vol. 4, pp. 12411–12415, 2016.

[275] E. Lökçü, N. Kaçar, M. Çayirli, R. C. Özden, and M. Anik, “Photoassisted charging of li-ion oxygen batteries using g-c3n4/rgo nanocomposite photocatalysts,” *ACS Applied Materials & Interfaces*, vol. 14, no. 30, pp. 34583–34592, 2022. PMID: 35861585.

[276] N. Kaçar, M. Çayirli, R. C. Özden, E. Lökçü, and M. Anik, “Photocatalytic efficiency of g-c3n4/graphene nanocomposites in the photo-assisted charging of the li-ion oxygen battery,” *ACS Omega*, vol. 8, no. 48, pp. 46227–46235, 2023.

[277] B. Palanivel, S. devi Mudisoodum perumal, T. Maiyalagan, V. Jayarman, C. Ayyappan, and M. Alagiri, “Rational design of znfe2o4/g-c3n4 nanocomposite for enhanced photo-fenton reaction and supercapacitor performance,” *Applied Surface Science*, vol. 498, p. 143807, 2019.

[278] L. Jiang, Y. Qu, Z. Ren, P. Yu, D. Zhao, W. Zhou, L. Wang, and H. Fu, “In situ carbon-coated yolkâ€“shell v2o3 microspheres for lithium-ion batteries,” *ACS Applied Materials & Interfaces*, vol. 7, no. 3, pp. 1595–1601, 2015. PMID: 25569599.

[279] L. Bai, J. Zhu, X. Zhang, and Y. Xie, "Reducing hydrated protons co-intercalation to enhance cycling stability of cuv2o5 nanobelts: a new anode material for aqueous lithium ion batteries," *J. Mater. Chem.*, vol. 22, pp. 16957–16963, 2012.

[280] Y. L. Cheah, V. Aravindan, and S. Madhavi, "Improved elevated temperature performance of al-intercalated v2o5 electrospun nanofibers for lithium-ion batteries," *ACS Applied Materials & Interfaces*, vol. 4, no. 6, pp. 3270–3277, 2012. PMID: 22616641.

[281] S. S. Patil, D. P. Dubal, M. S. Tamboli, J. D. Ambekar, S. S. Kolekar, P. Gomez-Romero, B. B. Kale, and D. R. Patil, "Ag:bivo4 dendritic hybrid-architecture for high energy density symmetric supercapacitors," *J. Mater. Chem. A*, vol. 4, pp. 7580–7584, 2016.

[282] Z. Khan, S. Bhattu, S. Haram, and D. Khushalani, "Swcnt/bivo4 composites as anode materials for supercapacitor application," *RSC Adv.*, vol. 4, pp. 17378–17381, 2014.

[283] K. Sayama, A. Nomura, T. Arai, T. Sugita, R. Abe, M. Yanagida, T. Oi, Y. Iwasaki, Y. Abe, and H. Sugihara, "Photoelectrochemical decomposition of water into h2 and o2 on porous bivo4 thin-film electrodes under visible light and significant effect of ag ion treatment," *The Journal of Physical Chemistry B*, vol. 110, no. 23, pp. 11352–11360, 2006. PMID: 16771406.

[284] A. Kudo, K. Omori, and H. Kato, "A novel aqueous process for preparation of crystal form-controlled and highly crystalline bivo4 powder from layered vanadates at room temperature and its photocatalytic and photophysical properties," *Journal of the American Chemical Society*, vol. 121, no. 49, pp. 11459–11467, 1999.

[285] H. Luo, A. H. Mueller, T. M. McCleskey, A. K. Burrell, E. Bauer, and Q. X. Jia, "Structural and photoelectrochemical properties of bivo4 thin films," *The Journal of Physical Chemistry C*, vol. 112, no. 15, pp. 6099–6102, 2008.

[286] Y. Ma, S. R. Pendlebury, A. Reynal, F. Le Formal, and J. R. Durrant, "Dynamics of photogenerated holes in undoped bivo4 photoanodes for solar water oxidation," *Chem. Sci.*, vol. 5, pp. 2964–2973, 2014.

[287] Long, Cai, and H. Kisch, "Visible light induced photoelectrochemical properties of n-bivo4 and n-bivo4/p-co3o4," *The Journal of Physical Chemistry C*, vol. 112, no. 2, pp. 548–554, 2008.

[288] D. P. Dubal, D. R. Patil, S. S. Patil, N. R. Munirathnam, and P. Gomez-Romero, "Bivo4 fern architectures: A competitive anode for lithium-ion batteries," *ChemSusChem*, vol. 10, no. 21, pp. 4163–4169, 2017.

[289] L. Zhou, S.-Y. Shen, X.-X. Peng, L. Wu, Q. Wang, C.-H. Shen, T.-T. Tu, L. Huang, J.-T. Li, and S.-G. Sun, "New insights into the structure changes and interface properties of li3vo4 anode for lithium-ion batteries during the initial cycle by in-situ techniques," *ACS Applied Materials & Interfaces*, vol. 8, no. 36, pp. 23739–23745, 2016. PMID: 27556414.

[290] Y. Li, M. A. Trujillo, E. Fu, B. Patterson, L. Fei, Y. Xu, S. Deng, S. Smirnov, and H. Luo, "Bismuth oxide: a new lithium-ion battery anode," *J. Mater. Chem. A*, vol. 1, pp. 12123–12127, 2013.

[291] M. M. Momeni, A. S. Renani, and B.-K. Lee, “Light-chargeable two-electrode photo-supercapacitors based on mns nanoflowers deposited on v2o5-bivo4 photoelectrodes,” *Journal of Alloys and Compounds*, vol. 962, p. 171204, 2023.

[292] T. S. Andrade, I. C. Sena, L. C. A. de Oliveira, P. Lianos, and M. C. Pereira, “Decreasing the charging voltage of a zinc-air battery using a bifunctional w:bivo4/v2o5 photoelectrode and sulfite as a sacrificial agent,” *Materials Today Communications*, vol. 28, p. 102546, 2021.

[293] Y. Li, J. Zhu, H. Chu, J. Wei, F. Liu, M. Lv, J. Tang, B. Zhang, J. Yao, Z. Huo, L. Hu, and S. Dai, “Bivo4 semiconductor sensitized solar cells,” *Science China Chemistry*, vol. 58, 03 2015.

[294] S. Daemi, S. Kaushik, S. Das, T. W. Hamann, and F. E. Osterloh, “Bivo4–liquid junction photovoltaic cell with 0.2% solar energy conversion efficiency,” *Journal of the American Chemical Society*, vol. 145, no. 47, pp. 25797–25805, 2023. PMID: 37964539.

[295] J. Zhang, W. Luo, W. Li, X. Zhao, G. Xue, T. Yu, C. Zhang, M. Xiao, Z. Li, and Z. Zou, “A dye-free photoelectrochemical solar cell based on bivo4 with a long lifetime of photogenerated carriers,” *Electrochemistry Communications*, vol. 22, pp. 49–52, 2012.

[296] W. Nareejun and C. Ponchio, “Novel photoelectrocatalytic/solar cell improvement for organic dye degradation based on simple dip coating wo3/bivo4 photoanode electrode,” *Solar Energy Materials and Solar Cells*, vol. 212, p. 110556, 2020.

[297] S. Safshekan, I. Herraiz-Cardona, D. Cardenas-Morcoso, R. Ojani, M. Haro, and S. Gimenez, “Solar energy storage by a heterostructured bivo4–pbox photocapacitive device,” *ACS Energy Letters*, vol. 2, no. 2, pp. 469–475, 2017.

[298] H. Gong, H. Xue, B. Gao, Y. Li, X. Fan, S. Zhang, T. Wang, and J. He, “Introduction of photo electrochemical water-oxidation mechanism into hybrid lithium–oxygen batteries,” *Energy Storage Materials*, vol. 31, pp. 11–19, 2020.

[299] C. Lin, J. Wang, H. He, X. Liu, F. Qiu, Q. Jin, H. Li, Y. Sun, S. Li, Y. Zhang, and T. Ma, “Self-charged dual-photoelectrode vanadium–iron energy storage battery,” *Advanced Energy Materials*, vol. 14, no. 2, p. 2303126, 2024.

[300] M. Dong, Y. Wang, A. Li, and C. Cheng, “Three-dimensional bivo4-based semiconductor photocathode for high efficiency photo-assisted zn-iodine redox flow batteries,” *Nanotechnology*, vol. 33, p. 265401, apr 2022.

[301] B. Zhang, Y. Xiang, M. Guo, J. Wang, K. Liu, W. Lin, and G. Ma, “Fabrication of a facet-oriented bivo4 photoanode by particle engineering for promotion of charge separation efficiency,” *ACS Applied Energy Materials*, vol. 4, no. 4, pp. 4259–4268, 2021.

[302] J. Wen, J. Xie, X. Chen, and X. Li, “A review on g-c3n4-based photocatalysts,” *Applied Surface Science*, vol. 391, pp. 72–123, 2017. 2nd International Symposium on Energy and Environmental Photocatalytic Materials.

[303] S. Ye, R. Wang, M.-Z. Wu, and Y.-P. Yuan, “A review on g-c3n4 for photocatalytic water splitting and co2 reduction,” *Applied Surface Science*, vol. 358, pp. 15–27, 2015.

[304] S. A. Thomas, M. R. Pallavolu, M. E. Khan, and J. Cherusseri, “Graphitic carbon nitride (g-c3n4): Futuristic material for rechargeable batteries,” *Journal of Energy Storage*, vol. 68, p. 107673, 2023.

[305] A. Walsh, Y. Yan, M. N. Huda, M. M. Al-Jassim, and S.-H. Wei, “Band edge electronic structure of bivo4: Elucidating the role of the bi s and v d orbitals,” *Chemistry of Materials*, vol. 21, no. 3, pp. 547–551, 2009.

[306] Y. Zhao, Y. Xie, X. Zhu, S. Yan, and S. Wang, “Surfactant-free synthesis of hyperbranched monoclinic bismuth vanadate and its applications in photocatalysis, gas sensing, and lithium-ion batteries,” *Chemistry–A European Journal*, vol. 14, no. 5, pp. 1601–1606, 2008.

[307] T. Zijian Zhao, W. M. Dose, and M. F. L. De Volder, “A combined lithium intercalation and plating mechanism using conductive carbon-fiber electrodes,” *Batteries & Supercaps*, vol. 5, no. 5, p. e202100399, 2022.

[308] A. Pujari, B.-M. Kim, F. N. Sayed, K. Sanders, W. M. Dose, A. Mathieson, C. P. Grey, N. C. Greenham, and M. De Volder, “Does heat play a role in the observed behavior of aqueous photobatteries?,” *ACS Energy Letters*, vol. 8, no. 11, pp. 4625–4633, 2023.

[309] A. Kraft, “What a chemistry student should know about the history of prussian blue,” *ChemTexts*, vol. 4, 10 2018.

[310] H. J. Buser, A. Ludi, W. Petter, and D. Schwarzenbach, “Single-crystal study of prussian blue: Fe4[fe(cn)6]2, 14h2o,” *J. Chem. Soc., Chem. Commun.*, pp. 1299–1299, 1972.

[311] A. Dostal, G. Kauschka, S. Reddy, and F. Scholz, “Lattice contractions and expansions accompanying the electrochemical conversions of prussian blue and the reversible and irreversible insertion of rubidium and thallium ions,” *Journal of Electroanalytical Chemistry*, vol. 406, no. 1, pp. 155–163, 1996.

[312] M. Okubo, D. Asakura, Y. Mizuno, J.-D. Kim, T. Mizokawa, T. Kudo, and I. Honma, “Switching redox-active sites by valence tautomerism in prussian blue analogues axmny[fe(cn)6]Â·nh2o (a: K, rb): Robust frameworks for reversible li storage,” *The Journal of Physical Chemistry Letters*, vol. 1, no. 14, pp. 2063–2071, 2010.

[313] F. Scholz and A. Dostal, “The formal potentials of solid metal hexacyanometalates,” *Angewandte Chemie International Edition in English*, vol. 34, no. 23-24, pp. 2685–2687, 1996.

[314] W. Wang, Y. Gang, Z. Hu, Z. Yan, W. Li, Y. Li, Z. Wang, S.-L. Chou, and S.-X. Dou, “Reversible structural evolution of sodium-rich rhombohedral prussian blue for sodium-ion batteries,” *Nature Communications*, vol. 11, 02 2020.

[315] C. Fang, Y. Huang, W. Zhang, J. Han, Z. Deng, Y. Cao, and H. Yang, “Routes to high energy cathodes of sodium-ion batteries,” *Advanced Energy Materials*, vol. 6, no. 5, p. 1501727, 2016.

[316] X. Wu, M. Shao, C. Wu, J. Qian, Y. Cao, X. Ai, and H. Yang, “Low defect fefe(cn)6 framework as stable host material for high performance li-ion batteries,” *ACS Applied Materials & Interfaces*, vol. 8, no. 36, pp. 23706–23712, 2016. PMID: 27556906.

[317] T. Wei, R. Zeng, Y. Sun, Y. Huang, and K. Huang, “A reversible and stable flake-like licoo2 cathode for lithium ion batteries,” *Chem. Commun.*, vol. 50, pp. 1962–1964, 2014.

[318] G. Dacarro, A. Taglietti, and P. Pallavicini, “Prussian blue nanoparticles as a versatile photothermal tool,” *Molecules*, vol. 23, no. 6, 2018.

[319] H. A. Hoffman, L. Chakrabarti, M. F. Dumont, A. D. Sandler, and R. Fernandes, “Prussian blue nanoparticles for laser-induced photothermal therapy of tumors,” *RSC Adv.*, vol. 4, pp. 29729–29734, 2014.

[320] G. Fu, W. Liu, S. Feng, and X. Yue, “Prussian blue nanoparticles operate as a new generation of photothermal ablation agents for cancer therapy,” *Chem. Commun.*, vol. 48, pp. 11567–11569, 2012.

[321] Q. Wang, Q. Sun, Y. Pu, W. Sun, C. Lin, X. Duan, X. Ren, and L. Lu, “Photo-thermal mediated li-ion transport for solid-state lithium metal batteries,” *Small*, vol. n/a, no. n/a, p. 2309501.

[322] Z. Zhang, M. Avdeev, H. Chen, W. Yin, W. Kan, and G. He, “Lithiated prussian blue analogues as positive electrode active materials for stable non-aqueous lithium-ion batteries,” *Nature Communications*, vol. 13, 12 2022.

[323] K. Hurlbutt, S. Wheeler, I. Capone, and M. Pasta, “Prussian blue analogs as battery materials,” *Joule*, vol. 2, no. 10, pp. 1950–1960, 2018.

[324] J. Li, X. Liu, L. Tan, Z. Cui, X. Yang, Y. Liang, Z. Li, S. Zhu, Y. Zheng, K. Yeung, X. Wang, and S. Wu, “Zinc-doped prussian blue enhances photothermal clearance of staphylococcus aureus and promotes tissue repair in infected wounds,” *Nature Communications*, vol. 10, 10 2019.

[325] W. W. Gärtner, “Photothermal effect in semiconductors,” *Phys. Rev.*, vol. 122, pp. 419–424, Apr 1961.

[326] W. Shockley and W. T. Read, “Statistics of the recombinations of holes and electrons,” *Phys. Rev.*, vol. 87, pp. 835–842, Sep 1952.

[327] M. Ghoussoub, M. Xia, P. N. Duchesne, D. Segal, and G. Ozin, “Principles of photothermal gas-phase heterogeneous co2 catalysis,” *Energy Environ. Sci.*, vol. 12, pp. 1122–1142, 2019.

[328] L. B. Hoch, P. Szymanski, K. K. Ghuman, L. He, K. Liao, Q. Qiao, L. M. Reyes, Y. Zhu, M. A. El-Sayed, C. V. Singh, and G. A. Ozin, “Carrier dynamics and the role of surface defects: Designing a photocatalyst for gas-phase co₂ reduction,” *Proceedings of the National Academy of Sciences*, vol. 113, no. 50, pp. E8011–E8020, 2016.

[329] G. Dacarro, A. Taglietti, and P. Pallavicini, "Prussian blue nanoparticles as a versatile photothermal tool," *Molecules*, vol. 23, no. 6, p. 1414, 2018.

[330] G. Fu, W. Liu, Y. Li, Y. Jin, L. Jiang, X. Liang, S. Feng, and Z. Dai, "Magnetic prussian blue nanoparticles for targeted photothermal therapy under magnetic resonance imaging guidance," *Bioconjugate chemistry*, vol. 25, no. 9, pp. 1655–1663, 2014.

[331] J. Cano-Mejia, R. A. Burga, E. E. Sweeney, J. P. Fisher, C. M. Bollard, A. D. Sandler, C. R. Y. Cruz, and R. Fernandes, "Prussian blue nanoparticle-based photothermal therapy combined with checkpoint inhibition for photothermal immunotherapy of neuroblastoma," *Nanomedicine: Nanotechnology, Biology and Medicine*, vol. 13, no. 2, pp. 771–781, 2017.

[332] X. Cai, W. Gao, L. Zhang, M. Ma, T. Liu, W. Du, Y. Zheng, H. Chen, and J. Shi, "Enabling prussian blue with tunable localized surface plasmon resonances: simultaneously enhanced dual-mode imaging and tumor photothermal therapy," *ACS nano*, vol. 10, no. 12, pp. 11115–11126, 2016.

[333] J. Wojdeł, I. Moreira, S. Bromley, and F. Illas, "On the prediction of the crystal and electronic structure of mixed-valence materials by periodic density functional calculations: The case of prussian blue," *The Journal of chemical physics*, vol. 128, p. 044713, 02 2008.

[334] Y. Tang, W. Zhang, L. Xue, X. Ding, T. Wang, X. Liu, J. Liu, X. Li, and Y. Huang, "Polypyrrole-promoted superior cyclability and rate capability of naxfe[fe(cn)6] cathodes for sodium-ion batteries," *J. Mater. Chem. A*, vol. 4, pp. 6036–6041, 2016.

[335] Y. You, H.-R. Yao, S. Xin, Y.-X. Yin, T.-T. Zuo, C.-P. Yang, Y.-G. Guo, Y. Cui, L.-J. Wan, and J. B. Goodenough, "Subzero-temperature cathode for a sodium-ion battery," *Advanced Materials*, vol. 28, no. 33, pp. 7243–7248, 2016.

[336] A. Kumar, S. M. Yusuf, and L. Keller, "Structural and magnetic properties of $Fe[Fe(CN)_6]4h_2O$," *Phys. Rev. B*, vol. 71, p. 054414, Feb 2005.

[337] X. Wu, M. Shao, C. Wu, J. Qian, Y. Cao, X. Ai, and H. Yang, "Low defect fefe(cn)6 framework as stable host material for high performance li-ion batteries," *ACS Applied Materials & Interfaces*, vol. 8, no. 36, pp. 23706–23712, 2016. PMID: 27556906.

[338] D. Yu, C. Fietzek, W. Weydanz, K. Donoue, T. Inoue, H. Kurokawa, and S. Fujitani, "Study of lifepo[sub 4] by cyclic voltammetry," *Journal of The Electrochemical Society*, vol. 154, pp. A253–A257, 04 2007.

[339] M. Park, X. Zhang, M. Chung, G. B. Less, and A. M. Sastry, "A review of conduction phenomena in li-ion batteries," *Journal of Power Sources*, vol. 195, no. 24, pp. 7904–7929, 2010.

[340] D. Abraham, S. Kawauchi, and D. Dees, "Modeling the impedance versus voltage characteristics of lini0.8co0.15al0.05o2," *Electrochimica Acta*, vol. 53, no. 5, pp. 2121–2129, 2008.

[341] M.-S. Wu, P.-C. Chiang, and J.-C. Lin, “Electrochemical investigations on advanced lithium-ion batteries by three-electrode measurements,” *Journal of The Electrochemical Society*, vol. 152, pp. A47–A52, 01 2005.

[342] G. Baffou, I. Bordacchini, A. Baldi, and R. Quidant, “Simple experimental procedures to distinguish photothermal from hot-carrier processes in plasmonics,” *Light: Science Applications*, vol. 9, p. 108, 06 2020.

[343] J. Zhu, L. Huang, F. Bao, G. Chen, K. Song, Z. Wang, H. Xia, J. Gao, Y. Song, C. Zhu, F. Lu, T. Zheng, and M. Ji, “Carbon materials for enhanced photothermal conversion: Preparation and applications on steam generation,” *Materials Reports: Energy*, p. 100245, 2023.

[344] T. yi Wang, H. bo Huang, H. liang Li, Y. kun Sun, Y. hua Xue, S. ning Xiao, and J. he Yang, “Carbon materials for solar-powered seawater desalination,” *New Carbon Materials*, vol. 36, no. 4, pp. 683–701, 2021.

[345] X. Chen, N. Yang, Y. Wang, H. He, J. Wang, J. Wan, H. Jiang, B. Xu, L. Wang, R. Yu, L. Tong, L. Gu, Q. Xiong, C. Chen, S. Zhang, and D. Wang, “Highly efficient photothermal conversion and water transport during solar evaporation enabled by amorphous hollow multishelled nanocomposites,” *Advanced Materials*, vol. 34, no. 7, p. 2107400, 2022.

[346] J. Zhu, L. Huang, F. Bao, G. Chen, K. Song, Z. Wang, H. Xia, J. Gao, Y. Song, C. Zhu, F. Lu, T. Zheng, and M. Ji, “Carbon materials for enhanced photothermal conversion: Preparation and applications on steam generation,” *Materials Reports: Energy*, vol. 4, no. 2, p. 100245, 2024.

[347] A. Mathieson, S. Feldmann, and M. De Volder, “Solid-state lithium-ion batteries as a method for doping halide perovskites with an in situ optical readout of dopant concentration,” *JACS Au*, vol. 2, no. 6, pp. 1313–1317, 2022.

[348] A. Pujari, B.-m. Kim, N. C. Greenham, and M. De Volder, “Identifying current collectors that enable light–battery interactions,” *Small Methods*, vol. n/a, no. n/a, p. 2301572.

[349] R. Cao, J.-S. Lee, M. Liu, and J. Cho, “Recent progress in non-precious catalysts for metal-air batteries,” *Advanced Energy Materials*, vol. 2, no. 7, pp. 816–829, 2012.

[350] T. Luttrell, S. Halpegamage, J. Tao, A. Kramer, E. Sutter, and M. Batzill, “Why is anatase a better photocatalyst than rutile? - model studies on epitaxial tio2 films,” *Scientific reports*, vol. 4, p. 4043, 02 2014.

[351] D. O. Scanlon, C. W. Dunnill, J. Buckeridge, S. A. Shevlin, A. J. Logsdail, S. M. Woodley, C. R. A. Catlow, M. J. Powell, R. G. Palgrave, I. P. Parkin, *et al.*, “Band alignment of rutile and anatase tio2,” *Nature materials*, vol. 12, no. 9, pp. 798–801, 2013.

[352] M. Mishra and D.-M. Chun, “α-fe2o3 as a photocatalytic material: A review,” *Applied Catalysis A: General*, vol. 498, pp. 126–141, 2015.

[353] Y.-S. Hu, L. Kienle, Y.-G. Guo, and J. Maier, “High lithium electroactivity of nanometer-sized rutile tio2,” *Advanced Materials*, vol. 18, no. 11, pp. 1421–1426, 2006.

[354] S. Liang, X. Wang, Y.-J. Cheng, Y. Xia, and P. Müller-Buschbaum, “Anatase titanium dioxide as rechargeable ion battery electrode - a chronological review,” *Energy Storage Materials*, vol. 45, pp. 201–264, 2022.

[355] X. Tian, Q. Gao, H. Zhang, Z. Li, H. Xiao, Q. Zhang, and L. Ma, “Uniform small-sized mos2 from novel solution-based microwave-assisted method with exceptional reversible lithium storage properties,” *Nanoscale*, vol. 10, pp. 15222–15228, 2018.

[356] Y. Hu, Y. Pan, Z. Wang, T. Lin, Y. Gao, B. Luo, H. Hu, F. Fan, G. Liu, and L. Wang, “Lattice distortion induced internal electric field in tio2 photoelectrode for efficient charge separation and transfer,” *Nature Communications*, vol. 11, no. 1, p. 2129, 2020.

[357] O. Nguyen, F. Sauvage, E. Courtin, N. Krins, C. Sanchez, and C. Laberty-Robert, “Shedding light on light-driven lithium ion de-insertion reaction: towards the design of a photo-rechargeable battery,” *J. Mater. Chem. A*, vol. 5, 03 2017.

[358] J. Zhang, P. Zhou, J. Liu, and J. Yu, “New understanding of the difference of photocatalytic activity among anatase, rutile and brookite tio 2,” *Physical Chemistry Chemical Physics*, vol. 16, no. 38, pp. 20382–20386, 2014.

[359] A. Pujari, B.-M. Kim, N. Greenham, and M. Volder, “Identifying current collectors that enable light-battery interactions,” *Small methods*, p. e2301572, 05 2024.

[360] C. Howard, T. Sabine, and F. Dickson, “Structural and thermal parameters for rutile and anatase,” *Acta Crystallographica Section B: Structural Science*, vol. 47, no. 4, pp. 462–468, 1991.

[361] D. Su, S. Dou, and G. Wang, “Anatase tio2: better anode material than amorphous and rutile phases of tio2 for na-ion batteries,” *Chemistry of Materials*, vol. 27, no. 17, pp. 6022–6029, 2015.